



Universiteit
Leiden
The Netherlands

Molecular fingerprints of star formation throughout the Universe : a space-based infrared study

Lahuis, F.

Citation

Lahuis, F. (2007, May 9). *Molecular fingerprints of star formation throughout the Universe : a space-based infrared study*. Retrieved from <https://hdl.handle.net/1887/11950>

Version: Corrected Publisher's Version

License: [Licence agreement concerning inclusion of doctoral thesis in the Institutional Repository of the University of Leiden](#)

Downloaded from: <https://hdl.handle.net/1887/11950>

Note: To cite this publication please use the final published version (if applicable).

Molecular fingerprints of star formation throughout the Universe

– a space-based infrared study –

Cover: *Pillars of Creation* by Marike Vrieling plus the observed spectra of the basic ingredients for life (Figure 1.3 and Chapter 7).

Printed by: Stichting Drukkerij C. Regenboog

Molecular fingerprints of star formation throughout the Universe

– a space-based infrared study –

PROEFSCHRIFT

ter verkrijging van
de graad van Doctor aan de Universiteit Leiden,
op gezag van Rector Magnificus Prof. mr. P. F. van der Heijden,
volgens besluit van het College voor Promoties
te verdedigen op woensdag 9 Mei 2007
klokke 13.45 uur

door

Frederik Lahuis
geboren te Smilde
in 1965

PROMOTIECOMMISSIE

Promotor: Prof. dr. E. F. van Dishoeck

Referent: Prof. dr. M. W. M. de Graauw (SRON Netherlands Institute
for Space Research)

Overige leden: Prof. dr. P. T. de Zeeuw
Prof. dr. N. J. Evans II (University of Texas, USA)
Dr. M. R. Hogerheijde
Prof. dr. F. P. Israel
Dr. P. R. Roelfsema (SRON Netherlands Institute
for Space Research)
Prof. dr. A. G. G. M. Tielens (NASA Ames Research Center)

Contents

1	Introduction	1
1.1	Star formation	4
1.1.1	Low-mass star formation	4
1.1.2	High-mass star formation	5
1.1.3	Ultraluminous infrared galaxies	6
1.2	Infrared spectroscopic data	7
1.3	Infrared space instruments	8
1.4	Physicochemical properties	9
1.4.1	Hot dense regions	10
1.4.2	High temperature chemistry	11
1.5	Outline of this thesis	11
2	ISO–SWS Signal Capture	13
2.1	Introduction	14
2.2	SWS detectors and detector read-out	14
2.2.1	Detectors artifacts	14
2.2.2	Reset of 24 Hz read-out signal	16
2.2.3	Read-out electronics	16
2.2.4	System noise	17
2.3	Calibration and data reduction	17
2.4	Deglitching of SWS low resolution data	19
2.5	Requirements	21
2.5.1	SWS glitch detection	22
2.5.2	Correcting the ramp derivative	22
2.5.3	Slope fitting	23
2.5.4	Deglitching results	23
2.6	Conclusions	24
3	From Molecular Cores to Planet Forming Disks – a c2d data legacy –	25
3.1	Introduction	26
3.2	Reduction of IRS pointed observations	29
3.2.1	Bad/hot pixels	29
3.2.2	Spectral extraction	31
3.2.3	The IRS cross dispersion PSF	33
3.2.4	Spectral Response Function (SRF)	34
3.2.5	Error propagation	35
3.2.6	Defringing	36
3.2.7	Order matching	37

3.3	Data products of IRS pointed observations	38
3.3.1	IRS c2d products	38
3.3.2	Source parameters	39
3.3.3	Extended emission	40
3.3.4	Final source spectrum	41
3.3.5	IRS artifacts	44
3.3.6	Spikes	44
3.3.7	Edge effects	45
3.3.8	Module mismatches	46
3.3.9	Spectral features	46
3.4	Summary	50
4	ISO-SWS Spectroscopy of Gas-Phase C₂H₂ and HCN Toward Massive Young Stellar Objects	53
4.1	Introduction	54
4.2	Observations and data reduction	56
4.2.1	Observations and sources	56
4.2.2	Data reduction	56
4.3	Model spectra and fits	58
4.3.1	Synthetic spectra	59
4.3.2	Hot bands	61
4.3.3	Model fits	62
4.4	Results	63
4.4.1	AFGL 2591	67
4.4.2	AFGL 2136	67
4.4.3	AFGL 4176	67
4.4.4	W 33 A	68
4.4.5	W 3 IRS 5	68
4.4.6	NGC 7538 IRS 1 and IRS 9	68
4.4.7	Other sources	68
4.5	Discussion	69
4.5.1	Excitation temperature	69
4.5.2	Column densities and abundances	71
4.5.3	Chemistry	73
4.6	Conclusions	74
5	c2d <i>Spitzer</i> IRS Spectra of Disks around T Tauri Stars	
	III. [Ne II] and H₂ gas-phase lines	75
5.1	Introduction	76
5.2	Observations	79
5.2.1	Source selection	79
5.2.2	SH mini maps	79
5.3	Data reduction	80
5.3.1	Separating disk and cloud emission – optimal extraction	80
5.3.2	1-D spectra	81
5.3.3	Spectral analysis	82

5.4	Results	82
5.4.1	Atomic fine-structure lines: Neon	82
5.4.2	Atomic fine-structure lines: Other species	84
5.4.3	Molecular hydrogen	84
5.4.4	Correlations	87
5.5	Discussion	88
5.5.1	[Ne II]	88
5.5.2	[Fe I] and [S I]	91
5.5.3	Molecular hydrogen	91
5.6	Conclusions	93
6	c2d <i>Spitzer</i> IRS Spectra of Embedded Protostars: Gas-phase Lines	103
6.1	Introduction	104
6.2	Observations and data reduction	105
6.3	Results	107
6.3.1	Atomic fine-structure lines	107
6.3.2	Molecular hydrogen	107
6.3.3	Correlations	110
6.4	Discussion	110
6.4.1	Extended emission	112
6.4.2	Spatially unresolved emission	112
6.4.3	Hot H ₂	114
6.5	Conclusions	115
7	Hot Organic Molecules Toward a Young Low-mass Star: a Look at Inner Disk Chemistry	125
7.1	Introduction	126
7.2	Observations	127
7.3	Analysis	128
7.4	Discussion	130
8	Infrared Molecular Starburst Fingerprints in Deeply Obscured (Ultra)Luminous Infrared Galaxy Nuclei	133
8.1	Introduction	134
8.2	Observations	135
8.3	Analysis	137
8.3.1	Molecular analysis	137
8.3.2	Fit results	138
8.3.3	Abundances	139
8.3.4	Gas temperature	140
8.4	Discussion	142
8.4.1	Warm molecular gas in (U)LIRGs	142
8.4.2	AGN activity and X-ray-driven chemistry	142
8.4.3	Static hot-core chemistry	144
8.4.4	Pressure confined starburst chemistry	144
8.5	Summary	145

Contents	iv
Bibliography	147
Nederlandse Samenvatting	155
Curriculum Vitae	161
Papers in Refereed Journals	162
Nawoord	163

Chapter 1

Introduction

“A wise person must be able to see the unseen and know the unknown.”

From: *The Greatest Power* by Demi
(author/illustrator of children's books)

The young emperor Ping wants to bring the harmony of the heavens, which he views through his telescope, to his kingdom. To accomplish this he invites all the children in his kingdom for a year-long quest in search of the greatest power. He sends them out with the instruction

“A wise person must be able to see the unseen and know the unknown.”

The child who succeeds will become prime minister. After a year the children present their findings. Some bring great weapons, others great beauty, great technology, or large amounts of money. The last child, a little girl named Sing, has reflected upon Ping's words.

She presents a lotus seed, splits it before emperor Ping and speaks,

“The nothing in this seed is the space in between where life exists.”

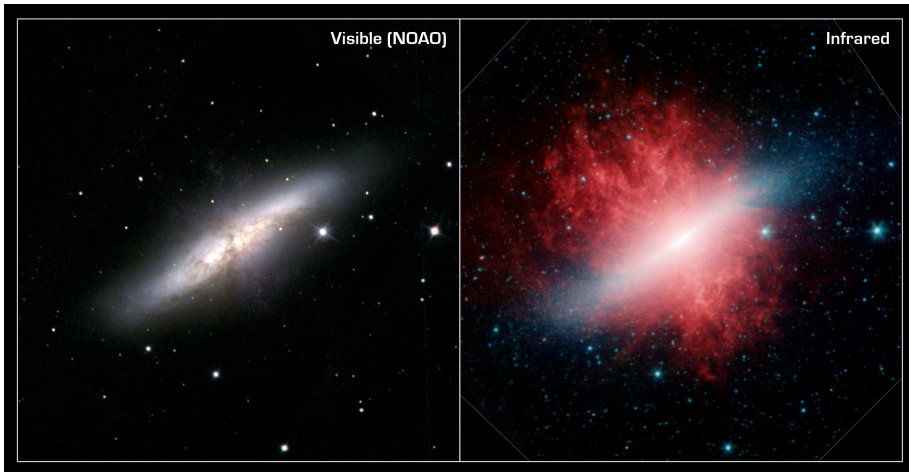
Emperor Ping is pleased and appoints her as prime minister.



© NASA/JPL-Caltech/L. Cieza (Univ. of Texas at Austin)

Figure 1.1 *Spitzer* IRAC 3.6, 4.5, 8.0 μm and MIPS 24 μm composite image of IC 348, a star forming cluster located 1,043 light years away from Earth in the Perseus Molecular Cloud. A large number of young stars still embedded in their envelope (reddish-pink dots) are seen in the midst of bright extended emission from heated polycyclic aromatic hydrocarbon (PAH) molecules and small dust grains in the cloud. PAH are excited by the radiation from neighboring stars and shine brightly in the infrared.

To see the unseen ... to know the unknown What could better apply to astronomy and in particular to the field of star formation. We now know that large numbers of young newborn stars exist in pieces of the sky that were previously believed to be devoid of stars – stars invisible in the visible. Star formation takes place in a mostly unseen world, i.e., unseen at visible wavelengths. Stars are born deep in dark molecular clouds and surrounded by dense envelopes – dust and gas-rich shells –, in which their initial growth takes place. When looked at in the infrared, these dark clouds prove to be very rich with a multitude of new-born stars. The first infrared satellite, the Infrared Astronomical Satellite (IRAS), operating in the eighties of the last century, mapped the complete sky in infrared light. It showed us an exciting and bright Universe filled with star formation from the local Universe in our Milky-Way out to the most distant galaxies. Figure 1.1 shows a *Spitzer* composite image of a star forming region in Perseus revealing multiple young stars in between the large scale emission of heated Polycyclic Aromatic Hydrocarbon (PAH) dust particles in the cloud.



© NASA/JPL-Caltech/C. Engelbracht (University of Arizona)

Figure 1.2 Images in visible (left) and infrared (right) light of the Starburst galaxy M82. In the visible M82 looks like a normal galaxy. However, in the infrared a completely different galaxy is seen. The massive stars formed in the starburst reside in what shows up as a white band across the infrared image. Above and below this are huge amounts of hot gas blown away by the massive stars. For the full story see the NASA press release at:

<http://www.spitzer.caltech.edu/Media/releases/ssc2006-09/>

This thesis takes us through the infrared Universe in a few big leaps, from the disks around low-mass protostars to the envelopes around massive protostars ending up in the nuclei of distant ultraluminous infrared galaxies. A specific type of source is clearly not the central theme of this thesis. Instead the common factor is star formation itself and the chemical and physical processes taking place in the (dense) warm gas involved in the process. The methods by which these can be studied, by using space-based infrared spectroscopic instruments, is the second key aspect of this thesis.

In the Earth's atmosphere most of the infrared radiation is absorbed by molecules, in particular water and carbon dioxide, prohibiting the observation of large parts of the infrared spectrum by ground-based instruments. Even from observatories at very high altitudes, like those on Mauna Kea in Hawaii, large parts of the infrared spectrum cannot be observed. Therefore the use of satellites, with infrared spectrometers, is essential for the study of star formation. In the last decade two major infrared satellites with strong spectroscopic capabilities (ISO and *Spitzer*, see §1.3 and Table 1.1) were launched with *Spitzer* still operational. In this thesis I make use of data from two mid-infrared spectrographs (the ISO-SWS and *Spitzer* IRS) on board of these satellites.

In molecular clouds where star formation takes place most of the radiation produced in the process is absorbed by the dust in the surrounding envelope and re-emitted in the infrared. Molecules and atoms in the cloud are heated and emit or absorb the radiation emitted by the dust. Each molecule or atom emits or absorbs light at very specific wavelengths, its spectral fingerprint. The detailed patterns of these fingerprints depend on the temperatures, the composition, the density, and the velocity structure of the gas. Thus, the analysis of these fingerprints provides the observer with

a physicochemical snapshot of the regions. The main aim of this thesis is to analyze the origin of the observed radiation and use these fingerprints to determine the nature and evolutionary phase of the sources.

1.1 Star formation

The stars in the Universe are extremely diverse. Stars with a large variation in mass and energy output (luminosity) are found, isolated or in groups. Low-mass stars like our Sun have masses and luminosities of a few tenth (down to the hydrogen burning limit of $0.08M_{\odot}$) up to a few times solar. Massive stars have masses up to tens of solar masses and an energy output of ten thousand to a hundred thousand times the energy output of the Sun. To date eight stars are known with masses more than forty times the mass of the Sun. The most massive stars (e.g. Pistol Star and Eta Carinae) have masses of 100 – 150 times the mass of the Sun and an energy output of a few million times higher. The very first stars of the Universe are believed to be even more extreme, up to 1000 times more massive than the Sun. All these stars do not form in the same way. §1.1.1 and §1.1.2 give a short introduction to low- and high-mass star formation.

Star formation may start by spontaneous collapse of a molecular core or by ‘triggered star formation’. A pressure wave passing through the molecular cloud, for example from a supernova explosion, can create a density enhancement and initiate a core collapse. The ultimate display of triggered star formation is observed in starburst galaxies and some ultraluminous infrared galaxies (see §1.1.3). In these galaxies the star formation occurs almost instantaneous across the entire galaxy or the central nucleus. The trigger is a near galaxy encounter or a galaxy collision. Figure 1.2 shows a spectacular display of triggered star formation in the starburst galaxy M82.

1.1.1 Low-mass star formation

The basic principles of low-mass star formation are well understood (Shu et al., 1987) and described in a four-stage evolutionary scenario (Lada, 1987; André & Montmerle, 1994) with sources in each phase identified as class 0, I, II, or III. The star formation process starts with the inside-out collapse of a pre-protostellar core in a molecular cloud. When the density in the center of the core becomes so large that the gravitational pressure is no longer balanced by magnetic fields or turbulence, the core collapses (Class 0). The protostar in the center continues to accrete matter, but part of the infalling material ends up in a rotating circumstellar disk to preserve the angular momentum. At this stage the young star and disk are still surrounded by a cold envelope (Class I). A bipolar outflow perpendicular to the disk gradually disperses the envelope and at a certain moment the star and disk become visible and a class II source is born. As the star evolves the gas in the disk is heated by stellar radiation or radiation from nearby massive stars and the gas in the disk starts to ‘evaporate’. At the same time the dust particles grow and settle toward the midplane into a thin disk from which planets may form (Class III). Eventually, the original interstellar gas and dust that did not make it into a planet or planetesimal will be dispersed and any small dust grains observed in these systems are produced by collisions of planetesimals – a so-called ‘debris’ disk. In the first stages when the envelope dominates, the spectral energy distribution (SED) is dominated by cold dust emission with strong silicate and ice absorption features in the

mid-infrared. As the envelope becomes thinner and gradually disappears, the silicate features go from absorption into emission and emission bands of polycyclic aromatic hydrocarbons (PAHs) appear.

The above evolutionary picture does however not mean that the low-mass star formation process is fully understood. Many questions are still unanswered or at best poorly answered. To name just a few: Which processes drive the envelope dispersal? How are the gas and dust coupled at the different evolutionary stages? How and when do the giant planets form? What drives the chemistry in the inner (< 10 AU) disk?

Low-mass stars are studied in Chapters 5, 6, and 7 of the thesis. In Chapter 5 emission from the gas in disks around young stars is studied. Chapter 6 describes the observations of gas around young low-mass sources still surrounded by an envelope. Chapter 7 presents one particular disk source in which the hot gas and its chemistry very close to the central star are studied (see Fig. 1.3).

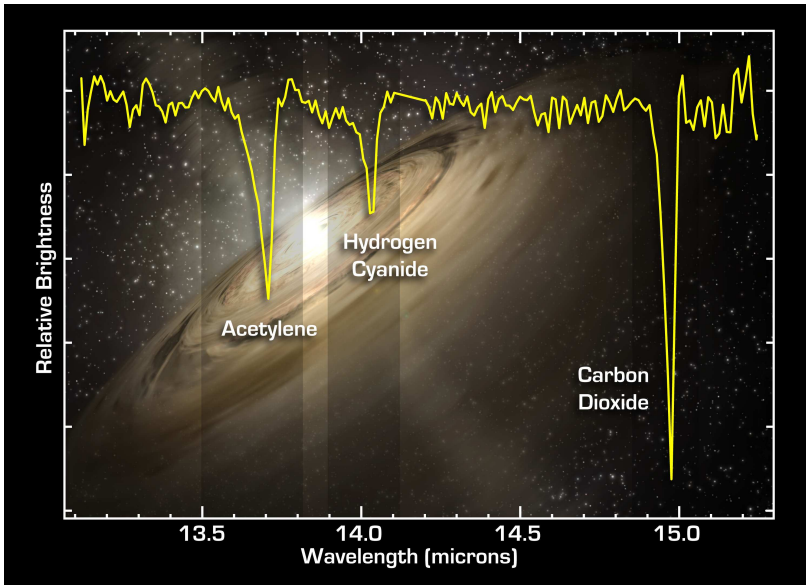
1.1.2 High-mass star formation

High-mass star formation is less well understood than low-mass star formation, mostly due to observational limitations. First, high-mass stars form fast (few 10^5 years, ~ 10 times faster than low-mass stars). Hence the number of high-mass protostars which can be observed is small. Second, high-mass protostars remain deeply embedded during most of the accretion phase making it difficult to study the formation processes close to the protostars.

An ongoing debate is whether high-mass protostars follow the same evolutionary track as low-mass protostars, including the formation of a circumstellar disk (Cesaroni, 2005b; Clarke, 2006). From the physics point of view, the formation of a disk is expected to preserve angular momentum. However, a disk forming around a massive star is subjected to vast amounts of hard UV radiation from the young star and the combination with the high accretion rates may quickly fragment the disk (Kratzer & Matzner, 2006). Recently, good kinematic evidence of disks around some massive stars has been presented (e.g. Beltrán et al., 2005; Cesaroni et al., 2005). This suggests that massive stars can also form by disk accretion and at least some of them may follow an evolutionary scenario similar to that of low-mass stars.

An observed phenomenon in high-mass star formation is the ‘hot-core’. This is generally thought to represent a short phase during the transition from the deeply embedded stage to the phase where ionizing photons can escape the protostellar accretion envelope and create a hyper-compact, and subsequently an ultra-compact, HII region (see review by Cesaroni, 2005a). The molecular composition of the hot core is very different from that of cold molecular clouds. This is thought to reflect the evaporation of ices when the envelope is heated by the newly formed star (Walmsley & Schilke, 1993). Subsequent high temperature gas-phase chemistry (see §1.4.2) significantly enhances the abundance of e.g. CH_4 (methane), C_2H_2 (acetylene) and HCN (hydrogen cyanide) (Viti & Williams, 1999; Doty et al., 2002; Rodgers & Charnley, 2003).

In Chapter 4 absorption spectra of C_2H_2 and HCN are used to observe the warm dense gas in the envelopes around the massive stars. The question is whether these molecules serve as good tracers of the envelope heating and if the observations can confirm the proposed evolutionary hot-core scenario.



© NASA / JPL-Caltech / F.Lahuis (Leiden Observatory, SRON)

Figure 1.3 Warm and abundant C_2H_2 (acetylene), HCN (hydrogen cyanide) and CO_2 (carbon dioxide) at 13 – 15 μm in the planet-forming zone of the circumstellar disk of IRS 46. This result was featured in NASA, Leiden Observatory, & SRON press releases. See the NASA press release at: <http://www.spitzer.caltech.edu/Media/releases/ssc2005-26/>

1.1.3 Ultraluminous infrared galaxies

Ultraluminous infrared galaxies (ULIRGs) are among the brightest objects in the Universe and emit most of their energy at infrared wavelengths. ULIRGs have a luminosity $L > 10^{12} L_{\odot}$, equal to the energy of hundreds of average galaxies together. ULIRGs are generally found in colliding or merging galaxy systems (e.g. Armus et al., 1987; Sanders et al., 1988b; Murphy et al., 1996). During a merger large amounts of gas and dust are driven into the nucleus under high pressure (e.g. Mihos & Hernquist, 1996). This initiates a massive starburst and can also feed massive black holes in the nucleus. The starburst and the accretion of matter onto black holes releases large amounts of energy into the gas and dust in the nucleus. This heats the dust making it extremely bright in the infrared. If the energy output of black holes dominates, the source is referred to as an active galactic nucleus (AGN), otherwise it is a starburst. ULIRGs are without doubt the most spectacular sites of star formation and the ultimate display of triggered star formation. If AGNs are present, ULIRGs reveal them in their earliest most hidden phase.

Much effort has gone in trying to identify the dominant heating sources of ULIRGs. This started with Genzel et al. (1998), who used infrared PAH emission bands and high ionization fine-structure lines as indicators of star formation activity or AGN activity, respectively. This has later been expanded to include more optical, near-infrared and submillimeter star formation and AGN indicators (e.g. Lutz et al., 1999; Bushouse et al., 2002; Spoon et al., 2007). However different indicators can result in conflicting identifications (see Armus et al., 2007).

A special group of ULIRGs are the (deeply) obscured ULIRGs, characterized by the presence of broad absorption of amorphous silicates centered at 10 and 18 μm (Spoon et al., 2005). Some of their near- and mid-infrared spectra strongly resemble those of starburst galaxies and are undoubtedly powered by massive starburst activity. Other obscured ULIRGs however have spectral energy distributions (SEDs) which show similarities to those of bona fide AGN-dominated spectra and lack signs of clear starburst activity. None of these show indisputable evidence that the nucleus is dominated by an AGN, however. But, if AGNs do not dominate the nuclei of these ULIRGs, a major question is why there are no traditional signs of starburst activity such as strong PAH emission.

Chapter 8 provides a possible answer through the detection of large amounts of hot molecules, C_2H_2 (acetylene) and HCN (hydrogen cyanide). These molecules are also seen in the inner regions of envelopes around massive young stars. In the normal stellar evolution the envelopes are dispersed as the stars evolve. However, due to the very high pressure in the ULIRG nuclei this may not happen and the stars remain embedded in ‘starburst cores’ for a much longer time. As a result the typical star formation features such as PAH emission are weak or absent.

1.2 Infrared spectroscopic data

Spectroscopic data are essential to learn about the composition of the dust and the gas and to extract physical parameters. The infrared spectral region is a true treasure cave given the richness and diversity of the observed spectral features (see van Dishoeck & Tielens, 2001, for a review). It contains solid-state features of dust and ices and gas-phase molecular and atomic lines. The infrared spectral features sample a very large range of physical environments, from the very cold outer regions of the envelopes and disks around young stars to the hottest and densest inner regions close to the stars. In this thesis gas-phase spectral features are studied originating from the warm ($T \sim 100 - 1000$ K), dense regions.

The molecular band presented in Figure 1.4 is called a vibration-rotation band by the nature of the molecular states involved in the transitions. Molecules can change their energy state by going from one rotational level to another rotational level. They may do so between rotational levels in one vibrational state – so-called pure rotational transitions –, or by going from a rotational level in one vibrational state to a rotational level in another vibrational state, so-called vibration-rotation or ro-vibrational transitions. The energies involved in pure rotational transitions are much smaller than in ro-vibrational transitions, so that they occur at lower frequencies. Most molecules have pure rotational transitions at far-infrared and submillimeter wavelengths. An exception is H_2 with pure rotational transitions in the mid- and near- infrared. Molecules without a permanent dipole, such as CO_2 and C_2H_2 , do not have strong rotational transitions in the submillimeter. Therefore infrared observations are required to observe these molecules.

Ro-vibrational transitions involving an electric dipole change of the molecule yield the strongest lines. These are called *P*-, *R*-, and *Q*-branch transitions depending on the rotational quantum level J change between the upper and lower vibrational state. *P*-, *R*-, and *Q*-branch transitions have a J change of respectively -1 , $+1$, and 0 . For some molecules or vibrational states the *Q*-branch transitions do not exist due to symmetry.

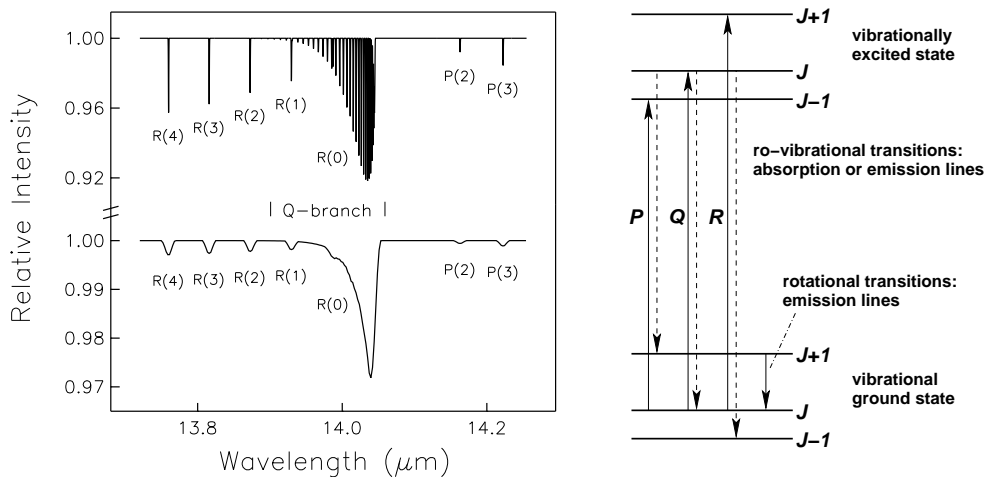


Figure 1.4 Left: absorption within the ν_2 vibration-rotation band of HCN showing the complete Q -branch and the lowest P - and R -branch lines. Since the energy differences of the various Q -branch transitions are very small, the individual lines can only be separated at very high spectral resolution. In the top spectrum, the band is shown at a spectral resolution of 30,000 and in the bottom one at 1800, typically for our data. At lower resolution the Q -branch lines blend into a single unresolved band and the unresolved P - and R -branch lines become weak (note difference in vertical scale). Right: an illustration of the state changes involved in P -, Q -, and R -branch ro-vibrational transitions and pure rotational transitions.

Figure 1.4 shows the central part of the absorption band of HCN at $14 \mu\text{m}$ typical for the molecules observed in this thesis. Lines from R -, P -, and Q -branches are indicated. The Q -branch lines are only resolved at very high spectral-resolution. At lower resolution they blend into a single resolved spectral feature. The relative strength of the lines (and therefore the shape of the Q -branch) depends on the temperature of the gas and their depth on the amount of molecules observed.

Chapters 5 and 6 present observations of unresolved molecular hydrogen and atomic fine structure line emission. Chapters 4, 7, and 8 present observations of gas-phase molecules which have a complex band structure.

1.3 Infrared space instruments

The last two and a half decades have been a golden age for infrared space astronomy with the successful missions of four large infrared satellites, the InfraRed Astronomical Satellite (IRAS), the Infrared Space Observatory (ISO), the *Spitzer* Space Telescope, and the *Akari* Infrared Space Telescope. Of these *Spitzer* and *Akari* are still operational. Within the next decade two major infrared space missions will fly, the Herschel satellite and the James Webb Space Telescope (JWST).

An overview of the near- and mid-IR spectroscopic capabilities of the past, present, and future missions is presented in Table 1.1. For the studies presented in this thesis data from the ISO-SWS and *Spitzer* IRS instruments are used, mostly from its medium resolution ($R = \lambda/\delta\lambda = 600 - 2000$) modes.

Table 1.1. Spectroscopic capabilities of near- and mid-IR space missions

Satellite	Operational period	Instrument	Wavelength range [μm]	Resolving power
IRAS	1983	Low Resolution Spectrograph – LRS	7 – 23	20 – 60
ISO	1995 – 1998	Short Wavelength Spectrometer – SWS	2.4 – 45	1,000 – 2,500
		SWS Fabry-Pérot	11.4 – 44.5	20,000 – 35,000
		Long Wavelength Spectrometer – LWS	43 – 197	150 – 200
		LWS Fabry-Pérot	43 – 197	6,800 – 9,700
		Camera+Circular Variable Filter – CAM-CVF	2.3 – 16.5	35 – 50
Spitzer	2003 – (2008)	Photometer-Spectrometer – PHT-S	2.5 – 5; 6 – 12	90
		Infrared Spectrograph – IRS		
		IRS low resolution SL & LL	5.2 – 38	60 – 120
Akari	2006 – 2007	IRS high resolution SH & LH	9.9 – 37.2	600
		Infrared Camera + prism/grism – IRC	1.7 – 26.5	20 – 50
JWST	(2013–)	Mid-Infrared Instrument – MIRI		
		MIRI Integral Field Spectrometer	5 – 28.3	2,000 – 4,000
		MIRI Low Resolution Spectrometer	5 – 10	100

1.4 Physicochemical properties

Retrieving fundamental physical and chemical properties is essential in trying to understand the process of star formation. This includes density, temperature, total mass, and the (relative) abundances of different species present in the gas. These are obtained by analyzing the observed spectra and combining them with theoretical models.

The spectral energy distribution reveals information about the temperature components of the dust with the cold dust emitting strongly in the far-infrared and warm/hot dust emitting strongly in the near- and mid-infrared part of the spectrum. From the optically thin millimeter continuum emission an estimate of the total dust mass can be obtained. Combined with a source size retrieved from imaging data this provides an average density. However, the density and temperature generally depend strongly on the location in the region and can have contributions from envelopes, disks and/or general cloud material. To retrieve that information, detailed modeling of the spectral energy distribution and millimeter line and continuum emission is required (e.g. van der Tak et al., 1999; Jørgensen et al., 2002; Young et al., 2004, and Chapter 7 of this thesis).

To understand the chemistry in clouds, envelopes or disks requires a similar approach. Observations of emission and absorption features of various species provide the first basic insight. Features sensitive to different temperature and density regimes are obtained to make the observational picture as complete as possible. Detailed chemical models, using among others the density and temperature structures and stellar radiation as input, are run. The input is derived from observations as described above or a generic model for the type of object (for example an envelope or a disk) is used. The modeled distributions of multiple species are then used to predict line intensities and profiles which can be compared to observations (e.g. Doty et al., 2002; Markwick et al., 2002).

In this thesis molecular and atomic spectral features are observed to derive physical and chemical parameters, in particular temperature and abundances. These results are compared against physico-chemical models from the literature to draw conclusions about the location of the observed species and the nature of the sources.

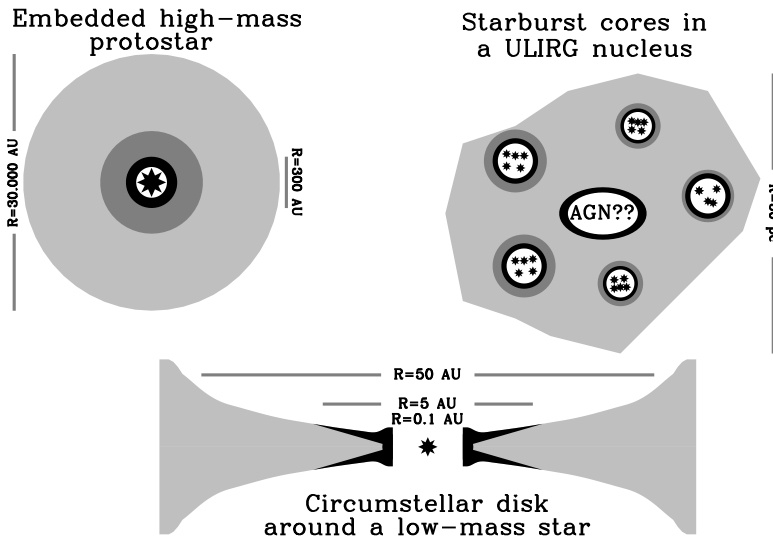


Figure 1.5 Illustration of the location of the warm dense regions in the disk of a young low-mass star and in the envelope around a young high-mass star, and around the starburst cores in the nucleus of a ULIRG. Typical size scales for the different types of objects are indicated.

1.4.1 Hot dense regions

Regions with hot dense gas are found in distinct stages of all forms of star formation. Hot dense gas is found in the inner disk regions around low-mass stars, the inner envelopes of high-mass stars, and in the swept-up medium close to compact starburst cores. Figure 1.5 illustrates the location of this dense warm gas in the types of sources studied in this thesis. The dense hot gas is ideally suited for observational studies in the near- and mid-infrared spectral region. Emission lines of molecular hydrogen (H_2) and atomic species, and emission or absorption bands of simple molecules such as carbon monoxide (CO), carbon dioxide (CO_2), water (H_2O), methane (CH_4), acetylene (C_2H_2), and hydrogen cyanide (HCN) have multiple transitions in the infrared spectral region. Chapter 5 and 6 show observed molecular hydrogen and atomic fine structure line emission from the disk and envelopes around low mass young stars.

A special technique for studying the warm gas is absorption spectroscopy toward embedded sources. The hot dust in the inner regions close to the central source provides the infrared continuum against which the molecules can be observed in absorption. The continuum emitting regions are generally small ($< 0.1''$). Therefore the absorption observations probe a single line-of-sight and the strength of the absorption is (almost) directly related to the amount of absorbing molecules in that line of sight. In contrast, emission lines have contributions from all lines of sight contained in the aperture of the spectrometer. Submillimeter lines are also affected by beam dilution when the emitting region becomes smaller than the telescope beam. This beam dilution makes it difficult to observe submillimeter high density tracers from the compact hot regions. Infrared absorption spectroscopy is used in Chapters 4, 7, and 8 to probe this hot gas.

1.4.2 High temperature chemistry

Hot dense regions close to the young stars are particularly interesting because an active chemistry takes place which is very different from that in the cold clouds out of which the stars form. High temperature chemistry is dominated by the evaporation of molecules from the grains with subsequent gas-phase processing. At very high temperatures, the hydrocarbon and nitrogen chemistry are particularly enhanced because most of the oxygen is converted into water by neutral-neutral reactions. The abundances of molecules such as C_2H_2 , CH_4 , and HCN can be increased by orders of magnitude (e.g. Doty et al., 2002; Rodgers & Charnley, 2003) while at the same time the formation of CO_2 is reduced because its primary formation route through OH is blocked. Thus the abundances of C_2H_2 and HCN increase with temperature by orders of magnitude in the hot 200 – 1000 K range in models that focus on the inner envelopes around massive stars. A similar chemistry applies to the inner regions of disks around low-mass stars. Recent inner disk models (e.g. Markwick et al., 2002) predict strongly enhanced abundances of HCN and C_2H_2 also for the very inner (1 – 5 AU) disk.

Chapter 7 presents the first observations of hot abundant C_2H_2 , HCN, and CO_2 in the inner disk of a young low-mass star, IRS 46. This attracted world-wide attention after the joint press-releases by NASA, Leiden Observatory, SRON, and Keck Observatory focusing on their importance for prebiotic chemistry in the planet-forming zones of circumstellar disks (see Fig. 1.3).

1.5 Outline of this thesis

This thesis presents observations of gas-phase mid-infrared spectral features associated with star formation processes. The observations are done using space-based spectrometers. The observed features trace warm mostly dense gas and they take us on a journey throughout the Universe. The molecules reveal the gas in disks around low-mass stars, in the inner envelopes around massive stars, and in the nuclei of ultraluminous infrared galaxies where they are associated with hidden starburst activity.

To reliably observe the often weak spectral features, the limits of the instruments need to be pushed. Chapters 2 and 3 of the thesis therefore pay attention to some aspects associated with reducing mid-infrared spectroscopic data. Chapter 2 presents the data reduction aspects important on the fundamental instrumental level, in particular the detector readout and spectral artifacts introduced by the electronics of the ISO-SWS instrument. Chapter 3 focuses on the spectral extraction of *Spitzer* IRS echelle data. The pipeline developed for the reduction of the IRS data of the *Spitzer* “Cores to Disks” legacy project is described.

Chapter 4 presents ISO-SWS observation of C_2H_2 (acetylene) and HCN (hydrogen cyanide) in the envelopes of massive young stellar objects. Chapter 5, 6, and 7 present data from the “Cores to Disks” legacy program with observations of a large sample of low-mass young stellar objects in five nearby star-forming regions. Chapter 5 presents molecular hydrogen and atomic fine structure line emission from circumstellar disks around low-mass stars. Chapter 6 presents these lines from the more embedded young stars and from edge-on disks dominated by absorption. The first detections of C_2H_2 , HCN, and CO_2 (carbon dioxide) from the inner planet-forming zone in a disk around a low-mass young star are shown in Chapter 7. Finally Chapter 8 takes us from our own

Galaxy to the nuclei of ultraluminous infrared galaxies where the spectral absorption features of C_2H_2 and HCN are observed and are shown to be associated with a phase of deeply embedded 'hidden' starburst activity.

The main conclusions of this thesis are:

- Observing gas-phase spectral features with infrared spectrographs is rewarding but also difficult. Since the features are often weak it puts high demands on the reliability and quality of the reduction. The results presented in this thesis show that it is important and worthwhile to invest a significant amount of resources in trying to achieve the most optimal data reduction possible.
- The mid-infrared vibration-rotation bands of C_2H_2 and HCN form unique probes of the warm dense gas associated with star formation toward different types of sources, both in our Galaxy and beyond.
- The observations of C_2H_2 and HCN in the envelopes of high-mass stars confirm the 'hot-core' scenario for these sources. Here the chemical structure is dominated by gradual heating of the inner envelope by the young star. As the envelope heats up, the molecules are evaporated off the ices followed by an active high temperature chemistry. This yields enhanced abundances of some molecules, among others CH_4 (methane), C_2H_2 , and HCN, by orders of magnitude.
- Lines of [Ne II] and [Fe I] emission are detected with the *Spitzer* IRS toward a significant fraction of disks around low-mass stars for the first time. The strong [Ne II] emission is a good tracer of X-ray/EUV irradiation of the disk. The [Fe I] emission may point to the presence of massive gas-rich disks around the sources for which it is observed.
- Hot ($T \gtrsim 500$ K) H_2 emission is observed toward some disk sources. The observed line fluxes are not reproduced by recent disk models which include heating of the gas by UV radiation or X-rays. Therefore this hot H_2 emission may be evidence of a new emission component in the circumstellar disk.
- The discovery of C_2H_2 , HCN, and CO_2 in the inner disk of IRS 46 proves the strength of mid-infrared absorption spectroscopy. Combined with submillimeter line emission and high spectral resolution near-infrared spectroscopy they give insight into the physics and chemistry of the gas in the inner disk and the process by which the gas in the disk is cleared.
- The mid-infrared absorption features of C_2H_2 and HCN are observed in the nuclei of a diverse sample of obscured ULIRGs and imply the presence of strong starburst activity. The high molecular abundances for a range of excitation temperatures point to the existence of an extended phase of deeply embedded star formation. The extreme pressures and densities of the nuclear starburst environment are believed to inhibit the expansion of HII regions and the global disruption of the star forming molecular cloud cores, and to have 'trapped' the star formation process in an extended Hot Core phase.

Chapter 2

ISO–SWS Signal Capture

Abstract

A description of the signal extraction of the ISO-SWS instrument is presented. It starts with the flux falling onto the ISO-SWS detectors up to the extracted slope signal. All known artifacts associated with the detectors and the cold and warm read out electronics are explained. The artifacts are described as well as their correction through software and calibration. The improvement of the deglitching for SWS low resolution data is described in more detail since this is an artifact which had a large impact on some science data.

Lahuis, F., Feuchtgruber, H., Golstein, H., Kester, D., Luinge, W., Shipman, R. F., & Wieprecht, E. 2003, "SWS Signal Capture: from Flux to Signal" in The Calibration Legacy of the ISO Mission (ESA SP-481), 387

Lahuis, F., Kester, D., & Shipman, R. F. 2003, "Deglitching of SWS Low Resolution Data" in The Calibration Legacy of the ISO Mission, poster contribution

2.1 Introduction

Starting with pre-flight laboratory tests (Feuchtgruber et al., 2003) during the ISO mission (Roelfsema et al., 2003; Shipman et al., 2003; Vandenbussche et al., 2003) and after the mission a continuous effort has been made to model known artifacts of the detectors and the electronics. Pre-flight laboratory tests were made to characterize individual components in as much detail as possible. Also tests under controlled circumstances have been made on the integrated system to monitor its behavior and optimize the instrument settings. The laboratory tests are at the base of the model presented in this chapter describing the integrated electronic system. The many in-flight calibration observations have helped to improve on the characterization of most instrumental artifacts. For some artifacts it has been possible to develop algorithms to correct for them. As much as possible these corrections are implemented in the SWS pipeline and or the SWS OSIA¹ (Wieprecht et al., 2003).

In the following sections the effects of the electronics are described from a data point of view. The electronics are viewed as being composed of single components or blocks of components which have a clearly identifiable impact on the observed data. Figure 2.1 shows a simplified scheme of the SWS electronics. Included are all components or component blocks which have been identified to affect the integrated signal in one way or another. All the artifacts observed in SWS data which can directly or indirectly be ascribed to the electronics are discussed. §2.3 describes how the artifacts are corrected for in the SWS calibration and data reduction of the SWS pipeline and the SWS Interactive Analysis (OSIA) (Lahuis et al., 1998; Wieprecht et al., 2003). §2.4 describes in more detail an advanced glitch detection ' for the SWS low resolution data where the standard glitch detection in many cases fails. This correction is included in the last SWS pipeline used to populate the ISO archive.

2.2 SWS detectors and detector read-out

The SWS instrument uses five types of detector materials. For the four grating arrays of 12 detectors each, InSb is used from 2.38 to 4.08 μm , Si:Ga from 4.08 to 12.0 μm , Si:As (BIBIB) from 12.0 to 29.0 μm and Ge:Be from 29.0 to 45.2 μm . For the Fabry Perot two 2-detector arrays are used with Si:Sb from 11.4 to 26.0 μm and Ge:Be from 26.0 to 44.5 μm . All detectors are used in combination with integrating pre-amplifiers with non-destructive read-out, employing heated JFET's.

2.2.1 Detectors artifacts

2.2.1.1 detector cross-talk

The SWS grating detectors exhibit a very clear crosstalk on the level of 10 to 15 percent. The main source of this is electrical crosstalk over the contacts to the detectors. The crosstalk matrix used to correct the observed data is derived from data taken from charged particle radiation tests in the laboratory and verified in orbit.

¹OSIA is a joint development of the ISO-SWS consortium. Contributing institutes are SRON, MPE, KUL and the ESA Astrophysics Division. <http://sws.ster.kuleuven.ac.be/osia/>

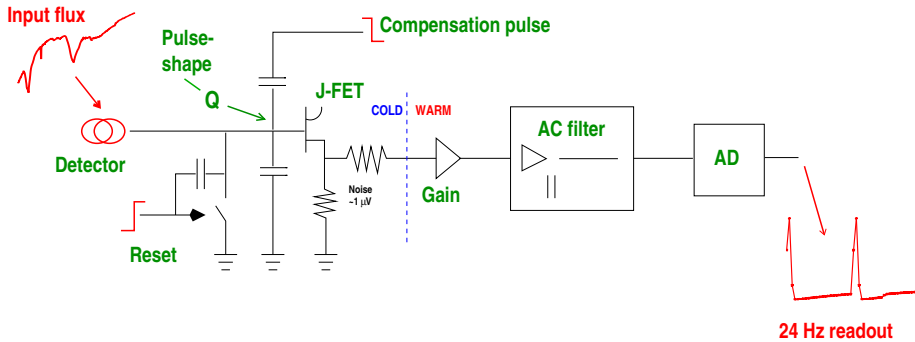


Figure 2.1 Top level scheme of the SWS Electronics showing all components known to affect the integrated signal from the detectors. The left-hand side of this scheme depicts the cold detector readout electronics located within the satellites cryostat. On the right-hand side the ‘warm’ electronics, the signal amplifier, filters and analog-to-digital converters.

2.2.1.2 memory effects

The SWS Si:Ga, Si:Sb and Ge:Be detectors all suffer from memory effects or transients. The InSb and Si:As detectors are both free from transient effects.

Already in the laboratory transient effects were observed. The existence of transient effects has carefully been taken into account in the design of the observing templates used for all general observations. The templates were designed such that transient effects were minimized and sufficient redundancy was present in each observation to be able to recognize transient effects in the time domain and possibly correct for them during or after the mission.

For the Si:Ga detectors a successful correction has been found in the model derived by Fouks and Schubert. This model and the application for the SWS Si:Ga detectors is discussed in detail in Kester (2003).

2.2.1.3 de-biasing

During the integration of the detector current, the capacitance at the input of the J-FET is charged and the voltage over the input to the J-FET increases. As a consequence the effective bias voltage over the detector is reduced as the integration continues and thus the responsivity of the detector changes over the reset. This effect is noticeable only at very high input signals (\lesssim few 10^4 Jy) and most conspicuous for the Ge:Be detectors.

For SWS this effect was studied but no correction was defined. For LWS de-biasing is also observed and an empirical correction algorithm was developed by the ISO-LWS instrument team.

2.2.1.4 particle impacts

All SWS detectors suffer from the impact of charged particles. When a particle impact occurs this is observed as a jump in the 24 Hz signal as a consequence of the additional charge deposited in the detector. These jumps are recognized and corrected for in the DSPD processing part of the pipeline (Wieprecht et al., 2000, and §2.4).

A secondary effect of the particle impact is the transient behavior after the impact. On time-scales of a few seconds transient tails are observed in particular for the Ge:Be and the FP detectors. In the pipeline no correction for this is available. In the SWS Interactive Analysis an experimental tool is available for the correction of the glitch tails (Wieprecht et al., 2000).

2.2.2 Reset of 24 Hz read-out signal

At the end of each integration ramp the system is reset by grounding the connection between the detectors and the input gate of the J-FET. This removes practically all charge from the input gate. This is directly followed by a compensation pulse, a positive or negative step depending on the bias direction. The amplitude of the compensation pulse depends on the voltage at the end of the previous integration ramp. The compensation pulse decays over the filter to the ground level centering the amplified ramps close to the ground level.

2.2.2.1 saturation

The application of the reset/compensation pulse is never perfect. A fraction of the compensation pulse is fed into the first few samples and these may go into saturation in the amplifier chain, e.g. in the operational amplifier in the high-pass filter. The reset time of this saturation is fast, less than a quarter of a second. The direct consequence however is that the first samples of the integration ramp cannot be used in the slope fit. Therefore for the default processing, for all resets the first six samples are not included in the determination of the slope.

2.2.2.2 reset-pulse aftermath

After the reset/compensation pulse has been applied a charge can be left before the input gate of the J-FET. This charge will decay over the combined capacitance of the cold electronics and is added to the charge built up by the integration of the detector current. This is seen as an additional exponentially decaying signal on the integrated 24 Hz signal. This is usually referred to as the pulse-shape effect. The pulse-shape is an additive effect and only important for low flux cases.

The pulse-shape signal is seen to change from observation to observation and often also within one observation. These can be slow or sudden changes. These changes are believed to result from variations in the deposited charge due to changes in the electronics.

2.2.3 Read-out electronics

The current from the SWS detectors is measured using integrating pre-amplifiers with heated J-FET's. The pre-amplifiers are read-out with non-destructive read-outs in a sampling of 24 Hz. The integration is done over integration resets of 1, 2 or 4 seconds depending on estimated source flux and detector. At the end of each reset a destructive read-out is applied to reset the electronic system (see §2.2.2).

The integrated signal is passed through the warm electronics where it is amplified, going through a high-pass filter, digitized and then sent down with the telemetry data.

2.2.3.1 gain amplification

SWS has three switchable gain settings, 1, 4 and 16, for all detectors. The electronic amplification factor is 225 for the grating detector and 450 for the FP detectors. The actual gain applied is the selected gain times the electronic amplification factor.

2.2.3.2 high-pass filter

A high pass filter is included to reduce the large DC voltage which would result from the amplification of the J-FET output offset. The typical RC time-constant is 2 seconds. In the laboratory individual time-constants have been derived for all 52 detectors. In orbit only for a few detectors small corrections were applied but for most detectors the time-constants derived in the laboratory are used.

2.2.3.3 A-D conversion

At the end the analogue signal is digitized. The amplified analogue signal ranges from ± 12 V. It is converted to a bitrange from 0 to 4095 corresponding to ± 10 V. So any analogue signal outside the ± 10 V range is set to 0 or 4095 and flagged as out of limit in the first stage of the processing and excluded from any later processing.

This sampling was chosen to just sample the system noise (§2.2.4). Any lower or higher sampling would have meant either a loss of sensitivity or a loss in the dynamic range of the instrument.

2.2.3.4 saturation

At very high signal levels (10^5 V/s) saturation effects come into play. First partial ramps become saturated and at even higher signal levels the complete ramp can become saturated. In the last case the ramp will be outside the measured range already after the first sample.

2.2.4 System noise

The effective root mean square (r.m.s.) noise as measured in the laboratory was typically in the range of $0.5 - 1.0 \mu\text{Vs}^{-1}$. With these noise values for the highest gain setting the noise is just sampled by two bits. In orbit the observed r.m.s. noise was higher by a factor of 1 to 10 depending on the detector band.

2.3 Calibration and data reduction

For as far as possible all the artifacts described above are corrected for in the Derive-SPD stage of the pipeline processing. The corrections are applied in the reverse order in which they physically occur. Below is a description of the processing steps which together with routines for the wavelength calibration make up the Derive-SPD stage. These are the top level routine names in the SWS Interactive Analysis or in OSIA. All the routines make use of the standard pipeline modules. In between brackets the calibration files relevant for this processing step are listed. The descriptions are given on the basis of the implementation in pipeline version 10.

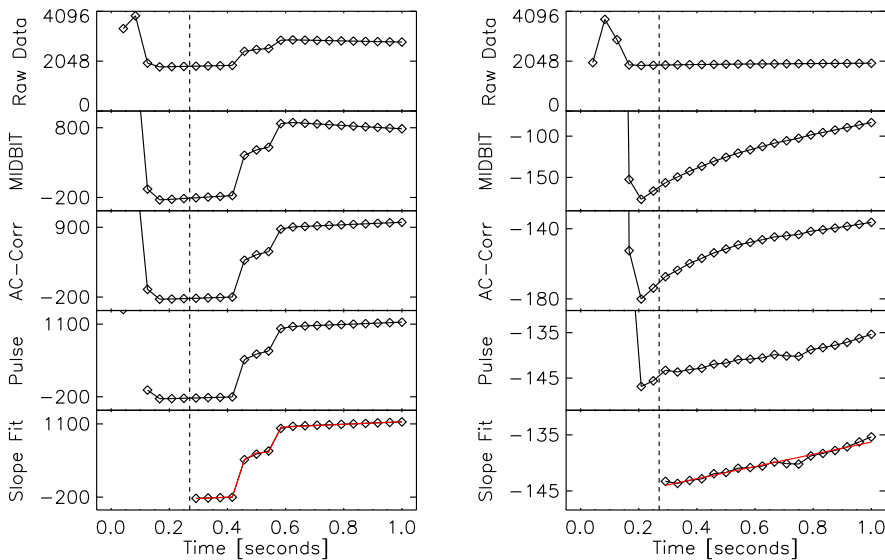


Figure 2.2 Examples of ramps at different stages of the processing for two one second resets. Shown left a reset with two glitches of which the first one is a double glitch. The right plot is a ramp without problems in which in particular the effect of the reset-pulse after effect is clearly illustrated. From top to bottom in both plots we see the raw data samples, the data after DRANGE and MIDBIT, the data after AC-correction, after pulse-shape correction and finally the glitch detection and slope-fit (including identified glitches). The fitted slope is overplotted on the data.

Figure 2.2 illustrates the effects of these corrections on two individual integration ramps.

DRANGE (CAL04)

The binary data limits are checked and data outside the limits are flagged as invalid. In the calfile the limits are listed for each detector and each gain setting.

MIDBIT (CAL02A)

The binary data is centered around the bit value corresponding to the electronic zero level of the system.

ACCOR (CAL02, CAL03)

Correction for the high pass filter. The exponential decay with a time-scale off approximately 2 seconds is approximated with a linear decay over each 1/24 second sample. At these time-scales this is an excellent approximation which allows for an efficient algorithmic implementation.

PULSE_SHAPE (CAL03, CAL05, CAL06)

A time-dependent reset-pulse aftermath correction derived from the observation data itself is applied. The applied correction is an exponential decay model with a single time-constant for the observation and a time-varying amplitude. This is subtracted from the individual ramps.

Table 2.1. Scan parameters for AOT-1 low resolution observations.

speed	reset length	dwel time	# steps	step size
1	24	3	6 (8)	4
2	48	3	14 (16)	2
3	48	3	14 (16)	1
4	48	6	7 (8)	1

Reset length and dwell time are in readout samples of 1/24 sec and grating steps in LVDT (grating scanner position). The number of readouts in between brackets is the total number in a reset, the first number the actual numbers of steps normally used in the slope calculation.

CROSSCOR (CAL01)

The crossstalk matrix for the grating arrays is multiplied over the twelve detectors at each read-out sample.

“GLITCH” (CAL03, CAL06)

Jumps in the integrated ramp are detected. In the pipeline the glitch detection and correction are integrated in the SLOPE sub-routines.

SLOPE (CAL03, CAL05, CAL06)

As a last step slopes are fit to the fully corrected ramps. For SWS low resolution data glitched samples are first corrected on the ramps (see Sec. 2.4) after which single slope is fit. For full resolution data the slopes and glitches are fit together including step functions at the identified glitch locations.

2.4 Deglitching of SWS low resolution data

All SWS science observations were performed with one of four pre-defined observation templates depending on the purpose of the observation. These templates are called AOT's, Astronomical Observing Templates. One of these, the AOT-1, operated the instrument in a reduced or low resolution mode.

During an observation in an AOT-1 low resolution configuration the grating scanner moved during resets. At each scanner position (LVDT) the scanner remained fixed for n read-outs of 1/24 sec and then moved to a new position (see Table 2.1 for details). There exist four speeds with which AOT-1 observations were performed. The difference between these four speeds is the duration for which the scanner remained fixed (the dwell time) and the number of scanner positions the scanner moved (step size). The resulting resolution varies from approximately 15 % of the maximum grating resolution for speed 1 to approximately 50 % for speed 4 (Lorente, 1998). Table 2.1 summarizes the scan parameters for all four AOT-1 speeds.

The resulting integrated ramp can thus contain varying slopes depending on the underlying spectral structure. The most extreme changes within a reset occur when the instrument scanned over an unresolved emission line. Considering that the instru-

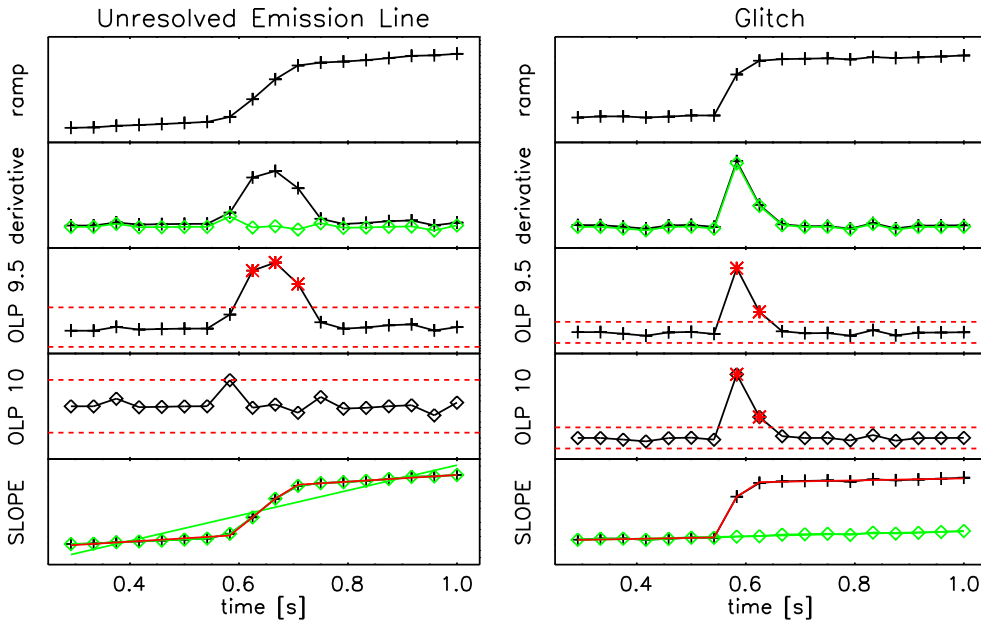


Figure 2.3 Glitch detection in low resolution data in OLP9.5 and OLP10 with examples of a reset scanning an unresolved line (left) and a glitched continuum reset. From top to bottom: – the input ramp – the uncorrected ramp derivative (black asterisks) and the corrected ramp derivative (green/gray diamonds)– glitch detection for OLP9.5 on the uncorrected ramp derivative. Samples outside the limits are flagged as glitches – glitch detection for OLP10 on the corrected ramp derivative. The emission line is not identified as containing glitches and the real glitch is properly identified. – slope fits. The OLP9.5 fit includes the identified glitch samples (false on the left and real on the right) and follows the integrated ramp. The OLP10 fit is done on the ramp after glitch correction (none on the left and two on the right). For the emission line reset (left) the OLP9.5 fit clearly underestimates (by 75%) the average signal across the reset. On the glitched continuum reset both signals agree.

mental resolution is approximately 4 to 5 LVDT's it is clear that especially in the case of speed 1 or 2 this may cause problems. When the instrument scanned over an unresolved line in a speed 1 or 2 observation only in one or possibly 2 of the reset positions the signal from the line is seen, in the rest the continuum signal is seen. When the contrast between the continuum and the line is large enough the signal from the line may be identified as a glitch and the inferred slope will be underestimated (see figure 2.3 for an example). It may be that only some resets within a line are affected, but also half of a line or a complete line can be removed in this way (see figure 2.4 for examples).

Here a solution is presented which has been introduced in the SWS Interactive Analysis environment and which will be used in OLP10, the final archive version. The general problem is described in §2.5 and a description of the modifications are given in §2.5.2 and §2.5.3. In §2.5.4 examples and comparisons between the two deglitching methods are given with plots and by comparing line fluxes and FWHM of emission lines.

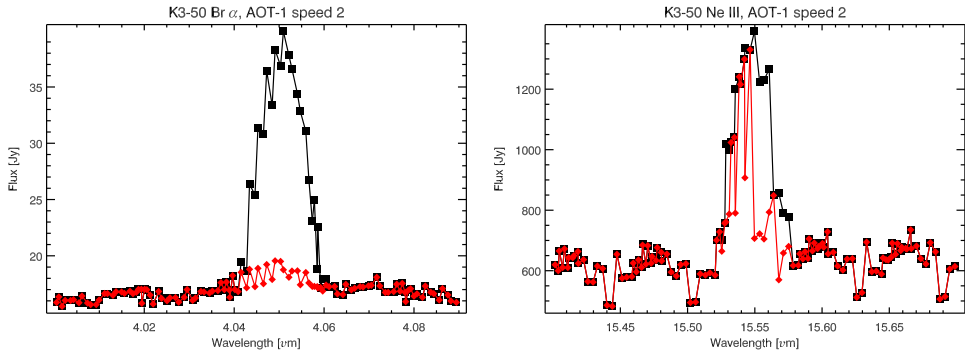


Figure 2.4 Br α and [Ne III] emission lines in an AOT-1 speed 2 of K3-50. Plotted in gray/red is the data as produced by OLP9.5 and in black the data using the updated deglitching and slope fitting, as used in IA and OLP 10. The OLP9.5 results clearly illustrate the problems with the old deglitching method. In the case of Br α the complete line is removed and in the case of [Ne III] half of the line disappears. In both cases the results from OLP 9.5 will be quite misleading.

2.5 Requirements

A usable deglitching algorithm for low resolution data had to fulfill the following requirements:

- it should:** *not* identify emission line signal as a glitch.
- it should:** perform identical to the old algorithm for continuum data.
- it should:** have *little or no* impact on the derived signal in case of error.
- it should:** be efficient so it can be implemented in the pipeline

To achieve this the following changes with respect to the previous standard glitch detection and correction algorithm were made:

1. identification of low resolution data in the observation. Information needed for this is contained in the SWS housekeeping data and readily accessible in OSIA or the pipeline.
2. correction of the ramp derivative (§2.5.2) used in the glitch detection for low resolution resets (note that the actual glitch detection method, as described in §2.5.1, is the same for low resolution resets and normal resets).
3. for low resolution data the slope and glitch fitting are decoupled. Instead the ramps are corrected for glitches using the glitch height as derived in the glitch detection before slope fitting (see §2.5.3).

2.5.1 SWS glitch detection

As illustrated in figure 2.3 the problem for the deglitching of low resolution data is the confusion between signal from a spectral feature and signal from a glitch. In the deglitching algorithm, glitches are identified using the integrated ramp derivative.

The standard deglitching is implemented by taking the derivative of the integrated ramp and calculating the median and the median width of its distribution. Two calibration parameters, ALPHA and MINWID, are then used to determine glitched samples. A sample is considered as glitched if the deviation of the derivative with respect to the median is larger than ALPHA times the median width and in absolute terms larger than MINWID. In the third and fourth row in figure 2.3 the limits, ALPHA times the median width and MINWID, are indicated with red and green horizontal lines. The samples identified as glitched are plotted in red. In §2.5.2 the modification to the glitch detection for low resolution data in OLP 10 is discussed.

2.5.2 Correcting the ramp derivative

To suppress false glitch detection due to scanner movement a distinction has to be made between a change in slope due to source signal and a change due to a glitch. In doing this care should be taken that the problem is not reversed and real glitches are not properly identified and corrected anymore.

To achieve this a source signal is estimated and used to correct the ramp derivative before the glitch detection. The source signal is estimated with the knowledge that source signal, contrary to the signal from a glitch, is always correlated over n samples (the dwell time, table 2.1). The estimated source signal is subtracted from the ramp derivative. Then the derivative is corrected for signal noise using a scaling based on the estimated source signal. The noise scaling is required to prevent the detection of spurious glitches as a result of signal noise.

After the correction of the ramp derivative the standard glitch detection algorithm is used to identify glitches. When a glitch is identified the glitch height is estimated from the corrected derivative without the noise scaling. In the second row of figure 2.3 the derivative (in black) and the corrected derivative (in green and in red with the signal noise correction) are plotted.

In figure 2.3 two examples illustrating the difference between the deglitching and slope fitting (see §2.5.3) of low resolution data in OLP 9.5 and OLP 10 are given. Shown are an example of a reset scanning over an unresolved emission line and an example of a glitched reset.

2.5.2.1 Problems

This correction works well in almost all cases. It only fails when there is a glitch which is seen in two samples and which in both samples has the same height or at least with a difference smaller than the noise on the integrated ramp. In such a case the glitch can be interpreted as being real signal with a negative glitch resulting in a larger signal. Any such point is however easily removed using standard spectral filtering methods.

Since these glitches are rare and are easy to remove from the final spectrum it has been decided to not try and cater for them. In view of the use in the pipeline this is also preferred to ensure maximum robustness and highest possible efficiency.

Table 2.2. Lineflux and FWHM comparison.

speed	flux	FWHM	flux	FWHM
OLP 9.5		OLP 10		
K3-50 Br α				
2	4.9 (-15)	325	4.9 (-14)	362
4	4.5 (-14)	1237	4.5 (-14)	1237
K3-50 [Ne III]				
2	1.1 (-13)	975	3.1 (-13)	499
4	2.6 (-13)	1452	2.6 (-13)	1452
NGC 7027 Br α				
1	3.4 (-14)	285	7.9 (-14)	465
2	7.4 (-15)	348	9.0 (-14)	355
3	8.1 (-14)	717	8.2 (-14)	699
4	9.2 (-14)	1200	9.2 (-14)	1200
NGC 7027 [Ne III]				
1	1.4 (-12)	569	1.4 (-12)	512
2	1.5 (-13)	4169	1.5 (-12)	458
3	1.4 (-12)	895	1.5 (-12)	828
4	1.1 (-12)	1400	1.1 (-12)	1391

2.5.3 Slope fitting

In OLP9.5 the slope fitting in all cases meant an integrated fit of slope and glitches. For a reset containing glitches a fit is made of a slope plus a step function for each glitch.

This procedure works perfect for normal slopes and optimizes the number of samples used in the fit. However in the case of low resolution data an integrated fit of the slope and glitches will lead to an underestimate of the flux when signal of an unresolved line is present in the reset.

For low resolution data therefore the glitches are not fitted but corrected. Before fitting, the ramps are corrected for the glitches using the glitch-height derived in the glitch detection (see example in Fig. 2.3).

2.5.4 Deglitching results

AOT-1 observations of K3-50 and NGC 7027 are used to compare the deglitching as it is in OLP9.5 and as it is in IA and OLP10.

Figure 2.4 shows plots of two unresolved emission lines in K3-50 showing typical examples of line-removal problems with in red the OLP9.5 result and in black the OLP10 result. One line which is almost completely removed and one line which is partly removed and appears to be much narrower than the instrumental resolution.

Table 2.2 gives a summary of the derived line fluxes and FWHM of Br α and [Ne III] in K3-50 and NGC 7027 at different AOT speeds. In particular for the speed 1 and 2 observations the results are dramatically improved. For the speed 3 the results are

marginally different and for speed 4 observations there is no difference seen for these observations. The derived line fluxes with the improved AOT-1 deglitching compare well between the observations at the different speeds. The observed differences are within the nominal uncertainties of SWS in particular taking into account that e.g. no correction has been made for fringing in the case of the [Ne III] line which may have a small impact on the derived line fluxes.

During the scientific validation of OLP 10 similar exercises have been done for other lines and other sources. In all cases where lines were affected in the OLP 9.5 data they were properly reduced in OLP 10. The deglitching on continuum data was always comparable.

2.6 Conclusions

Two important improvements in the SWS data reduction after the nominal ISO mission have been the development of a pulse-shape correction and the implementation of a dedicated deglitching scheme for SWS low resolution data. The major difference of these two corrections compared to the other correction such as ac-correction is that these two corrections are derived using the data itself, while the other are all corrections parametrized through calibration files.

The low resolution deglitching has been an effect which has had a direct and major impact on the science results for the affected data. Therefore a more detailed description of the implementation plus examples of this are given.

The pulse-shape correction results in a more stable zero level of the final spectrum leading to more reliable spectra for low signal sources.

For low resolution data false glitch detections on unresolved emission lines are highly suppressed and real glitches are still caught in the improved AOT-1 glitch detection algorithm. In rare cases glitches are detected where there is none, however these have little effect on the derived signal. Therefore no modifications are pursued to correct for these special cases in order not to make the algorithm overly complicated and thereby inefficient.

The pulse-shape and low resolution deglitching algorithms have been implemented efficiently to allow them to be incorporated in the SWS pipeline. This meant a significant improvement in the overall quality of the SWS data in the final ISO archive. Most importantly the archive will be free of data with suspect unresolved line features increasing the accessibility and reliability of the SWS data for the general observer and reducing the risk of misinterpretation of the spectra.

Acknowledgements

We would like to thank all the people who have been involved in ISO-SWS over the years. From the people involved in the very early development and laboratory work, the members of the SIDT in VILSPA and the support teams at the home institutes to the members of the SWS data centers and all the SWS observers in the world.

Chapter 3

From Molecular Cores to Planet Forming Disks – a c2d data legacy –

Abstract

The *Spitzer* legacy program “From Molecular Cores to Planet Forming Disks” (“Cores to Disks” or c2d) was one of the five initial *Spitzer* legacy programs. The program included mapping and spectroscopy of the nearby Chamaeleon, Lupus, Perseus, Ophiuchus, and Serpens star-forming regions. High-S/N spectra have been obtained within the 5-38 μm range for 226 sources at all phases of star and planet formation up to ages of ~ 5 Myr. This includes previously known young stars and new sources discovered in the IRAC and MIPS maps. The c2d program is complementary to the “The Formation and Evolution of Planetary Systems: Placing Our Solar System in Context” (FEPS) *Spitzer* legacy program. Together both programs covers stellar evolution from 0 – 3 Gyr. Previous spectroscopic studies, e.g., with ISO, had the sensitivity to probe only high- or intermediate-mass young stellar objects. *Spitzer* permits the first comprehensive mid-infrared spectroscopic survey of solar-type young stars. This Chapter describes the c2d pipeline developed to reduce and analyse the IRS pointed observations. The c2d pipeline is also developed to prepare the IRS legacy products delivered to the *Spitzer* Science Center (SSC) for distribution to the general public.

Based on Lahuis, F., Kessler-Silacci, J. E., Evans, N. J., II, Blake, G. A., van Dishoeck, E. F., Augereau, J.-C., Banhidi, Z., Boogert, A. C. A., Brown, J. M., Geers, V. C., Jørgensen, J. K., Knez, C., Merín, B., Olofsson, J., & Pontoppidan, K. M. 2006, “c2d Spectroscopy Explanatory Supplement,” (Pasadena: *Spitzer* Science Center)

3.1 Introduction

The c2d observing strategy is described in detail in Evans et al. (2003). The 75 hour c2d IRS program consists primarily of IRS (Houck et al., 2004) observations of point sources. A small portion of the observing time was dedicated to IRS spectral maps of the south-eastern Serpens molecular core (Banhidi & et al., 2007) and the Barnard 1 outflow. A number of followup mini-maps (see §5.2.2) were observed on a number of sources from the initial program. The mini-maps were intended to check for extended gas-phase emission lines and polycyclic aromatic hydrocarbon (PAH) emission around point-sources. High-S/N spectra were obtained within the 5–38 μm range (high resolution [$R \approx 600$] over the 10–37 μm range) for 226 sources at all phases of star and planet formation up to ages of ~ 5 Myr. Additionally, the MIPS () spectroscopy mode ($\lambda = 52 - 100 \mu\text{m}$ with a spectral resolution $R = \lambda/\delta\lambda = 15 - 25$) was used in the second year of the program to characterize the longer wavelength silicate and ice features of a small subsample of disks.

The c2d IRS program was divided into two sets with roughly equal time, the first-look (with the *Spitzer* observation program number (PID) #172) consisting of observations of known embedded, pre-main-sequence stars, and background stars and the second-look (PID #179) consisting of IRS follow-up spectroscopy of sources discovered in the IRAC and MIPS mapping surveys (Harvey et al., 2006; Jørgensen et al., 2006; Brooke et al., 2007; Rebull et al., 2007; Porras et al., 2007). The source list for the first-look program was restricted primarily to low-mass young stars, defined as having masses $M < 2 M_{\odot}$, with ages younger than ~ 5 Myr, for minimal overlap with existing infrared spectroscopy. Within these criteria, the selection contains a broad representative sample of young stars with ages down to 0.01 Myr and masses down to the hydrogen-burning limit or even less. The second-look IRS campaign was more focused on observations of new or interesting types of sources. The new sources were selected from the catalogues generated from the c2d IRAC and MIPS maps (PID 174, 175, 176, 177, and 178). Included in the second-look campaign are IRS staring observations of samples of very low-mass stars and brown dwarfs, weak-line T Tauri Stars, edge-on disks, very low luminosity objects (VeLLOs), and cold disks, as well as IRS mapping observations of extended outflows and followup mini-maps of extended gas-phase and PAH emission and 4 MIPS SED observations of interesting targets from the first-look campaign.

Almost all first-look targets were observed using the IRS staring mode in each of its four modules as listed in Table 3.1. The longest wavelength ends of SL1 and LL1 suffer from light leaks from higher orders and are therefore removed from the delivered spectra. For those sources that are part of various GTO programs involving the low-resolution modules, only the high-resolution 10–37 μm (SH,LH) spectra were acquired as part of the c2d IRS effort. In contrast to the scheduled *Spitzer* guaranteed time program observations (GTO) of large numbers of young stars, typically with the low-resolution IRS modules, the c2d IRS program focuses on long integration times in the high resolution modules, ensuring high dynamic range even on weak sources. For all first-look observations, the integration times for the short-high and long-high modules were fixed such that theoretical S/Ns of at least 100 and 50 were obtained for sources brighter and fainter than 500 mJy on the continuum, respectively. The spectra taken using the short-low modules always reach theoretical S/Ns of greater than 100. Second-look IRS staring targets were observed in various modules depending on the

Table 3.1. *Spitzer* IRS observing modules

Module	Wavelength range (μm)	Resolving power $R = \lambda/\delta\lambda$
SL1	7.4 – 14.5	60 – 120
SL2	5.2 – 8.7	60 – 120
LL1	19.5 – 48.0	60 – 120
LL2	14.0 – 21.3	60 – 120
SH	9.9 – 19.6	600
LH	18.7 – 37.2	600

SL1 and LL1 cover spectral order 1; SL2 and LL2 cover spectral order 2 and 3; SH and LH cover spectral orders 11 to 20.

source type and flux. S/Ns greater than 100 were achieved where possible, but since second-look consisted of primarily very weak sources, this was not always feasible. A full listing of all c2d IRS targets including observation details is included in the c2d IRS explanatory supplement¹ (Lahuis et al., 2006a).

As part of the second-look program, followup mini-maps of extended gas-phase and PAH emission around point source targets were taken using the IRS mapping mode. In addition, IRS spectral maps of the south-eastern Serpens molecular core and the Barnard 1 outflow were obtained. The Serpens molecular core was imaged over more than 7 arcmin² to a 1σ sensitivity of 2 mJy using the low-resolution IRS spectral mapping mode. This core contains several deeply embedded sources and possesses a complex physical structure with outflows on a scale of 30''–60'' (~ 0.05 – 0.1 pc) from the driving sources. The c2d IRS explanatory supplement gives details on the observing strategy, the IRS mapping reduction and the IRS mapping products provided included in the *Spitzer* legacy delivery.

To quickly assess the nature of the observed sources an automated feature identification of the most prominent spectral features is included in the c2d reduction pipeline and performed on all IRS staring observations and extracted spectra of individual map pointings. The identified features are listed in the product logfiles included in the legacy delivery. In the c2d IRS explanatory supplement master overview tables are included of all spectral features identified in the IRS spectra.

The MIPS SED observations taken as part of the second-look program were all "FixedSingle" observations, meaning that they were non-mapping, non-clustered AORs. The exposure time for all observations was 10 s, repeated as necessary to get S/N of 30–50 based on IRAS 60 μm and MIPS 70 μm fluxes and the 2004 sensitivity estimates for MIPS SED mode.

¹The c2d IRS explanatory supplement can be downloaded from <http://ssc.spitzer.caltech.edu/legacy/c2dhistory.html> or <http://peggysue.as.utexas.edu/SIRTF/> under the menu item Data Products.

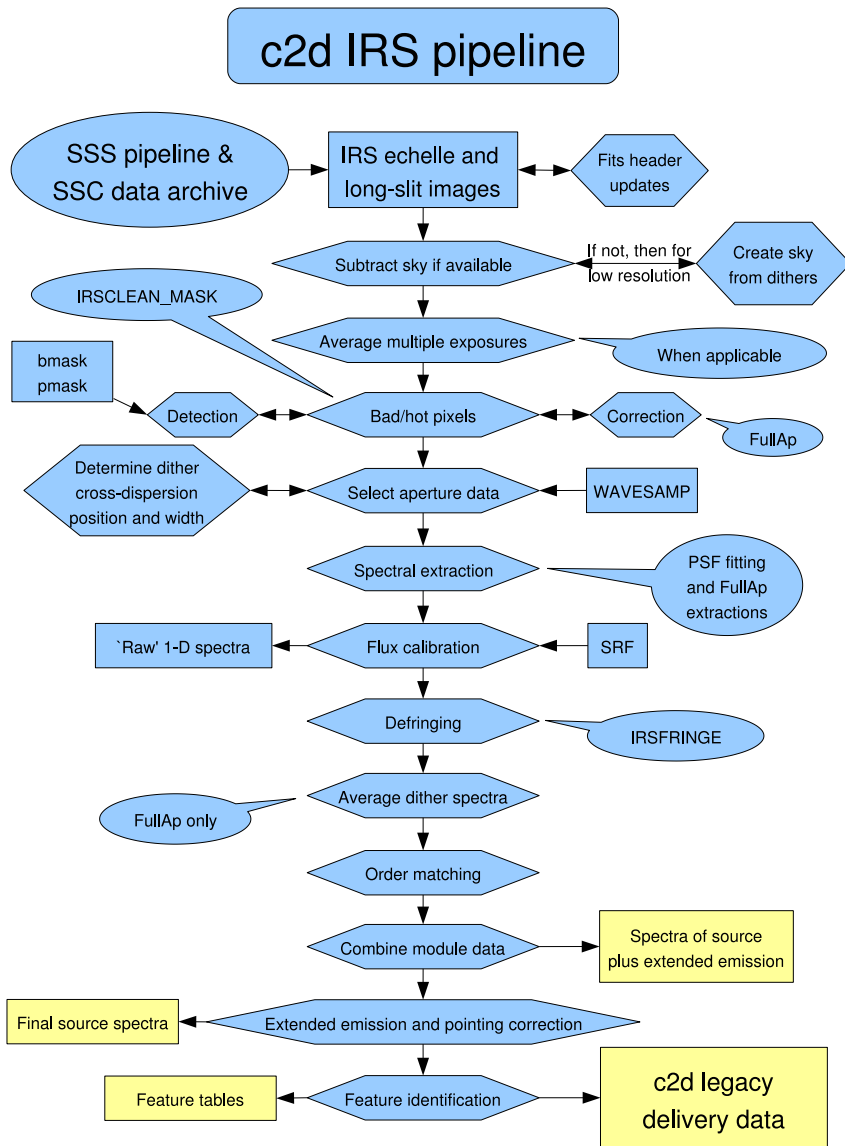


Figure 3.1 Schematic overview of the data reduction and legacy product generation for IRS staring mode observations in the c2d pipeline. Rectangles correspond data and products, polygons to tasks, and dialog balloons give short descriptions. The products in the white boxes are part of the c2d legacy delivery to the SSC. The data reduction process and products are described in detail in § 3.2 and § 3.3.

3.2 Reduction of IRS pointed observations

The *Spitzer* archive products include Basic Calibrated Data (BCD; *_bcd.fits) files, which are two dimensional spectra that have been processed through the SSC pipeline as described in the IRS data handbook². This process entails saturation flagging, dark-current subtraction, linearity correction, cosmic ray correction, ramp integration, droop correction, stray light removal or crosstalk correction, and flat-field correction.

The IRS reduction starts from the intermediate RSC products (*_rsc.fits), which have had the stray light removed (for SL) or cross-talk corrected (for SH,LH) but no flat-field applied. LL has no known stray light issues and therefore no corrections are made. In our reduction, 1-D spectra are extracted from the long-slit (SL,LL) and echelle (SH,LH) images using two extraction methods (see § 3.2.2). The first is a full aperture extraction (§ 3.2.2.1) from images in which known bad/hot pixels have been corrected (see § 3.2.1). The second is an optimal PSF extraction (§ 3.2.2.2) based on fitting an analytical cross dispersion point spread function plus extended emission (assumed to be uniform over the adopted extraction aperture) to all non bad/hot image pixels (see § 3.2.1). The optimal PSF extraction uses an analytical fit to the good pixels only, and therefore bad/hot pixel correction is not required. The 1-D spectra for both extraction methods are flux calibrated using dedicated spectral response functions (SRFs) derived from a suite of calibrator stars using Cohen templates and MARCS models provided by the *Spitzer* Science Center (Decin et al., 2004). After extraction, the 1-D spectra are corrected for instrumental fringe residuals (see § 3.2.6) and, finally, an empirical order matching is applied (see § 3.2.7). For all extracted spectra, a log file, overview plot and an IPAC spectral table are generated. In the log file a list of the strongest spectral features is given (see § 3.3.9).

The c2d pipeline incorporates routines from SMART³ (Higdon et al., 2004), OSIA,⁴ IRSFRINGE,⁵ and IRSCLEAN_MASK.⁶ The pipeline also uses advanced reduction tools and calibration routines developed by the c2d and FEPS⁷ legacy teams for full aperture extraction, optimal PSF extraction, automated product generation, and pointing correction (in development).

3.2.1 Bad/hot pixels

The 'pmask.fits' and 'bmask.fits' files provided by the SSC contain masks for permanently bad IRS array pixels ('hot' pixels), pixels affected by cosmic rays or full saturation, and a number of pixels with long-term transients as a result of solar flares or cosmic ray hits. The SSC pipeline interpolates over undefined pixels (pixels with the signal value 'NaN') in the images and ignores pixels flagged as fatal in the raw

²<http://ssc.spitzer.caltech.edu/irs/dh>

³<http://ssc.spitzer.caltech.edu/postbcd/smart.html>

⁴OSIA is a joint development of the ISO-SWS consortium. Contributing institutes are SRON, MPE, KUL and the ESA Astrophysics Division. <http://sws.ster.kuleuven.ac.be/osia/>

⁵IRSFINGE is developed for the *Spitzer* science community by the "Cores to Disks" c2d legacy team. IRSFRINGE has been integrated into SMART but is also available as a stand-alone package from <http://ssc.spitzer.caltech.edu/postbcd/irsfringe.html>

⁶The IRSCLEAN_MASK software was developed by the IRS Instrument Support Team at SSC in conjunction with the Cornell IRS Science Center. It can be retrieved from <http://ssc.spitzer.caltech.edu/archanaly/contributed/irsclean/>

⁷See <http://ssc.spitzer.caltech.edu/legacy/fepshistory.html> for the FEPS Data Explanatory Supplement.

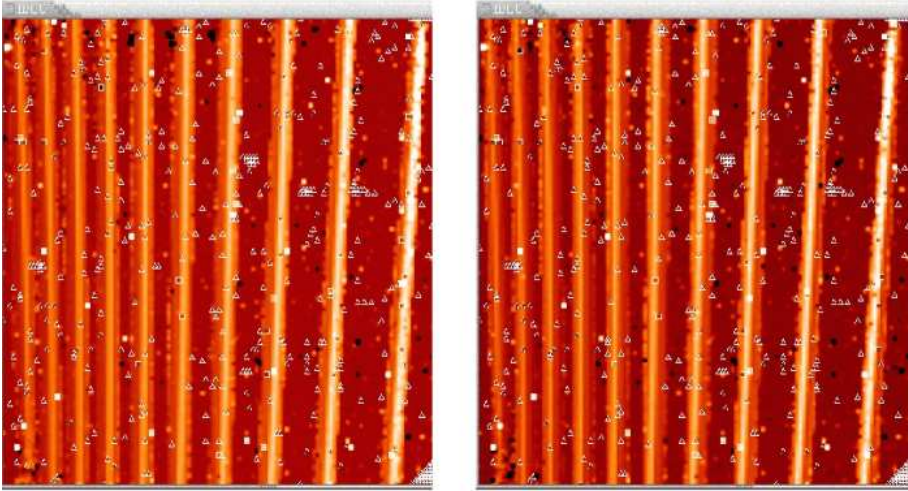


Figure 3.2 Two-dimensional BCDs of two dither positions in the LH module. Triangles and squares denote bad pixels, most of which are defined in the SSC bad pixel (`pmask` and `bmask`) files.

SSC pipeline. In our reduction, an attempt is made to identify additional bad pixels in the optimal PSF extraction, and to correct all known bad pixels for the full aperture extraction.

The LH array is particularly affected by bad or hot pixels (see Figure 3.2). Although only $\lesssim 7\%$ of the pixels in LH are affected, collapsing the spectra along the spatial dimension of the slit during the extraction process results in $\sim 20\%$ of the final spectral data points being affected. In reality, this number may be much larger, as the SSC mask files do not identify all transient, or ‘hot’ pixels, particularly at wavelengths $> 30 \mu\text{m}$. Correction of the identified bad pixels significantly improves the extracted spectra (Figure 3.3), but artifacts remain. In the SL, SH and LL modules the problem is much less severe but still requires attention as artifacts resulting from bad pixels may still be present.

It is particularly important to identify as many bad pixels as possible which fall within the extraction window before the 2-D data are processed into 1-D spectra to limit the number of possibly affected spectral samples in the 1-D spectra. These include the hot pixels identified by the `pmask.fits` files and bad pixels identified by the BCD pipeline that are included in the `bmask.fits` files. The latter includes pixels affected in the data acquisition and pixels for which the calibration or reduction in the BCD pipeline failed. Aside from the known bad/hot pixels, additional affected pixels are identified using the `IRSCLEAN_MASK` program provided by the *Spitzer* Science Center.⁸ A detailed description of the SSC pipeline processing is given in the IRS handbook⁹.

After identifying as many bad pixels as possible, the `c2d` pipeline interpolates over the bad pixels for the full aperture extraction and ignores the bad pixels for the optimal PSF extraction. Specifically, the bad pixel correction is done by interpolating

⁸<http://ssc.spitzer.caltech.edu/archanaly/contributed/irsclean/>

⁹<http://ssc.spitzer.caltech.edu/irs/dh>

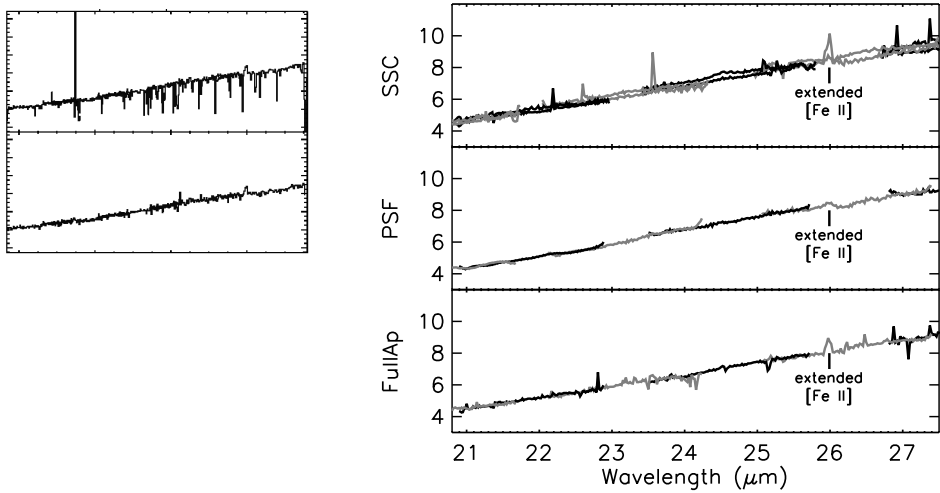


Figure 3.3 IRS LH spectra of IRAS 08242-5050 (HH46) affected by bad pixels. IRAS 08242-5050 was one of the legacy test cases observed directly after the in-orbit checkout. The first spectra produced by the SSC pipeline proved to be of poor quality as a result of the many LH bad pixels. The small plot shows the early archive spectrum in the top panel and one of the first c2d attempts at an optimal extraction in the lower panel. The right panel shows the current SSC pipeline and both c2d extractions (see § 3.2.2). The quality has improved significantly, however it is clear that artifacts resulting from bad pixels may still be present. The IRAS 08242-5050 spectrum also illustrates the appearance of extended emission lines between the PSF extraction and both full aperture extractions. The difference in strength reflects the difference between the IRS beam and the IRS aperture (see § 3.3.3).

over the bad pixels in the cross-dispersion direction for all apertures as defined by the `wavesamp` calibration file in the former case. The optimal PSF extraction profile is used as the interpolation function (see § 3.2.2.2). Significant improvement in data quality for both the SH and LH modules is thus achieved. (See Figure 3.3 for the result of the c2d bad pixel correction on part of a LH spectrum).

3.2.2 Spectral extraction

Once the bad/hot pixels have been corrected, the spectra are extracted using a full aperture or optimal PSF extraction. Prior to extraction, the c2d pipeline averages the RSC images of each dither position. For the full aperture extraction, 1-D spectra are extracted for each dither position, which are combined after correction for the spectral response function. For the optimal PSF extraction, both dither positions are combined and one single 1-D spectrum is extracted. This gives the best overall noise reduction and spectral stability, as is required for automated pipeline processing. Averaging before extraction also has the added benefit that missing pixels in one single image will be corrected for by good data in the other exposures.

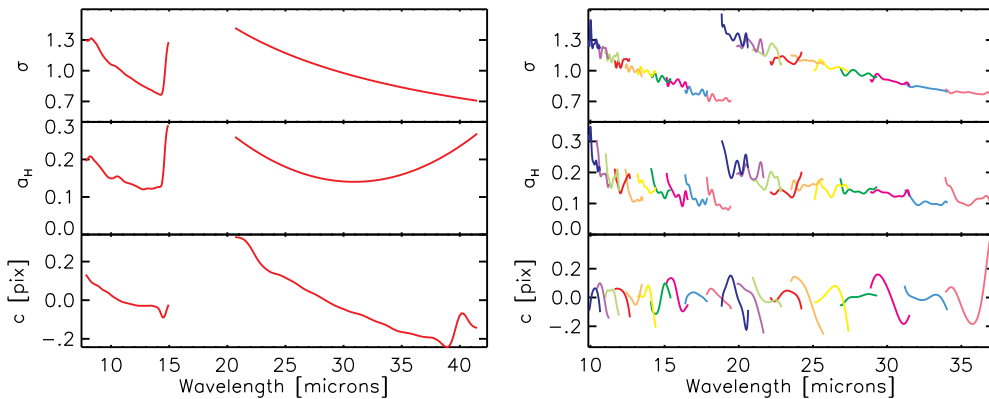


Figure 3.4 Parameters defining the IRS SL1, LL1, SH, and LH cross dispersion profiles for unresolved sources. The variation with wavelength within each order is, for high signal to noise calibrators, consistently reproduced from observation to observation and assumed to be real. These most likely result from mechanical and optical defects in the instrument.

3.2.2.1 Full aperture extraction

The first method of extraction employed in the c2d pipeline for both the low resolution and high resolution modules is similar to that employed in the SSC pipeline. The main difference is that the c2d pipeline performs a fixed-width aperture extraction from RSC products and then corrects for a spectral response function (SRF), while the SSC pipeline performs a varying aperture extraction from flat-field corrected BCD products. For the low resolution modules, the c2d pipeline implements an extraction aperture with a fixed width in pixels over the whole order. The source position in the slit is determined and the extraction aperture is centered on the source. The width is sufficiently wide that 99% of the flux of a point-source falls within the window. For the high resolution modules, the full slit width is used in the extraction. Figure 3.3 gives an example of a full aperture correction without and with bas-pixel correction.

The spectra are extracted separately for each dither position and later averaged into one single spectrum, with weights inversely dependent on the error.

For low resolution staring observations, the dither positions are used for the sky correction. For the high resolution modules, a sky estimate for the full aperture extraction is derived using the optimal PSF extraction method.

3.2.2.2 Optimal PSF extraction

Optimal extraction is performed on the combined RSC data after correcting for the cross dispersion offsets of the separate dither position images. The observed signal is assumed to be that of a point-source or slightly resolved source plus a uniform zero level (over the IRS extraction aperture). The zero level will in most cases represent the local extended emission close to the source, but it may also contain residuals of e.g., the raw pipeline dark current subtraction (see also § 3.3.3).

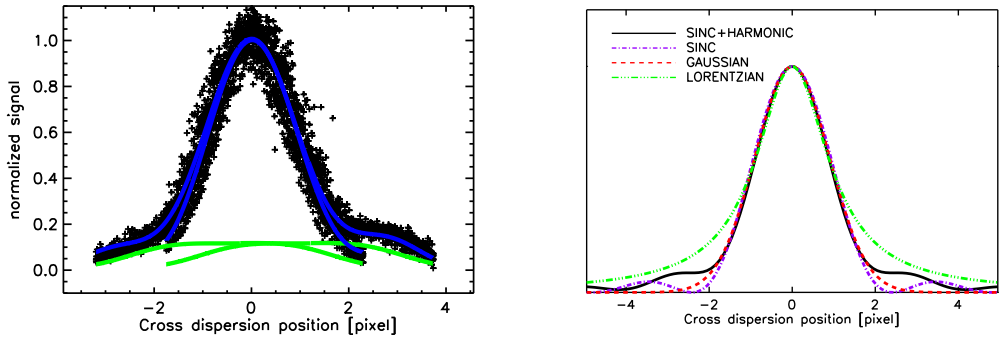


Figure 3.5 Example of the cross dispersion profile. The left plot shows a fit to the collapsed and cross-dispersion position corrected data (black pluses) from both dither positions of SH order 11 for GW Lup (see also Figure 3.8). The blue lines denote the source profile plus extended emission (green) for each dither position. The variations between the two dither positions reflect the flat-field profile of the zero level at the uncorrected slit position. The right plot shows a comparison of the IRS profile for a given width (σ) and harmonic amplitude compared to an undistorted sinc, a Gaussian, and a Lorentzian profile with the same FWHM. Note the significant variation in the strength and shape of the profile wings. The correct characterization of both the width and the wings of the profile is essential for reliably separating the compact source and extended emission components in the extraction.

3.2.3 The IRS cross dispersion PSF

Sky corrected high signal-to-noise calibrator data are used to define the IRS point spread function (PSF) in the cross dispersion direction. From these the detailed profile characteristics, the width of the profile, the offsets with respect to the pre-orbit definition of the order-traces, and the amplitude of the harmonic distortions are retrieved.

The IRS cross dispersion profile is approximated by the analytical function S ;

$$S(x, \lambda) = \text{sinc}^2(\sigma(\lambda) \times (x - c(\lambda))) + a_H(\lambda) \times H1(\lambda) + a_H(\lambda)^2 \times H2(\lambda).$$

The sinc width σ relates to the $FWHM$ by $\sigma = e/(2 * FWHM)$, c is the location of the profile center, more specifically the offset of the observed profile with respect to the pre-orbit defined order-trace, $H1$ and $H2$ are the first and second even harmonics (sinc overtones), and a_H the harmonic amplitude. The σ , c , and a_H wavelength dependence is shown in Figure 3.4. For SL and LL orders 2 and 3 the PSF is poorly defined as a result of spatial undersampling in the cross dispersion direction. For the extended emission within the aperture, the flat field cross-dispersion profile (describing the extended emission sensitivity) is used. The IRS flat fields have been derived by the *Spitzer* Science Center.

When applied to an individual observation, the cross dispersion offset of the trace and a scale factor for the width (for slightly extended sources) are determined from the collapsed order data (see Figure 3.5). Subsequently the 1-D spectra are extracted for all apertures defined in the IRS wavelength description (WAVESAMP) files. The PSF profile is fit to the aperture data keeping all parameters, except the profile amplitude and the zero level, fixed. After the extraction, the 1-D spectrum is flux calibrated using the SRF described in § 3.2.4.

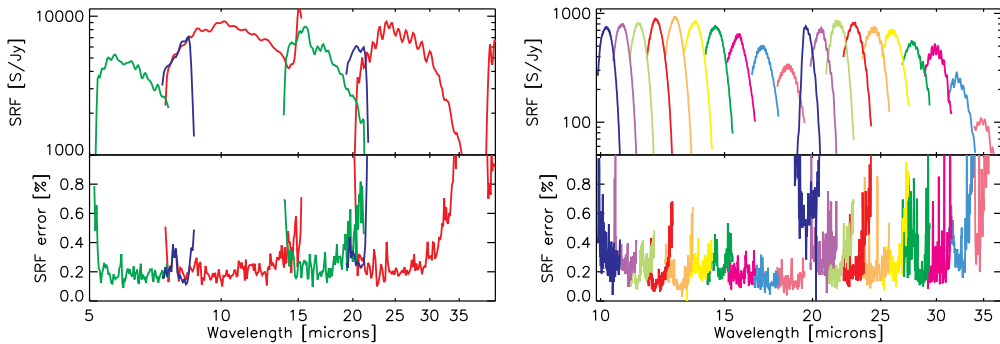


Figure 3.6 Spectral Response Function (SRF) for SH and LH for the optimal PSF extraction in units of S/Jy where S is the signal unit of the RSC echelle images. The orders are color coded, same for SH and LH. The SRF functions for the full aperture extraction show a similar profile and only change in detail and absolute level.

The advantages of PSF fitting are that it is less sensitive to bad data samples and unidentified bad pixels, that it gives an estimate of the data zero level and/or local sky contribution, and that it provides information on the extended nature of spectral features (see e.g. Geers et al., 2006).

The PSF fitting is sensitive to undersampling which can result in poorly defined continua. The short wavelength ends of the SH and LH modules suffer from this for some sources, but orders 2 and 3 of the SL and LL modules are most affected by undersampling. Therefore, we have chosen to include optimal extraction data only for the high resolution modules and for order 1 of the SL and LL modules. For the SL and LL order 2 and 3 data also no usable sky estimate can be obtained and these columns in the delivered IPAC tables contain zeros for these orders.

3.2.4 Spectral Response Function (SRF)

Both the full aperture extraction and the optimal PSF extraction are calibrated from standard stars observed within the regular *Spitzer* Calibration program. A set of Cohen templates and MARCS code model atmospheres (Decin et al., 2004) provided by the *Spitzer* Science Center¹⁰ are used to derive the spectral response functions. The low resolution full aperture calibration also includes a sample of stars observed within the FEPS legacy program to improve the detailed SRF shape. The low resolution full aperture calibration is discussed in detail in the FEPS Data Explanatory Supplement¹¹ and will therefore not be discussed in detail in this document.

Only standard stars observed with high accuracy pointing accompanied by dedicated sky observations are used to derive the spectral response function. A complete list of used for the calibration is included in the c2d IRS explanatory supplement. The same procedures used for the science extraction are used for the calibration, but the last stage of flux calibration is omitted. Despite the high accuracy pointing, small pointing errors will be present. To limit the impact of these on the final calibration, the obser-

¹⁰<http://ssc.spitzer.caltech.edu/irs/calib/templ/>

¹¹Available from the SSC FEPS legacy page <http://ssc.spitzer.caltech.edu/legacy/fepshistory.html>

Table 3.2. $1\text{-}\sigma$ flux calibration uncertainty (%) for high precision pointing

Order	— $1\text{-}\sigma$ uncertainty —			
	SL ^a	LL ^a	SH	LH
1	5.2	2.8
2	4.2	4.6
3	4.2	4.6
11	1.0	0.9
12	1.1	0.9
13	1.1	0.8
14	1.1	0.7
15	1.1	0.7
16	1.5	0.7
17	1.5	1.0
18	1.1	1.0
19	1.0	1.0
20	0.9	0.9

^aThe SL uncertainties are dominated by pointing error, the LL uncertainties by the low signal of the standard stars.

vations are sorted by signal strength and the observations from the weakest quarter (assumed to be the sources with the most extreme pointing error) are excluded.

For the optimal PSF extraction, the derivation of the SRF and the PSF parameters are intimately coupled. The derivation is done in steps. In the first iteration, the PSF function is characterized and then, in the second iteration, this PSF function is used in the extraction of the 1-D spectra used to derive the SRFs.

Figure 3.6 shows the derived SRFs and errors for SH and LH modules. The SRF errors depict the point-to-point uncertainty. Table 3.2 lists the average absolute flux calibration uncertainty per order and module for high precision pointing observations.

3.2.5 Error propagation

In the c2d spectral extraction procedure an error is calculated for each spectral data point. This error is propagated in each step of the c2d pipeline and includes the relative spectral response uncertainty (Figure 3.6), the absolute flux calibration uncertainty for high precision pointing (Table 3.2), and, for the full aperture extraction, the deviation between the dither positions. The archival data products delivered through the *Spitzer* Science Center do not contain fully propagated and usable errors (up to pipeline version S14) and are therefore not included. Full error propagation for the SSC pipeline is foreseen for S15, beyond the lifetime of the c2d legacy program.

The c2d extraction error is estimated from the residuals of the profile fit to the observed (source+sky) signal. The profile fitting is performed using the CURFIT routine provided by the OSIA package, which uses a non-linear least squares fit. The error is estimated from the fit residuals,

$$e_{\text{signal}}(\lambda) = \sqrt{\frac{\sum_{i=1}^n (\text{signal}(i) - \text{fit}(i))^2}{n \times (n - 1)}},$$

where $e_{\text{signal}}(\lambda)$ is the estimated extraction error for a given wavelength λ . $\text{signal}(i)$ is the observed source+sky signal for a RSC image pixel, $\text{fit}(i)$ is the fitted PSF profile plus extended emission, and n the number of good pixels in the aperture for the given wavelength λ as defined in the SSC `wavesamp` calibration file.

After the extraction, the absolute flux calibration and the SRF are applied to the signal and sky estimate. Then the SRF error (e_{SRF}) and the absolute flux calibration uncertainty (e_F) are added to the extraction error;

$$e_{\text{flux}}(\lambda) = \sqrt{e_{\text{signal}}(\lambda)^2 + \frac{\text{signal}^2(\lambda) * (e_{\text{SRF}}^2(\lambda) + e_F^2(\lambda))}{\text{SRF}^2(\lambda)}}.$$

The absolute flux uncertainty is valid for observations obtained with high precision pointing. For observations obtained with lower accuracy peakup or no peakup, the absolute flux uncertainty can be larger, see Figure 3.12 and § 3.3.4. The pointing error is a few % for the long wavelength modules and may be up to 20% for the SL module which as a result of its narrow beam suffers most from pointing errors.

For the full aperture extraction both dither position are averaged using a weighted mean with $1/e_{\text{flux}}^2(\lambda)$ as weights. At each wavelength the absolute difference of the flux in both dither positions is included in the final error.

3.2.6 Defringing

The fringes in IRS originate between plane-parallel surfaces in the light path of the instrument. These surfaces act as Fabry-Pérot etalons, each of which can add unique fringe components to the source signal. The major components in SH and LH originate from the detector substrates. The LL1 fringes are believed to be the result of a filter de-lamination discovered prior to launch. The SL data and LL2 data do not contain any identified fringe residuals.

The fringes observed in the final spectra are residuals of the observed fringes after flux calibration. The observed fringe spectrum is modified during calibration due to wavelength shifts resulting from pointing offsets or a complex source morphology within the slit. No application of a response function (be it the SRFs used in the c2d extractions or the flat field in the SSC BCD extraction) can therefore fully correct for these effects and small residual fringes will be present in most spectra. The amplitudes of the fringe residuals can be up to ~5% and depend on source morphology, pointing, order, and wavelength.

After extraction and flux calibration, the high resolution (SH and LH) and the LL order 1 spectra are defringed using the `IRSFEDGE` package developed by the c2d team. The `IRSFEDGE` documentation and software can be downloaded from the *Spitzer* Post-BCD website.¹² Also see Lahuis & Boogert (2003) for an introduction to IRS defringing.

`IRSFEDGE` uses a fringe model based on robust sine-wave fitting to remove fringe-residuals from the spectra. Figure 3.7 gives an illustration on how the defringing works

¹²<http://ssc.spitzer.caltech.edu/postbcd/irsfringe.html>

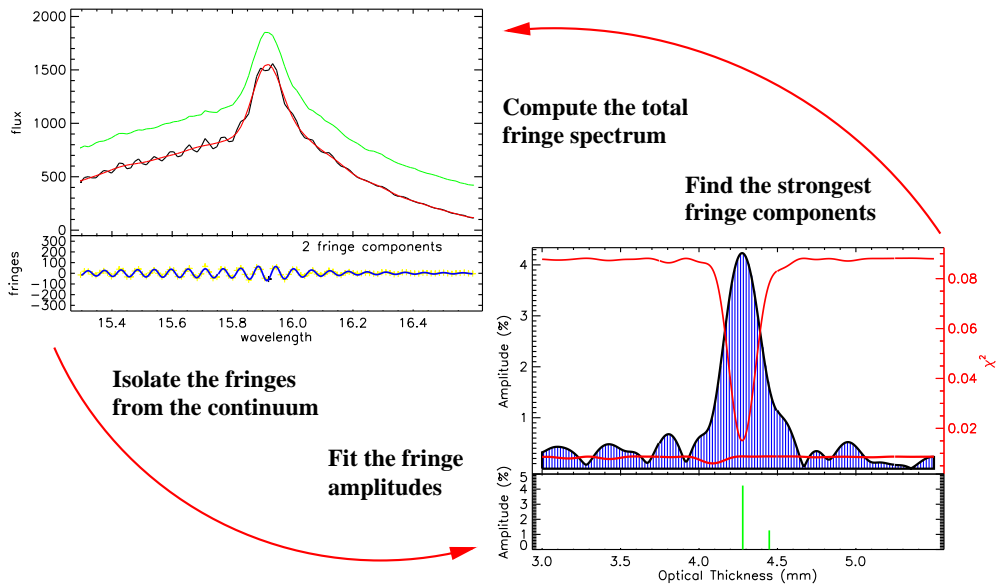


Figure 3.7 Defringing IRS spectra in practice. The left figure shows the original spectrum with the continuum overlotted. The final defringed spectrum is shown offset for clarity. In the lower panel, the continuum subtracted data and the computed fringe spectrum are plotted. In the right figure, the derived fringe amplitude and the effective decrease in chi-squared are plotted for the selected range of optical thickness. In the lower panel, the selected fringe components are shown.

(see also Lahuis & Boogert, 2003). To avoid overfitting, a conservative signal-to-noise cutoff is used in the defringing. This means that residual fringing can still be present in the delivered data and for specific science applications manual defringing may be required on all or part of the spectra.

3.2.7 Order matching

In order to produce cleaner spectra for the SH and LH modules, orders within each module are scaled in flux such that consecutive overlapping orders are matched. For SL and LL this is not done as order mismatches for these modules can be useful for assessing pointing errors. In the wavelength overlap region between SL and LL order 1 and 3 the impact of pointing is different. This difference is reflected in the observed flux loss.

First, the average wavelength and flux are determined from the data of all order overlap regions. These are used as the reference wavelengths and fluxes. The average wavelength and flux for each order in the order overlap regions is then determined for both sides of the order. The orders are finally corrected to the reference using a first order polynomial. For the first and the last order, only a single weighted wavelength and flux is calculated and a zero order correction is applied. The correction is made by scaling the flux of the order, unless the correction slope becomes negative within the order wavelength range, in which case the correction is made by adding/subtracting a

flux offset. This happens for a small number of very weak sources and in a few cases for orders where the flux becomes almost zero due to a very deep silicate $9.8\mu\text{m}$ absorption band.

To enable an evaluation of the consistency of the spectral slope in the inter-order regions, order clipping is not applied. For example, a slope discontinuity may be a signature that features have been introduced after order matching due to order tilts. This and other spectral artifacts will be discussed in detail in § 3.3.5.

3.3 Data products of IRS pointed observations

For all pointed IRS observations three products are generated:

1. A spectrum for each IRS target as a NASA/IPAC ASCII table.
2. Two PostScript files for each spectrum.
 - a. PostScript file with the spectrum and extended emission estimate.
 - b. PostScript file with the optimized source spectrum, see § 3.3.4.
3. A log file describing each observation (see Appendix A for an example).

A complete overview of all observations is included in the c2d IRS explanatory supplement. The following subsections describe the data products and how they can be used.

3.3.1 IRS c2d products

The IRS pipeline, calibration, and extraction procedures remain in a state of constant development. As a result, the most optimum end-to-end reduction for any observation depends on various parameters that are currently not yet fully understood. In any extracted spectrum, artifacts will be present at some level. Therefore, we employ a number of extraction methods in our reduction pipeline and deliver two spectra for each source.

The c2d observations consist primarily of single staring-mode observations. Since the majority of the sources lie in complex star forming regions, no individual sky observations were taken. For this reason, none of the spectra have been corrected using direct measurements of the local sky. An estimate of the local sky contribution (as estimated in the c2d optimal PSF extraction, see § 3.2.2) is therefore calculated and included in the delivered products. Also a best estimate source spectrum with extended emission and pointing corrections applied is included (see § 3.3.4). An example is given in Figure 3.8.

The products delivered to the SSC include an IPAC format ASCII table that contains the combined 1-D spectra extracted from all observed modules and log files that briefly describe each observation. Included in the log file is a list of the most prominent spectral features (see § 3.3.9). For a first impression, a PostScript plot of the combined spectrum has been generated for each target.

The IPAC tables can easily be read into an IDL data structure within IRSFRINGE or SMART using the command

```
STRUCT = IPAC2IRS( 'YOUR_FAVOURITE_SOURCE.TBL' ).
```

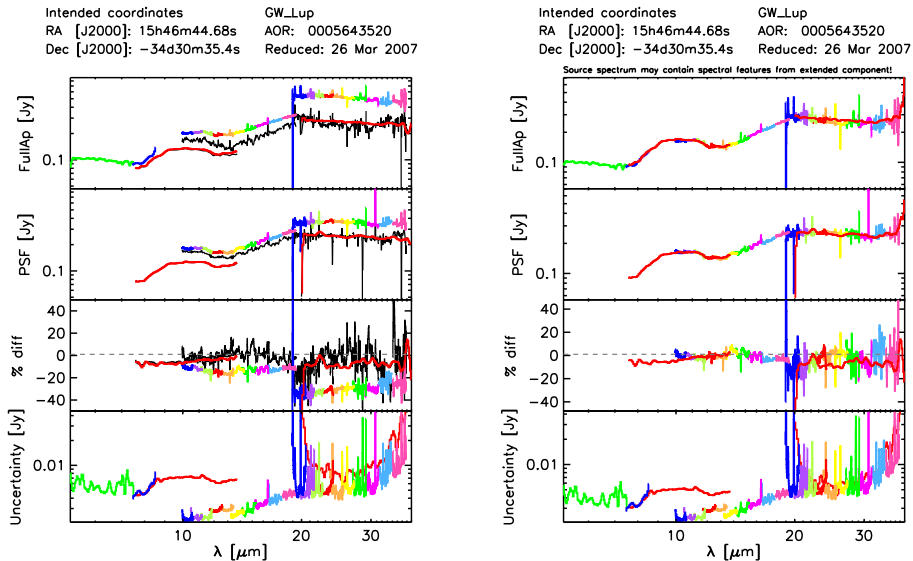


Figure 3.8 PostScript plots provided with the delivered spectra. Left: the extracted IRS spectra. Right: the final optimized source spectrum with an SED correction for the extended emission and a pointing correction to correct for module discontinuities. Shown from top to bottom are, (i) the full aperture extraction, (ii) the PSF extraction, (iii) the relative difference between Fullap and PSF, and (iv) the propagated errors. No error is yet assigned in the extended emission correction and no reverse error correction is applied in the pointing error correction. This source illustrates two issues with IRS spectral data: extended emission and pointing errors. The observed spectra show a strong offset of LH with respect to SH and LL, and of SH with respect to SL. After correcting for extended emission in SH and LH, both match. The discontinuity between SL1 and SL2 and SL1 and SH indicate a pointing error for SL; this is corrected for in the right plot (see § 3.3.4). Note that the final optimized spectra may still contain artifacts, see § 3.3.5 for more details and examples.

The log files include a summary of the source nomenclature and coordinates along with the observation date, mode, and integration times, basic source parameters and identified spectral features. Appendix A gives an example of one of the log files.

The PostScript plots give a quicklook overview of the spectra contained in the data files. Figure 3.8 shows an example of the two plots delivered for each observation.

3.3.2 Source parameters

Basic source characteristics, including the source size (after correction for the PSF size) and location within the slit, are determined within the PSF extraction. These are listed in the log file.

The source size is determined from the width of the PSF function fitted to the source compared to the width of the PSF function fit to standard calibrator stars. A source size of zero implies the source is not extended ($< \text{few}''$) to the *Spitzer* IRS instrument. For staring observations, cross-dispersion positions for both dither positions are deter-

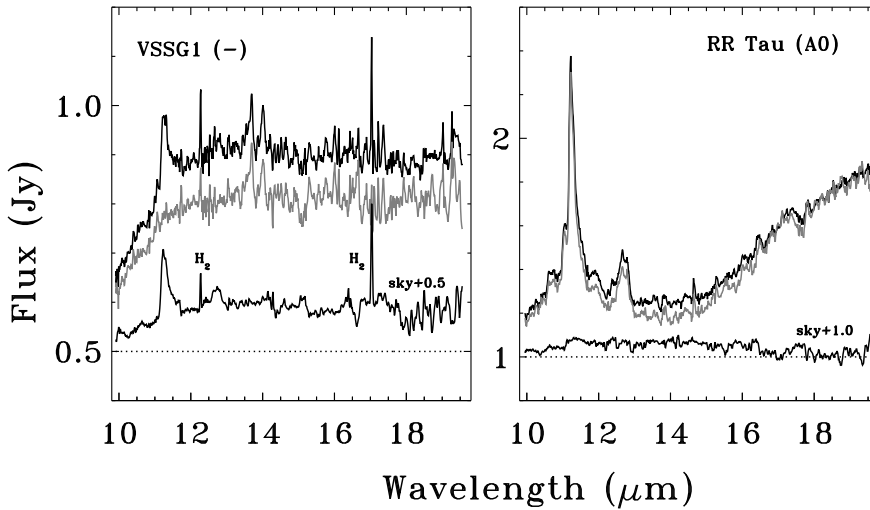


Figure 3.9 Example using the estimate of the local extended emission in the study of PAH spectral features. Shown are the observed spectra and estimated sky emission in black and the sky corrected spectrum in gray. Toward VSSG1, all PAH emission is extended and no PAH intrinsic to the source is observed. Toward RR Tau, all PAH emission is local to the source without confusion by extended emission in the IRS aperture. (Geers et al., 2006).

mined for all modules. The offset listed in the log file is the offset with respect to the average cross-dispersion positions for the sample of standard stars which have been observed with high accuracy peak-up. The cross dispersion offsets can be used as a first order estimate of the dispersion offset, and thereby the flux loss, of the orthogonal slits. This means the LH cross dispersion offset gives an estimate for the SH dispersion offset and vice versa. The same applies to the SL and LL modules.

3.3.3 Extended emission

The optimal PSF extraction and the full aperture extraction for the SL1, LL1, SH, and LH modules provide a direct measure of the amplitude of the zero level of the spectrum. This zero level is a combination of extended emission in the direct vicinity of the source, be it sky or envelope emission, and residuals of, e.g., the dark current subtraction in the SSC pipeline. For the full aperture extraction, the extended emission is estimated from the PSF extraction scaled to the full aperture size. Though for SL1 and LL1 a sky correction derived from the other dither position is applied, extended emission can still be present, e.g. as a result of incorrect straylight correction for SL1 or because the extended sky emission varies strongly over the grid.

The flux values delivered in the c2d products contain the signal of the source plus the extended emission. For the full aperture extraction the flux is in units of Jy/Aperture and for the PSF extraction it is in Jy/beam. Thus, for a point source without extended emission, this flux is in Jy.

It is possible to spot extended spectral features in the spectra in two ways. The first one is to directly subtract the estimated extended emission of the observed spectrum,

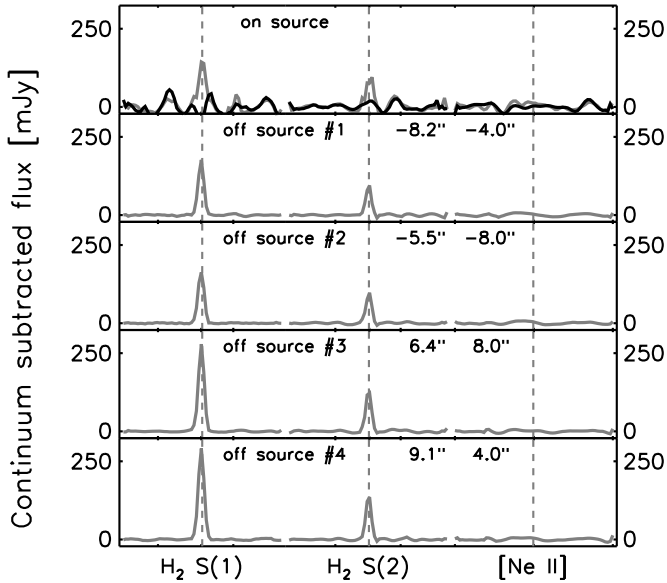


Figure 3.10 Example of extended molecular hydrogen line emission toward VSSG 1. Plotted in gray is the total observed emission. Plotted in black in the top panel is the emission after the estimated extended component is subtracted. This illustrates the problem of detecting unresolved emission toward young stars; the extended emission is often significantly stronger than the unresolved source component and can vary with position. In this example, no compact on-source emission has been detected.

see Figures 3.9 and 3.10 for examples. The second way is to compare the peak strength of the feature. For extended features, the peak strength in the full aperture extraction will be stronger than in the PSF extraction reflecting the difference in aperture ($\sim 10 - 12 \text{ pixel}^2$) versus beam ($\sim 3 - 5 \text{ pixel}^2$), see e.g. the $\text{H}_2 \text{ S}(1)$ emission line presented in Figure 3.13.

The estimate of the extended emission is, by nature of the fitting process, inherently more noisy and uncertain than the total signal. Therefore no automated correction is applied but it is left to the user to use the extended emission estimate. When used for SED analysis or the study of resolved features, a smoothed version of the extended emission spectrum can be used which does not introduce spectral noise (e.g., see studies of extended PAH emission by Geers et al. (2006) and the example in Figure 3.9). When analyzing unresolved features (e.g., studies of H_2 emission lines by Lahuis et al. (2007) and the example in Figure 3.10), a direct subtraction of the extended emission or a correction of a Gaussian line fit to the extended emission is required to obtain the unresolved source component.

3.3.4 Final source spectrum

In order to provide the most useful products that reflect more closely the on-source emission, additional corrections are applied to the results of the Fullap and PSF extractions (see Figures 3.11 and 3.8 for an example). First for SL1, LL1, SH, and LH the

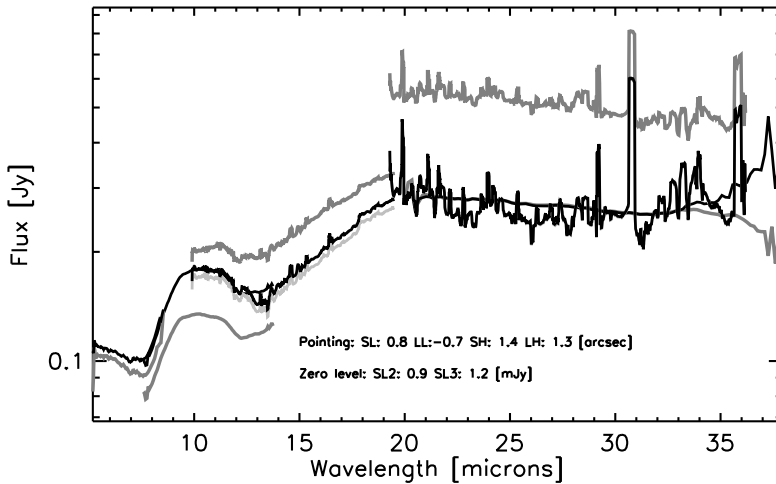


Figure 3.11 Producing a final spectrum for the source GWLup which has both extended emission and a pointing offset. In dark gray the observed signal (Fullap), in light gray the signal of SH and LH corrected for extended emission, and in black the final spectrum (see § 3.3.4 for details). Note that light gray and black for LH are virtually on top of each other. The optimum pointing offsets and zero level corrections are printed below the spectrum. Note that the final spectra often still contain artifacts, in particular the LH module, see § 3.3.5 for more details and examples. The pointing correction was done using a β -version of the pointing fluxloss calibration and software, a collaborative effort of the c2d and FEPS legacy teams.

estimated extended emission component (see § 3.3.3) is subtracted. After this, pointing errors are corrected based on optimal module matching. The optimization is done by minimizing the difference between the modules (see Table 3.1) over the complete overlap range to maximally exploit the strong wavelength dependence of the fluxloss functions (see Figure 3.12). The module overlap regions of SL2/SL1, SL1/SH, SH/LH, LL2/LL1, and LL/SH+LH are used.

Since the extended emission estimates inherently contain more noise and artifacts than the complete (source+extended emission) spectrum, a smoothed version over the complete module wavelength range is subtracted from the observed spectrum. The extended emission estimates are smoothed with a broad median filter and then fit with a low order polynomial (4th order for low resolution and 6th order for high resolution). To suppress edge effects the spectra are padded with the smoothed flux on both wavelength ends. For the low resolution modules, an extended emission correction is applied during extraction. Residual extended emission can still be present as a result of, e.g., a varying local sky, SL straylight residuals, or dark current residuals. For SL1 and LL1, the extended emission estimate is used for the correction, but this is not usable for SL and LL order 2 and 3. Instead, for these orders, an additional zero level correction is included in the module optimization.

If for a particular module *no* unresolved (or slightly extended) source component could be identified during extraction, the final source spectrum is set to zero for that module. For example, an extremely blue or extremely red object may have no detectable source signal in only the long or short wavelength modules, respectively. If the

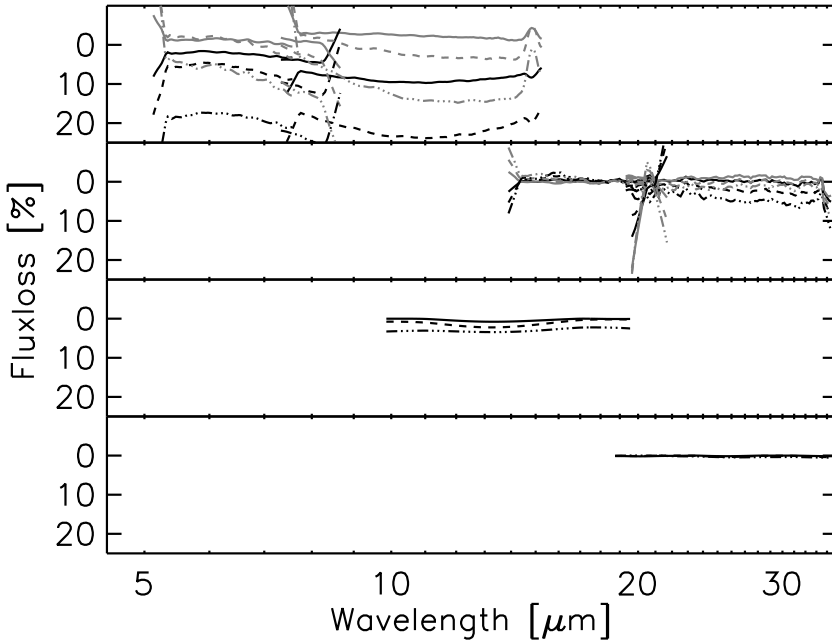


Figure 3.12 Pointing error flux loss for 0.4, 0.8, and 1.2". The SL and LL fluxloss functions are derived from standard star mapping observations, the SH and LH fluxloss functions are derived from the optimal extraction cross dispersion PSF assuming a spherical PSF. Empirical fluxloss functions for SH and LH are to be derived at a later date. For SL and LL it should be noted that the PSF is not centered on the slit and two curves are plot for each offset, for a positive and a negative pointing error. The characterization of the pointing fluxloss is a collaborative effort of the c2d and FEPS legacy teams.

source is fully extended in all modules, then the source spectrum contains the original spectrum without correction.

The pointing offsets (in arcseconds) and zero level offsets (in Jy) required to optimally match the modules in the spectra are listed in the IPAC table header. The pointing offset estimates are listed using the keywords SLPE.PSF (pointing offset for PSF spectrum), SLPE.SRF (pointing offset for FullAp spectrum) and similar for the other modules. The SL and LL zero level offsets are included in the header using SL2Z.PSF (SL order 2 zero level for PSF spectrum), and similar for order 3, the FullAp extraction (.SRF), and the LL modules (see Appendix B).

It should be noted that only a smoothed low resolution correction for the extended emission is applied. Therefore spatially extended unresolved spectral features, such as H₂ or forbidden line emission, are not removed from the final spectra. If extended spectral features are present, then a careful examination of the original spectrum and estimated extended emission (see § 3.3.3) is required in order to use the spectra for science analysis.

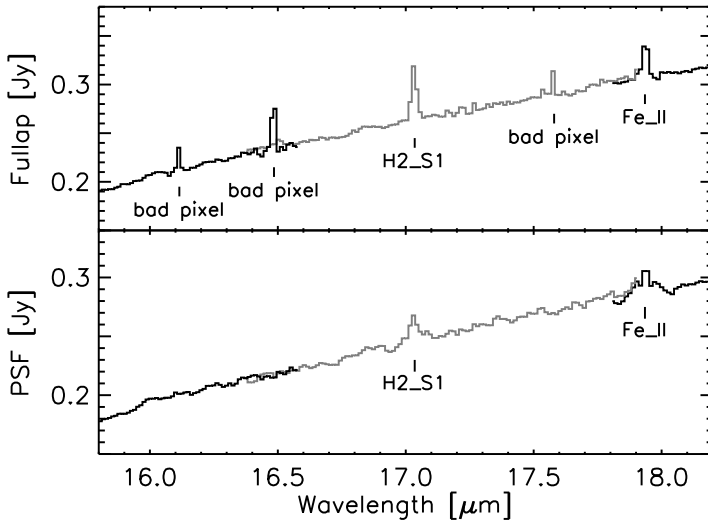


Figure 3.13 Example of a source spectrum (Sz 102) with bad pixels and gas-phase features. In this region of the spectrum, there are clearly identified bad pixels (near 16.1 and 17.6 μm), one multi-pixel spike near 16.5 μm , and strong multi-pixel gas phase lines (H₂S1 at 17.04 μm and Fe_II at 17.9 μm). Comparing the two spectra helps to identify the bad pixels. Note the difference in the strength of the H₂ S(1) and [Fe],II lines between the extractions as a result of the line emission being extended while the continuum emission comes from the unresolved source.

3.3.5 IRS artifacts

As noted above, the c2d correction of bad/hot pixels, as well as pixels flagged in the BCD pipeline, greatly improves the final S/N ratio of the spectra. This does not mean, however, that the spectra are free of artifacts. The inclusion of spectra extracted using two different extraction techniques can be used to recognize the presence of some artifacts, but this is not guaranteed to be foolproof. Artifacts, both resolved and unresolved, can be present in the delivered spectra and great care should be taken when interpreting any “features.”

Therefore, we will now discuss various types of artifacts that we have found to be present in the c2d spectra. This list is not meant to be all-inclusive, but should be viewed as examples of the types of artifacts that are most common. These artifacts may arise from a variety of factors.

3.3.6 Spikes

Narrow (1–2 pixel wide) spikes in the spectrum can often be associated with ‘hot’ or bad pixels that were not identified and corrected using the interpolation routines (see § 3.2.1 and Figures 3.2 and 3.3). As discussed above, these artifacts are most prominent in the LH spectra, but they also appear in the LL, SH, and, occasionally, SL modules. The PSF and Fullap extractions use different methods to correct for bad pixels; for the Fullap method, the pipeline finds and interpolates bad pixels prior to extraction and

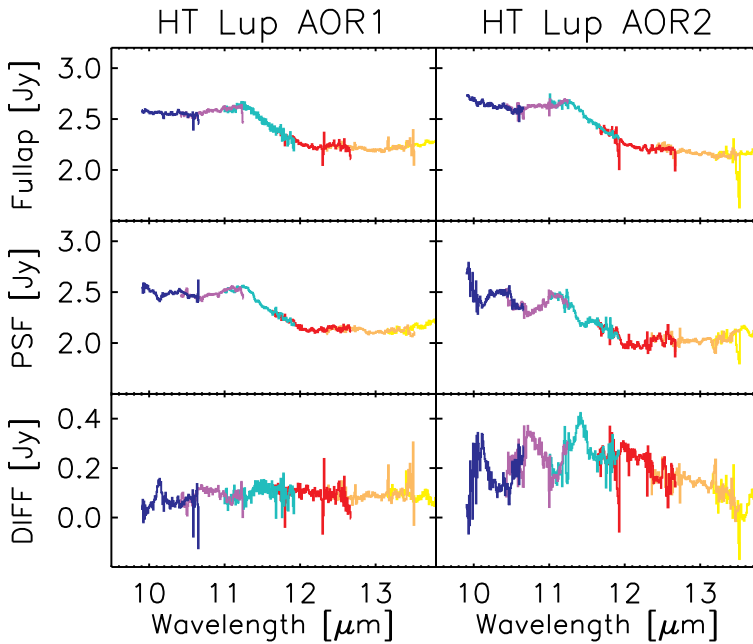


Figure 3.14 Extracted spectra for HT Lup AOR1 (IRS staring mode, left) and AOR2 (IRS mapping mode, right) are shown. The differences in the shapes of the lowest wavelength SH orders (where the spatial sampling to which the PSF extraction is sensitive becomes critical) between the extractions exemplifies order curvature type artifacts. The AOR2 spectrum shows that the PSF extraction becomes less reliable when used for the spectral extraction from single map pointings as a result of the narrower cross dispersion baseline compared to wider baseline in the combined two dither positions for the staring observation. Note that due to the order curvature artifacts, the user must be careful when interpreting the shape of the amorphous silicate $10\ \mu\text{m}$ feature and/or the identification of crystalline forsterite or PAH features (both near $11.3\ \mu\text{m}$). In the case of HT Lup, we are fortunate to have 2 different observations to compare, in most cases, one must use the error estimates and comparisons of PSF vs. Fullap extractions to determine whether order curvature is a factor.

the PSF method only includes pixels identified as “good” in the extraction. Therefore, comparing the resulting spectra from the two extractions can often help to identify bad pixels (see Figure 3.13), as they may appear in only one spectrum. Additionally, true gas-phase lines will usually be a bit broader (2-3 pixels wide) than spikes due to bad pixels, but it is often difficult to distinguish real emission and (1–2 pixel wide) spikes should always be treated with caution.

3.3.7 Edge effects

Artifacts located at the edges of orders may be present due to “order curvature,” “order tilt,” or “bad order matching” (that is, there can sometimes be large differences in flux or spectral shape between successive orders). Such problems often arise when the source is not centered in the slit. The PSF correction applied to both full slit and

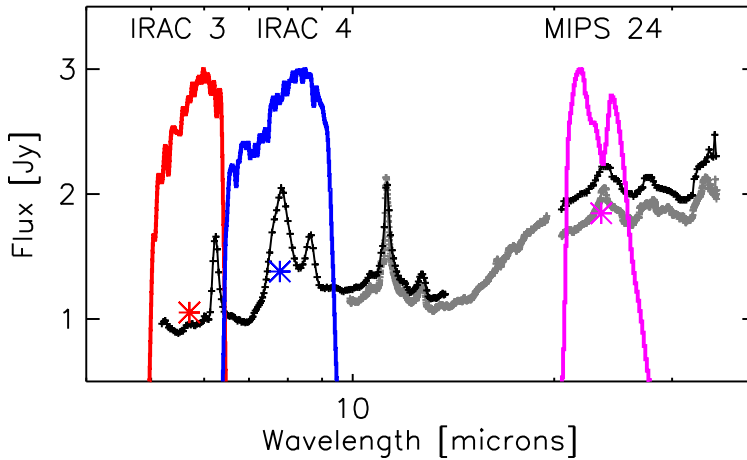


Figure 3.15 The observed *Spitzer* IRS spectrum of RR_Tau and the IRAC 3, IRAC 4, and MIPS 24 filter profiles used to derive the continuum values together with the feature identification. In grey are the SH and LH spectra and in black the SL and LL spectra.

source profile fitting extractions has reduced the frequency and severity of these types of artifacts, but they are still often present, and are particularly common in cases with large pointing offsets. Order curvature often results in “V” shaped dips or increases in the flux of the spectrum at the intersection of two orders. These can easily be misinterpreted as solid-state emission or absorption features (See Figure 3.14). Order tilt in successive orders, if corrected by scaling the orders to match in the overlap regions, can result in an increase in the continuum slope in the affected spectral region. If left uncorrected, order tilts or bad order matches result in sharp jumps in the spectrum in the order overlap region. In most cases, one must use the error estimates and comparisons of PSF vs. Fullap extractions to determine whether order curvature is an artifact. If the log file indicates that there is a pointing offset, order artifacts will likely be corrected in the final pointing corrected source spectrum.

3.3.8 Module mismatches

Additionally, there may be significant differences in the flux of consecutive modules (see Figure 3.11). This is particularly true in the overlap between high resolution and low resolution modules, particularly for the full slit extraction, due to differing contributions from background flux. Pointing offsets will also result in flux differences between modules, as the module slits are oriented perpendicular to one another. Again, if these issues are due to pointing offsets, then they should be corrected in the final source spectrum.

3.3.9 Spectral features

To provide a quick assessment of the nature of the observed sources, an automated feature identification, restricted to a selected set of spectral features (see Table 3.3), is included in the c2d pipeline. The identified features for each source are listed in the

log files (Appendix A) and complete lists of features found in all sources are presented in the c2d explanatory supplement. In these the integrated fluxes of the IRS spectra over the IRAC 3, IRAC 4, and MIPS 24 photometric bands using the instrumental filter profiles (see Figure 3.15 for an example) are also included. The feature tables have been checked by eye by c2d team members and comments (about suspect features, etc.) are noted in the logs. Given the complexity of the data and the observed features (e.g., the presence of extended emission and pointing uncertainties), no feature strengths or optical depths are derived. To do so requires more sophisticated fitting procedures.

In order to reduce the mis-identification of features the extended emission and pointing corrected spectra (see § 3.3.4) are used as input for the feature identification. Remaining offsets between consecutive modules are corrected such that the overlapping regions match in flux. The modules are matched pairwise, SL1 to SH, SL2 to SL1, LH to SH, and LL to combined data from SH and LH. This additional module matching is only done to facilitate the feature ID process. As mentioned in § 3.3.5, the difference in flux between modules is likely due to differences in background emission and/or pointing offsets. Simply scaling the modules may not be the correct approach for determining the strength or composition of features, but is acceptable for determining the *presence* of the strongest, most easily identified features, as done here.

Feature identification

Table 3.3 lists the feature information and constraints used by the feature identification script. The wavelength (λ) and FWHM are used to initialize the fit parameters of the feature profile and are allowed to vary within a limited range ($\sim 0.3 \times \text{FWHM}$). The continuum points define two regions on either side of the feature, one on the short wavelength side (between wavelengths cont 1a and cont 1b) and one on the long wavelength side (between cont 2a and cont 2b). These continuum regions are used to make an initial estimate of the continuum parameters. After parameter initialization, a Gaussian profile with a 2nd order polynomial is fitted to the data between cont 1a and cont 2b. When two values are listed for λ and FWHM in Table 3.3, a two component Gaussian fit is made. This is the case for overlapping features, e.g., ICE.6 and PAH.7,8, and for features with shapes that are non-Gaussian and require a multiple component fit, e.g., for CO.2, SiO.s, and SiO.b. Though a simple two-component fit is insufficient to accurately reproduce the shape of the latter bands, it is sufficient to establish their presence or absence.

Narrow lines

A number of gas-phase emission lines are searched for by the feature identification program. This includes all molecular hydrogen lines in the IRS range, from $\text{H}_2\text{S}(0)$ to $\text{H}_2\text{S}(7)$, and a number of atomic forbidden lines. As these lines are expected to be unresolved, the FWHM is set to the instrument resolution and wavelengths to determine the continuum are set to the following, cont 1a = $-4 \times \text{FWHM}$, cont 1b = $-1.5 \times \text{FWHM}$, cont 2a = $1.5 \times \text{FWHM}$, and cont 2b = $4 \times \text{FWHM}$. For all lines, a Gaussian profile with a center position and a width are fit to within 25% of the instrument resolution. A larger offset in the center position is not acceptable considering the accuracy of the IRS wavelength calibration.

Table 3.3. Input list for automatic feature identification

ID	em/abs/cnt	λ^a [μm]	FWHM ^b [μm]	cont 1a ^c [μm]	cont 1b ^c [μm]	cont 2a ^c [μm]	cont 2b ^c [μm]
H2.S0	em	28.219
H2.S1	em	17.035
H2.S2	em	12.279
H2.S3	em	9.665
H2.S4	em	8.025
H2.S5	em	6.91
H2.S6	em	6.109
H2.S7	em	5.511
Ne.II	em	12.814
Ne.III	em	15.56
Fe.I	em	24.042
Fe.II	em	17.936
Fe.II	em	25.988
S.I	em	25.249
S.III	em	18.71
Si.II	em	34.82
PAH.11.3	em	11.3	0.1	10.5	10.9	11.6	12.1
PAH.12	em	12.7	0.3	11.9	12.3	13.0	13.6
PAH.6	em	6.2	0.2	5.7	6.05	6.5	6.8
PAH.7.8	em	7.7 & 8.6	0.7 & 0.4	6.8	7.10	9.0	9.3
CO.2	abs	15.15& 15.5	0.35 & 0.5	14.40	14.75	15.87	16.39
ICE.6	abs	6.0 & 6.85	0.4 & 0.3	5.40	5.65	7.20	7.60
SiO.s	abs/em	9.7 & 11.0	1.5 & 1.5	7.1	7.9	13.0	14.0
SiO.b	abs/em	18.52 & 22.0	3.0 & 3.0	13.2	14.7	25.	30.
SiO.l	em	34.0	2.0	30.5	31.5	36.0	37.5
Em.11.3	em	11.3	0.6	10	10.7	11.7	12.5
IRAC 3	cnt	5.7
IRAC 4	cnt	7.8
MIPS 24	cnt	23.5

^aThe center wavelength of the Gaussian fitting profile. When two wavelengths are listed, the fitting profile is composed of two Gaussian components.

^bThe full width at half maximum of the Gaussian fitting profile. When two FWHM are listed, the fitting profile is composed of two Gaussian components.

^cThe continuum is defined as from cont 1a to cont 1b on the short wavelength side of the feature and from cont 2a to cont 2b on the long wavelength side of the feature. — If the FWHM and continuum wavelengths are not defined, then the feature is either unresolved or a continuum feature. For unresolved features, the FWHM is set to the instrument resolution and the continuum regions are defined as; cont 1a= $\lambda - 4 \times \text{FWHM}$, cont 1b= $\lambda - 1.5 \times \text{FWHM}$, cont 2a= $\lambda + 1.5 \times \text{FWHM}$, and cont 2b= $\lambda + 4 \times \text{FWHM}$.

Note. — For the continuum features, IRAC 3, IRAC 4, and MIPS 24, the instrumental filter profiles are used (see Figure 3.15).

PAH features

The most prominent features from polycyclic aromatic hydrocarbons (PAHs), near 6.2, 7.7, 8.6, 11.3 and 12.7 μm , are included in the c2d feature identification. The 6.2 and 12.7 μm features are fairly isolated, but the 7.5 and 8.6 μm features overlap with each other and the 11.3 μm feature overlaps with the broad 9.8 μm silicate feature. For this reason, the feature ID program groups the 7.5 and 8.6 features together as “PAH.7.8,” fitting a profile that is the combination of two Gaussian profiles. The feature fit for the 11.3 μm feature uses the underlying silicate feature as the “continuum” looking for a narrow feature with a width of $<0.2 \mu\text{m}$. PAH features, when identified, are subtracted from the spectrum before silicate features are fit.

Silicate bands

The c2d feature identification program searches for the most prominent silicate features, which are broad amorphous olivine/pyroxene Si-O stretching and O-Si-O bending modes, in emission or absorption, at 9.8 and 18 μm (labeled “SiO.s” and “SiO.b”), and a crystalline silicate (forsterite/enstatite) lattice mode emission feature at 33–35 μm (“SiO.l”). There are several crystalline silicate emission features overlapping with the broad amorphous features, but the exact wavelengths of these features are dependent on the grain size and composition (Kessler-Silacci et al., 2006). They are difficult to be reliably identified in this automated method and are therefore not included. The one exception is a crystalline forsterite feature near 11.3 μm , which often can be distinguished from the 9.8 μm amorphous feature. However, this feature overlaps with the narrow 11.3 μm PAH feature, but appears to be broader in sources with verified crystalline silicates. For this reason, in cases where a feature can be identified near 11.3 μm , but the feature is broader (width $\sim 0.6 \mu\text{m}$) than typically seen for PAH, we label it as “Em.11.3.” In some cases, identification of Em.11.3 could be due to an SiO.s feature with a flattened shape, possibly indicative of grain growth. Detailed compositional modeling of the spectra are required to determine if this feature is due to PAH or forsterite emission. The identification of the broad amorphous SiO.s and SiO.b features can sometimes be confused by the presence of strong, narrow crystalline silicate emission features. In addition, for a number of observations, SL order 1 data is not available, thus cutting off a part of the SiO.s feature. In some cases this may lead to a non-detection or a false detection.

Ices

There are several ice absorption features, but the c2d feature identification includes only the most prominent: the CO₂ feature near 15.1 μm and two overlapping ice features near 6.0 and 6.85 μm (combined as “ICE.6”).

Blended features

Several features in the spectra are blended with other features, e.g. H₂ emission lines on top of the ICE.6 band, PAH 11.3 μm emission on top of a Si-O stretching mode band, and CO₂ absorption on the very broad Si-O bending mode profile. For this reason, a feature is removed from the spectrum (only for the purposes of feature identification) after it has been positively identified.

Identified feature tables

Complete lists of features identified in the observed spectra are presented in the c2d IRS explanatory supplement. The first table lists the detection status for all gas phase molecular hydrogen and atomic lines and the second table lists the detection status for all solid-state features, including features from PAHs, ices, and silicates. Also listed, in the last 3 columns of second table, are the spectral fluxes integrated over the IRAC 3, IRAC 4, and MIPS 24 photometric bands. In both tables, a check mark (✓) denotes that the feature has been detected at $> 5\sigma$, averaged for both the full slit and source profile fitting extractions, and at least 3σ in both extractions. For the 9.8 and 18 μm silicate

bands, “ \checkmark (A)” and “ \checkmark (E)” denote that the feature was detected in absorption or emission, respectively. A question mark (?) denotes that the feature has been detected at $3 - 5\sigma$ in amplitude, averaged for both the full slit and source profile fitting extractions. Dashes (“-”) indicate non-detections. These tables can be used to get an overview of the most prominent features in each spectrum, but should not be considered as a complete or definitive inventory. In the case of extended emission, for example, the PSF extraction will show a much weaker feature than the full aperture extraction, and thus the feature may not meet the above criteria. In cases where the feature identifications made by the automated routine are determined by visual inspection to be incorrect or questionable, a note is made in the log file and in the tables, but the feature is still listed.

It should also be noted that many of the observed emission lines and several PAH features are resulting from extended emission close to the source (§ 3.3.3). Therefore, the features identified in the spectrum and attributed to a particular target in the tables and logfiles may not be due to on-source emission. For a number of these extended emission lines (Lahuis, in prep.) and PAH features (Geers et al., 2006) no source emission or only a (weak) source component is found by carefully using the sky estimate derived from the optimal PSF extraction.

3.4 Summary

This chapter describes the c2d reduction pipeline and the products it generates. This pipeline is used to generate the products used for the science analysis by the c2d team members (such as IRS data used in this thesis) and the products included in the final legacy data delivery of improved products to the *Spitzer* Science Center. It describes, in considerable detail, the products and the algorithms and calibration products used to derive them. The delivery consists for the most part of IRS staring observations, but also includes some MIPS SED and IRS mapping observations, however this Chapter focusses on the reduction of the IRS staring observations. The generated products include data tables, illustrative plots and informative logfiles.

Appendix A – IRS observation logfile

Logfile for the *Spitzer* IRS observation as shown in Figure 3.8.

Quality check file for *Spitzer*/IRS observation.

```
Source:          GW_Lup
Coordinates:    15h46m44.7s -34d30m35.4s [J2000]
Observer:       Neal Evans, OID 87
Program:        From Molecular Cores to Planets, continued
Obs. date:      2004-08-30
AOR:            0005643520
AOR label:      IRSS-0068
AOT type:       irsstare
Obs. mode:      TargetFixedSingle
Peak up mode:   --
IRS Pipeline:   S13.2.0
Modules:        SL1, SL2, LL1, SH, LH
```

The longslit images of the SL2 and LL2 modules are severely undersampled over most of their wavelength range. As a result the PSF extraction is unstable for these modules. Therefore the PSF, PSF_sky, and the FullAp_sky columns contain no data.

=====

Data summary:

SL integration: 14*1*2 (tint*ndce*nexp)
 SH integration: 121*2*2 (tint*ndce*nexp)
 LL integration: 14*4*2 (tint*ndce*nexp)
 LH integration: 60*4*2 (tint*ndce*nexp)

SL SNR: 20 STDEV: 5 [mJy]
 SH SNR: 66 STDEV: 2 [mJy]
 LL SNR: 34 STDEV: 7 [mJy]
 LH SNR: 49 STDEV: 6 [mJy]

SL source size : 1.1 [arcsec]
 SL X-dispersion offset : 0.2 [arcsec]
 SL pointing offset estimate: 0.8 ... 0.8 [arcsec]
 SH source size : 0.4 [arcsec]
 SH X-dispersion offset : 0.9 [arcsec]
 SH pointing offset estimate: -0.9 ... -0.6 [arcsec]
 LL source size : 1.9 [arcsec]
 LL X-dispersion offset : 1.0 [arcsec]
 LL pointing offset estimate: -0.9 ... -0.4 [arcsec]
 LH source size : 0.0 [arcsec]
 LH X-dispersion offset : -0.5 [arcsec]
 LH pointing offset estimate: 1.3 ... 3.2 [arcsec]

=====
 Most prominent spectral absorption and emission features identified in the Spitzer/IRS spectrum of GW_Lup

IRAC3, IRAC4, and MIPS24 give the flux of the observed spectra, if possible with a correction for extended emission and pointing errors, convolved with the respective passbands.

SNR estimate is the peak intensity or peak optical depth of the feature over the residual rms after feature fitting.

N.B. The identification is done using an automated script.
 Caution should therefore be taken at all times.

id	abs=2	lambda [um]	snr
	em=1	lambda [um]	snr
	cnt=-1	lambda [um]	flux [mJy]
SiO_s	1	9.700	17
Em_11.3	1	11.300	5
irac3	-1	5.702	96
irac4	-1	7.784	111
mips24	-1	23.512	264

#> -----
 - The spectra are good
 - Features identification is ok
 - Em_11.3 could also be caused by a broad SiOs feature.

Appendix B – IRS table header

Header of IRS spectral table for the *Spitzer* IRS observation as shown in Figure 3.8.

```
\c2d_irs_spectrum
\processing date Nov 2006
\char HISTORY =====
\char HISTORY The spectrum presented in this table is a combination
\char HISTORY of all Spitzer/IRS c2d data for the object GW_Lup
\char HISTORY The data have been observed, reduced and verified by the
\char HISTORY Spitzer c2d legacy team:
\char HISTORY 'From Molecular Cores to Planet Forming Disks'
\char HISTORY http://peggysue.as.utexas.edu/SIRTF/
\char HISTORY Before using this data please read the quality file accompanying
\char HISTORY this specific dataset and the complete documentation of the
\char HISTORY release of all the c2d legacy data.
\char HISTORY
\char HISTORY For questions please contact the Spitzer helpdesk
```

```

\char HISTORY          help@spitzer.caltech.edu
\char HISTORY who will answer your questions or forward them to one of
\char HISTORY the c2d IRS experts.
\char HISTORY =====
\char NAXIS            =                2 / STANDARD FITS FORMAT
\char ORIGIN = '      c2d Legacy team' / Organization generating this FITS file
\char TELESCOP= '          Spitzer' /
\char INSTRUME= '          IRSX' /
\char EQUINOX = '          2000.0' / Equinox
\char CREATOR = '          S13.2.0' / SSC Pipeline Version
\char OBJECT = '          GW_Lup' / Target Name
\char RA_HMS = '          15h46m44.68s' / [hh:mm:ss.ss] Commanded RA as sexagesimal
\char DEC_DMS = '          -34d30m35.4s' / [dd:mm:ss.s] Commanded Dec as sexagesimal
\real RA_SLT = '          236.68617' / [deg] RA at slit center
\real DEC_SLT = '          -34.50983' / [deg] DEC at slit center
\char DATE_OBS= '          2004-08-30' / Observation Date
\char AOT_TYPE= '          irsstare' / Observation Template Type
\char OBJTYPE = ' TargetFixedSingle' / Target Type
\char PEAKUP = '          --' / Peakup
\char AORLABEL= '          IRSS-0068' / AOR Label
\char AORKEY = '          0005643520' / AOR key. Astrnmy Obs Req Req
\char OBSRVR = '          Neal Evans' / Observer Name
\char OBSRVRID= '          87' / Observer ID of Principal Investigator
\char PROGID = '          172' / Program IDE
\char PROTITLE= 'From Molecular Cores to Planets, continued' / Program Title
\real SL_TINT = '          14.68' / SL Ramp integration time
\int SL_NDCE = '          1' / SL Commanded number of DCEs
\int SL_NEXP = '          2' / SL Number of exposures per DCE
\real SH_TINT = '          121.90' / SH Ramp integration time
\int SH_NDCE = '          2' / SH Commanded number of DCEs
\int SH_NEXP = '          2' / SH Number of exposures per DCE
\real LL_TINT = '          14.68' / LL Ramp integration time
\int LL_NDCE = '          4' / LL Commanded number of DCEs
\int LL_NEXP = '          2' / LL Number of exposures per DCE
\real LH_TINT = '          60.95' / LH Ramp integration time
\int LH_NDCE = '          4' / LH Commanded number of DCEs
\int LH_NEXP = '          2' / LH Number of exposures per DCE
\char SL_SIZE = '          1.1' / SL source size estimate
\char SL_XOFF = '          0.2' / SL cross dispersion offset
\char LL_SIZE = '          1.9' / LL source size estimate
\char LL_XOFF = '          1.0' / LL cross dispersion offset
\char SH_SIZE = '          0.4' / SH source size estimate
\char SH_XOFF = '          0.9' / SH cross dispersion offset
\char LH_SIZE = '          0.0' / LH source size estimate
\char LH_XOFF = '          -0.5' / LH cross dispersion offset
\real SLPE_PSF= '          0.77' / SL pointing offset for psf spectrum
\real SLPE_SRF= '          0.77' / SL pointing offset for fullap spectrum
\real LLPE_PSF= '          -0.86' / LL pointing offset for psf spectrum
\real LLPE_SRF= '          -0.42' / LL pointing offset for fullap spectrum
\real SHPE_PSF= '          -0.91' / SH pointing offset for psf spectrum
\real SHPE_SRF= '          -0.63' / SH pointing offset for fullap spectrum
\real LHPE_PSF= '          1.26' / LH pointing offset for psf spectrum
\real LHPE_SRF= '          3.20' / LH pointing offset for fullap spectrum
\real SL2Z_SRF= '          0.0100' / SL order 2 zero level for fullap spectrum
\real SL3Z_SRF= '          0.0100' / SL order 3 zero level for fullap spectrum
\char COMMENT =====
\char COMMENT The longslit images of the SL2 and LL2 modules are
\char COMMENT severely undersampled over most of their wavelength range.
\char COMMENT As a result the PSF extraction is unstable for these modules.
\char COMMENT Therefore the PSF and the FullAp_sky columns contain no data.
\char COMMENT =====
\char COMMENT The PSF_SRC and FULLAP_SRC columns contain the observed spectra
\char COMMENT corrected for extended emission within the IRS SH and LH aperture
\char COMMENT and flux loss due to pointing errors.
\char COMMENT Note that the extended emission correction uses a low resolution
\char COMMENT of the estimated sky and the resulting SRC spectrum may therefor
\char COMMENT still contain spectral features (e.g. H2 and PAH) from a
\char COMMENT spatially extended component.
\char END

```

Chapter 4

ISO-SWS Spectroscopy of Gas-Phase C₂H₂ and HCN Toward Massive Young Stellar Objects

Abstract

Observations of gas-phase C₂H₂ and HCN along the line of sight toward a large sample of deeply embedded massive young stellar objects (YSOs) have been performed using the Short Wavelength Spectrometer on board the Infrared Space Observatory. The ν_5 vibration-rotation band of C₂H₂ around 13.7 μm and the ν_2 band of HCN around 14.0 μm have been detected for most lines of sight. These wavelength regions are heavily affected by instrumental fringing and a detailed discussion of the data reduction techniques is given. Comparison with model spectra allows the excitation temperatures and the abundances of the molecules to be determined. The inferred excitation temperatures range from < 100 to 1000 K, and correlate well with each other, indicating that the two molecules probe the same warm gas component. The C₂H₂ and HCN column densities increase by more than an order of magnitude with increasing excitation temperature, and with the amount of heating of the ices. The corresponding abundances of C₂H₂ and HCN in the warm gas increase from $\sim 10^{-8}$ to $\sim 10^{-6}$ with increasing temperatures. The enhanced abundances are compared with a variety of chemical models. The observed gas-phase C₂H₂ most likely results from direct evaporation of interstellar ices, where C₂H₂ must be present at an abundance of $\sim 0.1 - 0.5\%$ with respect to H₂O ice. This abundance is consistent with the measured amount of C₂H₂ in cometary ices. The observed gas-phase HCN abundance shows a stronger increase with temperature and results from a combination of evaporation of ices and high-temperature gas-phase chemistry in the hot core.

Lahuis, F., & van Dishoeck, E.F. 2000, A&A, 355, 699

4.1 Introduction

Infrared absorption spectroscopy of gas-phase molecules can provide important complementary information on the physical and chemical structure of sources compared with submillimeter emission line data (Mitchell et al., 1990; Evans et al., 1991; Carr et al., 1995). Molecules without dipole moments such as C_2H_2 and CH_4 , which are among the most abundant carbon-bearing molecules, can only be observed through their vibration-rotation infrared spectra (Lacy et al., 1989, 1991). An additional advantage of infrared spectroscopy is that the full rotational population distribution of the molecule in its lowest vibrational state is obtained in a single infrared spectrum, whereas multiple frequency settings are needed at submillimeter wavelengths, often involving different telescopes and/or receivers. This allows direct constraints on the excitation conditions, in particular the temperature and density structure of the region. The infrared absorption data refer to pencil-beam lines of sight toward bright infrared sources, most of which are deeply embedded massive young stellar objects (YSOs). Such observations are therefore powerful probes of the chemical evolution of the gas and dust during the earliest stages of star formation (see van Dishoeck & Blake, 1998; Langer et al., 2000; van Dishoeck & Hogerheijde, 1999, for recent reviews) In this paper, observations of two molecules, C_2H_2 and HCN, obtained with the Short Wavelength Spectrometer (SWS) on board the Infrared Space Observatory (ISO) are used to probe the chemistry and temperature structure of the warm gas close to the massive YSOs.

The ISO-SWS provides the first opportunity for vibration-rotation spectroscopy of gas-phase molecules above the Earth's atmosphere. Although the low resolving power $R = \lambda/\Delta\lambda \approx 2000$ of the grating spectrometer prevents the detection of minor gas-phase species, abundant molecules such as H_2O , CO_2 and CH_4 have been seen with the SWS (e.g. Helmich, 1996; van Dishoeck & Helmich, 1996; Boogert et al., 1998; van Dishoeck, 1998; Dartois et al., 1998; Boonman et al., 1999). The observations of C_2H_2 and HCN presented here provide significant complementary information. C_2H_2 forms an important building block in the gas-phase formation of large organic molecules. For example, reactions of C_2H_2 with C^+ , C and small radicals lead to long unsaturated carbon chains, whereas reactions with CN produce cyanopolyynes such as HC_3N (Herbst, 1995). HCN is one of the more abundant nitrogen-bearing molecules in dense clouds, and has, in contrast with C_2H_2 , a large dipole moment. Since HCN can also be observed at submillimeter wavelengths, the combination of the infrared and submillimeter data provides important constraints on the source structure (Carr et al., 1995; van der Tak et al., 1999, 2000).

A major strength of infrared spectroscopy is that not only gas-phase molecules, but also the complementary solid-state species can be detected for the same line of sight. The gas/solid ratios of H_2O , CO_2 and CH_4 provide a new probe of the temperature structure and the evolutionary state of the objects (van Dishoeck et al., 1996; Boogert et al., 1998; Dartois et al., 1998; van Dishoeck, 1998) Moreover, the structure of the ice bands, in particular that of solid CO_2 , gives a direct indication of the thermal history of the ices (Ehrenfreund et al., 1997; Gerakines et al., 1999; Boogert et al., 2000) Solid C_2H_2 and HCN have not yet been detected, but limits are available from ground-based and ISO data (Boudin et al., 1998, Schutte 1998, private communication).

Table 4.1. Summary of observed sources

Target	R.A. (2000)	Dec (2000)	Obs. ID	Flux ^a (Jy) ^a	L/L_{\odot} (10 ⁵)	d (kpc)	Ref. ^b
AFGL 2136	18 ^h 22 ^m 26 ^s .3	-13° 30' 08''	12000925	280	0.7	2	1
AFGL 2591	20 ^h 29 ^m 24 ^s .7	+40° 11' 19''	19301928	910	0.2	1	1
AFGL 4176	13 ^h 43 ^m 02 ^s .1	-62° 08' 52''	11701404	430	1.8	4	2, 3
AFGL 4176	13 ^h 43 ^m 02 ^s .1	-62° 08' 52''	30601344	360	1.8	4	2, 3
NGC 3576	11 ^h 11 ^m 53 ^s .9	-61° 18' 25''	29200143	280	3.5	2.4	4, 3
NGC 7538 IRS 1	23 ^h 13 ^m 45 ^s .4	+61° 28' 09''	28301235	360	1.3	2.8	1
NGC 7538 IRS 9	23 ^h 14 ^m 01 ^s .6	+61° 27' 21''	28301334	80	0.4	2.8	1
W 33 A	18 ^h 14 ^m 39 ^s .4	-17° 52' 01''	46700521	50	1.0	4	1
W 3 IRS 5	02 ^h 25 ^m 40 ^s .9	+62° 05' 52''	42701224	750	1.7	2.2	1
S 140 IRS 1	22 ^h 19 ^m 18 ^s .2	+63° 18' 47''	26301731	520	0.2	0.9	1
G 333.3-0.4	16 ^h 21 ^m 30 ^s .9	-50° 25' 07''	45800340	150	6	3.9	5, 3
AFGL 2059	18 ^h 04 ^m 53 ^s .0	-24° 26' 45''	49302585	160	0.16	1.5	2, 3

^a Average flux from 13.5 to 14 μm derived from ISO-SWS spectra.

^b Sources of luminosities and distances; (1) van der Tak et al. (1999, 2000), (2) Distance from Henning et al. (1990) (3) Luminosity derived from ISO spectra, (4) Distance from Persi et al. (1987), and (5) Distance from Azcarate et al. (1986)

Some infrared lines in the ν_5 C₂H₂ bending mode at 13.7 μm and ν_2 HCN bending mode at 14.0 μm have been previously observed from the ground at high spectral resolution $R = \lambda/\Delta\lambda \approx 10,000$ by Lacy et al. (1989); Evans et al. (1991); Carr et al. (1995) in a few sources. These bands have been selected owing to their large oscillator strengths and because the infrared sources are up to an order of magnitude brighter at 14 μm than at 3 – 4 μm , where the corresponding stretching vibrations occur. The lower-resolution ISO data presented here cannot resolve the individual vibration-rotation lines, but can be used to detect the strong Q -branch without atmospheric interference in a much larger number of objects. Comparison with model profiles allows the physical conditions to be constrained over a wider range of parameters (Helmich, 1996). Unfortunately, the efficiency of the higher-resolution Fabry-Pérot of the ISO-SWS was too low to survey a large number of sources in HCN and C₂H₂ in a reasonable integration time.

In the following, we discuss first the observational data for C₂H₂ and HCN, with special emphasis on the data reduction techniques that have been used to extract the very weak lines (§4.2). We subsequently compare the observations with theoretical profiles constructed using a simple excitation model (§4.3). The resulting excitation temperatures are compared with each other and with those found for other molecules (§4.4). Finally, the inferred abundances are discussed in the context of the physical and chemical evolution of the sources (§4.5). An initial account has been given by Lahuis & van Dishoeck (1997).

4.2 Observations and data reduction

4.2.1 Observations and sources

Table 4.1 summarises the sources and the observational data used in this study. All objects are deeply embedded massive young stars with luminosities ranging from $10^4 - 2 \times 10^5 L_{\odot}$ for which complementary ISO data on ices and other gas-phase molecules are available. In addition, high-resolution gas-phase CO and ^{13}CO data have been obtained for most of the sources by Mitchell et al. (1990), from which information on the total column densities and excitation temperatures of both the hot and the cold gas along the lines of sight can be derived. Orion IRc2/BN is not included in this study, but is discussed separately by Boonman et al. (1999).

All observations were performed with the ISO-SWS mode AOT06 at full grating resolution (de Graauw et al., 1996). The wavelength range scanned was typically $12 - 16 \mu\text{m}$ (AOT-band 3A). The spectral region used in the analysis of the C_2H_2 and HCN bands is only $13.4 - 14.4 \mu\text{m}$, but the larger observed spectral range is necessary for a proper removal of instrumental fringes. The resolving power at these wavelengths is $R \approx 1800$, corresponding to $\sim 165 \text{ km s}^{-1}$. Thus, the lines are not resolved.

4.2.2 Data reduction

Our reduction is performed within the SWS Interactive Analysis system IA³ developed and used within the ISO-SWS consortium. For a detailed description of IA³ see Roelfsema et al. (1993); Wieprecht et al. (1998); Lahuis et al. (1998). The adopted reduction method uses a combination of standard pipeline software (version 7) and additional IA³ software. The pipeline software is identical to the software used in the ISO Standard Product Generation software which generates the data products distributed to the ISO observers and contained in the ISO data archive.

The depth of the C_2H_2 and HCN features is less than 10% of the continuum (for some observations of the order of 1 – 2%) at the resolution of the ISO-SWS grating. The ISO-SWS grating spectra in this spectral region are heavily affected by instrumental fringing which makes the identification and analysis of weak features very difficult. Special data reduction techniques need to be applied in order to extract these weak features.

4.2.2.1 Fringe removal

The main problem is the application of the Relative Spectral Response Function (RSRF), which is dominated by instrumental fringing in this wavelength region. This fringing is the result of the Fabry-Pérot effect within the ISO-SWS instrument at a number of locations in the light-path. Some of the properties of these interferences, in particular their shape and amplitude, change depending on the orientation and location of the source in the ISO-SWS aperture and are therefore different from source to source. The RSRF was derived in the laboratory using a fully extended blackbody source, whereas our astronomical sources are not fully extended and thus have a different fringe pattern. The net result of these effects is that it is difficult to correct for the fringes in the standard pipeline processing.

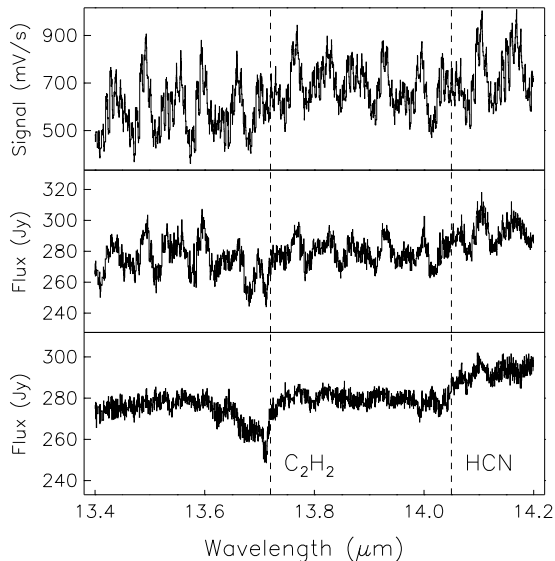


Figure 4.1 Example of the impact of fringes in the 13.4 – 14.4 μm (band 3A) part of the spectrum for AFGL 2136. In the top plot, the raw signal from the twelve detectors covering this spectral range is shown, in which the instrumental fringing is evident. The middle plot shows the result for all twelve detectors as produced with standard processing: large fringe residuals remain making the detection of weak spectral features very difficult. In the bottom plot, the result of improved data reduction is shown. Note the different flux scale. The fringe residuals are low and allow detection of spectral features of only a few percent. The vertical lines indicate the positions of the ν_5 vibration-rotation band of C₂H₂ and the ν_2 vibration-rotation band of HCN.

The amplitude of the remaining fringe-residuals after the application of the RSRF can be reduced significantly, however, by applying (any or a combination of) the following reduction methods within IA³:

- correcting for shifts caused by pointing or wavelength calibration inaccuracies via a cross-correlation of the data and the RSRF
- enhancing the amplitude of the RSRF to match the amplitude of the fringes in the data
- removing the fringe-residuals by fitting sinusoids or by Fourier filtering

For our reduction, we first made a shift and amplitude correction to the RSRF before applying it. Subsequently, we removed the residual fringes by fitting sinusoids. The two dedicated IA³ routines `RESP_INTER` and `FRINGES` have been used for this purpose.

In principle this procedure allows removal of the fringe residuals to a level of less than 1%, resulting in spectra with a signal-to-noise ratio on the continuum of 100 or better. However the presence of spectral features may complicate the application of these tools, especially if they have some regularity such as the *P*- and *R*-branches of molecular spectra. To test the stability of this procedure on the C₂H₂ and HCN molecular data, tests were made using synthetic spectra at a few different temperatures (and thus with more or less prominent *P*- and *R*-branches). The relative effect of the fringe

removal on the synthetic spectra is small, of the order of 1–2% (i.e. $\leq 0.1\%$ in the continuum subtracted spectra assuming a depth of the features of 10% or less), provided a large enough wavelength range is used.

With the current status of the calibration and data analysis, the unresolved Q -branches of C_2H_2 and HCN are clearly detected in most sources. However, it is not possible to analyse the corresponding P - and R -branch lines separately, since they have an absorption depth of approximately 0.5–1% or less. In most cases this is close to the noise level and the amplitude of the fringe-residuals after the fringe removal. Individual lines may match with observed features and are probably real, but they cannot be used as a decisive argument in favour of a particular model. They can, however, help to constrain the fits in some cases, e.g. to exclude a temperature or column density on the basis of the lack of detected P - and R -branch lines.

4.3 Model spectra and fits

Figure 4.2 illustrates the synthetic spectra of the $HCN \nu_2 = 1-0$ band at $R \approx 30,000$ and 1800 for an excitation temperature of 300 K, a typical column density of $1.10^{16} \text{ cm}^{-2}$ and $b = 5 \text{ km s}^{-1}$. The Q -branch in the lower resolution spectrum is clearly unresolved and less deep than in the higher resolution spectrum and the P - and R -branch lines become weak, making their detection difficult. However, the Q -branch consisting of many blended lines results in strong enough absorption to be detected, even at the

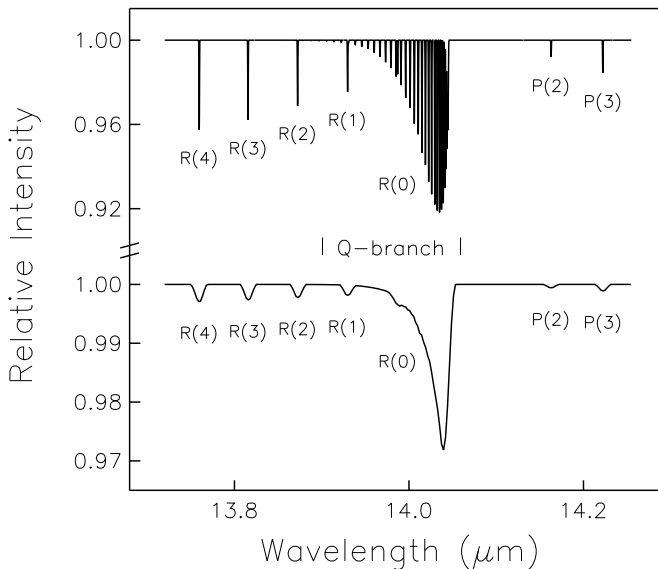


Figure 4.2 The Q -branch and lowest P - and R -branch lines of HCN at a resolving power of 30,000 and 1800 (reflecting the approximate resolutions of the ISO-SWS FP and grating in this spectral region), an excitation temperature of 300 K and a column density of $1.10^{16} \text{ cm}^{-2}$ and $b = 5 \text{ km s}^{-1}$. The P - and R -branch lines are marked in the spectra.

Table 4.2. HCN fundamental and ν_2 low-lying vibrational transitions

transition	ν_i (cm ⁻¹)	d_i	state	ν_i (cm ⁻¹) ^a	d_i
fundamental transitions			ν_2 vibrational states		
ν_1 (10 ⁰⁰) ^b	3311.5	1	(01 ¹ 0)	711.98	2
ν_2 (01 ¹ 0) ^a	711.98	2	(02 ⁰ 0)	1411.41	1
ν_3 (00 ⁰ 1) ^c	2096.8	1	(02 ² 0)	1426.53	2
			(03 ¹ 0)	2113.45	2
			(03 ³ 0)	2143.76	2
ν_2 H ¹³ CN ^a	705.97				
ν_2 HC ¹⁵ N ^a	711.03				

Molecular data from; (a) Duxbury & Gang (1989) (b) Choe et al. (1986), and (c) Choe et al. (1987)

lower resolution. The asymmetric shape of the Q -branch and the relative strength of the Q -branches originating from vibrationally excited levels can be used to constrain the excitation temperature (see §4.3.2). The depth is then used to determine the column density. It is these features which make vibrational bands of molecules with a Q -branch particularly well suited for low-resolution observations. The same holds for the Q -branch of the C₂H₂ ν_5 band presented in this paper. Another excellent example is provided by the ν_2 bending mode of CO₂, which has its Q -branch at 14.98 μm (e.g. van Dishoeck et al., 1996; Boonman et al., 1999).

4.3.1 Synthetic spectra

Model C₂H₂ and HCN spectra have been constructed assuming that the population distribution is in local thermodynamic equilibrium (LTE). For a rotational level J in the ground vibrational state,

$$\frac{N_J}{N} = \frac{g_n(2J+1)e^{-E_J/kT}}{Q(T)} \quad (4.1)$$

with N the total column density, E_J the energy of level J , and g_n the nuclear statistical weight with $g_n = 1$ for even J and $g_n = 3$ for odd J in the case of C₂H₂, and $g_n = 1$ for all J in the case of HCN. The partition function, $Q(T)$, is the product of the rotational partition function, $Q_r(T)$,

$$Q_r = \sum_J g_n(2J+1)e^{-E_J/kT} \quad (4.2)$$

summed over all levels J , and the vibrational partition function, $Q_v(T)$, which can be approximated by the product

$$Q_v \approx \prod_i (1 - e^{-E_{v_i}/kT})^{-d_i} \quad (4.3)$$

over all fundamental vibrational transitions v_i . Table 4.2 lists the frequencies ν_i and degeneracies d_i of all fundamental transitions of HCN and of the lower vibrationally

exited levels of the HCN ν_2 mode. At low temperatures, $T \ll 300$ K, Q_v goes to unity and thus the fraction of molecules in the vibrationally excited levels is negligible.

The fractional population in a vibrationally excited level is:

$$x_{v_i} = \frac{d_i e^{-E_{v_i}/kT}}{Q_v}. \quad (4.4)$$

Line oscillator strengths are derived from the transition probabilities listed in the HITRAN database (edition 1992, Rothman et al., 1992).

$$f_{ul} = 4.701755 \times 10^{-7} \nu R_{ul} \quad (4.5)$$

with the transition probability R_{ul} in Debye².

Using the populations in each level, the optical depths are calculated assuming a Voigt profile function. The final spectrum is reduced to the resolution of the observed ISO-SWS grating spectrum using a Gaussian profile.

Figure 4.3 illustrates the column densities at which the strongest C_2H_2 and HCN lines in the bands become optically thick for Doppler parameters b of 1.5, 5 and 10 km s^{-1} . Typical column densities for our sources range from a few $\times 10^{15}$ to a few $\times 10^{16}$ cm^{-2} (see §4). Thus, optical depth effects become significant only for C_2H_2 in cold sources with $b < 5$ km s^{-1} and $N(C_2H_2) > 10^{15}$ cm^{-2} . Our sample contains only one such object (W 33A, see §4.4), and for this source an accurate knowledge of the b value is needed to derive reliable column densities. In all other cases, the excitation temperatures are high and the results are not sensitive to the adopted value of b .

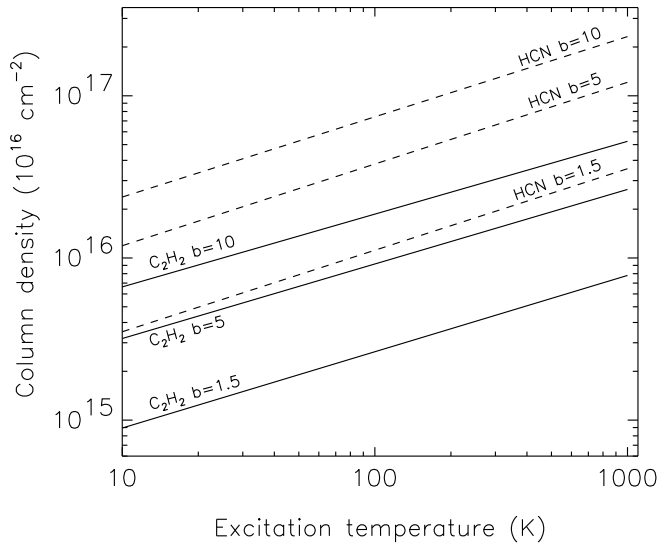
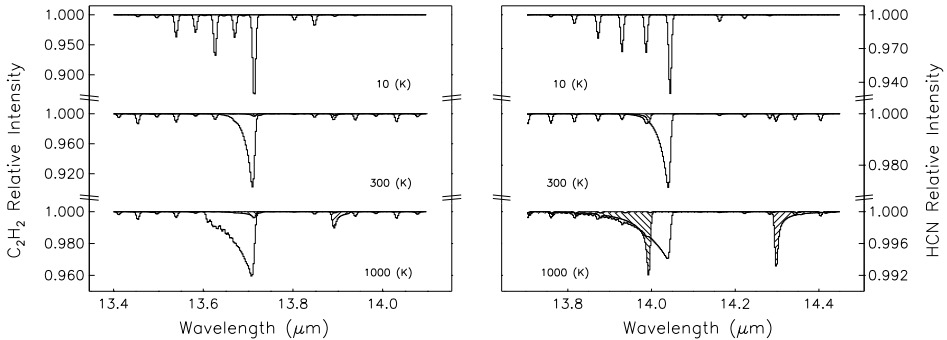


Figure 4.3 Column densities at which the strongest C_2H_2 and HCN absorption lines become optically thick ($\tau = 1$) for Doppler parameters b of 1.5, 5 and 10 km s^{-1} at excitation temperatures from 10 to 1000 K.



(a) C₂H₂ $\nu_5 = 1 - 0$ fundamental and $\nu_5 = 2 - 1$ hot bands. (b) HCN $\nu_2 = 1 - 0$ fundamental and $\nu_2 = 2 - 1$ hot bands.

Figure 4.4 Examples of the fundamental $1 - 0$ band and the $2 - 1$ hot bands of the ν_5 C₂H₂ band (Figure 4.4(a)) and the ν_2 HCN band (Figure 4.4(b)). For both molecules the synthetic spectra are shown for temperatures of 10, 300 and 1000 K at a column density of $1. \cdot 10^{16} \text{ cm}^{-2}$, $R = 1800$ and $b=5 \text{ km s}^{-1}$. The shaded regions indicate the hot band absorptions (see Tables 4.2 and 4.3 for details). Note the difference in scale between Figure 4.4(a) and 4.4(b). In particular, note the $\nu_5 = 2 - 1$ C₂H₂ hot band at $13.89 \mu\text{m}$. Although it is relatively weak compared to the fundamental $\nu_5 = 1 - 0$ C₂H₂ band its strength is of the same order as the ν_2 HCN bands.

A more detailed discussions on ro-vibrational lines and the use of band strengths, line strengths and partition functions can be found in Evans et al. (1991); Helmich (1996). They also list various conversions between units and notations used in the literature.

4.3.2 Hot bands

Some of the observed spectra (see §4.4) show evidence for gas at high temperatures up to 1000 K. At these temperatures the contribution of absorption from vibrationally excited states has to be considered, resulting in so-called “hot bands”. To illustrate the effect of hot bands, Figure 4.4 shows the synthetic spectra of C₂H₂ and HCN at temperatures of 10, 300 and 1000 K. Table 4.3 lists the relative populations in the vibrationally excited levels and the strengths of the hot bands with respect to the fundamental $\nu_i = 1 - 0$ band at temperatures of 100, 300 and 1000 K for both HCN and C₂H₂. The $\nu_i = 2 - 1$ bands are of $\Sigma - \Pi$ and $\Delta - \Pi$ -type and are split in two close-lying transitions at 720 cm^{-1} ($13.89 \mu\text{m}$) and 729 cm^{-1} ($13.72 \mu\text{m}$) for C₂H₂ and 699.4 cm^{-1} ($14.30 \mu\text{m}$) and 714.5 cm^{-1} ($14.00 \mu\text{m}$) for HCN. It is seen that for HCN, the hot bands have nearly 75 % of the intensity of the fundamental band at $T \approx 1000 \text{ K}$ and significantly affect the spectra. For C₂H₂, the effect is smaller, but is still detectable at the $\sim 15 \%$ level at the higher temperatures. Note that although the relative strength of the C₂H₂ hot band at $13.89 \mu\text{m}$ with respect to the fundamental band is small, its relative strength with respect to the HCN bands is larger since the C₂H₂ band is a factor of ~ 5 stronger than the HCN band. It is therefore important to include the C₂H₂ hot bands in the construction of the complete synthetic spectra.

Table 4.3. C₂H₂ and HCN $\nu_i = 1$ population and hot band strength

C ₂ H ₂ $\nu_5 = 1$				HCN $\nu_2 = 1$			
	T_{ex} (K)				T_{ex} (K)		
	100	300	1000		100	300	1000
population ^a	.00006	.051	.09	population ^a	.00007	.062	.28
S^b (720 cm ⁻¹)	.00005	.042	.08	S^b (699.4 cm ⁻¹)	.00008	.035	.28
S^b (729 cm ⁻¹)	.00004	.023	.05	S^b (714.5 cm ⁻¹)	.00011	.071	.55

^aFractional population of $\nu_i = 1$ level

^bRelative intensity with respect to fundamental band

The contribution of higher vibrational levels is small and the strength of the $\nu_i = 3 - 2$ bands is too small to be detected in these data. Thus, in the construction of the synthetic spectra no levels higher than the $\nu_i = 2 - 1$ bands are included. However, in calculating the population of the ground vibrational level, the populations of the higher levels are taken into account, since the population of the third vibrationally excited level can amount to 10 % for HCN.

4.3.3 Model fits

The parameters that enter the model fits are the excitation temperature(s) in K, the total column density in each temperature component in cm⁻², and the Doppler broadening parameter b of each component in km s⁻¹. The latter values can be constrained from high spectral resolution submillimeter lines of these sources, which indicate typical FWHM line widths $\Delta V = 1.665 b$ of 3 – 4 km s⁻¹ for molecules such as C¹⁷O and HCN (van der Tak et al., 1999, 2000). Comparison with high resolution infrared spectra indicates that the latter lines are generally broader than the submillimeter lines. Thus, $b = 1.5$ km s⁻¹ is taken as a lower limit in the model spectra, but values up to $b = 10$ km s⁻¹ have been explored. The resulting Q -branch spectra show no significant variation over this range of b -values. Most of the presented spectra use $b = 5$ km s⁻¹. At this value of b the C₂H₂ and HCN features stay optically thin at the inferred column densities and temperatures (see §4.3).

Fits of the model spectra to the observational data are made within the IDL package using the Powell optimisation routine. Different fits to the surrounding continuum were explored because of the uncertainty in the RSRF global shape. In some cases this improved the fits, but it had no major impact on the derived parameters. For each spectrum, fits were made with both a single temperature and with two temperature components. In the latter case, the two temperatures were taken from the Mitchell et al. (1990) study of CO and the column densities in each of the components were adjusted to give the best match to the spectrum. For the column densities involved, the absorptions of the two components are not saturated and can be added together in optical depth before convolution with the ISO-SWS Gaussian resolution.

Figure 4.5 shows the χ^2 distribution for one of the best sources, AFGL 2136. Illustrated here is a fit in HCN temperature and column density keeping the temperature and column density of C₂H₂ fixed at predefined values. Note that there is a clear

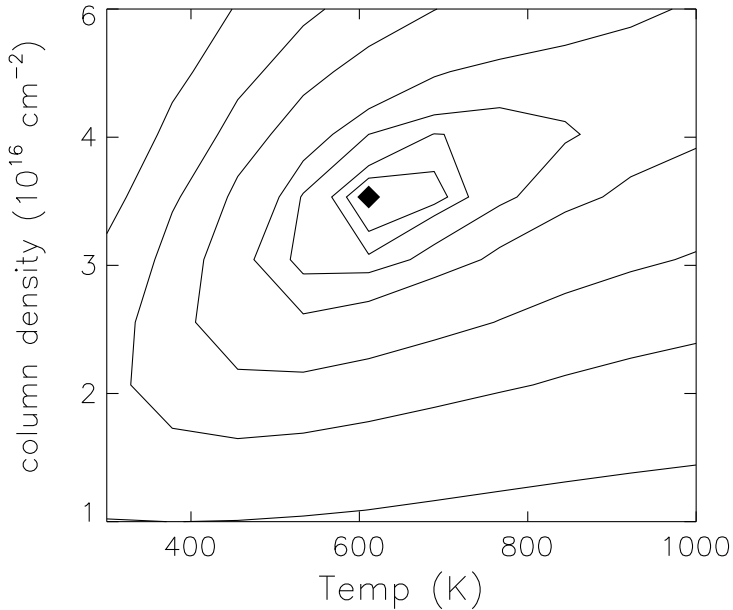


Figure 4.5 Example of χ^2 distribution in the case of AFGL 2136. Plotted are the minimum χ^2 (solid symbol) and the contours at 1.5, 2.5, 5, 10, 25, 50 and 100 % of the minimum χ^2 . At the sampling of the spectrum used for this fit a χ^2 increase of 2.5 % corresponds roughly to a 3σ deviation of the model to the observed spectral feature.

correlation between the inferred temperature and column density. Assuming a higher temperature results in a higher

It should be emphasised that the ISO-SWS Q -branch spectra are of sufficiently high quality to allow the detection of even small amounts of C₂H₂ and HCN with column densities of a few $\times 10^{14}$ cm⁻² in very cold gas with $T = 10 - 20$ K and small b -values of less than 2 km s⁻¹. This is in contrast with asymmetric rotors such as H₂O without a Q -branch, where the ISO-SWS ν_2 data at 6 μ m are primarily sensitive to much higher column densities in the warmer and/or less quiescent gas (Helmich, 1996).

4.4 Results

Table 4.4 summarises the best fit results for all targets, whereas the final spectra are presented in Figure 4.6. The upper half of Table 4.4 lists the best single temperature fit in which the excitation temperature and the column density are free parameters. The lower half gives a two temperature fit, in which the excitation temperatures are fixed at those found for CO by Mitchell et al. (1990) and the column densities are varied. Two component models in which both the temperature and column density are free parameters have been run as well, and provide slight improvements to the fits in some cases. However, the significance of the fit parameters for the second component is low and is therefore not given. The accuracy of the results for the low temperature

Table 4.4. Model fit^a C₂H₂ and HCN excitation temperatures T_{ex} and column densities N

Target	C ₂ H ₂ ^b		HCN ^b	
	T_{ex}	N	T_{ex}	N
	(K)	10 ¹⁶ (cm ⁻²)	(K)	10 ¹⁶ (cm ⁻²)
AFGL 2136	800 ⁺¹⁵⁰ ₋₁₀₀	1.5±0.3	600 ⁺⁷⁵ ₋₅₀	3.5±0.6
AFGL 2591	900 ⁺¹⁵⁰ ₋₁₂₀	2±0.3	600 ⁺⁷⁵ ₋₅₀	4±0.6
AFGL 4176 #1	700 ⁺¹⁷⁰ ₋₁₀₀	1±0.2	500 ⁺⁴⁰ ₋₃₀	2±0.4
AFGL 4176 #2	700 ⁺²⁵⁰ ₋₁₅₀	1±0.2	500 ⁺⁵⁰ ₋₅₀	2±0.4
NGC 3576	500 ⁺¹⁰⁰ ₋₆₀	0.4±0.1	400 ⁺⁵⁰ ₋₄₀	0.8±0.3
NGC 7538 IRS 1	800 ⁺²⁵⁰ ₋₁₅₀	0.8±0.2	600 ⁺⁵⁰ ₋₄₀	1±0.2
NGC 7538 IRS 9	300 ⁺¹⁰⁰ ₋₇₅	0.2±0.1	340 ⁺⁷⁵ ₋₆₅	0.8±0.3
W 33 A	10 ⁺¹⁰ ₋₅	0.5±0.2	80 ⁺¹⁰⁰ ₋₄₀	0.3±0.2
W 3 IRS 5	500 ⁺⁷⁵ ₋₆₅	0.3±0.1	400 ⁺⁵⁰ ₋₄₀	0.5±0.1
S 140 IRS 1	–	–	–	–
G 333.3–0.4	300 ^e	< 0.1	300 ^e	< 0.3
AFGL 2059	10 ^e	0.04±0.04	10 ^e	0.03±0.03

	Fit using CO temperatures ^c					
	T_{cold}^c	$N_{\text{C}_2\text{H}_2}$	N_{HCN}	T_{hot}^c	$N_{\text{C}_2\text{H}_2}$	N_{HCN}
	(K)	10 ¹⁶ (cm ⁻²)	10 ¹⁶ (cm ⁻²)	(K)	10 ¹⁶ (cm ⁻²)	10 ¹⁶ (cm ⁻²)
AFGL 2136	17	0.1	0.1	580	1.4	3.3
AFGL 2591	38	< 0.1	0.2	~ 1000	2.1	4.5
AFGL 4176 #1	–	–	–	≥ 500 ^d	0.9	2.1
AFGL 4176 #2	–	–	–	≥ 500 ^d	0.8	2.0
NGC 3576	–	–	–	≥ 500 ^d	0.4	1.2
NGC 7538 IRS 1	25	< 0.05	< 0.05	176	0.3	0.4
NGC 7538 IRS 9	26	0.05	< 0.01	180	0.1	0.2
W 33 A	23	0.1	0.03	120	0.2	0.3
W 3 IRS 5	66	< 0.01	0.03	577	0.3	0.6
S 140 IRS 1	28	< 0.005	< 0.01	390	< 0.1	< 0.1
G 333.3–0.4	–	–	–	–	–	–
AFGL 2059	–	–	–	–	–	–

^aFor all fits, a Doppler parameter $b=5 \text{ km s}^{-1}$ has been adopted

^bSingle component fits with both temperature and column density as free parameters

^cTwo component fits with temperatures fixed at the cold and hot temperatures found for CO by Mitchell et al. (1990)

^dTemperature fixed at value indicated by the ISO–SWS CO spectrum

^eTemperature fixed at assumed value

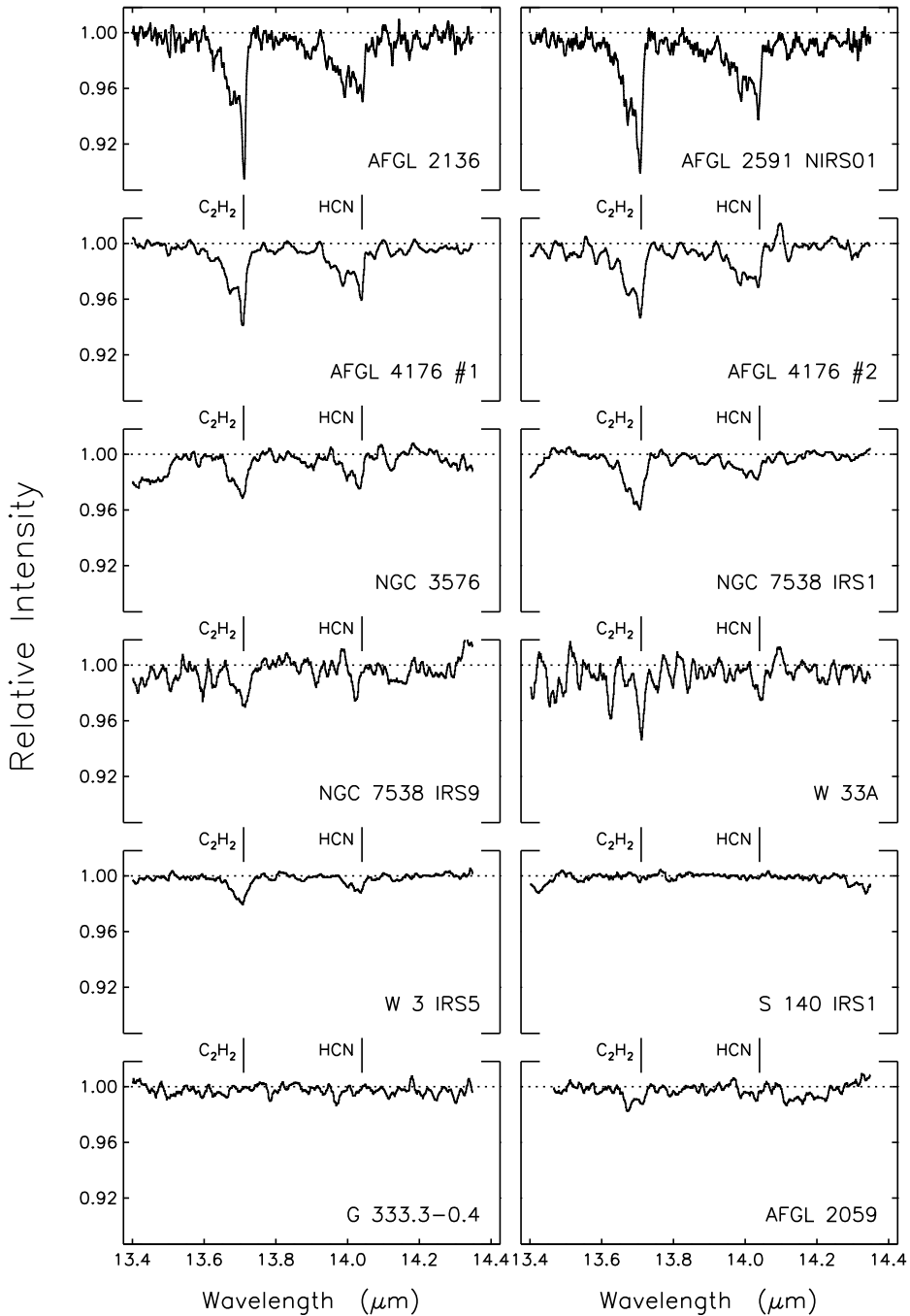


Figure 4.6 The final normalised spectra for all sources listed in Table 4.1. The positions of the ν_5 vibration-rotation band of C₂H₂ and the ν_2 vibration-rotation band of HCN are indicated.

component with T_{ex} fixed is also not high, but the results provide a good indication of the relative contributions from the cold and warm gas. Table 4.4 includes the 3σ error bars on the temperatures and column densities derived from the χ^2 fits for the single component fits and from comparison of different model fits.

For sources without a detection, the upper limits are based on an assumed temperature. Where available, this is taken to be the temperature of the warm CO given by Mitchell et al. (1990). In the case of G333.3-04, $T_{\text{ex}} = 300$ K is assumed. For AFGL 2059, the C_2H_2 spectrum hints at the presence of a cold gas component for which T_{ex} could be as low as a few K. The listed values assume $T_{\text{ex}} = 10$ K for both C_2H_2 and HCN to give an indication of the amount of cold gas, even though the uncertainty will be high.

No positive detection of H^{13}CN at $14.165 \mu\text{m}$ has been made. A nominal ratio $\text{H}^{12}\text{CN}/\text{H}^{13}\text{CN} = 60$ would yield an absorption due to H^{13}CN of only 0.5 – 1 %. This is close to or below the limit at which a positive detection of an isolated spectral feature can be made at this wavelength. The absence of any H^{13}CN absorption at the level of $\sim 2\%$ provides an independent confirmation that the Q -branch features are not highly optically thick.

In the following, the individual sources and spectra will be discussed in more detail, before turning to the more general discussion in §4.5.

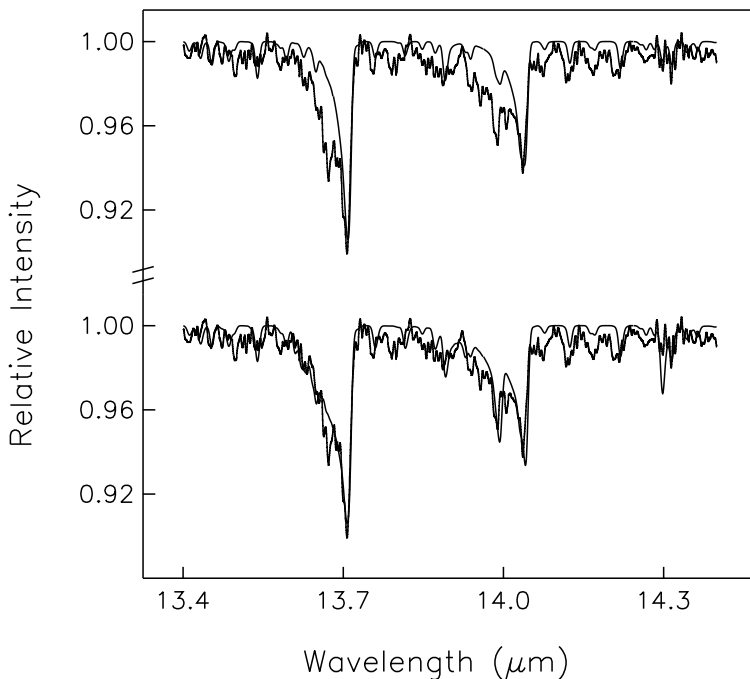


Figure 4.7 The upper plot illustrates a model fit for AFGL 2591 based on inferred temperatures and column densities by Carr et al. (1995). The lower plot illustrates a model fit based on temperatures and column densities inferred from the ISO-SWS spectrum (see Table 4.4).

4.4.1 AFGL 2591

The C₂H₂ and HCN *Q*-branches are clearly detected in the ISO-SWS data toward AFGL 2591. This is consistent with the ground-based results of Carr et al. (1995), who observed a number of low-*J* *Q*- and/or *R*-branch lines of C₂H₂ and HCN toward this object at higher spectral resolution. The inferred excitation temperatures and column densities are different, however. Carr et al. (1995) derived $T_{\text{ex}} = 410$ K and 340 K for C₂H₂ and HCN respectively, with column densities of $1.2 \cdot 10^{16}$ and $2.5 \cdot 10^{16} \text{ cm}^{-2}$. The top plot of Figure 4.7 shows the ISO-SWS spectrum compared to a model spectrum based on these temperatures and densities. It is clear that this model reproduces well the absorption of lines arising from lower *J* levels, but that an additional strong blue wing is seen in the ISO spectra for both molecules. The best-fitting single temperature results from the ISO data give 900 and 600 K, respectively, and the column densities are increased by a factor of two. The high temperatures are confirmed by the presence of hot bands in the spectra.

The ISO spectra of AFGL 2591 (see Figure 4.7 bottom plot), in particular the spectrum of C₂H₂, hint at the presence of a cold gas component ($10 \text{ K} < T_{\text{cold}} < 100 \text{ K}$) in addition to the dominant hot ($\sim 1000 \text{ K}$) component. At low temperatures the lower *R*-branch lines (for C₂H₂ at 13.625 and 13.67 μm) become more dominant (see Figure 4.4(a)). The temperature and column density of this cold gas are highly uncertain, however, because of the fringe residuals present in the spectrum. Nevertheless, the conclusion that the column density of the cold gas component for both C₂H₂ and HCN is only a small fraction ($\leq 10\%$) of that of the hot component is robust. A low temperature component with a significantly higher column density would have been readily detected (see the case of W 33 A).

4.4.2 AFGL 2136

The 13 – 15 μm ISO-SWS spectrum toward AFGL 2136 has been discussed previously by Boonman et al. (1999) in comparison with Orion IRC2/BN. Like AFGL 2591, this spectrum shows the presence of very warm C₂H₂ and HCN along the line of sight at temperatures of 800 and 700 K, respectively, with hot bands readily detected. The shape of the AFGL 2136 spectrum again hints at the presence of a small cold gas component with C₂H₂ and HCN column densities that are at most 10 % of those of the hot gas.

4.4.3 AFGL 4176

Two independent ISO-SWS spectra separated by almost one year have been taken toward the southern massive star-forming region AFGL 4176. The spectra agree well within the uncertainties of the calibration and data-reduction. Hot C₂H₂ and HCN are obviously present in both spectra, and the fit results agree within 10 % in derived temperature and column density. The only difference is the $\sim 50\%$ higher error on the temperature derived from the second observation.

4.4.4 W 33 A

W 33 A is one of the most luminous and massive objects in our sample, and lies in the direction of the Galactic center. Its infrared spectrum is characterised by very strong absorptions from interstellar ices seen from the ground (e.g. Willner et al., 1982; Allamandola et al., 1992) and by the ISO-SWS (e.g. Schutte et al., 1999; Gibb et al., 2000).

The 13–15 μm region of this object is interesting since it is the only case which shows a clear detection of cold C_2H_2 with $T_{\text{ex}} \approx 10$ K and possibly cold HCN at $T_{\text{ex}} \approx 80$ K. The inferred value of $N(\text{C}_2\text{H}_2)$ is sensitive to the adopted b -value (cf. Figure 4.3), and is increased by a factor of 2 if $b=1.5$ km s^{-1} rather than $b=5$ km s^{-1} is adopted. There is no definite detection of a warm component although it cannot be excluded. Upper limits on the warm C_2H_2 and HCN are a factor of 10 less than the column densities of warm gas found toward AFGL 2136 and AFGL 2591.

4.4.5 W 3 IRS 5

W 3 IRS 5 is also among the most luminous objects with a strong mid-infrared continuum. Large column densities of hot and cold CO have been detected along the line of sight by Mitchell et al. (1990), but the amount of hot and cold C_2H_2 and HCN is surprisingly low, nearly a factor of 5 less than found toward AFGL 2136 and AFGL 2591. A detailed JCMT 345 GHz line survey has been performed for this object by Helmich & van Dishoeck (1997), which also reveals low molecular abundances in general, except for sulfur-containing species.

4.4.6 NGC 7538 IRS 1 and IRS 9

The bright infrared sources in the massive star-forming region NGC 7538 provide an opportunity to compare the results for two massive YSOs which originate from the same parent cloud. The line of sight toward NGC 7538 IRS 9 is very rich in ices (e.g. Willner et al., 1982; Whittet et al., 1996), whereas that toward NGC 7538 IRS 1 has a much larger fraction of warm gas (Mitchell et al., 1990). This difference is also reflected in the C_2H_2 and HCN results: the excitation temperatures of both species are about a factor of 2 lower toward IRS 9. Nevertheless, the column densities of warm C_2H_2 and HCN are comparable in the two sources. Cold HCN seems to have very low abundances in both cases.

4.4.7 Other sources

Of the remaining sources, only the southern object NGC 3576 shows a clear detection of hot C_2H_2 and HCN, in agreement with the detection of hot CO along this line of sight in the ISO spectra. The spectrum of AFGL 2059 shows absorption peaks at the wavelengths of C_2H_2 and HCN and bluewards, which may indicate the presence of a cold component. However the quality of the spectra is insufficient to determine reliable temperatures and column densities. Column densities are derived at an assumed temperature to give an indication of the amount of cold gas. The upper limits on the column densities toward S 140 and G333.3-0.4 are about an order of magnitude lower than the column densities found toward AFGL 2136 and AFGL 2591.

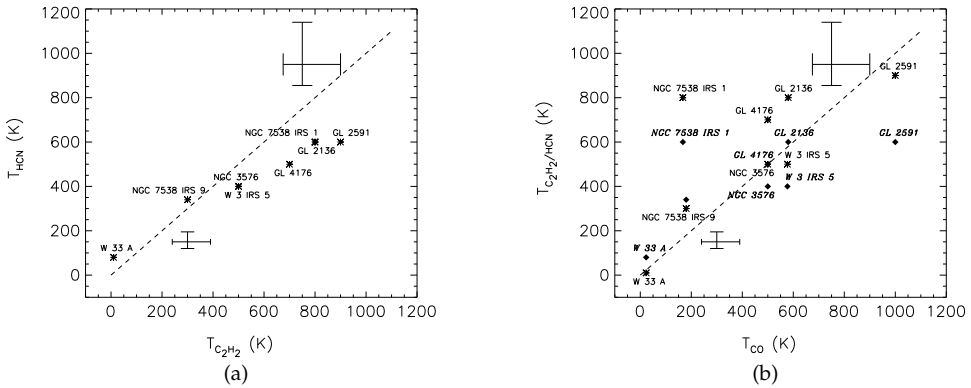


Figure 4.8 (a) Derived C₂H₂ excitation temperature versus derived HCN excitation temperature. (b) Inferred C₂H₂ and HCN excitation temperatures versus observed excitation temperature of the hot CO component (except for W 33A) by Mitchell et al. (1990). The C₂H₂ excitation temperatures are plotted as asterisks and the HCN excitation temperatures as diamonds.

4.5 Discussion

A few general conclusions are apparent from the above results (see Table 4.4). First, gas-phase C₂H₂ and HCN are detected for at least two-thirds of the sources. Second, where detected, the single temperature fits indicate high temperatures of 300 – 1000 K. The only clear exception is formed by W 33 A. Third, the column densities of cold C₂H₂ and HCN in the two temperature fits are generally an order of magnitude lower than the column densities found in the hot component. The main exception is again W 33 A. Fourth, the column densities and abundances increase with increasing excitation temperature, but there is no correlation with luminosity of the object. In the following, the results on the excitation temperatures and column densities are discussed in more detail.

4.5.1 Excitation temperature

In Figures 4.8(a) and 4.8(b), the inferred C₂H₂ and HCN excitation temperatures are compared with each other and with the temperatures determined from the CO infrared observations of Mitchell et al. (1990). Except in the case of W 33 A, the temperature of the hot CO component is used in the comparison, since mostly hot C₂H₂ and HCN is observed. The derived C₂H₂ and HCN excitation temperatures correlate well with each other (a correlation coefficient of 0.98), whereas the correlation with the CO excitation temperatures is lower (correlation coefficients of 0.69 for C₂H₂ and 0.62 for HCN). C₂H₂ and HCN are probably cleaner tracers of the hot gas than CO, because their abundances are enhanced by two orders of magnitude compared with the cold gas (see §4.5.2). In contrast, the CO abundance is not expected to vary by more than a factor of two between the cold and hot components, as long as the temperature is high enough (> 20 K) to prevent freeze-out of the molecule.

The differences in excitation temperature may also reflect different excitation mechanisms of the molecules. The two principal processes are collisional excitation in warm,

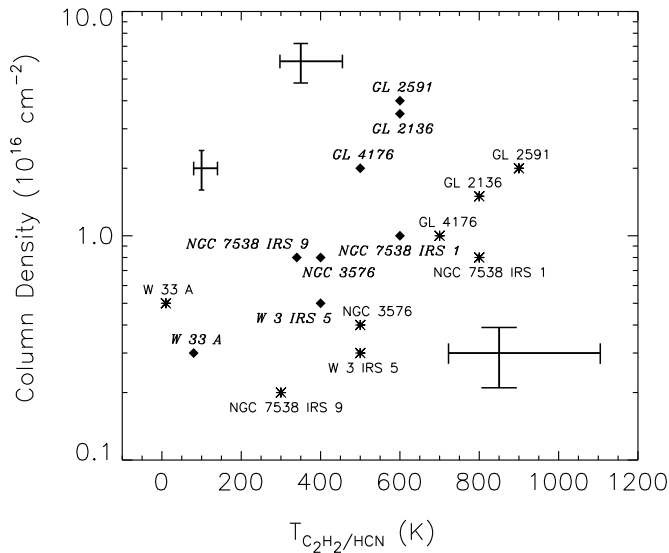


Figure 4.9 Column densities of C_2H_2 and HCN as functions of their excitation temperature. The column densities of C_2H_2 are shown as asterisks and the column densities of HCN as diamonds.

dense gas and radiative excitation by infrared radiation due to warm dust. In contrast with C_2H_2 , HCN has a large dipole moment so that its rotational energy levels can relax rapidly through spontaneous emission. Thus, any non-LTE effects on the excitation are expected to be much larger for HCN. The fact that the HCN and C_2H_2 excitation temperatures are similar indicates that either the density is much above the critical density of the high- J levels or that the radiative excitation rates are much more rapid than relaxation rates, so that the excitation temperatures reflect the colour temperature of the radiation field rather than the kinetic temperature. Both HCN and C_2H_2 can be efficiently pumped through the ν_2 and ν_5 bands at $14\ \mu\text{m}$. In contrast, CO can only be pumped through its vibrational transition at much shorter wavelengths around $4.6\ \mu\text{m}$.

A rough estimate of the relative importance of the collisional and radiative rates can readily be made. Consider as an example a high- J level of HCN, say $J = 10$, which lies at 234 K above ground. In gas with temperatures $> 100\ \text{K}$, collisional excitation occurs at a rate of $\sim 2 \times 10^{-10}\ n\ \text{s}^{-1}$. The spontaneous emission rate to lower levels is $A(J = 10 \rightarrow 9) = 4.6 \times 10^{-2}\ \text{s}^{-1}$. The mid-infrared continuum of the observed sources is due to emission from warm dust and can be fitted by blackbody emission with temperatures ranging from 50 K at long wavelengths to 700 K at the shorter wavelengths. At 300 K, the radiative excitation rate of HCN through the ν_2 vibrational band with $A_{1 \rightarrow 0} = 3.2\ \text{s}^{-1}$ is $\sim 10^{-1}\ \eta\ \text{s}^{-1}$, where η is a geometrical dilution factor. The HCN rotational excitation can therefore either be produced by collisions in warm gas with densities of order $10^9\ \text{cm}^{-3}$ or by radiative excitation in lower density gas. In the power-law density model of AFGL 2591 by van der Tak et al. (1999), the density reaches $10^9\ \text{cm}^{-3}$ only at unrealistically small distances of $< 10\ \text{AU}$, so that radiative pumping likely dominates. For C_2H_2 , the infrared pumping rate is comparable. For CO, however, the radiative

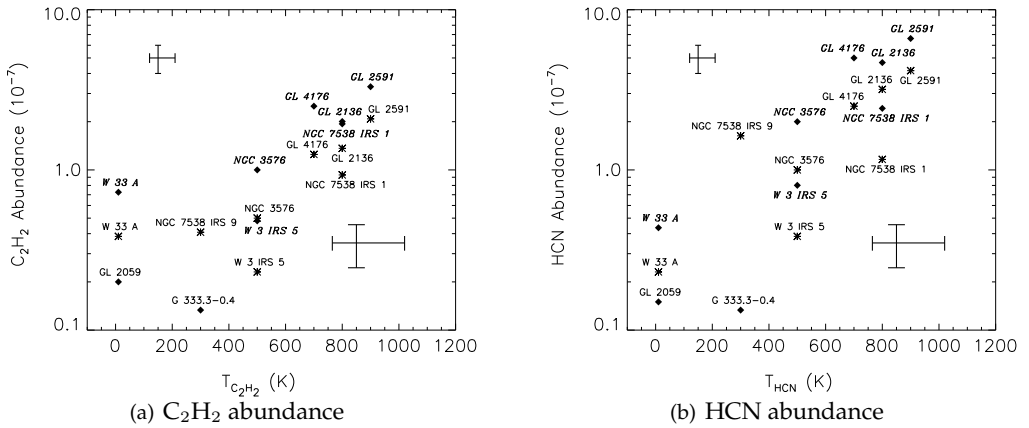


Figure 4.10 The C₂H₂ and HCN abundances as functions of excitation temperature. The abundances are shown with respect to the hot H₂ component (diamonds) and the total H₂ (asterisks).

excitation rate at 4.6 μm is at least two orders of magnitude lower, so that collisional excitation dominates over a larger fraction of the envelope for this molecule, leading to more direct constraints on kinetic temperature and density.

The low HCN and C₂H₂ excitation temperatures for W 33 A compared with other sources of similarly high luminosity are puzzling. The CO data indicate warm gas toward this source, but with temperatures only up to ~ 120 K. The detection of high excitation lines of CH₃OH at submillimeter wavelengths indicates that warm gas with $T_{\text{ex}} \approx 150$ K is present in the inner region (van der Tak et al., 2000). Either the source has only just started to evaporate the ices, or the more massive envelope results in a high optical depth at mid-infrared wavelengths, preventing observations of the inner, warmer gas.

4.5.2 Column densities and abundances

In Figure 4.9, the inferred column densities of C₂H₂ and HCN are shown as functions of the derived excitation temperatures of the molecules. Both species show a clear increase by nearly two orders of magnitude in the warmer gas. The corresponding abundances in the warm gas have been determined using the column densities of warm H₂ derived from the ¹³CO column densities of Mitchell et al. (1990) assuming an abundance ratio $^{13}\text{CO}/\text{H}_2 = 3.3 \times 10^{-6}$. For sources not observed by Mitchell et al. (1990), the total H₂ column density has been constrained from the C¹⁷O 2 – 1 emission line observed with the 15m SEST telescope and/or from the silicate optical depth observed by Willner et al. (1982). Since these sources are among the hottest sources, it is assumed that at least 50% of the gas is in the “warm” component.

Table 4.5 list the total H₂ column densities, the fraction of hot H₂, and the corresponding C₂H₂ and HCN abundances. Figures 4.10(a) and 4.10(b) include the abundances of the molecules as functions of excitation temperature. The C₂H₂ and HCN abundances increase from 10^{-8} to 10^{-6} , with HCN a factor of a few more abundant

Table 4.5. C₂H₂ and HCN abundances with respect to total H₂ and hot H₂.

Target	H ₂ _{tot.} ^a	x _{hot} ^b	C ₂ H ₂ abundance (10 ⁻⁷)		HCN abundance (10 ⁻⁷)	
			total H ₂	hot H ₂	total H ₂	hot H ₂
AFGL 2136	11.	0.68	1.4±0.3	2.0±0.2	3.2±0.6	4.7±0.8
AFGL 2591	9.6	0.63	2.1±0.3	3.3±0.5	4.2±0.6	6.6±1.0
AFGL 4176 #1	8.0	0.5 ^e	1.3±0.3	2.5±0.5	2.5±0.5	5.0±1.0
AFGL 4176 #2	8.0	0.5 ^e	1.3±0.3	2.5±0.5	2.5±0.5	5.0±1.0
NGC 3576	8 ^c	0.5 ^e	0.5±0.1	1.1±0.3	1.0±0.4	2.0±0.8
NGC 7538 IRS 1	8.6	0.48	0.9±0.2	1.9±0.5	1.2±0.2	2.4±0.5
NGC 7538 IRS 9	4.9	0.02	0.4±0.2	20±10	1.6±0.6	80±30
W 33 A	13.	0.53	0.5±0.2	1.0±0.4	0.2±0.1	0.4±0.3
W 3 IRS 5	13.	0.48	0.3±0.1	0.5±0.2	0.5±0.1	0.8±0.2
S 140 IRS 1	3.7	0.60	< 0.5	< 1.0	< 2.0	< 3.0
G333.3-0.4	15 ^c	0.5 ^e	< 0.1	< 0.2	< 0.2	< 0.4
AFGL 2059	4 ^d	0.5 ^e	0.1±0.1	0.2±0.2	0.1±0.1	0.2±0.2

^aTotal H₂ column density in 10²² cm⁻² derived from ¹³CO observations by Mitchell et al. (1990), assuming ¹²CO/¹³CO = 60 and ¹²CO/H₂ = 2 · 10⁻⁴.

^bFraction of hot H₂, $x_{hot} = N_{hot}(H_2)/N_{tot}(H_2)$

^cFrom SEST C¹⁷O 2-1 data

^dBased on 9.7 optical depth (Willner et al., 1982)

^eEstimate

than C₂H₂. At the highest temperatures, these molecules are among the most abundant carbon- and nitrogen-bearing molecules. The largest deviations are provided by NGC 7538 IRS1 and W 3 IRS5, where the HCN and C₂H₂ abundances are remarkably low for the high inferred excitation temperatures. For NGC 7538 IRS1, the HCN and C₂H₂ abundances would be consistent with the relation found for other sources if the lower excitation temperature of 180 K derived from CO is adopted. The data for G 333.3-0.4 are upper limits with an assumed temperature of 300 K.

The column densities and abundances of C₂H₂ and HCN in the cold gas component are only poorly constrained by our low-resolution data, but are at least an order of magnitude lower than those in the hot component. From detailed modeling of the submillimeter line emission, van der Tak et al. (1999, 2000) derive typical HCN abundances of a few × 10⁻⁹ in the extended envelope, similar to the values found here. The inner, warm region around AFGL 2591 has been probed with the OVRO millimeter array in the HCN 1 – 0 emission line. The fact that these interferometer data do not show enhanced HCN abundances indicates that the source size of the abundant HCN seen by ISO is restricted to less than 300 AU (van der Tak et al., 1999).

4.5.3 Chemistry

Steady-state gas-phase chemistry models of cold, dense clouds give typical HCN abundances of a few $\times 10^{-9}$ and C₂H₂ abundances ranging from 10^{-9} – 10^{-8} , depending on the importance of destruction by neutral-neutral reactions with atomic C (Lee et al., 1996; Millar et al., 1997). These model results are consistent with our observed abundances in the cold gas.

Increasing the temperature in these pure gas-phase models to ~ 200 K does not significantly affect the abundances of the molecules in steady-state. Higher abundances are found in time-dependent models at early times, if the gas is initially atomic carbon rich. However, neither C₂H₂ nor HCN reach abundances as high as a few $\times 10^{-7}$ in these models. Also, the limits on the observed atomic carbon column density for these sources rule out these models (van der Tak, private communication).

More relevant for the chemistry in the warm gas are the so-called ‘hot core’ models, in which ice mantles are sublimated from the grains into the gas (e.g. Millar et al., 1991; Charnley et al., 1992; Helmich, 1996; Charnley, 1997). The evaporated molecules subsequently drive a rapid gas-phase chemistry in the dense, warm gas resulting in complex organic molecules for a period of $\sim 10^5$ yr. None of these hot core models shows efficient C₂H₂ production in the warm gas, however. Thus, in order to explain the observed high C₂H₂ abundances of 10^{-7} , the molecule must originally be present in the ices on the grains. Solid C₂H₂ has not yet been detected, but the observed limits are not very stringent, since C₂H₂ mixed in H₂O ice does not have strong spectral signatures (Boudin et al., 1998, Schutte 1998, private communication). The inferred ratio for the ices, C₂H₂/H₂O < 0.1, corresponds to $x(\text{C}_2\text{H}_2) < 10^{-5}$. Our observed C₂H₂ abundances of $\sim 10^{-7}$ are 1–2 orders of magnitude lower. They can be explained if the molecule is present at an abundance of 0.1 – 0.5 % relative to H₂O in the ices and if the time scale since evaporation is less than 10^5 yr. C₂H₂ has been observed in cometary ices with an abundance of 0.1 – 0.9 % with respect to H₂O (Brooke et al., 1996; Bockelée-Morvan et al., 2000), providing support for this picture.

Solid HCN has also not been detected in interstellar ices, at abundances down to ~ 3 % of H₂O ice (Schutte 1998, priv. comm., using data from Bernstein et al., 1995). The corresponding abundance with respect to H₂ of a few *times* 10^{-6} is somewhat higher than the highest observed gas-phase HCN abundances in this work. If the molecule were present at the level of ~ 0.5 % in the ices, evaporation could explain our observed abundances. The observed HCN abundance in comets is slightly lower, 0.05 – 0.25 % (Irvine & Bergin, 2000; Bockelée-Morvan et al., 2000). In contrast with C₂H₂, HCN does participate actively in the high-temperature gas-phase chemistry. Indeed, van der Tak et al. (1999) argue from their HCN interferometer results that the high gas-phase HCN abundances observed by ISO cannot just be the result of grain mantle evaporation but that gas-phase chemistry must play a role as well. At high temperatures > 300 K, a large fraction of the oxygen is thought to be driven into gas-phase H₂O through the O + H₂ and OH + H₂ reactions. This results in a low gas-phase O₂ abundance, one of the principal destroyers of atomic C. The gas-phase HCN abundance is significantly increased with enhanced atomic C and N abundances. An alternative mechanism to enhance HCN would be through evaporation of NH₃ from the ices, followed by subsequent gas-phase reactions leading to HCN, similar to the case of the Orion hot core (Charnley et al., 1992). More detailed modeling of the HCN chemistry in hot cores up to temperature of 1000 K is needed to further interpret the results.

The sources with the highest HCN and C₂H₂ abundances are also those with the highest gas-phase H₂O abundances (e.g. van Dishoeck, 1998) and those which show the largest fraction of heated ice (Boogert et al., 2000; Gerakines et al., 1999). Since these diverse phenomena involve a range of temperatures from < 100 K to 1000 K, this indicates that the enhanced temperatures are communicated to both the inner and the outer parts of the envelope. van der Tak et al. (2000) suggest that this ‘global heating’ results from the gradual dispersion of the envelope with time, resulting in a lower ratio of envelope mass to stellar mass and higher temperatures throughout the envelope.

4.6 Conclusions

The main conclusions of our work can be summarised as follows:

- Gas-phase C₂H₂ and HCN have been detected toward two-thirds of the high-mass YSOs studied in this work.
- Where detected, the excitation temperatures of C₂H₂ and HCN are high, up to 1000 K. The only exception is formed by W 33A. The temperatures derived from the C₂H₂ and HCN data correlate well with each other (with a correlation coefficient of 0.98). The correspondence with the CO excitation temperature is slightly worse, indicating that these two molecules may be better probes of the hot core gas in massive YSOs.
- Except for W 33A, the C₂H₂ and HCN column densities in the cold (< 80 K) gas are at least an order of magnitude lower than those in the hot gas.
- The C₂H₂ and HCN abundances in the hot gas show a clear increase with excitation temperature from 10⁻⁸ to 10⁻⁶. For C₂H₂, such high abundances are plausibly explained by a passive hot core model, in which C₂H₂ is directly evaporated from the ices. The required C₂H₂ ice abundance of 0.1 – 0.5% with respect to H₂O ice is consistent with that found for cometary ices. For HCN, a combination of ice evaporation and high temperature gas-phase reactions likely plays a role.

The gas-phase HCN and C₂H₂ data presented here strengthen the picture based on other ISO observations that the heating of the surrounding envelope by the YSO and evaporation of ices play a dominant role in the physical and chemical evolution of these massive YSOs.

Acknowledgements

The data presented here were analysed with the support of the Dutch ISO Data Analysis Centre (DIDAC) at the Space Research Organisation Netherlands (SRON) in Groningen, the Netherlands. The authors are grateful to Frank Helmich, Annemieke Boonman and John Black for their help with the construction of the model spectra, to Willem Schutte for limits on the ices, to Floris van der Tak, Adwin Boogert, Pascale Ehrenfreund, Thijs de Graauw, Jacquie Keane, Do Kester, Xander Tielens, Doug Whittet and the members of the ex-SIDT in VILSPA for many useful discussions, and to Michiel Hogerheijde for obtaining the SEST spectra. This work was partly supported by NWO grant 614.41.003.

Chapter 5

c2d *Spitzer* IRS Spectra of Disks around T Tauri Stars III. [Ne II] and H₂ gas-phase lines

Abstract

We present a survey of mid-infrared gas-phase lines, in particular the pure rotational H₂ and atomic fine structure lines, toward a sample of 76 circumstellar disks around low mass pre-main sequence stars from the *Spitzer* "From Molecular Cores to Planet Forming Disks" (c2d) legacy program. We report the first detections of [Ne II] toward T Tauri stars in $\gtrsim 20\%$ of our sources. The observed [Ne II] line fluxes and upper limits are consistent with [Ne II] excitation in an X-ray irradiated disk around stars with X-ray luminosities $L_X = 10^{29} - 10^{31} \text{ erg s}^{-1}$. No compact H₂ 0-0 S(0) and S(1) disk emission is detected giving upper limits on the warm ($T \sim 100 - 200 \text{ K}$) gas mass of typically a few Jovian masses. Emission of hot ($T \gtrsim 500 \text{ K}$) gas is observed through the H₂ 0-0 S(2) and/or S(3) lines toward $\sim 7\%$ of our sources. Of these all but one show [Ne II] emission suggesting a possible common heating and excitation mechanism through X-rays or EUV. Analysis of the spatial profiles together with mini-maps for selected sources shows that this emission is compact and associated with the disk. The upper limits on the H₂ lines are consistent with the amount of warm ($> 100 \text{ K}$) gas and H₂ excitation in recent T Tauri disk models that include gas heating by stellar radiation. The detected S(2) and S(3) line fluxes are, however, higher by more than an order of magnitude than those found in recent disk models, even when X-ray and excess UV radiation is included. Similarly the [Ne II]/H₂ 0-0 S(2) ratios for these sources are lower than predicted, consistent with the presence of an additional hot molecular gas component not included in current disk models. No [S I] or [Fe II] is detected down to $\sim 10^{-6} L_\odot$ while [Fe I] has been detected toward $\sim 8\%$ of the sources at $\sim 10^{-5} - 10^{-4} L_\odot$ indicating the presence of gas-rich disks with masses of at least $0.1 M_J$. Oblique shocks due to stellar winds interacting with the disk can explain many aspects of the hot gas emission, but they are inconsistent with the non-detection of [S I] and [Fe II] lines.

Lahuis, F., van Dishoeck, E. F., Blake, G. A., Evans N. J. II, Kessler-Silacci, J. E., & Pontoppidan, K. M., 2007, submitted to ApJ

5.1 Introduction

Circumstellar disks are a natural and important phenomenon in low-mass star formation. The ability to trace the evolution of the disk dust and gas content is crucial to understanding their chemistry and physics and the formation of planets. Observed disks reveal a large source to source variation and suggest a complex evolution from young gas-rich disks to tenuous debris disks. Disk geometries are observed to range from almost flat to strongly flaring disks (Dullemond & Dominik, 2004), and disks with large inner cavities are found (Calvet et al., 2002; Bouwman et al., 2003; Forrest et al., 2004; Brown & et al., 2007). Observations of silicates and spectral energy distributions (SEDs) present evidence for grain growth and settling of large grains to the disk midplane (van Boekel et al., 2003; D'Alessio et al., 2006; Kessler-Silacci et al., 2006). Different degrees of grain heating and radial mixing in the disks (van Boekel et al., 2005), and varying PAH abundances affect the heating of the upper layers of the disk (Habart et al., 2006; Geers et al., 2006). Most of these disk properties are derived from infrared solid-state features and from near-infrared to millimeter continuum observations and associated SED modeling. However, such data give little information about the gas in the disk.

Gas plays an important role in the structure and evolution of disks, including the temperature and density gradients, chemistry, dust dynamics, and eventually the formation of gas-rich and gas-poor planets (Gorti & Hollenbach, 2004). Observational diagnostics of the physical conditions of the gas, in particular its mass and temperature, are therefore highly relevant to studies of disk evolution and planet formation. Central questions are how the gas in the disk is dissipated, what drives the disk heating and gas clearing, and what the associated timescales are. The small number of observed transitional objects between the classical T Tauri phase (large $H\alpha$ equivalent width, thought to be accreting) and the weak-line T Tauri phase (small $H\alpha$, non accreting), both with massive optically thick disks, and the more evolved phase with optically thin or no disks, suggests that disk clearing timescales are short (few $\times 10^5$ yr) compared to the disk lifetime of a few Myr (Cieza & et al., 2007; Haisch et al., 2001). In addition, combined near-infrared (IR), mid-IR, and millimeter observations imply that the disk clearing happens nearly simultaneously across the disk (see e.g. Kenyon & Hartmann, 1995; Hartmann et al., 2005; Takeuchi et al., 2005). Alexander et al. (2006) present a new evolutionary model combining viscous evolution with photoevaporation of the disk to address these issues. In this mechanism, the disk is cleared through an evaporative flow originating from the disk surface layers as a result of UV and/or X-ray heating (see e.g. Hollenbach et al., 2000; Clarke et al., 2001; Kamp & Dullemond, 2004; Dullemond et al., 2007). Information about the temperature and mass of the warm gas and constraints on the disk heating processes are vital for advancing the current models.

Models of gas heating include UV and X-ray radiation from the star itself as well as possible excess radiation due to accretion (e.g. Jonkheid et al., 2004; Gorti & Hollenbach, 2004; Kamp & Dullemond, 2004; Nomura & Millar, 2005; Jonkheid et al., 2007). The resulting gas temperatures in the surface layers out to large radii are significantly higher than those of the dust as a result of the photoelectric effect on small grains and PAHs. Gas temperatures may reach values of up to a few thousand K. Once grains have grown to μm sizes or larger, however, the gas temperature is significantly decreased unless PAHs are still present (Jonkheid et al. 2004, 2006, 2007). Nomura & Millar (2005) include explicitly the excitation of H_2 by UV and collisions for a disk around a T Tauri star with and without excess UV and make predictions for line intensities which can

be tested against observations. Glassgold et al. (2007) have studied the case of X-ray heating and have shown that the ionized neon fine-structure line emission may provide unique tracers of X-ray heating in the disk surface since neon cannot be photoionized by radiation with energies below 13.6 eV.

Observational studies of the gas and its temperature have mostly been limited to the hot inner disks, the low-density upper atmospheres, and the cold outer regions of disks. None of these trace the bulk of the disk gas. High-resolution CO $v=1-0$ vibration-rotation lines at $4.7 \mu\text{m}$ (Najita et al., 2003; Brittain et al., 2003; Blake & Boogert, 2004) show gas with temperatures $\sim 1000 - 3000$ K in the surface layers out to ~ 1 AU. H_2O emission from SVS 13 (Carr et al., 2004) and molecular absorption of C_2H_2 , HCN, and CO_2 in the disk of IRS 46 (Lahuis et al., 2006b) also indicate hot temperatures in the inner few AU of several hundred K. Bary et al. (2003) detected H_2 $2.1 \mu\text{m}$ $1-0$ S(1) emission most likely resulting from hot fluorescently excited gas from the low-density upper atmospheres out to radii of a few $\times 10$ AU. In contrast, millimeter CO surveys probe the cold gas throughout the outer disk where the dust is optically thin (e.g. Koerner & Sargent, 1995; Duvert et al., 2000; Thi et al., 2001; Dutrey et al., 2003; Dent et al., 2005). Its use as a gas mass tracer is however limited as a result of both strong photodissociation at low extinction and freeze-out in the disk interior. Gas temperature determinations range from < 20 K near the midplane (Dartois et al., 2003; Piétu et al., 2007) to 40 K or higher in the intermediate and surface layers (van Zadelhoff et al., 2001; Qi et al., 2006).

The mid-IR H_2 and atomic fine structure lines are best suited as direct tracers of the warm (~ 100 K) gas in the intermediate zones of disks at radii of a few AU out to several tens of AU, i.e., the planet-forming zones of disks. The Infrared Space Observatory (ISO) provided the first opportunity to probe this warm gas in disks around Herbig Ae and T Tauri stars. Thi et al. (2001) suggested that large amounts ($\sim 0.01 - 100 M_J$) of gas could reside in disks around young T Tauri stars, but this has not been confirmed by subsequent ground-based observations (Richter et al., 2002; Sheret et al., 2003; Sako et al., 2005).

The sensitive InfraRed Spectrograph (IRS) (Houck et al., 2004) on board the *Spitzer* Space Telescope (Werner et al., 2004) brings the detection of these lines within reach for young solar mass stars in nearby star forming regions. The combination of high sensitivity, moderate spectral resolution $R = \lambda/\Delta\lambda = 600$, and modest spatial resolution makes *Spitzer* well suited for the direct study of the gas in and around low-mass young stars in nearby ($\lesssim 300$ pc) clouds through the mid-IR lines of various species.

We present here an overview of gas-phase lines detected in disks observed in the *Spitzer* legacy program “From Molecular Cores to Planet Forming Disks” (“Cores to Disks” or c2d) (Evans et al., 2003), which has collected a large sample of IRS spectra toward sources in the nearby Chamaeleon, Lupus, Perseus, Ophiuchus, and Serpens star-forming regions. High-S/N $5-38 \mu\text{m}$ spectra have been obtained for 226 sources at all phases of star and planet formation up to ages of ~ 5 Myr. From this sample, 76 disk sources, identified by showing either the 10 or $20 \mu\text{m}$ silicate bands in emission, have been selected. In §5.2 and §5.3 the source selection and data reduction are explained. In §5.4 the observed atomic fine-structure and H_2 emission lines and the derived parameters are presented. In §5.5 the results are reviewed in the context of currently available disk models. This paper forms a complement to the searches for the mid-infrared lines of H_2 and other species toward more evolved disks studied in other *Spitzer* (legacy) programs (Hollenbach et al., 2005; Pascucci et al., 2006).

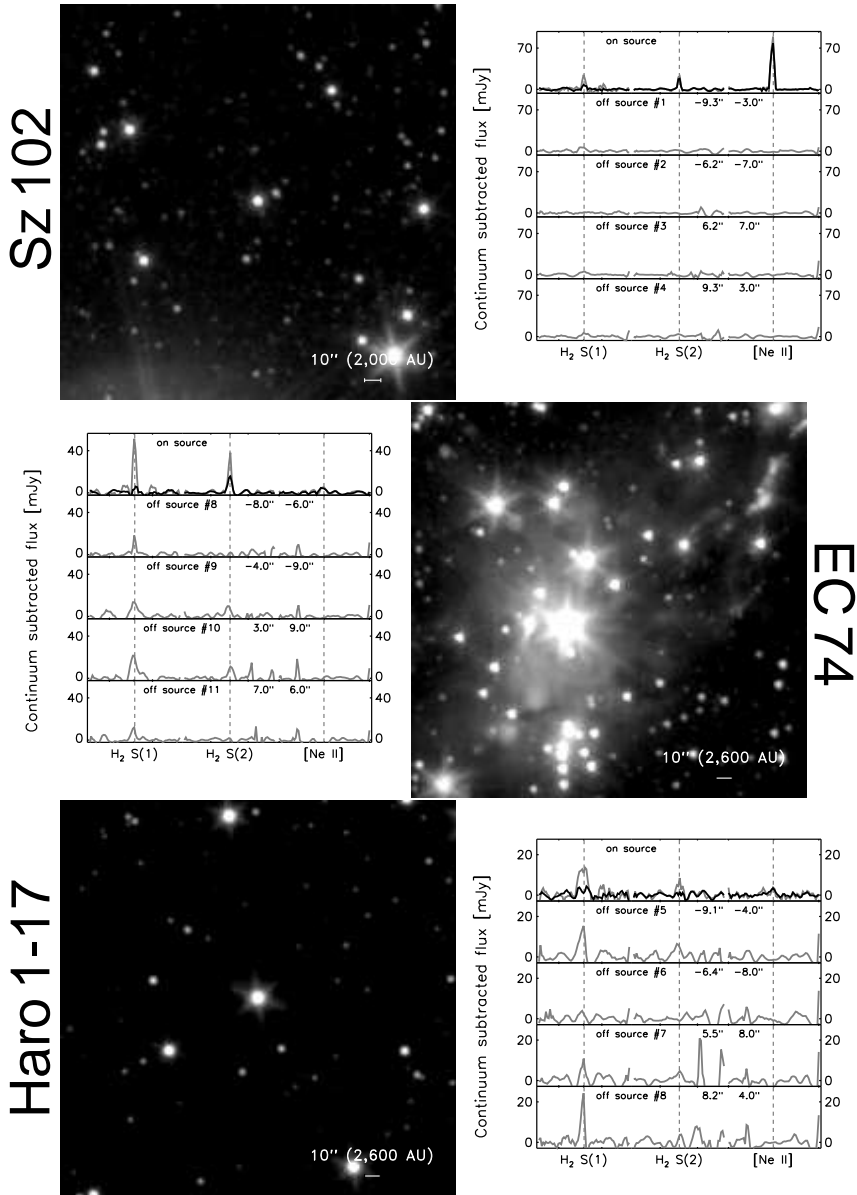


Figure 5.1 Observations of H_2 0-0S(1), S(2), and [Ne,II] emission observed on and off source toward Sz 102, EC 74, and Haro 1-17. The on source observations were observed in the c2d first-look program, the follow up off source observations in the second look program (see §5.2). The images show *Spitzer* IRAC images at $4.5 \mu\text{m}$ (including the high excitation H_2 S(9), S(10) and S(11) lines) with the sources in the middle. The gray lines in the spectra show the total (compact source plus extended component) observed emission. The black lines the source emission after correction for the extended component. Note that for the off source observations no compact source could be identified by the optimal extraction routine and consequently no compact source emission is plotted. Although the S/N in the off source positions is often poor, it illustrates the problem of extended and non-uniform H_2 emission. The [Ne II] is almost always limited to the source itself.

5.2 Observations

The data presented in this study were selected from the sample of IRS spectra observed within the *Spitzer* c2d legacy program. The c2d IRS program consists of two programs of comparable size, referred to as the first- and second-look programs. The first-look program (PID#172) was restricted primarily to known low-mass young stars, embedded YSOs and pre-main-sequence stars with disks with masses $M < 2 M_{\odot}$ and ages $\lesssim 5$ Myr, and a sample of background stars. A few Herbig Ae stars are included as well. The c2d source selection criteria were defined to be complementary to those of the *Spitzer* legacy program “The Formation and Evolution of Planetary Systems” (FEPS, Meyer et al., 2002). The second-look program (PID#179) was, for the most part, devoted to IRS follow-up spectroscopy of sources discovered in the IRAC and MIPS mapping surveys, including a newly discovered cluster of young stars in Serpens (Harvey et al., 2006). For all first-look observations, the integration times for the short-high (SH) and long-high (LH) modules ($R = 600, 10\text{--}37 \mu\text{m}$) were chosen such that theoretical signal to noise ratios (S/Ns) of at least 100 and 50 on the continuum were obtained for sources brighter and fainter than 500 mJy, respectively. Deeper integrations were not feasible within the c2d program. Spectra taken using the short-low (SL) or long-low (LL) modules ($R = 60 - 120, 5\text{--}14 \mu\text{m}$ and $14\text{--}38 \mu\text{m}$ respectively) always reach theoretical S/N ratios greater than 100. For the second-look IRS targets similar S/N limits were obtained wherever possible. However, since the second-look contained a number of very weak sources (down to a few mJy) this was not always achieved.

5.2.1 Source selection

The sources presented in this paper were all selected to show either of the $10 \mu\text{m}$ or $20 \mu\text{m}$ silicate bands in emission. A total of 76 sources were chosen; see Kessler-Silacci et al. (2006) for the 47 first-look disk sources with silicate emission. This selection excludes most edge-on disk sources ($i \gtrsim 65$ degrees) such as CRBR 2422.8-3423 (Pontoppidan et al., 2005), IRS 46 (Lahuis et al., 2006b) and the ‘Flying Saucer’ (Pontoppidan et al., 2007), with the exception of the high inclination sources EC82 (Pontoppidan & Dullemond, 2005) and VV Ser which are included in this paper. Gas-phase lines toward edge-on disk sources will be discussed in a separate paper together with the embedded class 0 and I sources (Lahuis et al., in prep.). The selected sources are listed in Table 5.1 which gives the basic observing and source parameters, e.g. the adopted distances.

5.2.2 SH mini maps

In an early phase of the c2d project molecular hydrogen and [Ne II] lines were detected toward some of the c2d sources. As part of the second-look program, follow-up mini-maps were taken using the SH module to check for extended emission at offsets positions of $\sim 10\text{--}15''$ with respect to the sources. Five maps were defined to include off source observations around eight sources. Three of these are disk sources included in our sample, Sz 102 (Krautter’s star), Haro 1-17, and EC74. Figure 5.1 shows the observed H_2 0-0 S(1), S(2), and [Ne II] emission from the first-look on source observations together with the off source observations from the second-look mini maps. The maps show that most of the H_2 emission is extended, especially for the S(1) line. However, fine-structure lines are usually seen to be limited to the source itself. Subsequent results

using the c2d optimal extraction procedure (see §5.3.1) confirm the conclusions drawn from the analysis of the mini-maps.

The SH maps are not complete since the time allocated for c2d spectroscopy did not allow to observe fully sampled maps. The prime purpose of the maps is to confirm the presence or absence of extended emission. More extended mapping observations will be required to study the detailed spatial distribution and extent of the large scale emission component.

5.3 Data reduction

The c2d reduction pipeline (see Chapter 3 and Lahuis et al., 2006a) was used to reduce the IRS data, starting from the S13 and S14 archive data. The same c2d pipeline products as included in the final c2d Legacy data delivery were used for the spectral line analysis (see §5.3.3). Most of the analysis focused on the SH and LH data, since the SL and LL data are generally limited by the low line/continuum ratio. The SL data were included and used to search for higher-excitation H₂ 0-0 lines, in particular the S(3) transition.

5.3.1 Separating disk and cloud emission – optimal extraction

A major concern when studying emission lines from young stellar objects (YSOs) is the possible contribution of extended (envelope or local cloud) emission in the sometimes complex star forming regions. The spatial distribution of the emission, both in the continuum and in spectral lines, often prohibits the use of ‘sky’ observations alone to correct for extended emission components. For this reason the c2d team has developed an optimal extraction algorithm for IRS pointed observations (see §3.2.2.2).

The *Spitzer* diffraction limited beam is $\sim 4 - 5$ arcsec for the SH module (10-19.5 μm) and $\sim 7 - 10$ arcsec for the LH module (19-37 μm). At a distance of 100 parsec this corresponds to physical sizes of ~ 400 -500 AU and ~ 700 -1000 AU, respectively. The clouds observed in the c2d program are located at distances ranging from 125 parsec (Ophiuchus) to 260 parsec (Serpens) increasing the physical area observed. The full IRS aperture in the SH and LH spatial direction is $\sim 2.5 - 3$ times larger than the beam size. At the observed cloud distances this means that the aperture probes physical scales of several thousand AU. This makes it ideally suited for detecting cold or shocked H₂ emission from the extended (remnant) envelope, outflows, or the diffuse local cloud emission. For the disk sources studied in this work however the local cloud emission will potentially confuse the compact disk emission. Distinguishing between compact (disk) and extended (remnant envelope, outflow, or diffuse cloud) emission is therefore of vital importance for studying the emission lines originating in the circumstellar disks. The optimal PSF extraction developed by the *Spitzer* c2d legacy team (see Chapter 2 in particular §3.2.2.2 Lahuis et al., 2006a) allows separation of the two components for all sources. The mini-maps (see §5.2.2) observed around selected sources confirm the results of the optimal extraction. See Figure 5.1 for an example of extended H₂ emission but compact [Ne II] emission. Other examples include Figures 3 and 4 in Geers et al. (2006) for separating extended cloud and compact disk PAH emission.

The c2d legacy data are accessible at <http://ssc.spitzer.caltech.edu/legacy/c2dhistory.html>.

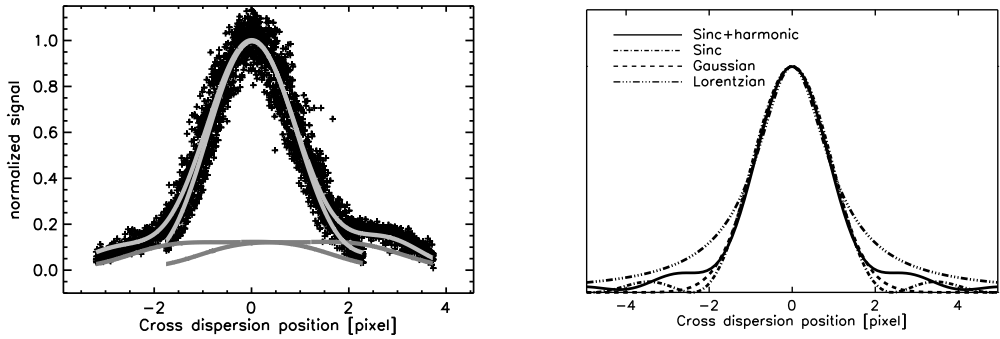


Figure 5.2 Illustration of the *Spitzer* IRS cross dispersion profile used in the optimal extraction (see §5.3.1). The left plot shows a fit to the IRS SH order 11 data of GW Lup, a source with a moderate but clear sky component in the IRS spectra. The rsc data (bcd data before flatfielding) of both dither position (black pluses) is shown, normalized, collapsed along the dispersion direction, and corrected for the cross dispersion dither offsets. Overplotted is the combined fit of the source profile plus the extended emission in gray and the extended emission in dark gray. The shape of the extended emission reflects the IRS flatfield of the (for this source) assumed uniform extended emission. The right plot shows a comparison of an IRS PSF profile (Sinc plus harmonics) compared to the profiles of an undistorted Sinc, a Gaussian, and a Lorentzian profile with the same FWHM. Note the significant variation in the strength and shape of the profile wings. The correct characterization of both the width and the wings of the profile for all IRS orders is essential for extracting the proper source and sky spectra.

The optimal extraction uses an analytical cross-dispersion point spread function (PSF) for the source profile plus an extended emission component to fit to the observed cross dispersion echelle data, see Figure 5.2 for an example. The characterization of the PSF is done using a suite of high S/N calibrator stars. A flux calibration tuned to the optimal extraction is derived from the same calibrator stars using Cohen templates and MARCS models provided by the *Spitzer* Science Center (Decin et al., 2004). The optimal extraction returns a total flux value (the source flux plus extended emission in the IRS beam) and the estimate of the extended emission component. Error estimates are derived for both the total emission and the extended emission component. The S/N of the extended emission component can vary significantly. It depends on the quality of the raw aperture data and on deviations of the extended emission from the assumed uniformity across the IRS slit. Therefore, care has to be taken when subtracting the extended emission from the total flux signal to retrieve the compact source emission. In some cases, a fit to the extended continuum and line emission is used to avoid adding in surplus noise from the often more noisy extended emission component. The uncertainty on the fit to the extended emission is then propagated into the error of the compact source signal.

5.3.2 1-D spectra

After extraction, the 1-D spectra are corrected for instrumental fringe residuals (Lahuis & Boogert, 2003), order matching is applied, and an estimate of the pointing error is obtained for the compact source component. Pointing offsets up to a few arcsec can have a significant impact on the derived fluxes of lines observed with the SH and SL mod-

ules, e.g. H₂ 0-0S(1), S(2), [Ne II], and [Ne III]. For example, dispersion offsets within the nominal 3σ pointing uncertainty of *Spitzer* ($\sim 1''$ for medium accuracy peakup) can lead to SL and SH flux losses up to $\sim 10\%$ depending on wavelength. For all targets, a combination of either the SH, LH, and SL, SH and LH, or SH and SL modules is available. This in principle allows a correction of the pointing related flux losses with an accuracy given by the S/N of the data in the module overlap areas. A detailed description of the c2d pipeline (including extraction, defringing, pointing correction) and the c2d legacy products is given in the “c2d Spectroscopy Explanatory Supplement” (Lahuis et al., 2006a).

5.3.3 Spectral analysis

The SH and LH modules of the IRS instrument cover the positions of the three lowest pure rotational lines of H₂ and emission of [Ne II] (12.8 μm), [Ne III] (15.55 μm), [Fe I] (24 μm), [Fe II] (17.9 and 26.0 μm), [S I] (25.25 μm), [S III] (18.7 μm), and [Si II] (34.8 μm) at a resolving power of $R = \lambda/\Delta\lambda = 600$. Line fitting and flux integration is done using routines from OSIA.

As discussed in §5.3.1, the extended emission component, both in the continuum and the spectral line, is subtracted from the spectrum prior to line fitting. Uncertainty estimates, as listed in Table 5.2, are derived from the residuals after line fitting, or, in the absence of a spectral line, using the line width derived from the instrumental resolution. The uncertainty derived from the extended emission is added into the uncertainty estimate of the source component. As a result, the $1\text{-}\sigma$ uncertainty estimates can vary widely for sources with a similar continuum flux and integration time. This may for example be the result of the presence of artifacts resulting from hot pixels or small variations in the extended emission which are not accounted for in the spectral extraction which assumes a constant extended emission component.

Typical mean 3σ uncertainties prior to subtraction of the extended component for the high resolution modules range from $\sim 1 \times 10^{-16} - 2 \times 10^{-15} \text{ erg cm}^{-2} \text{ s}^{-1}$ with extremes of $\sim 5 \times 10^{-17} \text{ erg cm}^{-2} \text{ s}^{-1}$ and $\sim 1 \times 10^{-14} \text{ erg cm}^{-2} \text{ s}^{-1}$. The uncertainties are comparable to those from Pascucci et al. (2006) for FEPS observations using on source integration times similar to those used for the c2d sample.

5.4 Results

5.4.1 Atomic fine-structure lines: Neon

Of all the atomic fine structure lines covered by the SH and LH modules, the [Ne II] 12.8 μm transition is most convincingly detected and shows the strongest source emission. The higher excitation [Ne III] 15.5 μm line is not detected toward any of the sources in our sample. Figure 5.3 shows all [Ne II] lines detected at 3σ or more; see also Fig. 1 of Geers et al. (2006) for the [Ne II] 12.8 μm line toward T Cha. Plotted in Figure 5.3 is the total continuum-subtracted observed [Ne II] emission in gray and the compact source emission after correction for extended line emission in black. Taken together, [Ne II] emission is observed in the spectra of 17 T Tauri sources and one Herbig Ae/Be

OSIA is a joint development of the ISO-SWS consortium. Contributing institutes are SRON, MPE, KUL and the ESA Astrophysics Division. <http://sws.ster.kuleuven.ac.be/osia/>

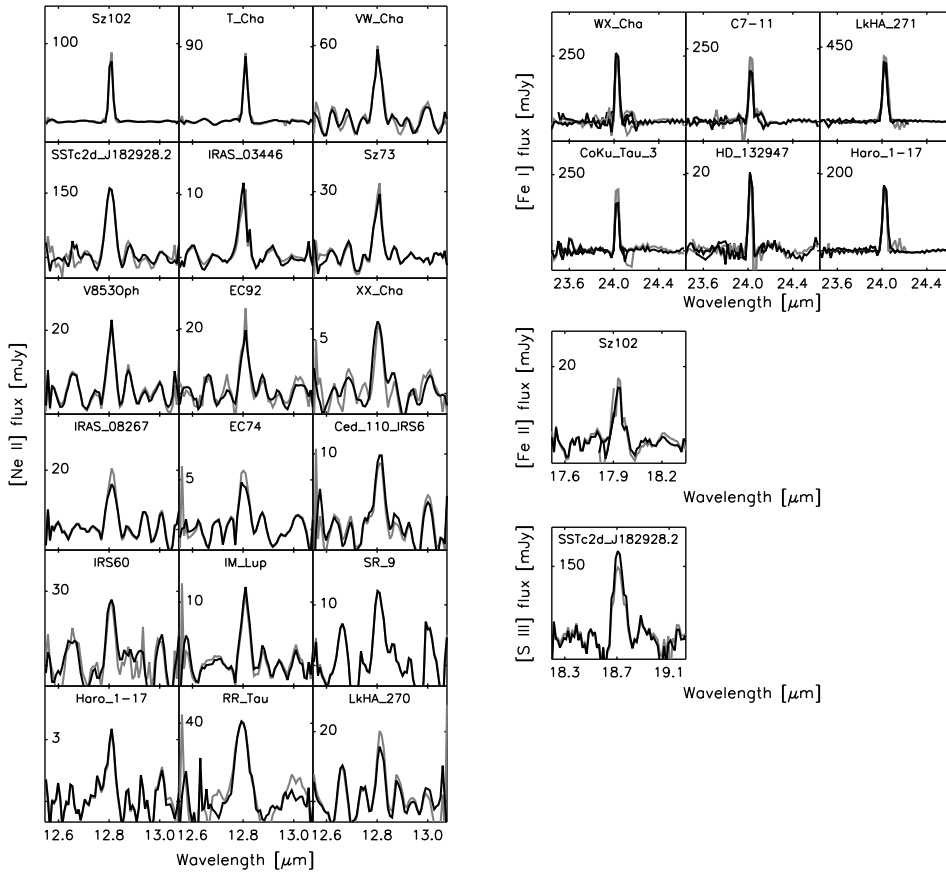


Figure 5.3 Detections of [Ne II], [Fe I], [Fe II], and [S III] at the 3σ level or more toward the c2d sample of T Tauri stars with disks. Of all the H_2 and atomic fine structure lines [Ne II] and [Fe I] are most convincingly detected toward $\gtrsim 20\%$ and $\sim 8\%$ of the sources respectively. Plotted in gray is the total observed emission (compact source + extended component) and in black the emission after correction of the estimated sky component. None of the sources show a significant extended component in any of the atomic fine structure lines.

star (RR Tau) ($\gtrsim 20\%$ of the sample). These are the first reported detections of [Ne II] toward disks around classical T Tauri stars. The optimal extraction method, together with the limited mini-maps (§5.2.2 and Fig. 5.1), show that the emission is indeed associated with the source itself.

The observed line fluxes and upper limits of [Ne II] and [Ne III] are listed in columns 8 and 9 of Table 5.2. When line fluxes are compared (observed or with models) the line strength is converted to solar luminosities since the sample is observed toward sources from multiple clouds and compared to model predictions using different assumed distances. Figure 5.4 shows the distribution of the observed line strengths (solid bars) and upper limits (hatched bars).

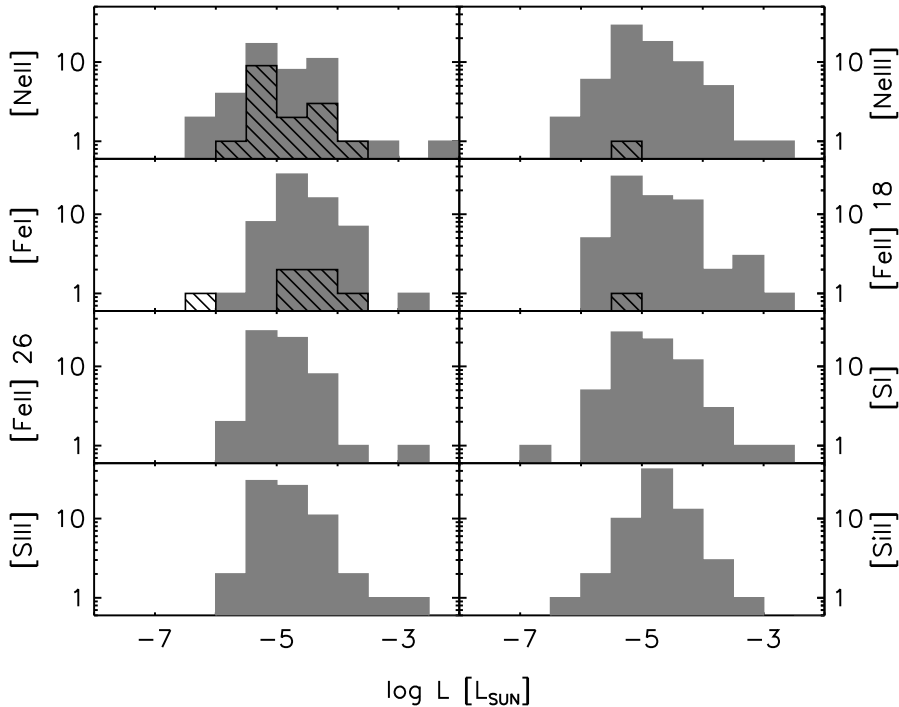


Figure 5.4 Observed line strengths (hatched bars) and upper limits (solid gray bars) of the major atomic lines. Included with vertical lines are model predicted line strengths for [Ne II] and [Ne III] by Glassgold et al. (2007). The model incorporates UV and X-ray heating of the circumstellar disk. The two lines represent two extreme thermal models, X-ray heating dominant (dotted line) or mechanical heating dominant (dashed line).

5.4.2 Atomic fine-structure lines: Other species

[Fe I] at $24\mu\text{m}$ is the only other species besides [Ne II] with clear detections toward six sources ($\sim 8\%$ of the sample). Of the other atomic lines there is one detection of [Fe II] at $18\mu\text{m}$ and one of [S III] at $18.7\mu\text{m}$, in different sources. [S I] at $25\mu\text{m}$, [Fe II] at $26\mu\text{m}$, and [Si II] at $34\mu\text{m}$ are not detected. The derived line fluxes and upper limits are listed in columns 9 – 14 in Table 5.2. The detected lines are plotted in Figure 5.3 whereas Figure 5.4 shows the distribution of the observed line strengths.

5.4.3 Molecular hydrogen

H_2 emission is detected toward a small number of sources. Figure 5.5 shows the observed H_2 0-0S(2) and S(3) emission lines detected at 3σ or more. The total (compact and extended line emission) observed H_2 emission (in gray) and the emission after subtraction of the extended line emission (in black) are shown. The H_2 0-0S(0) and S(1) lines are seen toward some sources such as HD 132947 and Sz 102 (Fig. 5.1) but they are always found to be extended, and hence not considered here. Neither S(0) nor S(1) are seen toward HD 135344 and HD 163296. The 3σ upper limits for HD 135344 are a factor of $\sim 2-3$ lower than the tentative detections in Thi et al. (2001), while for HD 163296 the

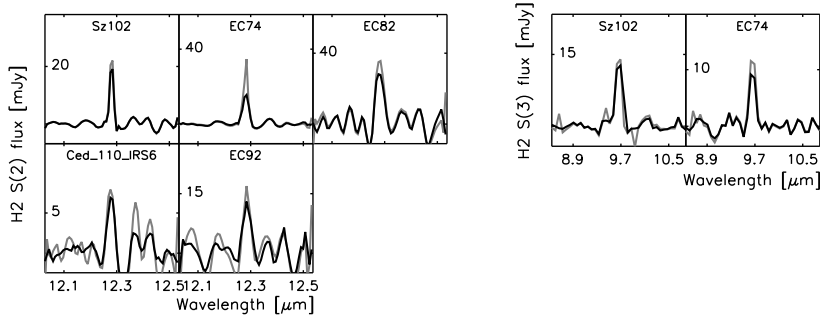


Figure 5.5 Detection of H_2 lines toward the c2d sample of T Tauri stars with disks. Only a few of the 76 sources show clear detections. Plotted in gray is the total observed emission (compact source + extended component) and in black the emission after correction of the estimated extended emission.

upper limits are comparable to the ISO SWS line fluxes. The observed line fluxes and upper limits of the H_2 0-0 S(0), S(1), S(2), and S(3) emission lines are listed in columns 4 – 7 of Table 5.2. Figure 5.6 shows the distribution of observed line strengths (solid bars) and upper limits (hatched bars) of H_2 0-0 S(0), S(1), S(2), and S(3).

In the simplest analysis, the H_2 excitation is assumed to be in local thermal equilibrium (LTE) (e.g., Thi et al., 2001) with an ortho-to-para ratio determined by the kinetic temperature of the gas (following Sternberg & Neufeld, 1999). For gas temperatures 100, 150, and ≥ 200 K, the ortho-to-para ratios are 1.6, 2.5, and 3, respectively. Assuming optically thin emission, the integrated flux of a rotational line $J_u \rightarrow J_l$ for a given temperature T_{ex} is

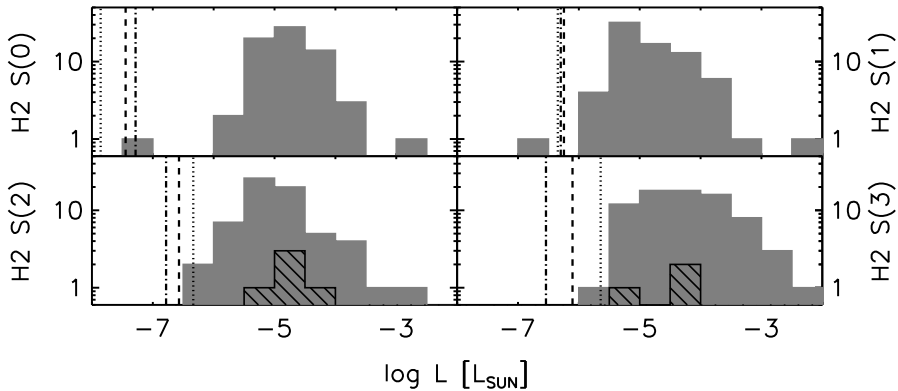


Figure 5.6 Observed line strengths (hatched bars) and upper limits (solid gray bars). The vertical lines present model T Tauri disk line strengths of H_2 S(0), S(1), S(2), and S(3) from Nomura et al. (2007). The models incorporate UV and X-ray heating of the circumstellar disk for three grain size distributions ($a_{\text{max}} = 10\mu\text{m}$, 1mm, and 10cm represented by dotted, dashed, and dashed-dotted lines respectively). For S(0) the line strength increases with increasing maximum grain size, while for S(2) and S(3) the line strength decreases as the maximum grain size increases.

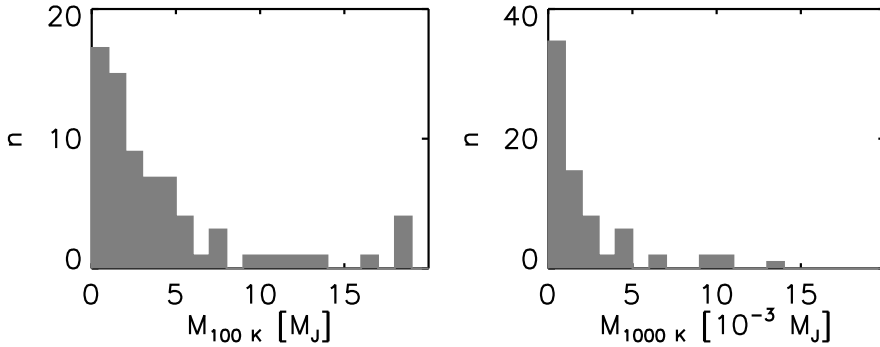


Figure 5.7 Distribution of H₂ mass upper limits derived for 100 and 1000 K gas. The bottom two panels are blow-ups with a smaller binsize of the upper panels.

$$F_{ul} = \frac{hc}{4\pi\lambda} N(\text{H}_2) A_{ul} x_u \Omega \text{ erg s}^{-1} \text{ cm}^{-2}, \quad (5.1)$$

where λ is the wavelength of the transition, $N(\text{H}_2)$ the total column density, A_{ul} the spontaneous transition probability, and Ω the source size. For high enough densities ($n \gtrsim 10^3 \text{ cm}^{-3}$), the population x_u follows the Boltzmann law

$$x_u = \frac{g_N(2J_u + 1)e^{-E_J/kT_{\text{ex}}}}{Q(T_{\text{ex}})} \quad (5.2)$$

where E_J is the energy of the upper level, g_N is the nuclear statistical weight (1 for para and 3 for ortho H₂), and $Q(T_{\text{ex}})$ the partition function for the given excitation temperature T_{ex} .

Using the above equations, excitation temperatures, column densities and H₂ gas masses can be derived from the observed line fluxes and upper limits. If either S(0) or S(1) are detected an upper or lower limit on the temperature of the warm gas is derived, but if neither are detected a temperature of 100 K is assumed for the warm gas. If two or more higher excitation lines (S(2) and higher) are detected a temperature for the hot component is derived, while if no or only one of the higher excitation lines is detected a temperature of 1000 K is assumed. For Sz 102 and EC74 temperatures of $T_{\text{hot}} \sim 700 - 800$ K could be found for the hot component. For all other sources no temperatures could be derived for either component.

The column density averaged over the IRS aperture can be derived from the above equations, given the distance to the source. For all sources in our sample the emitting source size in the disk is smaller than the IRS aperture (§5.3.1) and since this is unknown a typical emitting disk region is assumed. For the warm component a source with a radius $r = 100$ AU is assumed and for the hot component a source with a radius $r = 2$ AU. The derived or assumed temperature plus the (upper level) column densities give a total column density, which in turn gives the total H₂ gas mass in Jovian masses, $M = \pi r^2 \times N \times 2m_{\text{H}}/M_{\text{J}}$ with $m_{\text{H}} = 1.674 \cdot 10^{-24}$ gr and $M_{\text{J}} = 1.9 \cdot 10^{30}$ gr.

The derived H₂ parameters for both the warm and hot gas component are listed in Table 5.3. Figure 5.7 shows the distribution of the derived H₂ masses for the assumed temperatures of 100 K and 1000 K, respectively.

5.4.4 Correlations

Figure 5.8 shows the observed line strengths and upper limits of H_2 0-0S(2), [Ne II], and [Fe I] as functions of the mid-IR luminosities (in Solar luminosities) and the effective temperature. The mid-IR luminosity is also shown as a function of the effective temperature. The mid-IR luminosity is integrated over the 12.8 and 15.5 μm continuum points derived in the [Ne II] (12.8 μm) and [Ne III] (15.5 μm) spectral line fits. The effective temperature is derived from the stellar type (Gray & Corbally, 1994; Baraffe & Chabrier, 1996). In all panels the sources with H_2 0-0S(2), [Ne II], or [Fe I] detections are

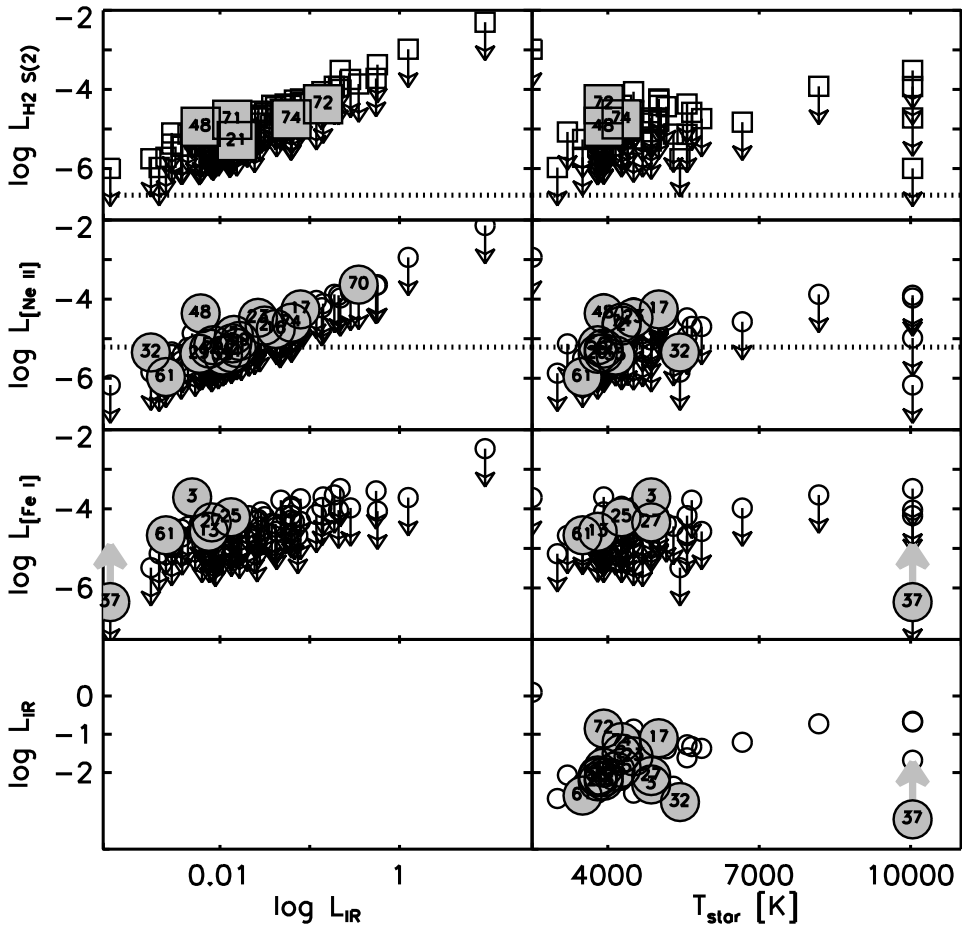


Figure 5.8 Comparison of the observed H_2 S(2) and [Ne II] fluxes in solar luminosities with a few observables. Plotted with the large filled symbols are the line detections, while the small symbols and arrows are all non-detections. Printed in the large filled symbols are the source index numbers. This allows identification of individual sources, in particular the outlier sources such as #32 – T Cha. The dotted lines in the H_2 and [Ne II] panels show the predicted linefluxes by Nomura et al. (2007) and Glassgold et al. (2007).

plotted with filled large numbered symbols whereas the sources without line detections are plotted with small open gray symbols.

For all sources with detections, both the H_2 0-0S(2) and [Ne II] line strengths show a positive correlation with the observed mid-IR luminosity. The correlation indicates that there are no low luminosity sources with strong H_2 0-0S(2) or [Ne II] emission. The upper limits clearly show a S/N selection effect and no conclusion can be drawn about a deviation from the observed correlation to lower H_2 0-0S(2) or [Ne II] emission fluxes.

The correlation with the effective temperature shows a differentiation between [Ne II] and [Fe I] compared with H_2 0-0S(2). The [Ne II] and [Fe I] line strengths show a similar correlation with effective temperature as with the mid-IR luminosity, but with more scatter. Also, upper limits are seen below the correlation line for sources with detections. There are a few detected sources deviating from the observed trend, such as the cold disk source T Cha (Brown & et al., 2007) detected in [Ne II] and the Herbig Ae star HD 132947 detected in [Fe I]. T Cha is located at a distance of 66 pc, much closer than the majority of sources in our sample. Sources with a similar [Ne II] line strength as T Cha but at the distances of the nearest star-forming clouds would go undetected at the sensitivity limits of the current sample. For HD 132947 the distance is unknown and the assumed distance of 60 pc is the lower limit from Tycho. The H_2 0-0S(2) line, although detected for only a small number of sources, differs from [Ne II] and [Fe I] in that all sources are concentrated around one effective temperature. This may be real, but it could also be the result of a S/N selection. More sensitive observations will be required to draw firm conclusions.

The mid-IR luminosity shows a correlation with the effective temperature for most sources. The correlation appears to be tighter for the sources with [Ne II] detections (with the exception of four sources among which T Cha) than for the sources without [Ne II] detections. However, higher sensitivity observations will be required to show the significance of this.

5.5 Discussion

5.5.1 [Ne II]

The most significant outcome of this survey is the detection of [Ne II] emission toward 17 T Tauri stars and one Herbig Ae/Be star, $\gtrsim 20\%$ of the sample. [Fe I] is also seen toward 6 sources, $\sim 8\%$ of the sample (see §5.4.1 and 5.4.2). Since neon cannot be ionized by photons with energies less than 21.4 eV (and Ne^+ 41.0 eV), the detection of [Ne II] is evidence for the presence of higher energy photons in the circumstellar environment, specifically EUV photons or X-rays originating from either the stellar chromosphere or (accretion) shocks. Alternatively, high-velocity shocks can result in ionized lines.

5.5.1.1 X-ray emission

T Tauri stars are known to be strong emitters of moderately hard X-rays. Feigelson & Lawson (2004) report X-ray luminosities toward young stars in the Chamealeon I north cloud of $L_X = 10^{28} - 10^{30} \text{ erg s}^{-1}$ whereas Telleschi et al. (2006) find X-ray luminosities toward young stars in the Taurus molecular clouds of $L_X = 10^{28} - 10^{31} \text{ erg s}^{-1}$ with a clear stellar mass dependence. A number of sources in our sample have been identified

with X-ray sources and have derived X-ray luminosities varying from $L_X \sim 4 \times 10^{28} - 10^{31} \text{ erg s}^{-1}$ (Table 5.4).

Recently Glassgold et al. (2007) modeled the excitation of neon in an X-ray irradiated flaring disk model according to D’Alessio et al. (1999) and predict [Ne II] and [Ne III] line intensities. For a source at 140 pc (the assumed distance in Glassgold et al. (2007)) [Ne II] line fluxes of $(0.6 - 1) \times 10^{-14} \text{ erg cm}^{-2} \text{ s}^{-1}$ and [Ne III] line fluxes of $(5 - 6.5) \times 10^{-16} \text{ erg cm}^{-2} \text{ s}^{-1}$ are predicted. The predicted [Ne II] line strength of $\sim 4 - 8 \times 10^{-6} L_\odot$ falls within the observed range of line strengths (see Table 5.4). The predicted [Ne III] line strength is below the *Spitzer* IRS [Ne III] upper limits. Interestingly the predicted [Ne II] line strength agrees well at 4000 K (the assumed effective temperature in the Glassgold et al. (2007) model) with the trend in the observed line strengths as shown in Figure 5.8.

The Glassgold et al. (2007) model is based on an assumed neon abundance of 10^{-4} and an X-ray luminosity and spectral temperature of $L_X = 2 \times 10^{30} \text{ erg s}^{-1}$ and $kT_X = 1 \text{ keV}$, appropriate for solar-mass pre-main sequence stars observed in Orion (Wolk et al., 2005). Lower mass, older, and accreting stars may have a lower X-ray luminosity (e.g. Feigelson & Lawson, 2004; Preibisch et al., 2005; Telleschi et al., 2006) leading to lower expected line intensities whereas higher X-ray luminosities, higher neon abundances (Drake et al., 2005; Cunha et al., 2006) or the inclusion of H atom collisions (not included in the Glassgold et al. (2007) calculations) may yield higher predicted line intensities. The neon line fluxes also scale with the disk mass surface density and are therefore sensitive to the disk geometry, e.g. flaring or non-flaring disks.

Of the sources with [Ne II] emission about 30% are identified as X-ray sources. The remaining sources may have escaped detection due to incomplete or sensitivity limited X-ray searches or due to source geometry prohibiting the detection of the X-rays. A more targeted deep X-ray search would be required to confirm a direct relation between observed [Ne II] emission and X-ray luminosities. Overall, variations in X-ray luminosities, age, stellar mass and geometry appear able to cover the two to three orders of magnitude range in the observed [Ne II] line fluxes.

5.5.1.2 EUV radiation

EUV radiation originating from the stellar chromosphere or the accretion shock may be an additional heating component of the disk surface and contribute to the neon excitation. EUV photons are however quickly absorbed by atomic hydrogen in the accretion column (Alexander et al., 2005) and for strong accretors will not reach the disk surface. However, for transitional objects like T Cha the accretion column can become optically thin to EUV photons and some EUV radiation may escape the immediate surroundings of the star and reach the disk surface, potentially contributing to the ionizing radiation at the factor of 2 level. The [Ne II]/[Ne III] ratio is expected to increase with the additional EUV contribution given the high (41.0 eV) ionization potential of Ne^+ . The [Ne III] upper limits do not permit any constraints on this (see Fig. 5.9), however. All [Ne II]/[Ne III] ratios are well below those predicted for X-ray excitation (indicated with the horizontal dashed line). Therefore any enhancement in the [Ne II]/[Ne III] ratio will remain undetected given the sensitivity limits of this sample.

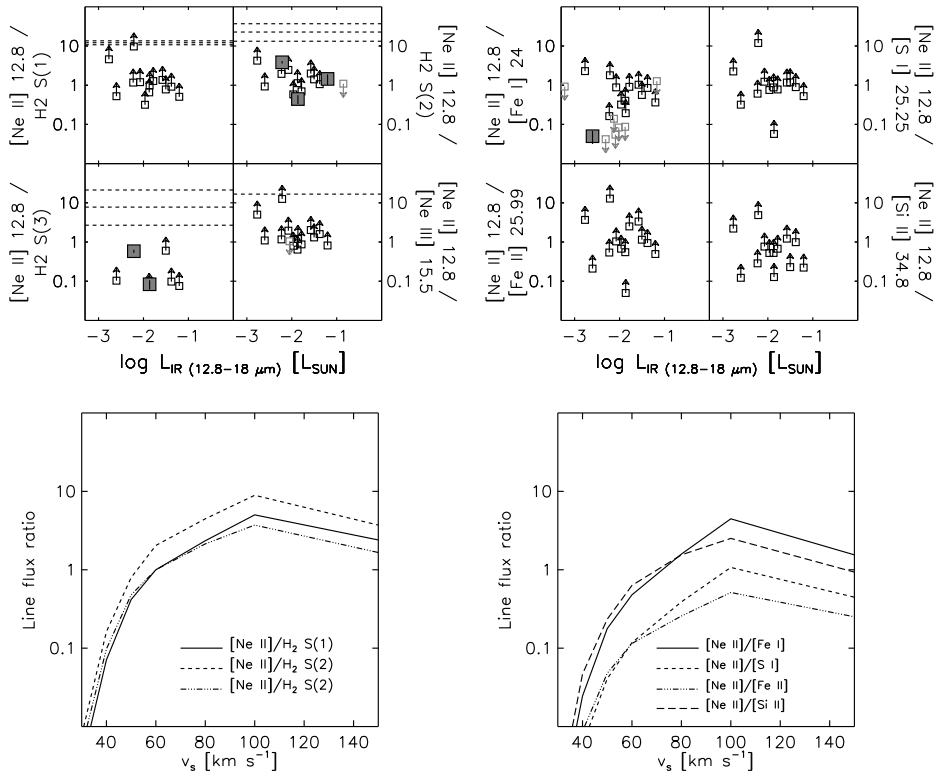


Figure 5.9 Line ratios of [Ne II] w.r.t. other species as functions of mid-IR luminosity. Large filled symbols are used for sources with both [Ne II] and the second line detected. Small open symbols with arrows indicate lower and upper limits of the line ratios. The dashed lines in the left plot show the line ratios for the predictions from the Glassgold et al. (2007); Nomura et al. (2007) models. The lower two plots show the ratios from shock models by Hollenbach & McKee (1989) for different shock velocities.

5.5.1.3 Disk shocks

The presence of strong [Ne II] could also indicate a possible origin of the observed [Ne II] emission induced by shocks in the disk. Hartmann & Raymond (1989) describe shocks resulting from the stellar wind striking the disk surface at an oblique angle. For typical wind velocities of 200 km s^{-1} shock velocities along the disk surface are estimated to be $\sim 30\text{--}40 \text{ km s}^{-1}$. For such shocks and a medium with a density of $10^5 - 10^6 \text{ cm}^{-3}$ Hollenbach & McKee (1989) predict [Ne II] line strengths of $\sim 10^{-6} - 10^{-4} \text{ erg cm}^{-2} \text{ s}^{-1} \text{ sr}^{-1}$. For a 100 AU disk at 100 pc, the upper end of this range implies a [Ne II] line flux of approximately $10^{-14} \text{ erg cm}^{-2} \text{ s}^{-1}$, of the same order as observed. However, Hollenbach & McKee (1989) also predict the H_2 0-0 S(1), S(2), and S(3) lines and the [Fe I] $24\mu\text{m}$, [Si I] $25.25\mu\text{m}$, [Fe II] $26\mu\text{m}$, and [Si II] $34.8\mu\text{m}$ spectral lines to be stronger than the [Ne II] line by 1 – 3 orders of magnitude for these velocities as illustrated in the lower right plot of Fig. 5.9. The top plots of Fig. 5.9 show the observed ratios and lower limits. For almost all of the line pairs, the ratios are roughly equal to or larger than unity, except for a small number of cases.

To account for line ratios equal to or larger than unity, higher velocity shocks would be required. At high shock velocities ($v \gtrsim 70 \text{ km s}^{-1}$) and high densities ($\gtrsim 10^5 \text{ cm}^{-3}$) the J-shock models presented in Hollenbach & McKee (1989) give [Ne II], [Fe I] 24 μm , [SI] 25.25 μm , [Fe II] 26 μm , and [Si II] 34.8 μm lines all of comparable strength of $\sim 0.004 \text{ erg cm}^{-2} \text{ s}^{-1} \text{ sr}^{-1}$ (see bottom right plot in Figure 5.9). To produce a line flux of $\sim 10^{-14} \text{ erg cm}^{-2} \text{ s}^{-1}$ the shocked emission would have to come from a region of the disk with a radius of $\sim 10 \text{ AU}$ at a distance of 100 pc. Higher velocity shocks may produce the observed line flux ratios and lower limits, but a possible origin for such high velocity shocks is unclear. Another problem lies in the non-detection of the [SI] 25.25 μm , the [Fe II] 26 μm , and the [Si II] 34.8 μm lines. In particular the [SI] line should be detected if high velocity shocks are the origin of the observed line emission: the [SI] line is predicted to be stronger whereas the detection limits for [Fe I] and [SI] are comparable in our data (see Fig. 5.4).

5.5.2 [Fe I] and [S I]

As mentioned in § 5.5.1 the detection of [Fe I] in combination with the non-detection of other atomic lines, in particular [SI] and [Si II], is significant.

Gorti & Hollenbach (2004) modeled the line emission from intermediate aged optically thin disks around G and K stars. For disks with low gas masses (10^{-3} to $10^{-2} M_J$), the [SI] 25.2 μm , [Fe II] 26 μm , and [Si II] 35.4 μm lines are expected to be the strongest mid-infrared emission lines. However as the disk mass increases a larger fraction of the sulfur turns molecular and the [Si II] and [Fe II] emission becomes optically thick. At the same time the [Fe I] lines are predicted to become increasingly stronger and will at some point, around a $0.1 M_J$, dominate over the [SI] emission. Although specific calculations for these optically thick disks are lacking, the six sources (WX Cha, C7-11, LkH α 271, Coku Tau 3, HD 132947, and Haro 1-17) which show strong [Fe I] emission may well have optically thick massive gas-rich disks.

5.5.3 Molecular hydrogen

The second significant result of our survey is the non-detection of the H₂ 0-0S(0) and S(1) lines for 76 T Tauri and Herbig Ae/Be stars. This puts constraints on the mass of warm ($T \sim 100 - 200 \text{ K}$) H₂ gas in the disks around these stars of typically a few M_{Jup} as illustrated in Figure 5.7. Models of disk heating by stellar UV photons show that the gas temperature in the surface layers can be significantly higher than that of the dust down to an optical depth for UV photons of ~ 1 . The precise temperatures depend on the model details, in particular the presence of PAHs, the grain size, the gas/dust ratio, and the presence of excess UV over that of the stellar photosphere (Jonkheid et al., 2004; Kamp & Dullemond, 2004; Nomura & Millar, 2005; Nomura et al., 2007; Jonkheid et al., 2006, 2007). For interstellar-sized grains ($\sim 0.1 \mu\text{m}$), the models readily give surface temperatures of 100 K or more out to at least 100 AU. Even models in which the dust grains have grown and settled to the midplane have warm surface layers as long as some PAHs are still present. The total mass contained in this warm layer is however small, $\sim 1\%$ or less of the total disk mass. For the specific $0.07 M_{\odot}$ disk studied by Jonkheid et al. (2004) the mass at $T > 100 \text{ K}$ is $\sim 0.7 M_J$. Thus, for a typical disk mass of $0.01 M_{\odot}$, this would be of order $0.1 M_{\text{Jup}}$, below our upper limits.

The H₂ line fluxes from a protoplanetary disk representative of that around TW

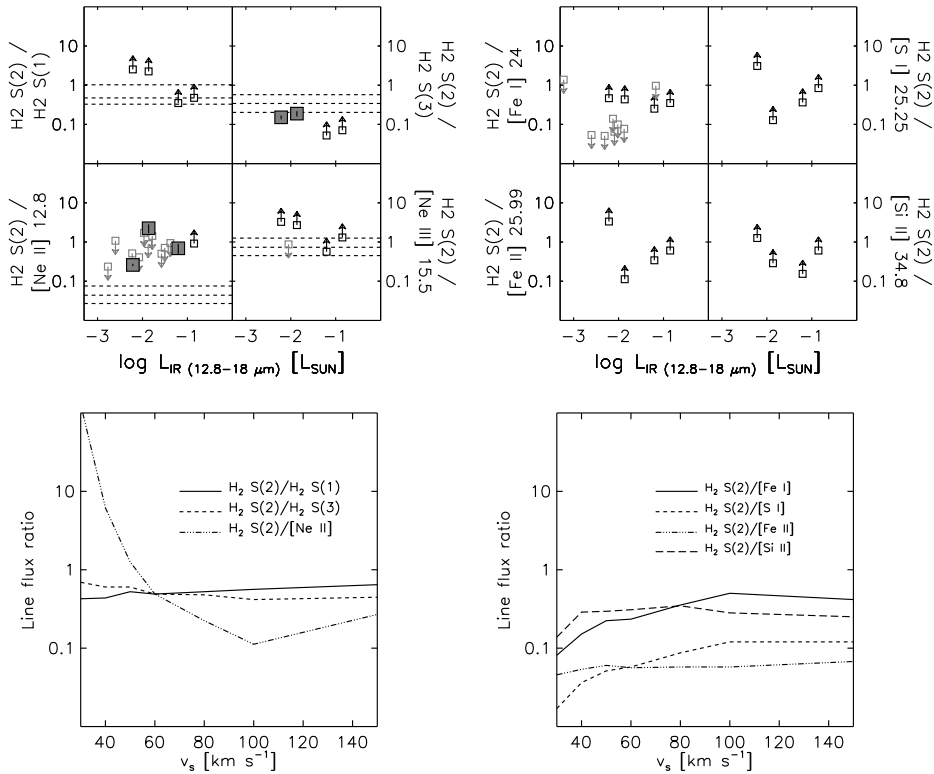


Figure 5.10 Line ratios of H_2 S(2) w.r.t. other species as functions of the mid-IR luminosity. Large filled symbols are used for sources with both H_2 S(2) and the second line detected. Small open symbols with arrows indicate lower and upper limits of the line ratios. The dashed lines in the left plot show the line ratios for the predictions from the Glassgold et al. (2007); Nomura et al. (2007) models. The lower two plots show the ratios from shock models by Hollenbach & McKee (1989) for different shock velocities.

H₂ have been modeled by Nomura & Millar (2005). These models include not just thermal excitation but also UV pumping of the H_2 levels. Nomura et al. (2007) include X-ray irradiation and the effect of grain size distributions. For the higher excitation lines the grain size distribution is particularly important with a distribution toward smaller grain sizes producing higher line strengths. This result is consistent with that of Jonkheid et al. (2007), who find lower temperatures in models with grain growth. Figure 5.6 shows the distribution of the observed line strengths with the predicted line strengths for the Nomura et al. (2007) model included for grain size distributions with maximum grain sizes of $a_{\text{max}} = 10\mu\text{m}$, 1mm, and 10cm. It is seen that the observed upper limits are all consistent with this model, even if excess UV is included. Note, however, that pure rotational H_2 line fluxes are extremely sensitive to the model details: small changes in the heating and cooling processes, as well as the treatment of the H/ H_2 transition zone, can result in significant differences in gas temperatures and an order of magnitude variation in predicted line fluxes (see discussion in Li et al., 2002; Roellig et al., 2007). Therefore, comparison of the total mass of warm gas between

models and observations is equally relevant.

Toward five sources ($\sim 7\%$ of the sample), H_2 0-0 S(2) and/or S(3) emission is observed, which provides evidence for the presence of a significant hot ($T \gtrsim 500$ K) gas component in the disks. Hot gas ($T \gtrsim 500$ K) is observed toward a number of sources through the H_2 0-0 S(2) line, most convincingly toward Sz 102, EC 82, Ced IRS IRS6, EC 74, and EC 92. For Sz 102 a number of higher transition lines are also seen. The observed H_2 0-0 S(2) line strengths are more than a factor of 10 higher than those predicted in Nomura & Millar (2005); Nomura et al. (2007) (see Fig. 5.6). Given the non-detection of the S(1) line toward the same sources, which is predicted to have a similar strength, this is an indication that these disks have an additional source of emission from hot molecular hydrogen. The upper limits for H_2 0-0 S(2) and S(3) are higher for almost all sources than the Nomura & Millar (2005) predicted values. An additional hot component may therefore be present in these sources as well below our detection limit.

None of the sources with evidence for an additional hot component show evidence for PAH emission (see Geers et al., 2006). Of the five sources with detected H_2 0-0 S(2), four show strong [Ne II] emission, giving support to the idea of a common heating and excitation mechanism through X-rays or EUV. Of the [Ne II] sources two, T Cha and RR Tau, show strong PAH emission. Considering the limitations in observing the PAH emission as described by Geers et al. (2006) we can at this stage draw no conclusions about the relation between the hot H_2 emission, [Ne II] emission, and the importance of PAHs and small grains.

An origin in a high velocity shock as discussed in §5.5.1.3 could produce the enhanced S(2) and S(3) line strengths while keeping the line strengths of S(0) and S(1) reduced. However, as discussed in §5.5.1.3, the main problem with invoking shocks to explain [Ne II] and H_2 is to accommodate both the detections of [Fe I] and the non-detections of [SI] and [Fe II] $26\mu\text{m}$. Figure 5.10 shows the observed and model line ratios with respect to H_2 , similar those in Fig. 5.9. An origin in an oblique stellar wind shock faces the same problems as discussed for [Ne II] in §5.5.1.3.

5.6 Conclusions

A survey of the mid-infrared gas phase pure rotational lines of molecular hydrogen and a number of atomic fine structure transitions has been carried out toward a significant sample of 76 circumstellar disks with the *Spitzer* IRS. The principal findings include:

- [Ne II] is detected toward $\gtrsim 20\%$ of the sources. These present the first detections of [Ne II] toward T Tauri stars. The detections are consistent with disk heating and excitation of [Ne II] through X-rays as presented in Glassgold et al. (2007). Excitation through EUV radiation may contribute. Better constraints on the X-ray luminosities and [Ne III] upper limits are required to distinguish the two contributions.
- [Fe I] is detected toward $\sim 8\%$ of the sources. No other low excitation atomic lines, such as [Fe II], [SI] and [Si II], are detected. This suggests that these sources may possess optically thick disks with gas masses of at least a $0.1M_J$.

- No compact H₂ 0-0S(0) and S(1) emission is observed toward any of the sources in our sample, setting limits of a few Jovian masses on the mass of the warm $T_{\text{ex}} = 100$ K gas in the disks. These limits are above model predictions. The H₂ line flux upper limits are also consistent with recent T Tauri disk model predictions by for example Nomura et al. (2007). Earlier tentative ISO detections of H₂ in two Herbig Ae disks are not confirmed.
- Hot ($T \gtrsim 500$ K) H₂ gas has been detected toward $\sim 7\%$ of the sources. Given the high upper limits on the rest of the sources, the fraction may be higher. The detection of the hot gas suggests the presence of an additional source of hot H₂ emission not included in the most recent disk models (e.g. Nomura et al., 2007).
- Of the five sources with hot H₂ emission four show [Ne II] emission suggesting a possible common heating and excitation mechanism through X-rays or EUV.
- Lower limits of the line flux ratios of [Ne II] with H₂ and [Ne III] are consistent with recent T Tauri disk models presented in Glassgold et al. (2007); Nomura et al. (2007).
- An origin of the enhanced H₂ emission in oblique shocks due to winds interacting with the disk surface is not consistent with the non-detection of atomic lines, in particular the non-detections of [S I] and [Fe II] 26 μm .

The bright [Ne II] lines detected at 12.8 μm are excellent targets for follow-up observations with high dispersion echelle spectrometers on 8-10m class telescopes (TEXES, VISIR). The measured spatial profiles and line shapes would provide exacting tests of the X-ray mediated disk emission proposed here and could definitely rule out any high-velocity shock mechanism.

Acknowledgements

The authors would like to thank Jes Jørgensen for making the *Spitzer* IRAC mosaics, and Hideko Nomura for communicating her latest disk model results. Astrochemistry in Leiden is supported by a NWO Spinoza grant and a NOVA grant. Support for this work, part of the *Spitzer* Legacy Science Program, was provided by NASA through contracts 1224608, 1230779, and 1256316 issued by the Jet Propulsion Laboratory, California Institute of Technology, under NASA contract 1407. We thank the Lorentz Center in Leiden for hosting several meetings that contributed to this paper.

Table 5.1. Source list

#	Source	RA	Dec	AOR	tint [s] (SL/SH/LH)/ndith. [5]	Class	D ^a [pc] [7]	Age [Myr] [8]	Spectral type [9]
	[1]	[2]	[3]	[4]		[6]			
1	RNO 15	3 ^h 27 ^m 47 ^s .7	30° 12' 04''.3	5633280	(14*1/31*2/60*1)*2	TTs	250	-	-
2	Lk H α 270	3 ^h 29 ^m 17 ^s .7	31° 22' 45''.1	5634048	(14*2/31*2/60*2)*2	TTs	250	0.014	K2.5-K7
3	Lk H α 271	3 ^h 29 ^m 21 ^s .9	31° 15' 36''.4	11827968	(14*2/121*2/60*2)*2	TTs	250	-	K3-K5
4	Lk H α 326	3 ^h 30 ^m 44 ^s .0	30° 32' 46''.7	5634304	(14*2/31*4/60*1)*2	TTs	250	0.28	G-M0
5	Lk H α 327	3 ^h 33 ^m 30 ^s .4	31° 10' 50''.5	5634560	(14*1/6*2/14*2)*2	TTs	250	0.70-1.4	A9-K2
6	Lk H α 330	3 ^h 45 ^m 48 ^s .3	32° 24' 11''.9	5634816	(14*1/31*1/60*1)*2	CTTs	250	5.72	G3
7	IRAS 03446+3254	3 ^h 47 ^m 47 ^s .1	33° 04' 03''.4	5635072	(14*1/121*2/60*1)*2	TTs	250	-	-
8	LkCa 8	4 ^h 24 ^m 57 ^s .1	27° 11' 56''.4	9832960	(-/31*8/60*2)*2	CTTs	140	-	M0-M0Ve
9	IQ Tau	4 ^h 29 ^m 51 ^s .6	26° 06' 45''.0	9832704	(-/31*2/60*2)*2	WTTs	140	1.2	M0-M0.5
10	FX Tau	4 ^h 30 ^m 29 ^s .6	24° 26' 45''.2	9832448	(-/31*2/60*2)*2	C+WTTs	140	-	M1-M4
11	V710 Tau	4 ^h 31 ^m 57 ^s .8	18° 21' 36''.4	5636608	(-/121*2/60*4)*2	C+WTTs	140	-	M0.5-M1-M2-M3
12	DN Tau	4 ^h 35 ^m 27 ^s .4	24° 14' 58''.9	9831936	(-/31*4/60*2)*2	CTTs	140	-	M0
13	CoKu Tau 3	4 ^h 35 ^m 40 ^s .9	24° 11' 08''.5	9831936	(-/31*4/60*2)*2	CTTs	140	-	M1
14	CoKu Tau 4	4 ^h 41 ^m 16 ^s .8	28° 40' 00''.5	5637888	(-/31*2/60*4)*2	CTTs	140	1.2-1.6	M1.5
15	BF Ori	5 ^h 37 ^m 13 ^s .3	-6° 35' 00''.6	5638144	(14*1/31*1/60*1)*2	H AeBe	400	2.0	A5-F6
16	RR Tau	5 ^h 39 ^m 30 ^s .5	26° 22' 27''.1	5638400	(14*1/31*1/60*1)*2	H AeBe	160	0.6	A5-B8
17	IRAS 08267-3336	8 ^h 28 ^m 40 ^s .7	-33° 46' 22''.4	5639168	(14*1/31*2/60*1)*2	TTs	400?	1.96	K2-K2.5-K3
18	SX Cha	10 ^h 55 ^m 59 ^s .7	-77° 24' 40''.0	5639424	(-/121*1/60*2)*2	TTs	178	1.15-1.4	M0.5
19	SY Cha	10 ^h 56 ^m 30 ^s .5	-77° 11' 39''.5	5639424	(-/121*1/60*2)*2	TTs	178	1.35-2.5	M0
20	TW Cha	10 ^h 59 ^m 01 ^s .1	-77° 22' 40''.8	5639680	(-/121*2/60*2)*2	TTs	178	16.82-20	K0-M0
21	Ced 110 IRS6	11 ^h 07 ^m 09 ^s .2	-77° 23' 04''.2	5639680	(-/121*2/60*2)*2	1	178	-	-
22	B35	11 ^h 07 ^m 21 ^s .5	-77° 22' 11''.7	5639680	(-/121*2/60*2)*2	TTs	178	0.1	M2
23	VW Cha	11 ^h 08 ^m 01 ^s .5	-77° 42' 28''.8	5639680	(-/121*2/60*2)*2	CTTs	178	2.39-0.2-1.0	K2-K5-K5K7
24	VZ Cha	11 ^h 09 ^m 23 ^s .8	-76° 23' 20''.8	5640448	(-/121*2/60*2)*2	TTs	178	5.71-4-10	K6-K7
25	WX Cha	11 ^h 09 ^m 58 ^s .8	-77° 37' 08''.8	5640192	(-/121*1/60*2)*2	TTs	178	0.79-1-5	K7-M0
26	ISO-Cha237	11 ^h 10 ^m 11 ^s .4	-76° 35' 29''.0	5640448	(-/121*2/60*2)*2	TTs	178	-	M0
27	C7-11	11 ^h 10 ^m 38 ^s .0	-77° 32' 39''.9	5640192	(-/121*1/60*2)*2	TTs	178	0.2-1	K3
28	HM 27	11 ^h 10 ^m 49 ^s .6	-77° 17' 51''.7	5640192	(-/121*1/60*2)*2	TTs	178	2.38-30-40	K7
29	XX Cha	11 ^h 11 ^m 39 ^s .7	-76° 20' 15''.0	5640448	(-/121*2/60*2)*2	TTs	178	1.87-2-40	M1-M2
30	HD 98922	11 ^h 22 ^m 31 ^s .7	-53° 22' 11''.3	5640704	(-/6*1/14*1)*2	H AeBe	ζ 540	-	B9

Table 5.1—Continued

#	Source	RA	Dec	AOR	tint [s] (SL/SH/LH)/ndith.	Class	D ^a [pc]	Age [Myr]	Spectral type
	[1]	[2]	[3]	[4]	[5]	[6]	[7]	[8]	[9]
31	HD 101412	11 ^h 39 ^m 44 ^s .5	-60° 10' 27".8	5640960	(14*1/31*1/60*1)*2	HAeBe	160	-	B9.5V
32	T Cha	11 ^h 57 ^m 13 ^s .5	-79° 21' 31".3	5641216	(-/31*2/60*1)*2	TTs	66	4.14- ζ 12.5	G2-G8-K0
33	IRAS 12535-7623	12 ^h 57 ^m 11 ^s .8	-76° 40' 11".6	11827456	(-/121*1/60*2)*2	TTs	178	0.19	M0
34	Sz50	13 ^h 00 ^m 55 ^s .4	-77° 10' 22".1	11827456	(-/121*1/60*2)*2	TTs	178	1.74	K7-M3
35	ISO-ChaII 54	13 ^h 00 ^m 59 ^s .2	-77° 14' 02".8	15735040	(14*2/31*4/-)*2	BD	178	-	-
36	DL Cha	13 ^h 06 ^m 08 ^s .4	-77° 06' 27".4	5642240	(-/6*2/6*5)*2	TTs	178	-	III-M6
37	HD 132947	15 ^h 04 ^m 56 ^s .0	-63° 07' 52".7	5643008	(14*1/31*2/241*2)*2	HAeBe	ζ 60	-	A0
38	HD 135344	15 ^h 15 ^m 48 ^s .4	-37° 09' 15".8	5657088	(-/121*1/60*2)*2	HAeBe	140	17	A0-F4
39	HT Lup	15 ^h 45 ^m 12 ^s .9	-34° 17' 30".5	5643264	(14*1/31*1/60*1)*2	TTs	145	2.29-0.4-0.8	K2
40	HT Lup	15 ^h 45 ^m 12 ^s .9	-34° 17' 30".5	9829120	(14*2/31*2/60*2)*1	TTs	145	2.29-0.4-0.8	K2
41	GW Lup	15 ^h 46 ^m 44 ^s .7	-34° 30' 35".3	5643520	(14*1/121*2/60*4)*2	TTs	100	3.40-1.3-3.2	M2-M4
42	Sz73	15 ^h 47 ^m 57 ^s .0	-35° 14' 35".2	5644032	(14*1/31*1/60*1)*2	TTs	100	3.24-2.6-5.4	K2-K5-M0-M
43	GQ Lup	15 ^h 49 ^m 12 ^s .1	-35° 39' 05".0	5644032	(14*1/31*1/60*1)*2	TTs	100	0.96-0.1-0.6	K7-M0
44	IM Lup	15 ^h 56 ^m 09 ^s .2	-37° 56' 06".4	5644800	(14*1/31*2/60*1)*2	TTs	140	1.51-0.1-0.6	M0
45	RU Lup	15 ^h 56 ^m 42 ^s .3	-37° 49' 15".6	5644800	(14*1/31*2/60*1)*2	CTTs	140	0.82-0.1-0.5	K3-K7-M0
46	RY Lup	15 ^h 59 ^m 28 ^s .4	-40° 21' 51".1	5644544	(14*1/31*1/60*1)*2	TTs	150	2.67-1.6-3.2	K0-K4
47	EX Lup	16 ^h 03 ^m 05 ^s .5	-40° 18' 24".8	5645056	(14*1/31*1/60*1)*2	TTs	150	5.62-1.4-3.0	M0
48	Sz102	16 ^h 08 ^m 29 ^s .7	-39° 03' 11".2	9407488	(14*1/121*2/60*1)*2	TTs	200	-	M0
49	AS 205	16 ^h 11 ^m 31 ^s .3	-18° 38' 26".2	5646080	(6*2/6*2/14*2)*2	TTs	120	0.43-0.1	K5
50	Haro 1-1	16 ^h 21 ^m 34 ^s .7	-26° 12' 27".0	9833472	(14*1/31*4/60*1)*2	CTTs	125	13.1	K5-K7
51	Haro 1-4	16 ^h 25 ^m 10 ^s .5	-23° 19' 14".5	9833216	(-/31*2/60*1)*2	TTs	125	0.80	7-K4-K6
52	DoAr 24E	16 ^h 26 ^m 23 ^s .4	-24° 21' 00".0	5647616	(-/31*1/14*2)*2	TTs	125	2.46-1.5	K0-K1
53	SR 21	16 ^h 27 ^m 10 ^s .3	-24° 19' 12".4	5647616	(-/31*1/14*2)*2	TTs	125	3.04-1	F4-G1,G2.5
54	IRS51	16 ^h 27 ^m 39 ^s .8	-24° 43' 15".2	9829888	(-/31*2/14*2)*2	2	125	0.79	G5-K7
55	SR 9	16 ^h 27 ^m 40 ^s .3	-24° 22' 04".1	12027392	(-/31*1/60*2)*2	TTs	125	0.83	K5,M2-K8
56	V853Oph	16 ^h 28 ^m 45 ^s .3	-24° 28' 18".8	12408576	(-/31*4/60*4)*2	TTs	125	0.78	M1.5
57	ROX42C	16 ^h 31 ^m 15 ^s .7	-24° 34' 01".9	6369792	(-/31*2/60*1)*2	TTs	125	3.7-(Fi)	K4-K5-K6
58	ROX43A	16 ^h 31 ^m 20 ^s .1	-24° 30' 05".0	15914496	(-/31*1/60*2)*2	TTs	125	12.2	G0
59	IRS60	16 ^h 31 ^m 30 ^s .9	-24° 24' 39".6	6370048	(-/31*1/60*1)*2	-	125	-	-
60	Haro 1-16	16 ^h 31 ^m 33 ^s .5	-24° 27' 37".1	12664064	(-/31*1/60*1)*2	TTs	125	1.92-0.5	K2-K3

Table 5.1—Continued

#	Source	RA	Dec	AOR	tint [s]	Class	D ^a	Age	Spectral type
		[1]	[2]	[3]	[4]		(SL/SH/LH)/ndith.	[5]	
61	Haro 1-17	16 ^h 32 ^m 21 ^s .9	-24° 42' 14''.8	11827712	(60*1/121*4/60*4)*2	TTs	125	-	M2.5
62	RNO 90	16 ^h 34 ^m 09 ^s .2	-15° 48' 16''.9	5650432	(14*1/31*1/14*2)*2	TTs	140	6	G5
63	Wa Oph 6	16 ^h 48 ^m 45 ^s .6	-14° 16' 35''.8	5650688	(14*1/31*1/60*1)*2	2	140	0.85	K7
64	V1121 Oph	16 ^h 49 ^m 15 ^s .3	-14° 22' 08''.8	5650688	(14*1/31*1/60*1)*2	CTTs	125	0.53	K5
65	HD 163296	17 ^h 56 ^m 21 ^s .3	-21° 57' 22''.0	5650944	(-6*2/14*2)*2	HAeBe	122	4-6	A0-A2
66	HD 163296	17 ^h 56 ^m 21 ^s .3	-21° 57' 22''.0	9830144	(-6*4/14*4)*1	HAeBe	122	4-6	A0-A2
67	VV Ser	18 ^h 28 ^m 47 ^s .9	0° 08' 39''.8	5651200	(6*2/31*1/60*1)*2	HAeBe	260	0.6	A3-B1
68	SSTc2d J182900.9+02931	18 ^h 29 ^m 00 ^s .9	0° 29' 31''.6	13210112	(14*1/31*2/-)*2	-	260	-	-
69	SSTc2d J182909.8+03446	18 ^h 29 ^m 09 ^s .8	0° 34' 45''.8	13210624	(14*1/31*1/-)*2	-	260	-	-
70	SSTc2d J182928.2+02257	18 ^h 29 ^m 28 ^s .2	-0° 22' 57''.4	13210368	(14*1/31*2/-)*2	-	260	-	-
71	EC74	18 ^h 29 ^m 55 ^s .7	1° 14' 31''.6	9407232	(14*1/121*1/60*2)*2	2	260	-	-
72	EC82	18 ^h 29 ^m 56 ^s .9	1° 14' 46''.7	9407232	(14*1/121*1/60*2)*2	TTs	260	-	M0
73	EC90	18 ^h 29 ^m 57 ^s .7	1° 14' 06''.0	9828352	(6*2/31*1/14*1)*2	TTs	260	-	-
74	EC92	18 ^h 29 ^m 57 ^s .9	1° 12' 51''.5	9407232	(14*1/121*1/60*2)*2	TTs	260	-	K7-M2
75	CK4	18 ^h 29 ^m 58 ^s .2	1° 15' 21''.6	9407232	(14*1/121*1/60*2)*2	TTs	260	6.81	K3
76	Lk H α 348	18 ^h 34 ^m 12 ^s .6	-0° 26' 21''.8	9831424	(6*2/6*2/14*2)*2	-	260	-	-

^a Assumed cloud distances; Chamaeleon (178 pc Whittet et al., 1997) Lupus I, IV (150 pc) and Lupus III (200 pc) Cameron in prep., Ophiuchus (125 pc de Geus et al., 1989), Perseus (250 pc, see discussion in Enoch, Young, Glenn, Evans, Golwala, Sargent, Harvey, Aguirre, Goldin, Haig, Huard, Lange, Laurent, Maloney, Maukopf, Rossinot, & Sayers, 2006), Taurus-Auriga (160 pc Kenyon et al., 1994), Serpens (260 pc Straizys, Cernis, & Bartasiute, 1996), except for T Cha, HD 98922, & HD 163296 (van den Ancker et al., 1998), BF Ori, (Parenago, 1954), HD 101412 & HD 135344 (de Zeeuw et al., 1999), & HD 132947 (minimum Tycho distance)

A literature reference list is included in the source table of the published ApJ paper.

Table 5.2. Observed linefluxes and 1σ uncertainties ($10^{-16}\text{erg cm}^{-2}\text{s}^{-1}$)

#	Source	Dis. [pc]	H ₂ S(0)	H ₂ S(1)	H ₂ S(2)	H ₂ S(3)	[Ne II]	[Ne III]	[Fe I]	[Fe II] 18	[Fe II] 25	[S I]	[Si II]
[1]	[2]	[3]	[4]	[5]	[6]	[7]	[8]	[9]	[10]	[11]	[12]	[13]	[14]
1	RNO 15	250	– (63)	– (93)	– (28)	– (640)	– (95)	– (74)	– (74)	– (88)	– (50)	– (50)	– (41)
2	Lk H α 270	250	– (37)	– (47)	– (26)	– (61)	110 (36)	– (28)	– (65)	– (37)	– (32)	– (31)	– (160)
3	Lk H α 271	250	– (48)	– (11)	– (17)	– (42)	– (14)	– (8)	1000 (140)	– (16)	– (18)	– (25)	– (200)
4	Lk H α 326	250	– (36)	– (33)	– (23)	– (150)	– (26)	– (28)	– (86)	– (26)	– (15)	– (38)	– (120)
5	Lk H α 327	250	– (89)	– (90)	– (55)	– (320)	– (72)	– (57)	170 (49)	– (90)	– (41)	– (54)	– (45)
6	Lk H α 330	250	– (140)	– (62)	– (27)	– (210)	– (21)	– (34)	– (170)	– (42)	– (110)	– (110)	– (89)
7	IRAS 03446+3254	250	– (89)	– (12)	– (9)	– (73)	64 (9)	– (14)	– (87)	– (18)	– (40)	– (49)	– (110)
8	LkCa 8	140	– (20)	– (17)	– (12)		– (13)	– (12)	– (64)	– (16)	– (31)	– (28)	– (120)
9	IQ Tau	140	– (45)	– (27)	– (25)		– (30)	86 (26)	– (59)	– (22)	– (19)	– (38)	– (150)
10	FX Tau	140	– (43)	– (34)	– (40)		– (22)	– (24)	– (98)	– (29)	– (30)	– (16)	– (140)
11	V710 Tau	140	– (63)	– (16)	– (12)		– (8)	– (12)	– (100)	– (15)	– (34)	– (33)	– (73)
12	DN Tau	140	– (33)	– (25)	– (27)		– (18)	– (17)	– (73)	– (18)	– (26)	– (38)	– (86)
13	CoKu Tau 3	140	– (26)	– (27)	– (20)		– (20)	– (16)	430 (69)	– (28)	– (31)	– (15)	– (61)
14	CoKu Tau 4	140	– (60)	– (34)	– (26)		– (13)	– (17)	– (110)	– (37)	– (37)	– (39)	– (100)
15	BF Ori	400	– (120)	– (58)	– (48)	– (1400)	– (53)	– (43)	– (90)	– (62)	– (33)	– (230)	– (51)
16	RR Tau	160	– (65)	– (80)	– (69)	– (750)	220 (72)	– (46)	– (86)	– (52)	– (78)	– (82)	– (74)
17	IRAS 08267-3336	400?	– (43)	– (29)	– (23)	– (85)	110 (25)	– (23)	– (72)	– (32)	– (24)	– (26)	– (32)
18	SX Cha	178	– (61)	– (28)	– (20)		– (27)	– (20)	– (49)	– (29)	– (25)	– (32)	– (38)
19	SY Cha	178	– (45)	– (17)	– (14)		– (13)	– (11)	– (64)	– (23)	– (38)	– (22)	– (58)
20	TW Cha	178	– (62)	– (24)	– (15)		– (12)	– (19)	– (73)	– (18)	– (28)	– (39)	– (46)
21	Ced 110 IRS6	178	– (73)	– (38)	50 (12)		59 (17)	– (22)	– (59)	– (36)	– (51)	– (49)	– (48)
22	B35	178	– (52)	– (14)	– (11)		– (6)	– (15)	– (48)	– (13)	– (16)	– (16)	– (60)
23	VW Cha	178	– (84)	– (83)	– (57)		340 (40)	– (56)	– (110)	– (61)	– (34)	– (97)	– (93)
24	VZ Cha	178	– (64)	– (23)	– (34)		– (28)	– (36)	– (58)	– (24)	– (38)	– (29)	– (38)
25	WX Cha	178	– (29)	– (29)	– (16)		– (18)	– (26)	620 (49)	– (27)	– (61)	– (24)	– (39)
26	ISO-Cha237	178	– (43)	– (23)	– (11)		– (23)	– (18)	– (94)	– (27)	– (36)	– (40)	– (45)
27	C7-11	178	– (28)	– (11)	– (10)		– (8)	– (12)	460 (48)	– (15)	– (36)	– (20)	– (38)
28	HM 27	178	– (38)	– (21)	– (12)		– (10)	– (23)	360 (55)	– (22)	– (50)	– (20)	– (39)
29	XX Cha	178	– (36)	– (12)	– (7)		42 (9)	– (12)	– (86)	– (14)	– (26)	– (23)	– (49)
30	HD 98922	ζ 500	– (510)	– (1200)	– (1100)		– (1600)	– (750)	– (730)	– (1100)	– (380)	– (500)	– (180)
31	HD 101412	160	– (83)	– (120)	– (110)	– (930)	– (140)	– (74)	– (120)	– (120)	– (36)	– (77)	– (66)
32	T Cha	66	– (47)	– (24)	– (26)		330 (21)	– (22)	– (48)	– (33)	– (30)	– (49)	– (50)
33	IRAS 12535-7623	178	– (63)	– (21)	– (12)		– (20)	– (13)	– (66)	– (19)	– (30)	– (25)	– (45)
34	Sz50	178	– (48)	– (19)	– (17)		– (15)	– (13)	– (43)	– (15)	– (47)	– (21)	– (80)
35	ISO-ChaII 54	178		– (15)	– (17)	– (130)	– (13)	– (11)		– (24)			
36	DL Cha	178	– (400)	– (1000)	– (2100)		– (2300)	– (1500)	– (390)	– (1100)	– (430)	– (360)	– (140)
37	HD 132947	ζ 60	– (2)	– (7)	– (18)	– (180)	– (12)	– (20)	39 (6)	– (29)	– (5)	– (4)	– (18)
38	HD 135344	140	– (150)	– (68)	– (62)		– (34)	– (45)	– (220)	– (67)	– (150)	– (140)	– (160)

Table 5.2—Continued

#	Source	Dis. [pc]	H ₂ S(0)	H ₂ S(1)	H ₂ S(2)	H ₂ S(3)	[Ne II]	[Ne III]	[Fe I]	[Fe II] 18	[Fe II] 25	[S I]	[Si II]
[1]	[2]	[3]	[4]	[5]	[6]	[7]	[8]	[9]	[10]	[11]	[12]	[13]	[14]
39	HT Lup	145	– (120)	– (110)	– (48)	– (760)	– (110)	– (75)	– (160)	– (81)	– (63)	– (100)	– (74)
40	HT Lup	145	– (200)	– (250)	– (120)	– (1100)	– (170)	– (200)	– (210)	– (260)	– (130)	– (170)	– (110)
41	GW Lup	100	– (49)	– (13)	– (6)	– (65)	– (8)	– (16)	– (47)	– (28)	– (42)	– (11)	– (29)
42	Sz73	100	– (46)	– (47)	– (41)	– (150)	180 (32)	– (43)	– (81)	– (44)	– (41)	– (44)	– (50)
43	GQ Lup	100	– (27)	– (43)	– (36)	– (230)	– (30)	– (45)	– (81)	– (57)	– (45)	– (31)	– (84)
44	IM Lup	140	– (52)	– (36)	– (21)	– (330)	71 (22)	– (37)	– (59)	– (34)	– (43)	– (27)	– (45)
45	RU Lup	140	– (150)	– (150)	– (130)	– (830)	– (100)	– (130)	– (140)	– (130)	– (110)	– (160)	– (72)
46	RY Lup	150	– (100)	– (54)	– (40)	– (490)	– (38)	– (42)	– (100)	– (120)	– (78)	– (81)	– (90)
47	EX Lup	150	– (58)	– (39)	– (35)	– (230)	– (23)	– (54)	– (94)	– (46)	– (52)	– (43)	– (110)
48	Sz102	200	– (34)	– (12)	91 (6)	600 (52)	350 (7)	– (9)	– (65)	67 (15)	– (9)	– (9)	– (24)
49	AS 205	120	– (280)	– (540)	– (390)	– (3700)	– (270)	– (450)	– (480)	– (450)	– (280)	– (310)	– (160)
50	Haro 1-1	125	– (26)	– (26)	– (17)	– (55)	– (19)	– (15)	– (43)	– (22)	– (23)	– (39)	– (52)
51	Haro 1-4	125	– (26)	– (35)	– (36)		– (25)	– (31)	– (81)	– (49)	– (38)	– (44)	– (120)
52	DoAr 24E	125	– (110)	– (140)	– (150)		– (120)	– (150)	– (170)	– (240)	– (120)	– (77)	– (98)
53	SR 21	125	– (320)	– (340)	– (61)		– (110)	– (180)	– (430)	– (410)	– (450)	– (460)	– (260)
54	IRS51	125	– (160)	– (65)	– (30)		– (47)	– (36)	– (86)	– (61)	– (110)	– (65)	– (91)
55	SR 9	125	– (53)	– (81)	– (44)		77 (24)	– (32)	– (80)	– (81)	– (38)	– (34)	– (49)
56	V853Oph	125	– (42)	– (39)	– (19)		140 (25)	– (24)	– (53)	– (31)	– (45)	– (38)	– (61)
57	ROX42C	125	– (48)	– (46)	– (23)		– (23)	– (41)	– (41)	– (39)	– (18)	– (29)	– (73)
58	ROX43A	125	– (73)	– (150)	– (75)		– (83)	– (92)	– (110)	– (120)	– (49)	– (110)	– (67)
59	IRS60	125	– (33)	– (47)	– (86)		180 (52)	– (69)	– (66)	– (50)	– (24)	– (77)	– (89)
60	Haro 1-16	125	– (48)	– (82)	– (35)		– (38)	– (51)	– (120)	– (56)	– (25)	– (72)	– (81)
61	Haro 1-17	125	– (57)	– (14)	– (7)	– (71)	22 (6)	– (6)	440 (82)	– (21)	– (35)	– (23)	– (60)
62	RNO 90	140	– (160)	– (240)	– (140)	– (870)	– (110)	– (170)	– (220)	– (180)	– (130)	– (230)	– (99)
63	Wa Oph 6	140	– (37)	– (100)	– (67)	– (470)	– (61)	– (68)	– (43)	– (47)	– (17)	– (30)	– (21)
64	V1121 Oph	125	– (56)	– (260)	– (120)	– (2200)	– (200)	– (140)	– (87)	– (280)	– (59)	– (93)	– (52)
65	HD 163296	122	– (400)	– (910)	– (510)		– (540)	– (370)	– (400)	– (800)	– (270)	– (400)	– (170)
66	HD 163296	122	– (650)	– (1400)	– (1300)		– (460)	– (1300)	– (1400)	– (1300)	– (220)	– (430)	– (350)
67	VV Ser	260	– (94)	– (250)	– (170)	– (2600)	– (140)	– (160)	– (100)	– (130)	– (73)	– (89)	– (83)
68	SSTc2d J182900.9	260		– (36)	– (30)	– (170)		– (16)	– (35)	– (52)			
69	SSTc2d J182909.8	260		– (66)	– (44)	– (340)		– (53)	– (35)	– (88)			
70	SSTc2d J182928.2	260		– (170)	– (130)	– (1500)	1100 (150)	– (160)		– (250)			
71	EC74	260	– (78)	– (12)	81 (7)	430 (55)	36 (8)	– (10)	– (62)	– (17)	– (240)	– (210)	– (94)
72	EC82	260	– (90)	– (140)	200 (38)	– (940)	– (73)	– (51)	– (190)	– (130)	– (110)	– (79)	– (110)
73	EC90	260	– (230)	– (570)	– (180)	– (6900)	– (210)	– (320)	– (270)	– (890)	– (290)	– (280)	– (210)
74	EC92	260	– (110)	– (79)	83 (20)	– (530)	120 (22)	– (49)	– (110)	– (67)	– (81)	– (76)	– (180)
75	CK4	260	– (34)	– (29)	– (18)	– (81)	– (15)	– (25)	– (47)	– (26)	– (19)	– (22)	– (62)
76	LkH α 348	260	– (55)	– (190)	– (400)	– (3100)	– (220)	– (290)	– (83)	– (760)	– (32)	– (42)	– (27)

Table 5.3. Diagnostic parameters of the disk gas contents.

# ^a	Source	$T_{\text{warm}}^{\text{b}}$ [K]	$N_{\text{warm}}^{\text{b}}$ ($r = 100 \text{ AU}$) ^c [10^{22} cm^{-2}]	$M_{\text{warm}}^{\text{b}}$ [M_{J}]	$T_{\text{hot}}^{\text{b}}$ [K]	N_{hot} ($r = 2 \text{ AU}$) ^c [10^{22} cm^{-2}]	M_{hot} [$10^{-3} M_{\text{J}}$]
1	RNO 15		< 60	< 7.4		< 82	< 4.0
2	Lk H α 270		< 35	< 4.4		< 27	< 1.4
3	Lk H α 271		< 28	< 3.5		< 25	< 1.3
4	Lk H α 326		< 34	< 4.2		< 67	< 3.3
5	Lk H α 327		< 85	< 10.6		< 137	< 6.9
6	Lk H α 330		< 130	< 16.7		< 95	< 4.7
7	IRAS 03446+3254		< 30	< 3.8		< 62	< 3.1
8	LkCa 8		< 6	< 0.7		< 10	< 0.5
9	IQ Tau		< 13	< 1.7		< 19	< 0.9
10	FX Tau		< 13	< 1.6		< 30	< 1.4
11	V710 Tau		< 12	< 1.5		< 7	< 0.4
12	DN Tau		< 9	< 1.2		< 20	< 1.0
13	CoKu Tau 3		< 7	< 1.0		< 16	< 0.8
14	CoKu Tau 4		< 18	< 2.2		< 20	< 1.0
15	BFOri		< 300	< 36.7		< 275	< 13.5
16	RR Tau		< 26	< 3.2		< 192	< 9.5
17	IRAS 08267-3336		< 110	< 13.2		< 95	< 4.7
18	SX Cha		< 30	< 3.7		< 23	< 1.2
19	SY Cha		< 21	< 2.7		< 15	< 0.8
20	TW Cha		< 30	< 3.7		< 17	< 0.9
21	Ced 110 IRS6		< 35	< 4.4		< 22	< 1.1
22	B35		< 18	< 2.2		< 11	< 0.6
23	VW Cha		< 41	< 5.1		< 77	< 3.8
24	VZ Cha		< 30	< 3.7		< 27	< 1.4
25	WX Cha		< 14	< 1.8		< 21	< 1.0
26	ISO-Cha237		< 21	< 2.6		< 14	< 0.7
27	C7-11		< 14	< 1.7		< 10	< 0.5
28	HM27		< 18	< 2.3		< 15	< 0.8
29	XX Cha		< 16	< 2.0		< 8	< 0.4
30	HD 98922		< 2300	< 280.8		< 14250	< 711.6
31	HD 101412		< 33	< 4.0		< 182	< 9.0
32	T Cha		< 3	< 0.4		< 4	< 0.2
33	IRAS 12535-7623		< 27	< 3.3		< 14	< 0.7
34	Sz50		< 23	< 2.9		< 18	< 0.9
35	ISO-ChaII 54		< 18	< 2.3		< 21	< 1.1
36	DL Cha		< 200	< 24.4		< 2250	< 111.7
37	HD 132947		< 0.1	< 0.0		< 3	< 0.2
38	HD 135344		< 45	< 5.6		< 42	< 2.1
39	HT Lup		< 39	< 4.9		< 65	< 3.2
40	HT Lup		< 64	< 7.9		< 107	< 5.3
41	GW Lup		< 5	< 0.6		< 4	< 0.2
42	Sz73		< 7	< 0.9		< 16	< 0.8

Table 5.3—Continued

# ^a	Source	$T_{\text{warm}}^{\text{b}}$ [K]	$N_{\text{warm}}^{\text{b}}$ ($r = 100 \text{ AU}$) ^c [10^{22} cm^{-2}]	$M_{\text{warm}}^{\text{b}}$ [M_{J}]	$T_{\text{hot}}^{\text{b}}$ [K]	N_{hot} ($r = 2 \text{ AU}$) ^c [10^{22} cm^{-2}]	M_{hot} [$10^{-3} M_{\text{J}}$]
43	GQ Lup		< 4	< 0.5		< 18	< 0.9
44	IM Lup		< 15	< 1.9		< 25	< 1.3
45	RU Lup		< 44	< 5.5		< 87	< 4.4
46	RY Lup		< 35	< 4.3		< 45	< 2.2
47	EX Lup		< 20	< 2.5		< 24	< 1.2
48	Sz102		< 19	< 2.3	828	62	3.1
49	AS 205		< 62	< 7.7		< 185	< 9.2
50	Haro 1-1		< 6	< 0.8		< 13	< 0.7
51	Haro 1-4		< 6	< 0.8		< 23	< 1.2
52	DoAr 24E		< 26	< 3.3		< 97	< 4.8
53	SR 21		< 77	< 9.5		< 40	< 2.0
54	IRS51		< 38	< 4.7		< 18	< 0.9
55	SR 9		< 13	< 1.6		< 30	< 1.5
56	V853Oph		< 10	< 1.2		< 12	< 0.6
57	ROX42C		< 11	< 1.4		< 15	< 0.7
58	ROX43A		< 17	< 2.2		< 50	< 2.5
59	IRS60		< 7	< 1.0		< 42	< 2.1
60	Haro 1-16		< 12	< 1.4		< 24	< 1.2
61	Haro 1-17		< 8	< 1.1		< 4	< 0.2
62	RNO 90		< 48	< 5.9		< 102	< 5.1
63	Wa Oph 6		< 11	< 1.4		< 42	< 2.2
64	V1121 Oph		< 13	< 1.7		< 55	< 2.7
65	HD 163296		< 91	< 11.2		< 325	< 16.5
66	HD 163296		< 150	< 18.3		< 800	< 39.7
67	VV Ser		< 98	< 12.1		< 775	< 38.3
68	SSTc2d J182900.9		< 98	< 12.2		< 62	< 3.0
69	SSTc2d J182909.8		< 180	< 22.3		< 150	< 7.4
70	SSTc2d J182928.2		< 470	< 57.7		< 350	< 17.6
71	EC74		< 32	< 4.0	781	87	4.4
72	EC82		< 93	< 11.5		< 190	< 9.5
73	EC90		< 240	< 29.8		< 875	< 43.6
74	EC92		< 110	< 13.8		< 80	< 3.9
75	CK4		< 35	< 4.3		< 42	< 2.1
76	Lk H α 348		< 57	< 7.0		< 1000	< 49.9

^aSource number from Tables 5.1 and 5.2.

^bIf not specified, 100 K is assumed for the warm component and 1000 K for the hot component. The derived column density and mass of the warm component depend strongly on the assumed temperature. A temperature of 150 and 200 K reduces the column density and mass by respectively a factor of ~ 30 and 140.

^cAssumed emitting source sizes for the warm and hot component to estimate a column density.

Table 5.4. Summary of data for sources with detected H₂, [Ne II], or [Fe I] emission

# ^a	Source	log <i>L</i> H ₂ S(2) [<i>L</i> _⊙]	log <i>L</i> H ₂ S(3) [<i>L</i> _⊙]	log <i>L</i> [Ne II] [<i>L</i> _⊙]	log <i>L</i> [Fe I] [<i>L</i> _⊙]	log <i>L</i> IR [<i>L</i> _⊙]	T _{star} [K]	Age [Myr]	Class	log <i>L</i> _X [erg s ⁻¹]
27	C7-11	< -5.5	-	< -5.6	-4.3	-2.1	4860	0.6	TTs	-
75	CK4	< -4.9	< -4.3	< -5.0	< -4.5	-1.6	4860	6.8	TTs	30.5
21	Ced 110 IRS6	-5.3	-	-5.2	< -4.8	-1.8	-	-	1	28.6
13	CoKu Tau 3	< -5.4	-	< -5.4	-4.6	-2.1	3800	-	CTTs	30.8
12	DN Tau	< -5.3	-	< -5.5	< -4.9	-2.1	3918	-	CTTs	30.1
52	DoAr 24E	< -4.7	-	< -4.8	< -4.6	-1.4	5160	2.0	TTs	29.8
71	EC74	-4.8	-4.0	-5.1	< -4.4	-1.9	-	-	2	30.5
72	EC82	-4.4	< -3.2	< -4.3	< -3.9	-0.9	3918	-	TTs	-
73	EC90	< -3.9	< -2.4	< -3.9	< -3.8	-0.3	-	-	TTs	31.0
74	EC92	-4.8	< -3.5	-4.6	< -4.2	-1.2	4273	-	TTs	-
37	HD 132947	< -6.2	< -5.2	< -6.4	-6.4	-3.2	10040	-	HAeBe	-
61	Haro 1-17	< -5.9	< -5.0	-6.0	-4.7	-2.6	3500	-	TTs	-
44	IM Lup	< -5.4	< -4.2	-5.4	< -5.0	-1.9	3918	0.7	TTs	-
7	IRAS 03446+3254	< -5.2	< -4.4	-4.9	< -4.3	-1.8	-	-	TTs	-
17	IRAS 08267-3336	< -4.5	< -3.9	-4.3	< -4.0	-1.1	5010	2.0	TTs	-
54	IRS51	< -5.4	-	< -5.2	< -4.9	-1.6	5570	0.8	2	30.9
59	IRS60	< -4.9	-	-5.1	< -5.0	-1.8	-	-	-	-
26	ISO-Cha237	< -5.5	-	< -5.2	< -4.6	-1.9	3918	-	TTs	29.2
2	Lk Hα 270	< -4.8	< -4.4	-4.7	< -4.4	-1.5	4273	0.01	TTs	-
3	Lk Hα 271	< -5.0	< -4.6	< -5.1	-3.7	-2.3	4860	-	TTs	-
16	RR Tau	< -4.8	< -3.7	-4.8	< -4.7	-1.4	-	0.6	HAeBe	-
53	SR 21	< -5.1	-	< -4.8	< -4.2	-1.2	6665	2.0	TTs	29.6
55	SR 9	< -5.2	-	-5.4	< -4.9	-2.0	4155	0.8	TTs	-
70	SSTc2d J182928.2	< -4.1	< -3.0	-3.6	-	-0.5	-	-	-	-
48	Sz102	-4.9	-4.1	-4.4	< -4.6	-2.2	3918	-	TTs	28.6
42	Sz73	< -5.4	< -4.9	-5.3	< -5.1	-2.1	3918	3.7	TTs	-
32	T Cha	< -6.0	-	-5.3	< -5.7	-2.8	5430	2.1	TTs	30.1
56	V853Oph	< -5.6	-	-5.2	< -5.1	-2.1	3800	0.8	TTs	-
23	VW Cha	< -4.8	-	-4.5	< -4.5	-1.6	4510	1.2	CTTs	31.0
25	WX Cha	< -5.3	-	< -5.3	-4.2	-1.9	4273	2.3	TTs	30.2
29	XX Cha	< -5.7	-	-5.4	< -4.6	-2.2	3800	14.6	TTs	-

^aSource number from Tables 5.1 and 5.2.

Chapter 6

c2d *Spitzer* IRS Spectra of Embedded Protostars: Gas-phase Lines

Abstract

We present a survey of mid-infrared pure rotational H_2 and atomic fine structure lines toward a sample of 56 young stellar objects. The sample consists of low-mass embedded protostars and edge-on disks around pre-main sequence stars selected from the *Spitzer* "From Molecular Cores to Planet Forming Disks" (c2d) legacy program on the basis of silicate absorption at $10\ \mu\text{m}$. Both spatially unresolved and extended emission is observed. The extended component on scales of several thousand AU is dominated by the [Si II] line and warm ($\lesssim 700\ \text{K}$) H_2 emission observed in the H_2 S(1) and S(2) lines. The extended emission is shown to be consistent with a photodissociation region (PDR) in the beam. The extended PDR emission is mostly observed toward sources with a low apparent optical depth of the $9.8\ \mu\text{m}$ silicate band. This suggests that the PDRs exist in a thin envelope heated by the central star or that the PDRs are heated by the external radiation field which influences the envelope characteristics. Hot H_2 emission ($T_{\text{ex}} \gtrsim 500\ \text{K}$) and emission from [Ne II] $12.8\ \mu\text{m}$, [Fe I] $24\ \mu\text{m}$, [Fe II] $18\ \mu\text{m}$, and [S I] $25.2\ \mu\text{m}$ is observed mostly toward the compact source component, and most likely results from shocked gas close to the central star. For three sources excitation temperatures of $\sim 1300 - 1500\ \text{K}$ and gas masses of $\sim (0.2 - 1) \times 10^{-3} M_{\text{J}}$ are derived, putting an upper on the size of the emitting region of $r \lesssim 50\ \text{AU}$.

Lahuis, F., van Dishoeck, E. F., Jørgensen, J. K., Blake, G. A., Evans, II, N. J 2007, in preparation

6.1 Introduction

The interstellar medium (ISM) surrounding forming stars is subject to highly energetic processes. Strong ultraviolet (UV) radiation heats the ISM to form a photon-dominated or photodissociation region (PDR) (Hollenbach et al., 1991; Hollenbach & Tielens, 1999). In the PDR layer closest to the star most molecular material is dissociated and the atomic species are ionized resulting in fine structure lines such as [O I], [Fe I], and [S I]. Further out H_2 is excited and the lower pure rotational H_2 lines become strong (e.g. Kaufman et al., 2006, applied to regions of massive star formation).

The young accreting stars produce strong stellar and/or disk winds generating a bipolar outflow cavity and entraining material. The winds impact onto the surrounding material producing supersonic shock fronts that compress and heat the gas. Two types of shocks are identified, low velocity continuous shocks, *C*-shocks, and high velocity discontinuous or ‘jump’ shocks, *J*-shocks (Hollenbach, 1997; Walmsley et al., 2005).

Low velocity shocks ($v_s \lesssim 40 \text{ km s}^{-1}$) compress the ionized material and magnetic fields ahead of the shock. The gas can be heated up to $\sim 1000 \text{ K}$ and most of the cooling is through molecular lines (e.g. Neufeld & Kaufman, 1993; Kaufman, 1995). In high velocity shocks ($v_s \gtrsim 40 \text{ km s}^{-1}$) the neutral pre-shock gas is heated through viscous heating in a thin shock front in which radiative cooling is weak. The post-shock gas can be heated up to $\sim 10,000 \text{ K}$ in which most of the molecular material is dissociated and a large fraction of the atoms are ionized resulting in strong emission lines of singly and doubly ionized atoms. Further downstream from the shock hydrogen recombines in the cooled down gas and strong emission of high-*J* pure rotational lines are expected (Hollenbach & McKee, 1989).

So far, PDRs and shocks have mostly been studied in the general ISM near massive young stars or supernova remnants. Previous observations of low mass young stars using ground-based instruments or the ISO-SWS instrument (de Graauw et al., 1996; van den Ancker, 1999) either lacked the sensitivity or spatial resolution to separate the various emitting regions. The sensitive InfraRed Spectrograph (IRS) (Houck et al., 2004) on board the *Spitzer* Space Telescope (Werner et al., 2004) brings the detection of the mid-IR H_2 pure rotational and atomic fine structure lines within reach for young solar mass stars in nearby star forming regions. The combination of high sensitivity, moderate spectral resolution $R = \lambda/\Delta\lambda = 600$, and modest spatial resolution makes *Spitzer* well suited for the study of the gas in the ISM around low-mass young stars in nearby ($\lesssim 300 \text{ pc}$) clouds. These lines can help to identify the heating processes, PDR or shock-driven, taking place.

A general complication in the interpretation of emission from the environments of young embedded stars are contributions from multiple unrelated processes along the line of sight. In particular emission of the extended (remnant) envelope on scales of $10,000 \text{ AU}$ and the small inner envelope near the young star on scales of $< 1000 \text{ AU}$ trace completely distinct physical processes. The *Spitzer* IRS beam in principle makes it possible to resolve structures up to $\sim 1000 \text{ AU}$ in size for nearby star forming regions at distances up to a few hundred pc. However, the IRS full-slit extraction for the high resolution echelle modules and the fixed-width extraction for the low resolution long-slit modules do not allow a separation of extended envelope and small-scale emission.

We present here an overview of the mid-IR gas-phase lines detected in embedded sources and edge-on circumstellar disks observed in the *Spitzer* legacy program “From Molecular Cores to Planet Forming Disks” (“Cores to Disks” or c2d) (Evans

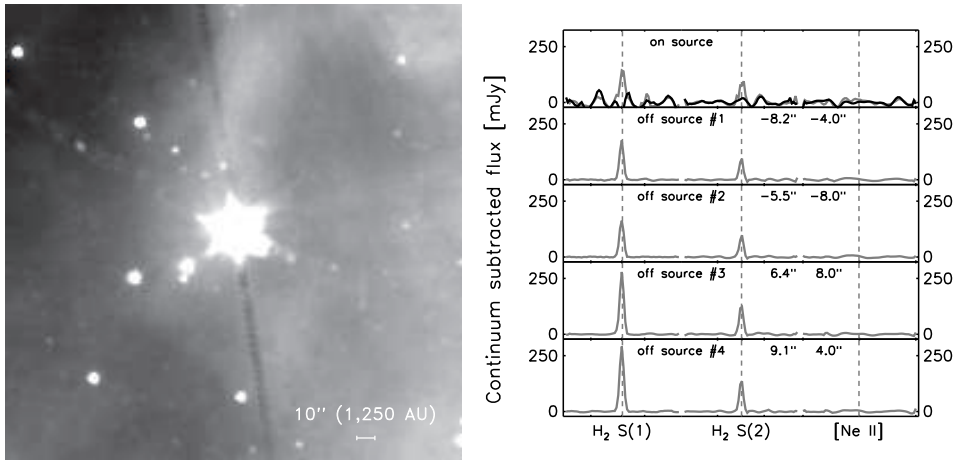


Figure 6.1 SH minimap observed around VSSG1 in Ophiuchus. The left plot displays an IRAC image at $4.5 \mu\text{m}$ (including the high excitation H_2 S(9), S(10) and S(11) lines) showing the star plus diffuse extended emission. The right plot shows the observed emission of the on-source observation (top panel) and the off-source observations from the minimap. In gray the total observed emission and in black the unresolved source emission toward VSSG1.

et al., 2003), which has collected a large sample of IRS spectra toward sources in the nearby Chamaeleon, Lupus, Perseus, Ophiuchus, and Serpens star-forming regions. High-S/N spectra have been obtained within the $5 - 38 \mu\text{m}$ range for 226 sources at all phases of star and planet formation up to ages of ~ 5 Myr. The observations presented in this chapter show the results of an optimal extraction method, developed by the c2d team, which does allow the separation of both spatial components within the IRS aperture. We will demonstrate the importance of being able to do so for the study of young embedded objects. In Section 6.2 the source selection and data reduction are explained. In Section 6.3 the observed atomic fine-structure and H_2 emission lines and the derived parameters are presented. In Section 6.4 the results are reviewed in the context of PDR and shock heating.

6.2 Observations and data reduction

A description of the c2d program is included in §3.1 and §5.2. The 56 sources presented in this chapter were all selected for showing the $10 \mu\text{m}$ silicate band in absorption. This criterion includes embedded Class 0 and Class I sources plus edge-on disk (Class II) sources ($i \gtrsim 65$ degrees) which were excluded from the gas-disk study presented in Lahuis et al. (2007) such as CRBR 2422.8-3423 (Pontoppidan et al., 2005) and IRS 46 (Lahuis et al., 2006b). The selected sources are listed in Table 6.1 which gives the basic observing and source parameters and the adopted distances. Note that in most cases, it is not possible to determine whether the infrared source is dominated by an envelope or a disk without spatially resolved infrared or (sub)millimeter data. Known or candidate edge-on disks are labeled in the table. Even though the majority of the remaining sources are thought to be embedded protostars, there may be additional cases dominated by an edge-on disk.

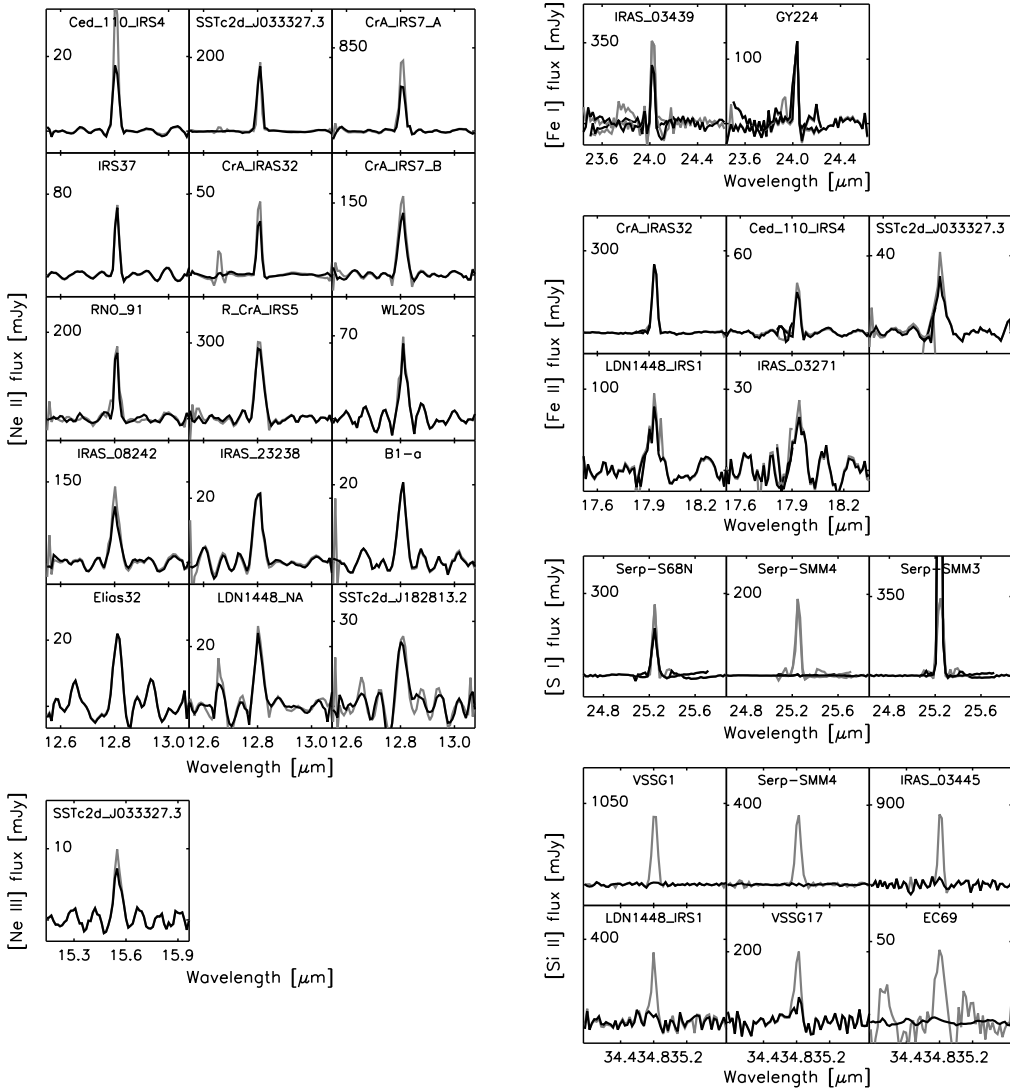


Figure 6.2 Detections of [Ne II], [Ne III], [Fe I], [Fe II] $18\mu\text{m}$, [S I] and [Si II] at the $\geq 4\sigma$ level toward the c2d sample of embedded T Tauri stars and T Tauri stars with edge-on disks. Plotted in gray is the total observed emission (compact source + extended component) and in black the emission after correction of the estimated sky component.

A major concern in the analysis of observations toward these young stars is the confusion of compact source and extended emission. The c2d team has developed an optimal extraction (see §3.2.2.2) which allows the separation of both components in the IRS apertures. §5.3 describes the data reduction of both the observations presented in Chapter 5 and this chapter. §5.2.2 describes the mini-maps used to confirm the presence of extended emission and to verify the extended emission components observed with the optimal extraction. Figure 6.1 gives an example of one of the observed minimaps toward VSSG1, one of the embedded sources presented in this chapter.

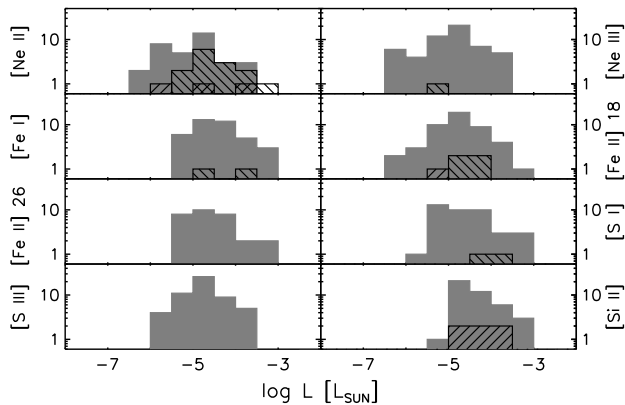


Figure 6.3 Observed line strengths in solar luminosities (hatched bars) and upper limits (solid gray bars) of the major atomic lines. The gray bars include sources without a line detection. The hatched left angled bars are detections of unresolved source emission while the right angled hatched bars are detections of extended line emission.

6.3 Results

6.3.1 Atomic fine-structure lines

Figure 6.2 presents the observed atomic fine-structure lines toward the 56 sources in our sample, while Figure 6.3 shows the distribution of the observed line fluxes and upper limits of the major lines. The gray bars reflect the 4σ upper limits, while the hatched bars represent the detections. Line fluxes for the unresolved and extended components and line flux upper limits are listed in Table 6.2.

Emission lines of [Ne II], [Ne III], [Fe I], [Fe II] $18\mu\text{m}$ (the [Fe II] $26\mu\text{m}$ line is not detected), [S I], and [Si II] are observed toward $\sim 35\%$ of the sources. Of these $\sim 25\%$ show emission from more than one line. The [Ne II], [Ne III], [Fe I], and [Fe II] emission are predominantly unresolved spatially. The [Si II] emission, observed toward $\sim 10\%$ of the sources, is on the other hand always extended. No 4σ detections of [Fe II] $26\mu\text{m}$ and [S III] have been made. The upper limits are of the same order as the line fluxes of the detections (see Figure 6.3).

6.3.2 Molecular hydrogen

Figure 6.4 shows the detections of H_2 emission lines toward the 56 sources in our sample. Except for the H_2 S(0) and S(6) lines all lines observable with the *Spitzer* IRS have been observed toward one or more sources. The H_2 line fluxes for the unresolved and extended components and the line flux upper limits are listed in Table 6.3.

The warm gas ($T_{\text{ex}} \sim 100 - 300$ K traced by the lower rotational lines) is mostly extended. The highest rotational lines ($J = 5$ and 7) are observed toward two sources, IRAS 03271+3013 and SSTc2d J033327.3+310710 and trace hot ($T_{\text{ex}} \sim 1000 - 1500$ K) gas. For $J \geq 5$ no estimate of extended emission is available because the IRS is undersampled at these wavelength and the optimal extraction does not work. Since the $J = 2, 3$, and 4 lines of both sources are mostly unresolved, the observed $J = 5$ and 7 lines are assumed to be unresolved as well in our further analysis.

Care should be taken with the $J = 4$ lines. This line is located near the edge of SL order 1 and is most sensitive to artifacts. Some of the lines presented in Figure 6.4 may therefore be suspect.

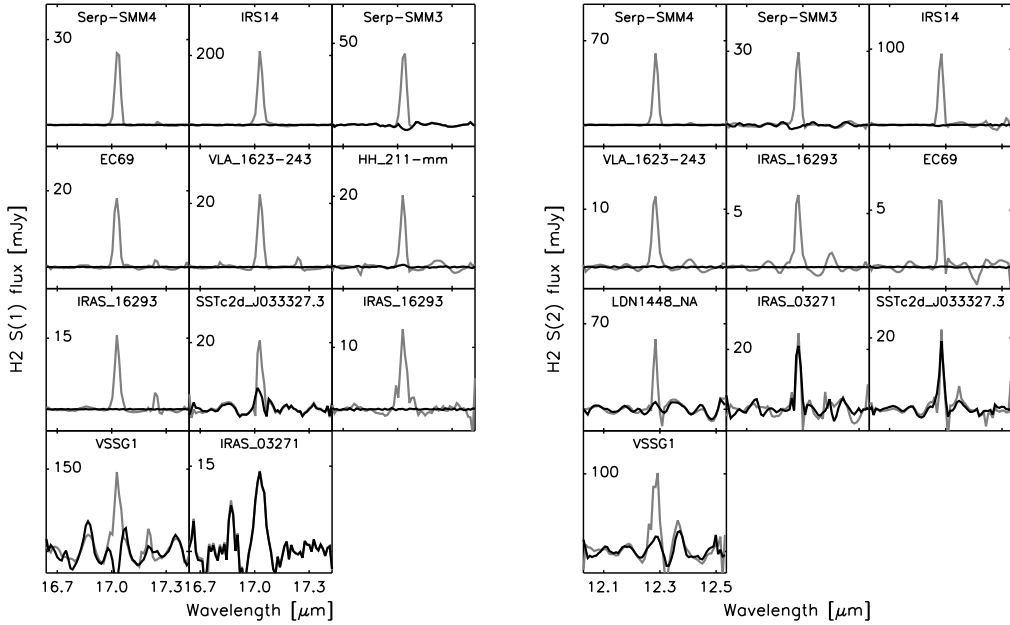


Figure 6.4 Detections of H_2 emission lines at the $\geq 5\sigma$ level toward the c2d sample of embedded T Tauri stars or T Tauri stars with edge-on disks. Plotted in gray is the total observed emission (compact source + extended component) and in black the emission after correction of the estimated sky component. For H_2 S(5) and S(7) no extended emission estimates are available.

In the simplest analysis, the H_2 excitation is assumed to be in local thermal equilibrium (LTE) (e.g., Thi et al., 2001) with an ortho-to-para ratio determined by the kinetic temperature of the gas (following Sternberg & Neufeld, 1999). For gas temperatures 100, 150, and ≥ 200 K, the ortho-to-para ratios are 1.6, 2.5, and 3, respectively. Assuming optically thin emission, the integrated flux of a rotational line $J_u \rightarrow J_l$ for a given temperature T_{ex} is

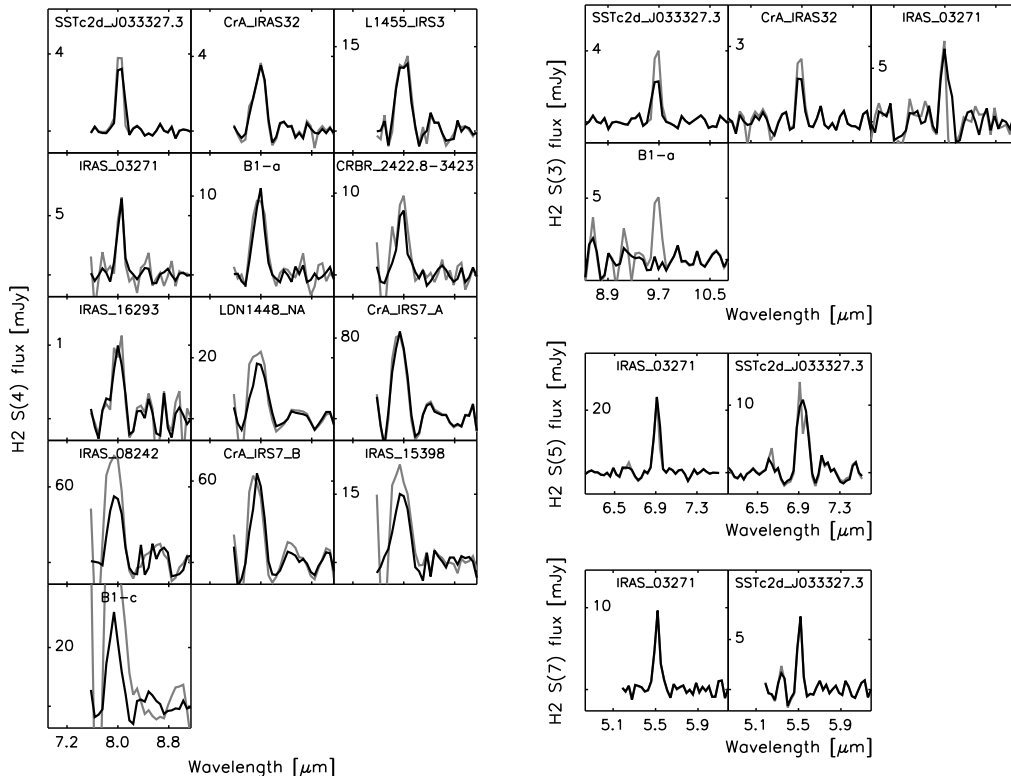
$$F_{ul}(T_{\text{ex}}) = \frac{hc}{4\pi\lambda} N(\text{H}_2) A_{ul} x_u(T_{\text{ex}}) \Omega \text{ erg s}^{-1} \text{ cm}^{-2}, \quad (6.1)$$

where λ is the wavelength of the transition, $N(\text{H}_2)$ the total column density, A_{ul} the spontaneous transition probability, and Ω the source size. For high enough densities ($n \gtrsim 10^3 \text{ cm}^{-3}$), the population x_u follows the Boltzmann law

$$x_u(T_{\text{ex}}) = \frac{g_N(2J_u + 1)e^{-E_J/kT_{\text{ex}}}}{Q(T_{\text{ex}})} \quad (6.2)$$

where E_J is the energy of the upper level, g_N is the nuclear statistical weight (1 for para and 3 for ortho H_2), and $Q(T_{\text{ex}})$ the partition function for the given excitation temperature T_{ex} .

Using the above equations, excitation temperatures, column densities and H_2 gas masses, or limits on these, can be derived from the observed line fluxes and upper limits. If either S(0) or S(1) are detected, an upper or lower limit on the temperature of



– Figure 6.4 continued –

the warm gas is derived, but if neither are detected a temperature of 100 K is assumed for the warm gas. If two or more higher excitation lines (S(2) and higher) are detected an additional temperature for the hot component is derived; otherwise a temperature of 1000 K is assumed for this component. This is done for both spatial components. For five sources a temperature for the extended component can be derived (see §6.4.1.2 and Figure 6.8) and for three sources a temperature of the hot component spatially unresolved component can be derived (see §6.4.3 and Figure 6.10).

The column density averaged over the IRS aperture is derived from the above equations, given the distance to the source. For all unresolved source emission the emitting source size is smaller than the IRS aperture (Sec. 5.3) and since this is unknown a typical size $r = 50$ AU is assumed (see Section 6.4.3) for the emitting region (the derived column density scales as $1/r^2$). The fitted or assumed excitation temperature plus the (upper level) column densities give a total column density or upper limit thereof, which in turn gives the total H_2 gas mass in Jovian masses, $M = \pi r^2 \times N \times 2m_H/M_J$ with $m_H = 1.674 \cdot 10^{-24}$ gr and $M_J = 1.9 \cdot 10^{30}$ gr. Note that the derived gas mass is independent of the assumed beam or source size. The derived H_2 parameters of the unresolved source component for both the warm and hot gas are listed in Table 6.4.

Figure 6.6 shows the distribution of the derived H_2 masses for assumed excitation temperatures of 100 K and 1000 K. The gray bars are upper limits on the gas mass. The hatched bars include sources with H_2 detected. Sources with the S(1) line detected are

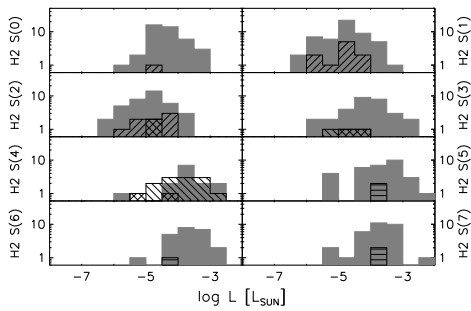


Figure 6.5 Observed H₂ line strengths in solar luminosities (hatched bars) and upper limits (solid gray bars). The gray bars include sources without a line detection. The hatched left angled bars are detections of unresolved source emission while the right angled hatched bars are detections of extended line emission. The horizontal hatched bars indicate that for these lines the optimal extraction does not work and hence no unresolved or extended classification can be assigned.

included in the 100 K distribution and sources with any of the higher J lines detected are included in the 1000 K distribution.

6.3.3 Correlations

Figure 6.7 shows the observed line strengths as functions of the apparent optical depth of the $9.8\mu\text{m}$ SiO band estimated from the *Spitzer* IRS spectra. The panels on the left show the observed extended emission. Both the detected [Si II] and the H₂ S(1) and S(2) lines are concentrated toward sources with a low optical depth, $\tau_{9.8} \lesssim 1$ (see §6.4.1.2). The detected H₂ S(4), [Ne II] and [Fe II] $18\mu\text{m}$ lines are more evenly spread with $\tau_{9.8}$. No similar line strength correlation or separation in the distribution is found for other parameters such as the mid-IR luminosity or the mid-IR spectral slope.

6.4 Discussion

Atomic fine structure lines and H₂ pure rotational emission lines are detected toward approximately half of the sources. Both unresolved and extended emission is observed. The unresolved emission is dominated by [Ne II], [Fe II] $18\mu\text{m}$, and high- J H₂ emission lines, while the extended emission is dominated by emission of [Si II] and H₂ S(1) and S(2) emission lines. In the following sections we will compare the observations with shock and PDR models.

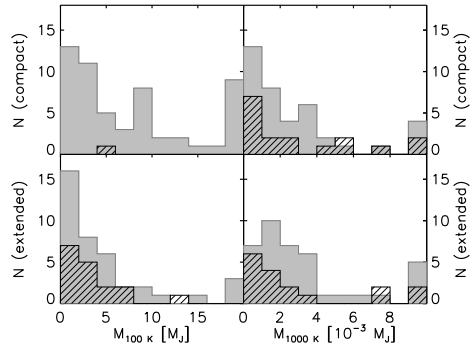


Figure 6.6 Distribution of H₂ masses for both the compact and the extended component assuming $T_{\text{ex}} = 100$ and 1000 K. The gray bars represent upper limits on the gas mass, while the hatched bars indicate sources where H₂ is detected at 4σ or more. For 100 K this includes sources with the H₂ S(1) line detected and for 1000 K sources with any of the higher J lines detected. The highest bar also includes all sources with masses higher than the upper plot limit.

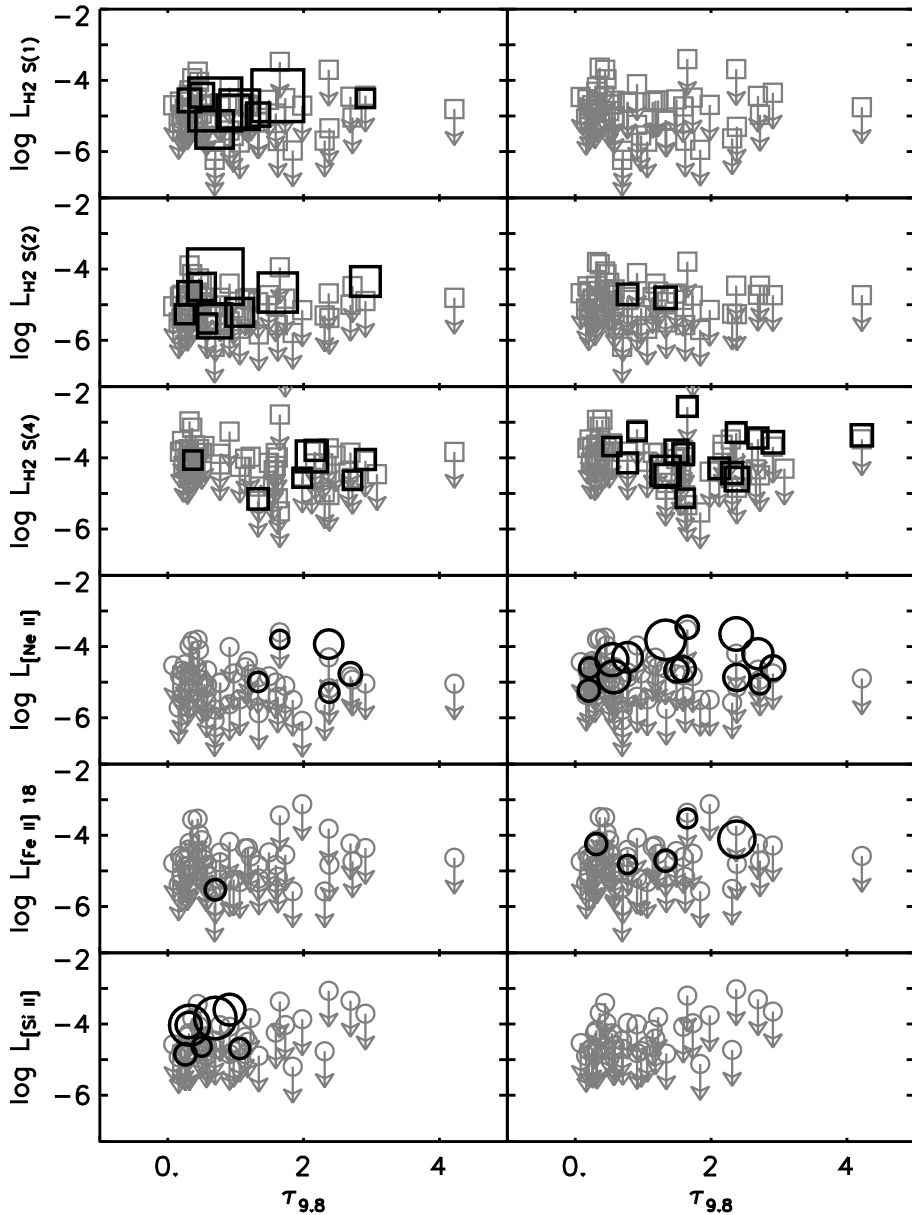


Figure 6.7 Observed line strengths and upper limits (in solar luminosities) as functions of the apparent silicate optical depth estimated from the IRS spectra. The left panel displays the extended emission component, the right the spatially unresolved component. Plotted with the black symbols are the line detections (at 4σ for H_2 and 3σ for the atomic lines), while plotted with small gray symbols and arrows are the upper limits for all non-detections. The size of the black symbols is proportional to the line $\text{SNR}^{1/3}$.

6.4.1 Extended emission

[Si II] and H₂ S(1) and S(2) are the strongest emission lines detected in the spatially extended emission. The observed line fluxes range from $\sim (0.1 - 2) \times 10^{-13} \text{ erg cm}^{-2} \text{ s}^{-1}$ for [Si II] and $\sim (0.01 - 1) \times 10^{-13} \text{ erg cm}^{-2} \text{ s}^{-1}$ for H₂. For the fully extended emission from IRS this corresponds to $\sim 2 \times 10^{-6} - 4 \times 10^{-5} \text{ erg cm}^{-2} \text{ s}^{-1} \text{ sr}^{-1}$ for [Si II] and $\sim 10^{-6} - 10^{-4} \text{ erg cm}^{-2} \text{ s}^{-1} \text{ sr}^{-1}$ for H₂ given the IRS apertures of ~ 230 and 60 arcsec^2 , assuming filling factors of unity.

For a number of sources both the H₂ S(1) and S(2) lines are observed. Figure 6.8 shows the excitation diagrams for five embedded sources. The excitation temperatures derived from both lines, assuming a single component, range from $\sim 350 - 700 \text{ K}$.

6.4.1.1 Shock excitation

[Si II] is predicted to be one of the strongest mid-IR lines for low velocity $\lesssim 40 \text{ km s}^{-1}$ shocks (Hollenbach & McKee, 1989). For moderate density gas ($n \sim 10^3 \text{ cm}^{-3}$) the predicted line intensity is comparable to the observed line strengths. However the predicted H₂ $J = 0, 1$ and 2 line strengths are orders of magnitude lower. Higher H₂ line strengths are predicted for higher densities. However, for higher densities other fine structure lines such as [S I] and [Fe II] become stronger and would have been detected given the current sensitivity. A shock origin of the spatially extended [Si II] and H₂ emission is therefore unlikely.

6.4.1.2 PDR excitation

Models of photodissociation regions (PDRs) predict line strengths for [Si II] and H₂ S(1) and S(2) comparable to the observed line strengths for $n \sim 10^2 - 10^5 \text{ cm}^{-3}$ and a radiation field of $\sim 10^1 - 10^3 G_0$ (Hollenbach et al., 1991; Kaufman et al., 2006). The predicted line strengths for [Fe II] and H₂ S(0) are $\sim 5 - 10$ times weaker, consistent with their non-detection in our sample. The H₂ excitation temperatures of $\sim 350 - 700 \text{ K}$ (see Figure 6.8) are consistent with gas surface temperatures for PDRs with the range of densities and radiation fields mentioned above (Kaufman et al., 1999, and the PDRT¹).

The extended [Si II] and H₂ S(1) and S(2) emission is observed more toward sources with low extinction ($\tau_{9.8} \lesssim 1$ or $A_v \lesssim 18$). Two PDR heating scenarios are possible. The first is that the PDRs in the extended envelope are heated by the internal sources and can therefore only be seen for sources with a thin envelope. The second possibility is that the PDRs are on the outer surface of the envelope heated by the external radiation field. The fact that the PDRs are preferentially seen toward low extinction sources could then imply that the environment, among others a strong radiation field, is determining the envelope characteristics of the embedded sources.

6.4.2 Spatially unresolved emission

Spatially unresolved emission is observed in [Ne II], [Fe I], [Fe II], [S I], and H₂. Most unresolved H₂ emission is seen in the H₂ S(4) line suggesting the presence of hot ($T_{\text{ex}} \gtrsim 500 \text{ K}$) gas. For two embedded sources, IRAS 03271+3013 and SSTc2d J033327.3+310710,

¹Photo Dissociation Region Toolbox <http://dustem.astro.umd.edu/pdrt/>

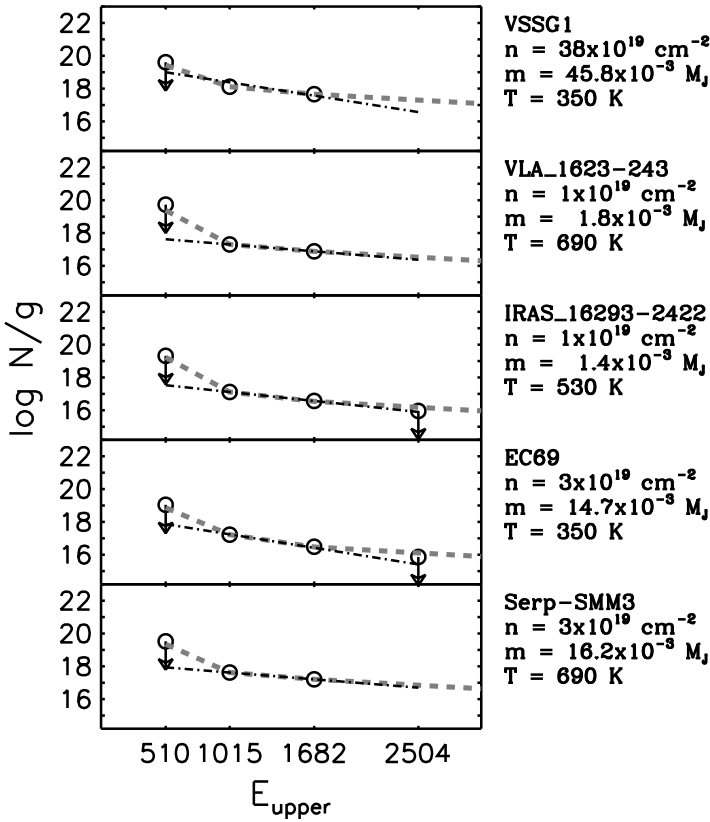


Figure 6.8 Excitation diagrams for five of the sources with multiple extended H_2 emission. The black dash-dot line shows a single temperature fit to the detected S(1) and S(2) emission. The upper limits on S(0) do not exclude the presence of colder ($T_{\text{ex}} \sim 100 \text{ K}$) gas. The gray dashed line is a fit to both detections and upper limits assuming the two temperatures of 100 K and 1000 K used in Table 6.4.

emission up to the S(7) line is observed. Excitation temperatures of $\sim 1300 - 1500 \text{ K}$ are derived for these sources (see §6.4.3).

The detection of strong atomic lines and hot H_2 suggests the presence of high velocity J -shocks (Hollenbach & McKee, 1989). The observed line fluxes of $\sim 10^{-14} - \text{few} \times 10^{-13}$ for a source unresolved for IRS corresponds to line strengths in the range of $\sim 10^{-4} - 10^{-3} \text{ erg cm}^{-2} \text{ s}^{-1} \text{ sr}^{-1}$ or more. This is consistent with the typical line strength predicted for high velocity ($v_s \gtrsim 50 \text{ km s}^{-1}$) shocks for $n \gtrsim 10^5 \text{ cm}^{-3}$.

Figure 6.9 shows the line ratios of [Ne II] with other atomic and H_2 lines plus the ratios derived from the models presented in Hollenbach & McKee (1989). This shows that the observed line flux ratios and the lower limits for most sources are consistent with those predicted by high velocity J -shocks. The limited number of multiple line detections for individual sources prohibits a more quantitative characterization of the observed shock phenomena, however.

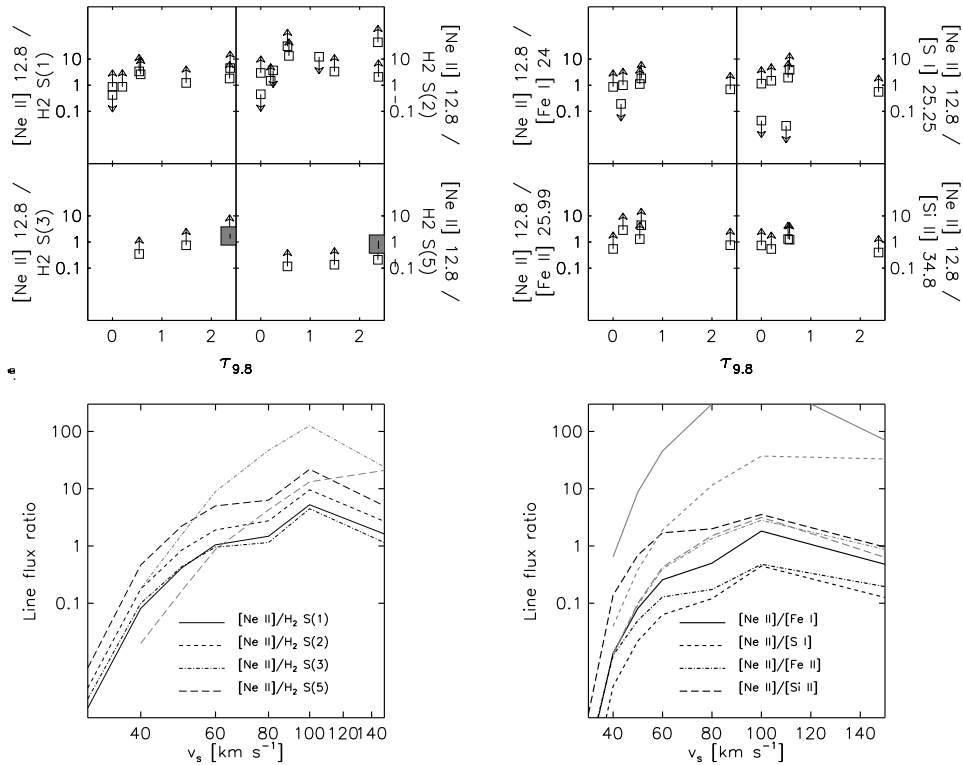


Figure 6.9 [Ne II] line ratios as function of the apparent silicate optical depth. Large filled symbols are used for sources with both [Ne II] and the second line detected. Small open symbols with arrows indicate upper limits or lower limits of the line ratios. The lower two plots show the ratios from shock models by Hollenbach & McKee (1989).

6.4.3 Hot H₂

Toward three sources a temperature of the hot ($T_{\text{ex}} \sim 1300 - 1500$ K) H₂ component can be derived. Figure 6.10 shows the excitation diagrams for these sources. Since the emission is unresolved and no size for the hot gas emitting region is known, a source size has to be assumed to derive a column density. It should be noted that for all three sources the H₂ S(3) ($E_u = 2504$ K) line appears to be weaker than expected given the observed fluxes and upper limits of the other H₂ lines. The S(3) line coincides with the SiO 9.8 μm feature, therefore its reduced line strength shows the emitting region is embedded and located near the central star rather than near the outer surface of the envelope.

For CrA IRAS32 only the S(3) and S(4) lines are observed giving an added uncertainty on the derived excitation temperature. The excitation temperature can however not be higher given the upper limits of the S(5) to S(7) lines. This again illustrates the effect of extinction on the S(3) line. A lower limit of $T_{\text{ex}} \sim 1000$ K is obtained from the upper limits on the S(1) and S(2) lines. This gives an upper limit on the column density and mass of $N \sim 1 \times 10^{20} \text{ cm}^{-2}$ and $M \sim 0.015 M_{\text{J}}$.

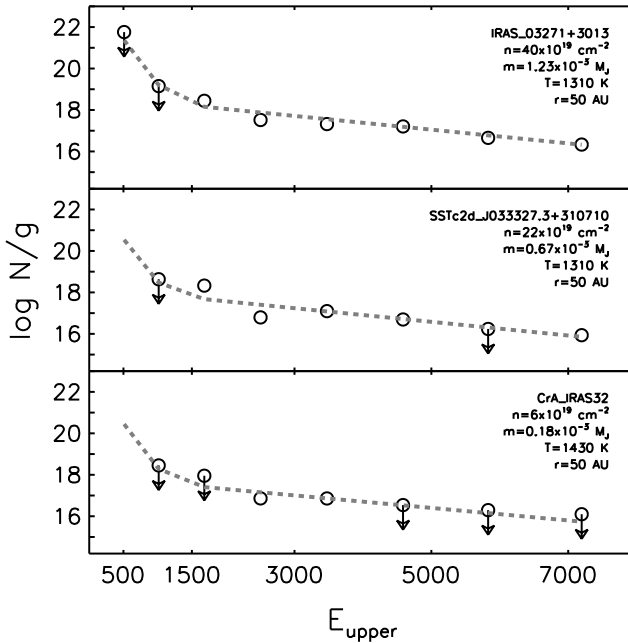


Figure 6.10 Excitation diagrams of the sources revealing hot spatially unresolved H_2 emission. A source size for the emitting region of $r = 50$ AU is assumed to obtain an estimate of the column density. The dashed line shows the fit assuming 100 K for the warm component.

The observed gas masses of a few $10^{-3} M_J$ imply an emission area $r \lesssim 50$ AU assuming a density $n \gtrsim 10^5 \text{ cm}^{-3}$, as suggested by the shock models. It is therefore possible that the observed unresolved emission lines are tracing shocks associated with the base of the outflows close to the embedded star, or shocks due to the accretion onto the disk. The reduced S(3) line strength suggesting a large extinction toward the emitting region is consistent with this. An origin through shocks in the extended envelope as a result of the outflow seems less likely given the small surface area of the emission and the extinction observed through the S(3) line.

6.5 Conclusions

A survey of the mid-infrared gas phase pure rotational lines of molecular hydrogen and a number of atomic fine structure transitions has been carried out toward a sample of 56 embedded protostars and edge-on circumstellar disks with the *Spitzer* IRS. Both spatially resolved and unresolved emission has been detected toward multiple sources. The principal findings include:

- [Ne II], [Fe I], [Fe II], and [Si I] emission is observed predominantly as compact emission toward $\sim 35\%$ of the sources. In contrast, [Si II] is only observed from the extended component.
- The lower pure rotational H_2 emission lines, S(1) and S(2) are detected mostly as extended emission while S(3) and S(4) emission is mostly unresolved.
- The extended [Si II] and warm H_2 emission ($T_{\text{ex}} \lesssim 700$ K) likely originates in a photodissociation region, or PDR, associated with the extended envelope.

- The PDRs are concentrated toward sources with a low apparent optical depth of the $9.8\mu\text{m}$ silicate band ($\tau_{9.8} \lesssim 1$ or $A_v \lesssim 18$). This suggests the PDRs exist in a thin envelope heated by the central star or the PDRs are heated by the external radiation field which influences the envelope characteristics.
- The spatially unresolved atomic fine structure and H_2 lines are consistent with an origin in high velocity J -shocks.
- The observed masses of the hot shocked gas set a size limit to the emitting regions of $r \lesssim 50$ AU suggesting suggesting that the shocks are associated with the outflow base close to the star, or shocks due to the accretion onto the disk.
- Intuitively, spatially unresolved PDR emission from the inner envelope and extended shock emission from the outflow impacting on the envelope would be expected. This is not observed. On the contrary, we observe extended PDR emission and unresolved shock emission.

The sources revealing atomic fine structure line emission and H_2 emission are excellent candidates for follow up with future near-IR and far-IR instruments. Higher spectral and spatial resolution constraints on the mid-IR line emission plus the major cooling lines of [OI] and [CII] in the far-IR, will be important to test the proposed excitation mechanisms of the observed emission. Spectrally resolved line profiles can further distinguish shocks from PDRs whereas high spatial resolution subarcsec data can confirm our conclusions on compact versus extended emission.

Acknowledgements

Astrochemistry in Leiden is supported by a NWO Spinoza grant and a NOVA grant. Support for this work, part of the Spitzer Legacy Science Program, was provided by NASA through contract 1224608 issued by the Jet Propulsion Laboratory, California Institute of Technology, under NASA contracts 1407, 1256316, and 1230779. We thank the Lorentz Center in Leiden for hosting several meetings that contributed to this paper.

Table 6.1. Source list

#	Source	RA	Dec	AOR	tint [s] (SL/SH/LH)/ndith.	D ^a [pc]
1	LDN1448 IRS1	3 ^h 25 ^m 09 ^s .4	30° 46' 21".7	5656832	(14*1/31*2/60*1)*2	250
2	LDN1448 NA	3 ^h 25 ^m 36 ^s .5	30° 45' 21".2	5828096	(60*1/121*2/60*1)*2	250
3	IRAS 03245+3002	3 ^h 27 ^m 39 ^s .0	30° 12' 59".4	6368000	(14*4/31*4/60*1)*2	250
4	L1455 SMM1	3 ^h 27 ^m 43 ^s .2	30° 12' 28".8	15917056	(60*2/121*2/-)*2	250
5	L1455 IRS3	3 ^h 28 ^m 00 ^s .4	30° 08' 01".3	15917568	(14*4/121*2/-)*2	250
6	IRAS 03254+3050	3 ^h 28 ^m 34 ^s .5	31° 00' 51".1	11827200	(14*2/31*2/60*1)*2	250
7	IRAS 03271+3013	3 ^h 30 ^m 15 ^s .2	30° 23' 48".8	5634304	(14*2/31*4/60*1)*2	250
8	IRAS 03301+3111	3 ^h 33 ^m 12 ^s .8	31° 21' 24".1	5634560	(14*1/6*2/14*2)*2	250
9	B1-a	3 ^h 33 ^m 16 ^s .7	31° 07' 55".2	15918080	(14*4/31*2/-)*2	250
10	B1-c	3 ^h 33 ^m 17 ^s .9	31° 09' 31".0	13460480	(14*2/31*2/-)*2	250
11	SSTc2d J033327.3+310710	3 ^h 33 ^m 27 ^s .3	31° 07' 10".2	15918336	(60*3/121*2/-)*2	250
12	HH 211-mm	3 ^h 43 ^m 56 ^s .8	32° 00' 50".4	5826304	(-/31*2/60*2)*2	250
13	IRAS 03439+3233	3 ^h 47 ^m 05 ^s .4	32° 43' 08".4	5635072	(14*1/121*2/60*1)*2	250
14	IRAS 03445+3242	3 ^h 47 ^m 41 ^s .6	32° 51' 43".9	5635328	(14*1/6*2/14*1)*2	250
15	IRAS 08242-5050	8 ^h 25 ^m 43 ^s .8	-51° 00' 35".6	5638912	(14*1/6*2/14*1)*2	460
16	IRAS 08261-5100	8 ^h 27 ^m 38 ^s .9	-51° 10' 37".2	5638912	(14*1/6*2/14*1)*2	400
17 ^b	Ced 110 IRS4	11 ^h 06 ^m 46 ^s .6	-77° 22' 32".5	5639680	(-/121*2/60*2)*2	178
18	IRAS 12553-7651	12 ^h 59 ^m 06 ^s .6	-77° 07' 40".1	9830912	(14*1/31*1/60*1)*2	178
19	IRAS 13546-3941	13 ^h 57 ^m 38 ^s .9	-39° 56' 00".2	5642752	(14*1/31*2/60*1)*2	630
20	IRAS 15398-3359	15 ^h 43 ^m 02 ^s .3	-34° 09' 06".8	5828864	(14*2/31*6/60*1)*2	100
21	VSSG1	16 ^h 26 ^m 18 ^s .9	-24° 28' 19".6	5647616	(-/31*1/14*2)*2	125
22 ^b	GSS30-IRS1	16 ^h 26 ^m 21 ^s .4	-24° 23' 04".2	5647616	(-/31*1/14*2)*2	125
23	GY23	16 ^h 26 ^m 24 ^s .1	-24° 24' 48".2	5647616	(-/31*1/14*2)*2	125
24	VLA 1623-243	16 ^h 26 ^m 26 ^s .4	-24° 24' 30".2	9828096	(-/121*4/60*4)*2	125
25	IRS14	16 ^h 26 ^m 31 ^s .0	-24° 31' 05".2	12664576	(60*2/31*1/-)*2	125
26	WL12	16 ^h 26 ^m 44 ^s .2	-24° 34' 48".4	5647616	(-/31*1/14*2)*2	125
27	OphE-MM3	16 ^h 27 ^m 05 ^s .9	-24° 37' 08".0	6370816	(60*5/31*8/60*2)*2	125
28	GY224	16 ^h 27 ^m 11 ^s .2	-24° 40' 46".6	9829888	(-/31*2/14*2)*2	125
29	WL19	16 ^h 27 ^m 11 ^s .7	-24° 38' 32".3	9829888	(-/31*2/14*2)*2	125
30	WL20S	16 ^h 27 ^m 15 ^s .6	-24° 38' 45".6	9829888	(-/31*2/14*2)*2	125
31	IRS37	16 ^h 27 ^m 17 ^s .6	-24° 28' 56".6	5647616	(-/31*1/14*2)*2	125
32	WL6	16 ^h 27 ^m 21 ^s .8	-24° 29' 53".2	5647616	(-/31*1/14*2)*2	125
33 ^b	CRBR 2422.8-3423	16 ^h 27 ^m 24 ^s .6	-24° 41' 03".1	9346048	(14*1/121*1/241*2)*2	125
34	Elias32	16 ^h 27 ^m 28 ^s .4	-24° 27' 21".2	12664320	(-/31*2/60*2)*2	125
35 ^b	IRS46	16 ^h 27 ^m 29 ^s .4	-24° 39' 16".2	9829888	(-/31*2/14*2)*2	125
36	VSSG17	16 ^h 27 ^m 30 ^s .2	-24° 27' 43".6	5647616	(-/31*1/14*2)*2	125
37	IRS63	16 ^h 31 ^m 35 ^s .7	-24° 01' 29".6	9827840	(-/31*1/14*1)*2	125
38	L1689-IRS5	16 ^h 31 ^m 52 ^s .1	-24° 56' 15".4	12664064	(-/31*1/60*1)*2	125
39	IRAS 16293-2422B	16 ^h 32 ^m 22 ^s .6	-24° 28' 32".2	15735808	(60*1/121*4/60*4)*2	125
40	IRAS 16293-2422	16 ^h 32 ^m 22 ^s .9	-24° 28' 36".1	11826944	(60*1/121*4/60*4)*2	125
41 ^b	RNO 91	16 ^h 34 ^m 29 ^s .3	-15° 47' 01".3	5650432	(14*1/31*1/14*2)*2	140
42	SSTc2d J182813.2+00313	18 ^h 28 ^m 13 ^s .2	0° 03' 13".0	13210368	(14*1/31*2/-)*2	260
43	SSTc2d J182849.4+00604	18 ^h 28 ^m 49 ^s .4	-0° 06' 04".7	13210624	(14*1/31*1/-)*2	260
44	SSTc2d J182901.8+02954	18 ^h 29 ^m 01 ^s .8	0° 29' 54".2	13210112	(14*1/31*2/-)*2	260
45	SSTc2d J182914.8+00424	18 ^h 29 ^m 14 ^s .8	-0° 04' 23".9	13210112	(14*1/31*2/-)*2	260
46	SSTc2d J182916.2+01822	18 ^h 29 ^m 16 ^s .2	0° 18' 22".7	13210112	(14*1/31*2/-)*2	260
47	Serp-S68N	18 ^h 29 ^m 48 ^s .1	1° 16' 42".6	9828608	(-/121*4/60*4)*2	260
48	EC69	18 ^h 29 ^m 54 ^s .4	1° 15' 01".8	9407232	(14*1/121*1/60*2)*2	260
49	Serp-SMM4	18 ^h 29 ^m 56 ^s .6	1° 13' 15".2	9828608	(-/121*4/60*4)*2	260
50	EC88	18 ^h 29 ^m 57 ^s .6	1° 13' 00".5	9407232	(14*1/121*1/60*2)*2	260
51	Serp-SMM3	18 ^h 29 ^m 59 ^s .2	1° 14' 00".2	9828608	(-/121*4/60*4)*2	260
52	R CrA IRS5	19 ^h 01 ^m 48 ^s .0	-36° 57' 21".6	9835264	(14*1/6*2/-)*2	130
53	CrA IRS7 A	19 ^h 01 ^m 55 ^s .3	-36° 57' 22".0	9835008	(14*1/31*3/60*2)*2	170
54	CrA IRS7 B	19 ^h 01 ^m 56 ^s .4	-36° 57' 28".1	9835008	(14*1/31*3/60*2)*2	170
55	CrA IRS32	19 ^h 02 ^m 58 ^s .7	-37° 07' 34".7	9832192	(60*1/31*8/-)*2	170
56	IRAS 23238+7401	23 ^h 25 ^m 46 ^s .7	74° 17' 37".3	9833728	(14*1/31*8/60*2)*2	250

^aSee footnote *a* of Table 5.1.^bKnown or candidate edge-on-disks

Table 6.2. Observed linefluxes and 1σ uncertainties ($10^{-16}\text{erg cm}^{-2}\text{s}^{-1}$)

#	Source	[Ne II]			[Ne III]			[Fe I] 24.04		
		src	ext	upp	src	ext	upp	src	ext	upp
1	LDN1448 IRS1	-	-	(36)	-	-	(57)	-	-	(68)
2	LDN1448 NA	130	-	(18)	-	-	(23)	-	-	(100)
3	IRAS 03245+3002	-	-	(3)	-	-	(13)	-	-	(56)
4	L1455 SMM1	-	-	(12)	-	-	(5)	-	-	-
5	L1455 IRS3	-	-	(15)	-	-	(8)	-	-	-
6	IRAS 03254+3050	-	-	(28)	-	-	(29)	-	-	(140)
7	IRAS 03271+3013	-	-	(14)	-	-	(13)	-	-	(89)
8	IRAS 03301+3111	-	-	(110)	-	-	(92)	-	-	(140)
9	B1-a	110	-	(17)	-	-	(19)	-	-	-
10	B1-c	-	-	(13)	-	-	(7)	-	-	-
11	SSTe2d J033327.3	790	-	(25)	34	-	(6)	-	-	-
12	HH 211-mm	-	-	(18)	-	-	(3)	-	-	(39)
13	IRAS 03439+3233	-	-	(7)	-	-	(17)	700	-	(99)
14	IRAS 03445+3242	-	-	(110)	-	-	(59)	-	-	(100)
15	IRAS 08242-5050	530	-	(91)	-	-	(77)	-	-	(140)
16	IRAS 08261-5100	-	-	(67)	-	-	(69)	-	-	(67)
17	Ced 110 IRS4	74	13	(4)	-	-	(9)	-	-	(65)
18	IRAS 12553-7651	-	-	(61)	-	-	(50)	-	-	(150)
19	IRAS 13546-3941	-	-	(18)	-	-	(21)	-	-	(44)
20	IRAS 15398-3359	-	-	(17)	-	-	(13)	-	-	(55)
21	VSSG1	-	-	(55)	-	-	(54)	-	-	(55)
22	GSS30-IRS1	-	-	(730)	-	-	(1000)	-	-	(2000)
23	GY23	-	-	(160)	-	-	(82)	-	-	(68)
24	VLA 1623-243	-	-	(3)	-	-	(1)	-	-	(77)
25	IRS14	-	-	(16)	-	-	(4)	-	-	-
26	WL12	-	-	(200)	-	-	(180)	-	-	(180)
27	OphE-MM3	-	-	(13)	-	-	(3)	-	-	(31)
28	GY224	-	-	(18)	-	-	(24)	280	-	(38)
29	WL19	-	-	(16)	-	-	(16)	-	-	(42)
30	WL20S	310	-	(34)	-	-	(59)	-	-	(120)
31	IRS37	290	-	(17)	-	-	(23)	-	-	(53)
32	WL6	-	-	(110)	-	-	(77)	-	-	(140)
33	CRBR 2422.8-3423	-	-	(7)	-	-	(17)	-	-	(66)
34	Elias32	120	-	(24)	-	-	(26)	-	-	(40)
35	IRS46	-	-	(38)	-	-	(32)	-	-	(59)
36	VSSG17	-	-	(99)	-	-	(63)	-	-	(59)
37	IRS63	-	-	(72)	-	-	(64)	-	-	(94)
38	L1689-IRS5	-	-	(150)	-	-	(97)	-	-	(130)
39	IRAS 16293-2422B	-	-	(16)	-	-	(5)	-	-	(48)
40	IRAS 16293-2422	-	-	(2)	-	-	(2)	-	-	(33)
41	RNO 91	700	-	(41)	-	-	(95)	-	-	(210)
42	SSTe2d J182813.2	-	-	(30)	-	-	(24)	-	-	-
43	SSTe2d J182849.4	-	-	(150)	-	-	(49)	-	-	-
44	SSTe2d J182901.8	-	-	(20)	-	-	(23)	-	-	-
45	SSTe2d J182914.8	-	-	(17)	-	-	(18)	-	-	-
46	SSTe2d J182916.2	-	-	(27)	-	-	(35)	-	-	-
47	Serp-S68N	-	-	(6)	-	-	(6)	-	-	(38)
48	EC69	-	-	(3)	-	-	(1)	-	-	(11)
49	Serp-SMM4	-	-	(1)	-	-	(2)	-	-	(26)
50	EC88	-	-	(14)	-	-	(24)	-	-	(72)
51	Serp-SMM3	-	-	(6)	-	-	(5)	-	-	(42)
52	R CrA IRS5	1600	-	(120)	-	-	(180)	-	-	-
53	CrA IRS7 A	2500	1300	(140)	-	-	(480)	-	-	(1200)
54	CrA IRS7 B	700	190	(50)	-	-	(130)	-	-	(680)
55	CrA IRAS32	150	-	(16)	-	-	(10)	-	-	-
56	IRAS 23238+7401	120	-	(16)	-	-	(14)	-	-	(56)

Table 6.2. – continued –

	[Fe II] 17.94			[Fe II] 25.99			[S I]			[Si II]		
	src	ext	upp	src	ext	upp	src	ext	upp	src	ext	upp
1	290	-	(60)	-	-	(67)	-	-	(51)	-	480	(68)
2	-	-	(53)	-	-	(100)	-	-	(76)	-	-	(230)
3	-	-	(770)	-	-	(85)	-	-	(120)	-	-	(180)
4	-	-	(20)									
5	-	-	(27)									
6	-	-	(31)	-	-	(67)	-	-	(94)	-	-	(160)
7	-	-	(25)	-	-	(36)	-	-	(55)	-	-	(110)
8	-	-	(120)	-	-	(110)	-	-	(82)	-	-	(110)
9	-	-	(37)									
10	-	-	(27)									
11	99	-	(20)									
12	-	-	(5)	-	-	(9)	-	-	(12)	-	-	(18)
13	-	-	(12)	-	-	(39)	-	-	(39)	-	-	(58)
14	-	-	(87)	-	-	(99)	-	-	(69)	-	1300	(100)
15	-	-	(130)	-	-	(180)	-	-	(150)	-	-	(190)
16	-	-	(130)	-	-	(64)	-	-	(110)	-	-	(82)
17	110	68	(15)	-	-	(29)	-	-	(23)	-	-	(45)
18	-	-	(96)	-	-	(44)	-	-	(130)	-	-	(140)
19	-	-	(43)	-	-	(37)	-	-	(43)	-	-	(43)
20	-	-	(20)	-	-	(49)	-	-	(37)	-	-	(120)
21	-	-	(52)	-	-	(33)	-	-	(50)	-	1900	(64)
22	-	-	(1300)	-	-	(1400)	-	-	(1800)	-	-	(1600)
23	-	-	(92)	-	-	(65)	-	-	(60)	-	-	(89)
24	-	-	(4)	-	-	(73)	-	-	(53)	-	-	(140)
25	-	-	(28)									
26	-	-	(210)	-	-	(230)	-	-	(130)	-	-	(160)
27	-	-	(11)	-	-	(16)	-	-	(19)	-	-	(31)
28	-	-	(19)	-	-	(23)	-	-	(41)	-	-	(52)
29	-	-	(26)	-	-	(28)	-	-	(24)	-	-	(63)
30	-	-	(120)	-	-	(190)	-	-	(90)	-	-	(140)
31	-	-	(33)	-	-	(22)	-	-	(25)	-	-	(79)
32	-	-	(67)	-	-	(140)	-	-	(64)	-	-	(100)
33	-	-	(29)	-	-	(44)	-	-	(32)	-	-	(61)
34	-	-	(33)	-	-	(14)	-	-	(27)	-	-	(74)
35	-	-	(38)	-	-	(50)	-	-	(48)	-	-	(100)
36	-	-	(58)	-	-	(34)	-	-	(41)	-	290	(68)
37	-	-	(62)	-	-	(64)	-	-	(73)	-	-	(79)
38	-	-	(75)	-	-	(58)	-	-	(70)	-	-	(120)
39	-	-	(14)	-	-	(42)	-	-	(51)	-	-	(220)
40	-	-	(4)	-	-	(38)	-	150	(60)	-	-	(180)
41	-	-	(88)	-	-	(180)	-	-	(120)	-	-	(180)
42	-	-	(22)									
43	-	-	(69)									
44	-	-	(27)									
45	-	-	(30)									
46	-	-	(38)									
47	-	-	(16)	-	-	(16)	460	-	(26)	-	-	(45)
48	-	-	(4)	-	-	(2)	-	-	(3)	-	97	(23)
49	-	-	(3)	-	-	(30)	-	370	(15)	-	700	(19)
50	-	-	(29)	-	-	(42)	-	-	(74)	-	-	(100)
51	-	-	(69)	-	-	(24)	740	-	(39)	-	-	(37)
52	-	-	(250)									
53	-	-	(410)	-	-	(1100)	-	-	(1500)	-	-	(2100)
54	-	-	(130)	-	-	(240)	-	-	(310)	-	-	(1100)
55	860	-	(35)									
56	-	-	(25)	-	-	(36)	-	-	(78)	-	-	(86)

Table 6.3. Observed linefluxes and 1σ uncertainties ($10^{-16}\text{erg cm}^{-2}\text{s}^{-1}$)

#	Source	H2 S(1)			H2 S(2)			H2 S(3)		
		src	ext	upp	src	ext	upp	src	ext	upp
1	LDN1448 IRS1	-	-	(49)	-	-	(35)	-	-	(120)
2	LDN1448 NA	-	-	(46)	-	230	(19)	-	-	(200)
3	IRAS 03245+3002	-	-	(21)	-	-	(7)	-	-	(23)
4	L1455 SMM1	-	-	(11)	-	-	(35)	-	-	(22)
5	L1455 IRS3	-	-	(14)	-	-	(15)	-	-	(42)
6	IRAS 03254+3050	-	-	(28)	-	-	(24)	-	-	(67)
7	IRAS 03271+3013	-	-	(26)	100	-	(17)	260	-	(50)
8	IRAS 03301+3111	-	-	(110)	-	-	(73)	-	-	(180)
9	B1-a	-	-	(30)	-	-	(21)	-	240	(49)
10	B1-c	-	-	(18)	-	-	(19)	-	-	(43)
11	SSTc2d J033327.3	-	56	(7)	80	-	(12)	100	74	(14)
12	HH 211-mm	-	68	(2)	-	-	(8)	-	-	-
13	IRAS 03439+3233	-	-	(13)	-	-	(7)	-	-	(61)
14	IRAS 03445+3242	-	-	(80)	-	-	(79)	-	-	(350)
15	IRAS 08242-5050	-	-	(120)	-	-	(49)	-	-	(930)
16	IRAS 08261-5100	-	-	(91)	-	-	(55)	-	-	(290)
17	Ced 110 IRS4	-	-	(10)	-	-	(8)	-	-	-
18	IRAS 12553-7651	-	-	(50)	-	-	(33)	-	-	(120)
19	IRAS 13546-3941	-	-	(28)	-	-	(23)	-	-	(200)
20	IRAS 15398-3359	-	-	(15)	-	-	(36)	-	-	(97)
21	VSSG1	-	560	(97)	-	430	(70)	-	-	-
22	GSS30-IRS1	-	-	(810)	-	-	(350)	-	-	-
23	GY23	-	-	(82)	-	-	(54)	-	-	-
24	VLA 1623-243	-	86	(2)	-	72	(2)	-	-	-
25	IRS14	-	760	(8)	-	450	(11)	-	-	(23)
26	WL12	-	-	(110)	-	-	(160)	-	-	-
27	OphE-MM3	-	-	(4)	-	-	(8)	-	-	(7)
28	GY224	-	-	(34)	-	-	(32)	-	-	-
29	WL19	-	-	(23)	-	-	(21)	-	-	-
30	WL20S	-	-	(120)	-	-	(24)	-	-	-
31	IRS37	-	-	(37)	-	-	(44)	-	-	-
32	WL6	-	-	(110)	-	-	(110)	-	-	-
33	CRBR 2422.8-3423	-	-	(30)	-	-	(13)	-	-	(66)
34	Elias32	-	-	(46)	-	-	(22)	-	-	-
35	IRS46	-	-	(40)	-	-	(25)	-	-	-
36	VSSG17	-	-	(63)	-	-	(61)	-	-	-
37	IRS63	-	-	(76)	-	-	(46)	-	-	-
38	L1689-IRS5	-	-	(140)	-	-	(86)	-	-	-
39	IRAS 16293-2422B	-	50	(4)	-	-	(6)	-	-	(11)
40	IRAS 16293-2422	-	56	(2)	-	35	(2)	-	-	(17)
41	RNO 91	-	-	(69)	-	-	(62)	-	-	(670)
42	SSTc2d J182813.2	-	-	(15)	-	-	(23)	-	-	(140)
43	SSTc2d J182849.4	-	-	(61)	-	-	(150)	-	-	(400)
44	SSTc2d J182901.8	-	-	(28)	-	-	(31)	-	-	(170)
45	SSTc2d J182914.8	-	-	(13)	-	-	(39)	-	-	(86)
46	SSTc2d J182916.2	-	-	(35)	-	-	(24)	-	-	(110)
47	Serp-S68N	-	-	(19)	-	-	(10)	-	-	-
48	EC69	-	71	(1)	-	29	(2)	-	-	(41)
49	Serp-SMM4	-	100	(1)	-	290	(2)	-	-	-
50	EC88	-	-	(31)	-	-	(17)	-	-	(32000)
51	Serp-SMM3	-	180	(20)	-	150	(12)	-	-	-
52	R CrA IRS5	-	-	(150)	-	-	(87)	-	-	(710)
53	CrA IRS7 A	-	-	(460)	-	-	(76)	-	-	(340)
54	CrA IRS7 B	-	-	(81)	-	-	(42)	-	-	(280)
55	CrA IRAS32	-	-	(11)	-	-	(12)	88	-	(17)
56	IRAS 23238+7401	-	-	(19)	-	-	(14)	-	-	(61)

Table 6.3. – continued –

	H2 S(4)			H2 S(5)			H2 S(6)			H2 S(7)		
	src	ext	upp	src	ext	upp	src	ext	upp	src	ext	upp
1	-	-	(240)	-	-	(160)	-	-	(110)	-	-	(170)
2	1400	460	(210)	-	-	(420)	-	-	(380)	-	-	(380)
3	-	-	(42)	-	-	(43)	-	-	(88)	-	-	(67)
4	-	-	(33)	-	-	(57)	-	-	(78)	-	-	(46)
5	950	-	(150)	-	-	(66)	-	-	(57)	-	-	(93)
6	-	-	(140)	-	-	(170)	-	-	(240)	-	-	(160)
7	370	-	(70)	1100	-	(50)	470	-	(92)	640	-	(44)
8	-	-	(200)	-	-	(250)	-	-	(240)	-	-	(230)
9	770	-	(95)	-	-	(270)	-	-	(140)	-	-	(110)
10	2200	-	(340)	-	-	(570)	-	-	(660)	-	-	(680)
11	220	36	(13)	680	-	(68)	-	-	(30)	540	-	(56)
12												
13	-	-	(120)	-	-	(95)	-	-	(100)	-	-	(79)
14	-	-	(650)	-	-	(760)	-	-	(470)	-	-	(720)
15	4200	-	(810)	-	-	(2500)	-	-	(2000)	-	-	(1800)
16	-	-	(300)	-	-	(330)	-	-	(280)	-	-	(200)
17												
18	-	-	(280)	-	-	(300)	-	-	(560)	-	-	(410)
19	-	-	(300)	-	-	(300)	-	-	(210)	-	-	(150)
20	1200	-	(190)	-	-	(260)	-	-	(250)	-	-	(310)
21												
22												
23												
24												
25	-	-	(36)	-	-	(37)	-	-	(53)	-	-	(46)
26												
27	-	-	(12)	-	-	(38)	-	-	(33)	-	-	(21)
28												
29												
30												
31												
32												
33	640	-	(81)	-	-	(160)	-	-	(170)	-	-	(150)
34												
35												
36												
37												
38												
39	78	-	(11)	-	-	(24)	-	-	(25)	-	-	(27)
40	-	-	(23)	-	-	(30)	-	-	(33)	-	-	(37)
41	-	-	(830)	-	-	(2000)	-	-	(2200)	-	-	(2100)
42	-	-	(310)	-	-	(590)	-	-	(570)	-	-	(260)
43	-	-	(1100)	-	-	(1400)	-	-	(2600)	-	-	(700)
44	-	-	(180)	-	-	(160)	-	-	(180)	-	-	(180)
45	-	-	(140)	-	-	(280)	-	-	(230)	-	-	(280)
46	-	-	(140)	-	-	(310)	-	-	(150)	-	-	(200)
47												
48	-	-	(74)	-	-	(89)	-	-	(110)	-	-	(120)
49												
50	-	-	(51000)	-	-	(470)	-	-	(590)	-	-	(520)
51												
52	-	-	(950)	-	-	(1900)	-	-	(1200)	-	-	(870)
53	5700	-	(1100)	-	-	(4000)	-	-	(850)	-	-	(880)
54	4000	-	(740)	-	-	(1100)	-	-	(1400)	-	-	(1000)
55	280	-	(32)	-	-	(58)	-	-	(74)	-	-	(94)
56	-	-	(170)	-	-	(91)	-	-	(140)	-	-	(97)

Table 6.4. H₂ excitation parameters.

#	Source	Warm H ₂ ^a				Hot H ₂ ^a			
		Compact ^b		Extended		Compact ^b		Extended	
		[10 ²² cm ⁻²]	[M _J]	[10 ²⁰ cm ⁻²]	[M _J]	[10 ²⁰ cm ⁻²]	[10 ⁻³ M _J]	[10 ¹⁸ cm ⁻²]	[10 ⁻³ M _J]
1	LDN1448 IRS1	< 440	< 13.5	< 9	< 4.4	< 8	< 2.6	< 5	< 2.7
2	LDN1448 NA	< 640	< 19.4	9	4.8	8	2.8	15	7.3
3	IRAS 03245+3002	< 520	< 16.4	< 14	< 6.9	< 1	< 0.4	< 1	< 0.7
4	L1455 SMM1	< 96	< 3.0	< 4	< 2.3	1	0.6	< 1	< 0.9
5	L1455 IRS3	< 108	< 3.3	< 1	< 0.9	4	1.5	< 8	< 4.1
6	IRAS 03254+3050	< 276	< 8.6	< 7	< 3.5	< 7	< 2.2	< 2	< 1.4
7	IRAS 03271+3013	< 388	< 12.0	< 11	< 5.2	9	2.9	< 2	< 1.2
8	IRAS 03301+3111	< 880	< 26.9	< 9	< 4.6	< 13	< 4.2	< 16	< 7.8
9	B1-a	< 264	< 8.2	< 14	< 7.5	5	1.6	< 3	< 1.9
10	B1-c	< 68	< 2.1	< 8	< 3.9	13	4.3	< 2	< 1.4
11	SSTc2d J033327.3	< 34	< 1.1	8	3.9	4	1.4	1	0.5
12	HH 211-mm	< 56	< 1.7	3	1.6	< 1	< 0.6	7	3.5
13	IRAS 03439+3233	< 280	< 8.6	< 8	< 4.3	< 4	< 1.3	< 2	< 1.2
14	IRAS 03445+3242	< 600	< 18.4	< 12	< 6.1	29	9.0	< 13	< 6.4
15	IRAS 08242-5050	< 2760	< 86.1	< 20	< 32.3	220	68.3	< 23	< 38.1
16	IRAS 08261-5100	< 1840	< 56.7	< 6	< 7.6	< 38	< 11.8	< 16	< 20.0
17	Ced 110 IRS4	< 80	< 2.5	< 4	< 1.0	< 1	< 0.3	< 1	< 0.5
18	IRAS 12553-7651	< 304	< 9.4	< 14	< 3.7	< 6	< 2.0	< 5	< 1.3
19	IRAS 13546-3941	< 1600	< 49.1	5	15.6	< 68	< 21.5	8	25.2
20	IRAS 15398-3359	< 28	< 0.9	< 2	< 0.2	1	0.5	< 3	< 0.3
21	VSSG1	< 144	< 4.4	12	1.5	< 9	< 3.0	66	7.9
22	GSS30-IRS1	< 2160	< 66.8	< 210	< 25.6	< 24	< 7.4	< 44	< 5.3
23	GY23	< 192	< 5.9	< 17	< 2.1	< 3	< 1.1	< 17	< 2.1
24	VLA 1623-243	< 30	< 0.9	10	1.3	< 0.2	< 0.1	5	0.6
25	IRS14	< 16	< 0.5	99	12.3	0.6	0.2	30	3.7
26	WL12	< 256	< 7.9	< 16	< 2.0	< 11	< 3.4	< 28	< 3.4
27	OphE-MM3	< 12	< 0.4	< 1	< 0.2	< 0.3	< 0.1	< 1	< 0.2
28	GY224	< 108	< 3.4	< 14	< 1.7	< 2	< 0.7	< 3	< 0.4
29	WL19	< 76	< 2.4	< 9	< 1.1	< 1	< 0.4	< 2	< 0.3
30	WL20S	< 268	< 8.4	< 14	< 1.9	< 1	< 0.5	< 13	< 1.6

Table 6.4—Continued

#	Source	Warm H ₂ ^a				Hot H ₂ ^a			
		Compact ^b		Extended		Compact ^b		Extended	
		[10 ²² cm ⁻²]	[M _J]	[10 ²⁰ cm ⁻²]	[M _J]	[10 ²⁰ cm ⁻²]	[10 ⁻³ M _J]	[10 ¹⁸ cm ⁻²]	[10 ⁻³ M _J]
31	IRS37	< 88	< 2.8	< 5	< 0.6	< 3	< 0.9	< 15	< 1.8
32	WL6	< 160	< 4.9	< 11	< 1.3	< 11	< 3.6	< 27	< 3.3
33	CRBR 2422.8-3423	< 84	< 2.6	< 9	< 1.1	1	0.5	< 2	< 0.3
34	Elias32	< 44	< 1.4	< 2	< 0.3	< 3	< 1.1	< 14	< 1.7
35	IRS46	< 116	< 3.6	< 12	< 1.6	< 1	< 0.5	< 8	< 1.0
36	VSSG17	< 132	< 4.1	< 7	< 0.9	< 4	< 1.3	< 20	< 2.5
37	IRS63	< 200	< 6.2	< 18	< 2.1	< 3	< 1.0	< 13	< 1.6
38	L1689-IRS5	< 120	< 3.7	< 4	< 0.5	< 13	< 4.3	< 29	< 3.6
39	IRAS 16293-2422B	< 44	< 1.3	6	0.7	0.3	0.1	2	0.3
40	IRAS 16293-2422	< 31	< 1.0	7	0.9	< 0.3	< 0.1	2	0.3
41	RNO 91	< 304	< 9.5	< 20	< 3.2	18	5.7	< 15	< 2.3
42	SSTc2d J182813.2	< 32	< 1.0	< 2	< 1.4	< 16	< 5.1	< 5	< 2.9
43	SSTc2d J182849.4	< 480	< 14.5	< 18	< 9.7	< 36	< 11.3	< 20	< 10.7
44	SSTc2d J182901.8	< 224	< 7.0	< 9	< 5.1	< 9	< 3.0	< 6	< 3.2
45	SSTc2d J182914.8	< 48	< 1.5	< 4	< 2.2	< 10	< 3.3	< 4	< 2.2
46	SSTc2d J182916.2	< 288	< 8.9	< 17	< 9.1	< 9	< 3.0	< 4	< 2.2
47	Serp-S68N	152	4.8	5	2.8	< 3	< 0.9	2	1.3
48	EC69	< 56	< 1.7	7	3.8	< 3	< 1.1	4	2.1
49	Serp-SMM4	< 34	< 1.1	3	1.6	< 0.6	< 0.2	20	10.4
50	EC88	< 368	< 11.4	< 5	< 3.0	< 80	< 24.4	< 95	< 50.0
51	Serp-SMM3	< 316	< 9.8	9	5.0	< 3	< 1.0	20	10.3
52	RCrA IRS5	< 296	< 9.2	< 61	< 8.0	< 14	< 4.5	< 21	< 2.7
53	CrA IRS7 A	< 3320	< 102.3	< 150	< 34.5	25	7.9	< 17	< 3.8
54	CrA IRS7 B	< 800	< 25.1	< 46	< 10.2	16	5.0	< 9	< 2.2
55	CrA IRAS32	< 44	< 1.3	< 6	< 1.3	1	0.4	< 1	< 0.2
56	IRAS 23238+7401	< 352	< 10.9	< 7	< 3.6	< 5	< 1.7	< 3	< 1.6

^a100 K is assumed for the warm component and 1000 K for the hot component. The derived column density and mass of the warm component depend strongly on the assumed temperature. A temperature of 150 and 200 K reduces the column density and mass by respectively a factor of ~ 30 and 140. For the hot component 1500 K instead of 1000 K may result in a reduction of column density and mass up to a factor of 10.

^bFor the unresolved emission a source with $r = 50$ AU is assumed to obtain an estimate of the column density.

Chapter 7

Hot Organic Molecules Toward a Young Low-mass Star: a Look at Inner Disk Chemistry

Abstract

Spitzer Space Telescope spectra of the low mass young stellar object (YSO) IRS46 ($L_{\text{bol}} \approx 0.6 L_{\odot}$) in Ophiuchus reveal strong vibration-rotation absorption bands of gaseous C_2H_2 , HCN, and CO_2 . This is the only source out of a sample of ~ 100 YSOs that shows these features, and this is the first time that they are seen in the spectrum of a solar-mass YSO. Analysis of the *Spitzer* data combined with Keck *L*- and *M*-band spectra reveals excitation temperatures of $\gtrsim 350$ K and abundances of 10^{-6} to 10^{-5} with respect to H_2 , orders of magnitude higher than those found in cold clouds. In spite of this high abundance, the HCN $J = 4 - 3$ line is barely detected with the James Clerk Maxwell Telescope (JCMT), indicating a source diameter less than 13 AU. The (sub)millimeter continuum emission and the absence of scattered light in near-infrared images limits the mass and temperature of any remnant collapse envelope to less than $0.01 M_{\odot}$ and 100 K, respectively. This excludes a hot-core type region as found in high-mass YSOs. The most plausible origin of this hot gas rich in organic molecules is in the inner (< 6 AU radius) region of the disk around IRS46, either the disk itself or a disk wind. A nearly edge-on two-dimensional disk model fits the spectral energy distribution (SED) and gives a column of dense warm gas along the line of sight that is consistent with the absorption data. These data illustrate the unique potential of high-resolution infrared spectroscopy to probe the organic chemistry, gas temperatures, and gas kinematics in the planet-forming zones close to a young star.

Lahuis, F., van Dishoeck, E. F., Boogert, A. C. A., Pontoppidan, K. M., Blake, G. A., Dullemond, C. P., Evans, II, N. J., Hogerheijde, M. R., Jørgensen, J. K., Kessler-Silacci, J. E., & Knez, C. 2006, *ApJ*, 636, L145

7.1 Introduction

The presence of gas-rich disks around young stars is well established observationally and theoretically (see review by Greaves, 2005), but comparatively little is known about their chemical structure. A good understanding of the chemistry is important since some of the gases and solids in protoplanetary disks will end up in future solar systems where they may form the basis for prebiotic species (see reviews by Ehrenfreund & Charnley, 2000; Markwick & Charnley, 2004). Virtually all observational studies of molecules other than CO have been limited to the outer regions, where simple organic molecules such as HCO^+ , CN, HCN, and H_2CO have been detected at millimeter wavelengths (e.g. Dutrey et al., 1997; Kastner et al., 1997; Qi et al., 2003; Thi et al., 2004). Because of beam dilution, these observations cannot probe radii < 50 AU from the star, which is the relevant zone for planet formation. High-resolution infrared (IR) spectroscopy has found CO emission from the warm dense gas in the inner disk region (Najita et al., 2003; Brittain et al., 2003; Blake & Boogert, 2004), but H_2O is the only molecule besides CO and H_2 that has been convincingly detected (Carr et al., 2004).

Models of inner disk chemistry initially focused on our own primitive solar nebula (see review by Prinn, 1993) but now also consider exosolar systems. They have grown considerably in sophistication, including non-equilibrium chemistry, gas-solid interactions, radial and vertical mixing, and the effects of UV radiation and X-rays from the central star on the gas temperature and molecular abundances (e.g., Markwick et al., 2002; Gail, 2002; Ilgner et al., 2004; Glassgold et al., 2004; Gorti & Hollenbach, 2004). Large concentrations of organic molecules like C_2H_2 and HCN are predicted in some models in the inner few AU, but no observational tests have been possible to date.

The sensitive Infrared Spectrograph (IRS) on board the *Spitzer* Space Telescope opens a new window to study molecules in disks through IR pencil-beam line-of-sight absorption spectroscopy. The *Spitzer* c2d legacy program “From Molecular Cores to Planet-Forming Disks” (Evans et al., 2003) is collecting a coherent sample of IRS spectra of low-mass YSOs in five nearby star-forming regions. To date more than 100 Class I and Class II sources have been observed. Of these only one source, IRS 46, shows strong gas-phase absorption bands of hot molecules. These gas-phase bands have previously been seen only toward deeply embedded high-mass YSOs, where they have been associated with the inner ($\lesssim 1000$ AU) warm dense regions of the spherical envelopes, also known as ‘hot cores’ (Carr et al., 1995; Lahuis & van Dishoeck, 2000; Boonman et al., 2003). The sources studied with *Spitzer* have factors of $10^4 - 10^5$ lower luminosity, thus limiting the maximum temperatures and amount of warm gas in the envelope.

IRS 46, also known as YLW16b and GY274, is part of the Ophiuchus cloud at a distance of ~ 125 pc (de Geus et al., 1989). It is classified as a Class I source, i.e., a protostar with a compact accretion disk embedded in a more extended and collapsing envelope, based on its near- and mid-IR colors (André & Montmerle, 1994) with $L_{\text{bol}} \approx 0.6 L_{\odot}$ (Bontemps et al., 2001). However, the complete SED is also consistent with a Class II source viewed nearly edge-on, i.e., a pre main-sequence star with a disk but without a significant collapsing envelope (see Sect. 7.4). It is similar to the SED of the nearly edge-on disk CRBR 2422.8 3423 (Pontoppidan et al., 2005), but IRS 46 has a smaller column of dense foreground material. The favorable inclination of CRBR 2422.8-3423 allows for the study of ices in the outer region of the circumstellar disk. IRS 46, also profiting from a favorable inclination, may prove to offer us a unique opportunity to directly study the gas temperature and hot gas-phase organic chemistry in the inner disk.

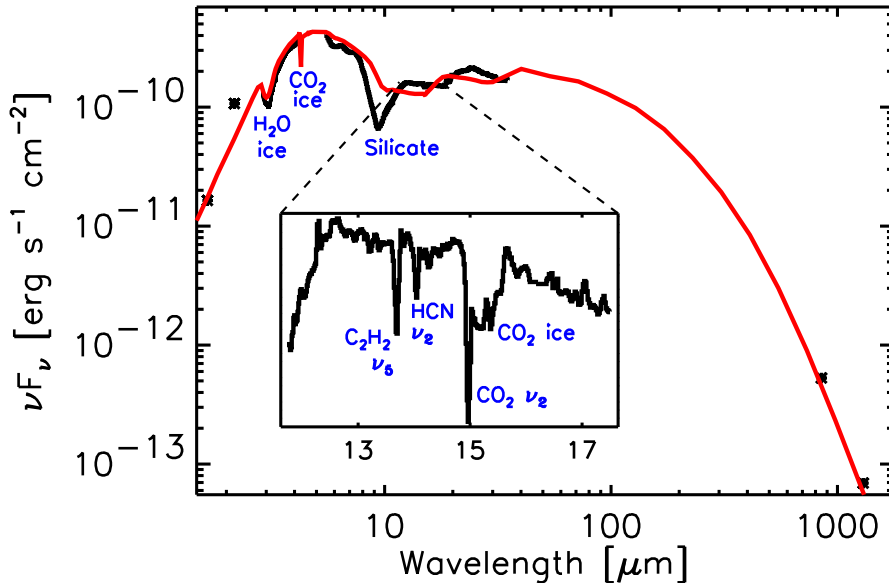


Figure 7.1 Composite SED of IRS 46 from 1.25 μm to 1.3 mm including the full *Spitzer* IRS spectrum from 10–37 μm , 2MASS *J*, *H*, *Ks* imaging and photometry ($F_J = 0.33$ mJy, $F_H = 9.03$ mJy, $F_{Ks} = 77.5$ mJy), a VLT-ISAAC *L*-band spectrum at $R \approx 1200$ (Pontoppidan et al., 2003), an ISOCAM-CVF 5–16 μm spectrum at $R \approx 50$, $F_{850 \mu\text{m}} = 150$ mJy (see Ridge et al., 2006), and $F_{1.3 \text{ mm}} = 28$ mJy (André & Montmerle, 1994). Overplotted is an SED disk model of a nearly edge-on self-shadowed flaring disk of 60 AU radius with $L_{\text{bol}} \approx 0.6 L_{\odot}$ and a disk mass of $\sim 0.03 M_{\odot}$ seen at an inclination of $\sim 75^{\circ}$. The insert shows a zoom-in on the mid-IR containing the observed C_2H_2 , HCN, and CO_2 molecular absorption features and the CO_2 ice band at 15 μm .

7.2 Observations

IRS 46 was observed with *Spitzer* IRS in the Short-High (9.9–19.6 μm) and Long-High (18.7–37.2 μm) medium-resolution ($R = \lambda/\delta\lambda = 600$) modes. The observation was positioned at $16^{\text{h}}27^{\text{m}}29^{\text{s}}.4 - 24^{\circ}39'16''.3$ (J2000) and acquired on 2004 August 29 as part of AOR# 0009829888. Observations with the Short-Low and Long-Low modes are scheduled as part of the *Spitzer* Guaranteed Time Observation program but have not yet been taken. Data reduction started from the Basic Calibrated Data images using S12.0.2 *Spitzer* archive data. The processing includes bad-pixel correction, extraction, defringing, and order matching using the c2d analysis pipeline (Chapter 3 of this thesis; Kessler-Silacci et al., 2006).

Figure 7.1 shows the SED composed from the full *Spitzer* IRS spectrum and complementary archival and literature data. Figure 7.2 shows the part of the (normalized) IRS spectrum revealing the $\text{C}_2\text{H}_2 \nu_5 = 1 - 0$, HCN $\nu_2 = 1 - 0$, and $\text{CO}_2 \nu_2 = 1 - 0$ bending mode ro-vibrational absorption bands. Included is a best-fit synthetic spectrum (see §7.3).

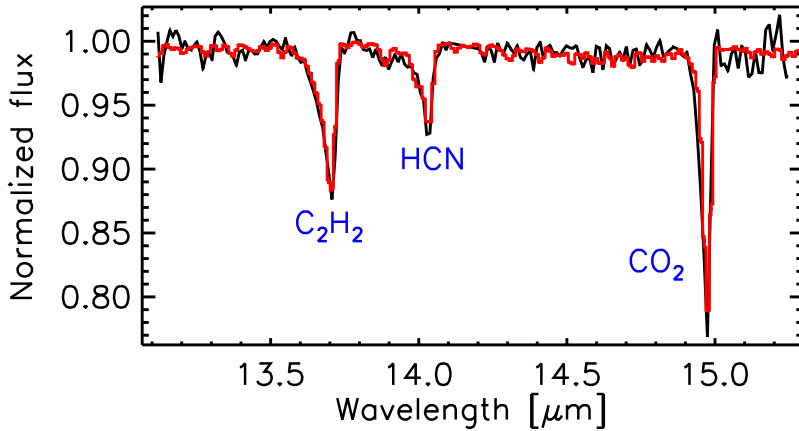


Figure 7.2 Blow-up of the IRS 46 normalized *Spitzer* IRS spectrum covering the C_2H_2 $\nu_5 = 1 - 0$, HCN $\nu_2 = 1 - 0$, and CO_2 $\nu_2 = 1 - 0$ bending mode ro-vibrational absorption bands. Included in gray (red in the online version) is a best-fit synthetic spectrum.

To constrain the source size of the warm gas, JCMT HCN $J = 4 - 3$ and CO $J = 3 - 2$ spectra at 354 and 345 GHz, respectively, were obtained using receiver B3. A weak HCN line with $T_{MB} = 0.035$ K and $\Delta V \approx 6$ km s $^{-1}$ at $V_{LSR} = 4.4$ km s $^{-1}$ is detected. The CO $J = 3 - 2$ line is strong, $T_{MB} \approx 10$ K at the same velocity. A small CO map around IRS 46 reveals only a red wing, most likely associated with the outflow from IRS 44.

High-resolution L - and M -band spectra ($R \approx 25,000$) were obtained with NIR-SPEC at the Keck II telescope to provide kinematic information and confirmation of the *Spitzer* HCN detection through the CO $\nu = 1 - 0$ 4.7 μ m and HCN $\nu_3 = 1 - 0$ 3.0 μ m stretching mode ro-vibrational bands (see Figure 7.3). The ^{13}CO absorption lines are unresolved at the quiescent cloud velocity of $V_{LSR} \approx 4$ km s $^{-1}$. However, the resolved ^{12}CO ($\Delta V \approx 30$ km s $^{-1}$) and HCN ($\Delta V \approx 20$ km s $^{-1}$) absorption lines are observed to be shifted, at $V_{LSR} \approx -20$ km s $^{-1}$. Of these no counterpart is observed in the HCN $J = 4 - 3$ and CO $J = 3 - 2$ JCMT spectra. We associate the HCN, C_2H_2 , and CO_2 absorptions seen in the *Spitzer* spectra with the blue-shifted components.

7.3 Analysis

The *Spitzer* spectra are analyzed using a pure absorption model assuming local thermodynamic equilibrium (LTE) excitation of the levels at a single temperature. The adopted method is described in detail in Lahuis & van Dishoeck (2000) and Boonman et al. (2003), and includes references to the molecular parameters and data used in the model. The main fit parameters are the average temperature and integrated column

The JCMT is operated by the JAC in Hilo, Hawaii on behalf of PPARC (UK), NRC (Canada) and NWO (Netherlands)

The W.M. Keck Observatory is operated as a scientific partnership among Caltech, the University of California and NASA, made possible by the W.M. Keck Foundation

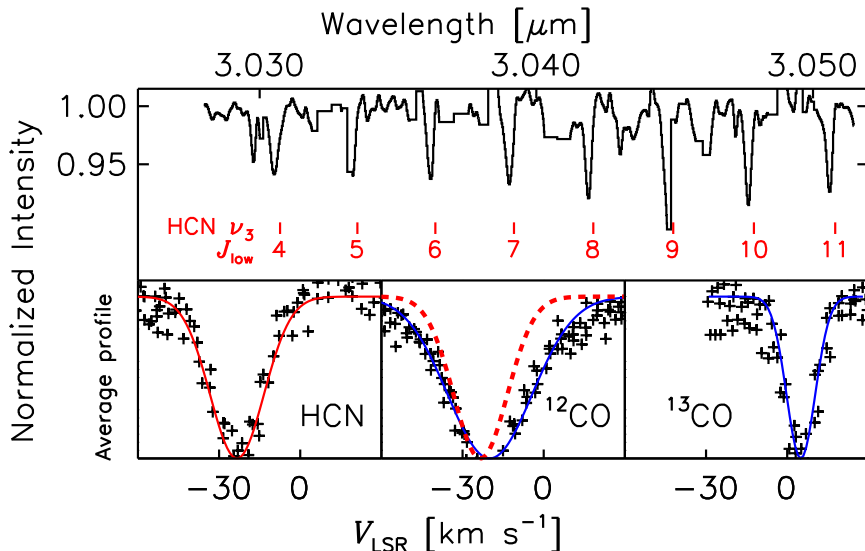


Figure 7.3 *Top*: Keck-NIRSPEC *L*-band spectrum showing HCN ν_3 C-H stretching mode absorption lines with tickmarks at the rest wavelengths. *Bottom*: HCN, high- J ^{12}CO and ^{13}CO velocity components derived from Keck-NIRSPEC *L*- and *M*-band spectra using absorption lines with an atmospheric transmission $> 40\%$. Plus symbols show the observed data; solid lines the fitted Gaussian velocity profiles. In the ^{12}CO profile plot the HCN profile is included (dashed line) showing that the HCN and CO lines are blue-shifted by a similar amount but that the CO profile is broader.

density along the line of sight for a given intrinsic line width, defined by the Doppler b -value. The resolved HCN ν_3 lines can be the result of multiple unresolved components along the line of sight, so that the intrinsic b -value can be smaller than the observed line width. For small b -values $< 2 \text{ km s}^{-1}$, no good fit can be made to the $\text{C}_2\text{H}_2 \nu_5$ and $\text{CO}_2 \nu_2$ profiles. Therefore, b is taken to range from 2 to 12 km s^{-1} .

The best fits to the $\text{C}_2\text{H}_2 \nu_5$, HCN ν_2 , and $\text{CO}_2 \nu_2$ bands observed in the IRS spectrum give T_{ex} of ~ 700 , 400 , and 300 K and column densities of 3 , 5 , and $10 \times 10^{16} \text{ cm}^{-2}$ respectively for $b \approx 5 \text{ km s}^{-1}$. The uncertainty in b results in an uncertainty of 25% in these values. The blue-shifted $\text{CO } \nu = 1 - 0$ absorption band gives $T_{\text{ex}} = 400 \pm 100 \text{ K}$ and $N = (2 \pm 1) \times 10^{18} \text{ cm}^{-2}$ corresponding to a minimum H_2 column density of $1 \times 10^{22} \text{ cm}^{-2}$ assuming a CO abundance of 2×10^{-4} (all gas-phase carbon in CO), as appropriate for warm dense gas. The $9.7 \mu\text{m}$ silicate depth corresponds to $N_{\text{H}} = 3 \times 10^{22} \text{ cm}^{-2}$ assuming a conversion factor: $N_{\text{H}} = \tau_{9.7} \times 3.5 \times 10^{22} \text{ cm}^{-2}$ (see Draine, 2003). X-ray observations give $N_{\text{H}} = 11(\pm 7) \times 10^{22} \text{ cm}^{-2}$ (Imanishi et al., 2001). Assuming most hydrogen is in H_2 and allowing for some foreground absorption in the latter two determinations, all estimates are consistent with $N(\text{H}_2) = 1 \times 10^{22} \text{ cm}^{-2}$ within a factor of two. The resulting abundance estimates are 3 , 5 , and 10×10^{-6} for C_2H_2 , HCN, and CO_2 , respectively. The density of the gas is at least 10^8 cm^{-3} , required to thermalize HCN and C_2H_2 .

Additional constraints can be obtained from a combined analysis of the HCN ν_2 and ν_3 bands (Figure 7.3). Assuming the same excitation temperature for both bands,

the required column density to fit the ν_3 band is higher by a factor of 4 than that found from the ν_2 band. This suggests that geometrical effects and emission filling in the absorption may play an important role (see Boonman et al., 2003). One possibility is that the absorbing region is smaller than the continuum-emitting region, the size of which may depend on wavelength. Similar increases may be expected for C_2H_2 and CO_2 . Thus, the above cited abundances are lower limits. The inferred HCN abundance, with respect to both H_2 and CO , is up to four orders of magnitude larger than that found in cold interstellar clouds.

7.4 Discussion

Where does this hot gas rich in organic molecules reside? The first clue comes from the HCN submillimeter JCMT spectrum. For a HCN column density of $> 10^{17} \text{ cm}^{-2}$ derived from the IR data, the $J=4-3$ pure rotational line is highly optically thick. Thus, T_{MB} is expected to be close to the excitation temperature of $\sim 400 \text{ K}$ if the emission would fill the beam. Although a weak emission line is observed at $V_{\text{LSR}} \approx 4 \text{ km s}^{-1}$, the broad -20 km s^{-1} component is not detected with a 3σ limit of 0.02 K in a 1 km s^{-1} bin. This gives a beam dilution $\gtrsim 2 \times 10^4$ that, for the JCMT beam size of $15''$, implies a source diameter for the hot gas of $\lesssim 0.11''$ or 13 AU diameter at the distance of Ophiuchus. A similar limit follows from the lack of a blue wing on the $\text{CO } J=3-2$ line.

The second clue comes from the high temperatures and densities of the molecular gas. In general, temperatures of a few hundred K are found in YSO environments only in the innermost part of envelopes or in the inner disks. The velocity of the hot gas provides a final clue. The radial velocity of IRS 46 is unknown, and it is possible that IRS 46 itself is at a velocity of -20 km s^{-1} (Doppmann et al., 2005). More likely, however, IRS 46 is close to the nominal cloud velocity of 4.4 km s^{-1} , and the hot gas is blue-shifted by $\sim 25 \text{ km s}^{-1}$.

Based on these arguments, three possibilities are considered for the location of this hot gas: (i) the inner layer of any remnant collapsed envelope on scales $\lesssim 100 \text{ AU}$ around IRS 46; (ii) the inner $\lesssim 10 \text{ AU}$ regions of a nearly edge-on disk; and (iii) dense hot gas at the footpoint of a wind launched from the inner disk. The first two options are examined through radiative transfer models to constrain the physical parameters of the source environment.

To explore the first option, a spherically symmetric model with a power-law density distribution was constructed by reproducing the SCUBA submillimeter continuum map and the SED of IRS 46 from mid-IR to submillimeter wavelengths following Jørgensen et al. (2002). This model has two severe problems: to reproduce the mid-IR continuum emission, the temperature in the innermost envelope cannot exceed roughly 100 K ; and an $\sim 0.01 M_{\odot}$ envelope (estimated from the submillimeter continuum data) produces a significant scattering nebulosity at near-IR wavelengths that is not observed in VLT-ISAAC images (Pontoppidan et al., 2005). The envelope model also cannot explain the line widths and velocities unless IRS 46 itself is at -20 km s^{-1} . Thus, most of the IR and submillimeter continuum emission must arise from the disk around IRS 46.

To investigate the second option, the physical structure of the IRS 46 disk was constrained from the observed SED in a manner similar to CRBR 2422.8-3423 (Pontoppidan et al., 2005) using the two-dimensional axisymmetric Monte Carlo radiative transfer

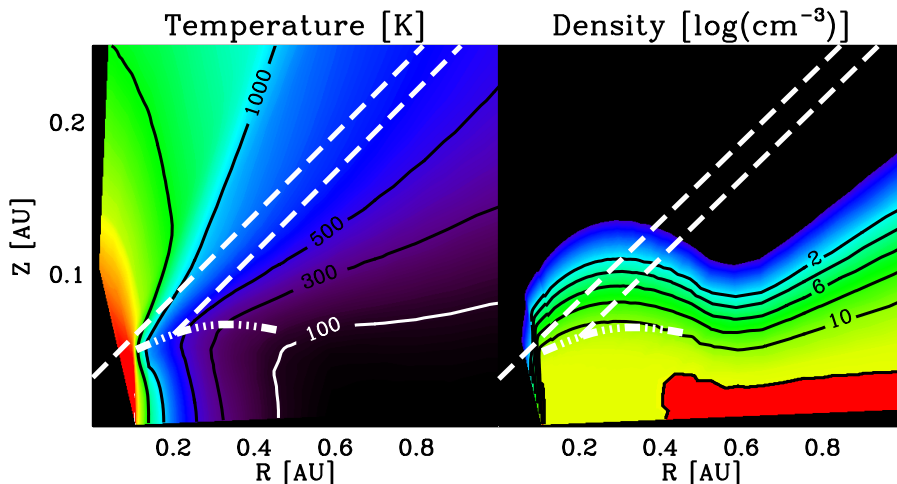


Figure 7.4 Two dimensional distribution of the temperature (*left*) and density (*right*) in the inner disk for the best-fitting model to the SED. Included are the $\tau = 1$ photosphere at $14 \mu\text{m}$ (*dot-dashed curves*) and two lines of sight (*dashed lines*) at the disk inclination of 75° . Most of the molecular absorption originates along the lines of sight toward the photosphere in the hot ($> 300 \text{ K}$) inner rim and toward the hot surface (1500 K) of the inner rim on the opposite side of the star (see §7.4).

code of Dullemond & Dominik (2004). Figure 7.4 shows the temperature and density structure of the hot inner part of the nearly edge-on self-shadowed flaring disk, and Figure 7.1 shows the best-fitting SED. There is some degeneracy in the parameters of the best-fitting model (see the discussion in Pontoppidan et al., 2005), but spatially resolved data are needed to further constrain the fits. The fit to the silicate feature is sensitive to the assumed opacities, emission from the outer disk, and the presence of foreground absorption; these uncertainties have little impact on the part of the disk model relevant to this work, i.e., the dense inner disk region.

The main continuum contribution from the disk at $3 - 14 \mu\text{m}$ comes from the puffed up inner rim and inner rim wall on the far side of the star. In the disk model, the integrated column of dense gas ($> 10^8 \text{ cm}^{-3}$) toward these areas is in the range $(1 - 2) \times 10^{22} \text{ cm}^{-2}$ with average temperatures of $300 - 1500 \text{ K}$. This is consistent with the H_2 column density and temperatures derived from the observations (see §7.3). Indeed, more generally, the observed temperatures are consistent with disk models that explicitly calculate the gas temperature in the inner disk. The gas temperatures may be even higher than the dust temperatures in the upper layers (Glassgold et al., 2004; Gorti & Hollenbach, 2004). The velocity-broadened CO and HCN profiles (Figure 7.3) could result from absorption in the Keplerian inner rim at 0.1 AU ($V_{\text{kep}} \simeq 70 \text{ km s}^{-1}$ for a $0.5 M_\odot$ star). If IRS 46 is at the cloud velocity of $+4 \text{ km s}^{-1}$, the blue-shifted absorption implies a deviation from Keplerian rotation in the disk plane, for example as the result of a close binary. A near edge-on disk explanation is consistent with a detection toward only one in a hundred objects, since a very small fraction of sources should have the right orientation.

A blue-shifted velocity may also indicate that the observed absorption features originate in a wind emanating from the inner disk. Possibilities include a magnetocentrifu-

gal wind (either an *X*-wind launched within 0.1 AU or a disk wind launched farther out), a photoevaporative flow, or a stellar wind interacting with the upper layer and entraining molecular material (see, e.g., Eisloffel et al., 2000). For the gas to be seen in absorption, it must be comparable in size to the inner disk region responsible for the 14 μm background, i.e., a few AU in radius. For a smaller region the background continuum will dominate, whereas for a much larger region line emission from the warm molecular gas will fill in or dominate the absorption. For a few AU region, the mass-loss rate would be of order 10^{-7} to $10^{-6} M_{\odot} \text{ yr}^{-1}$, assuming a density of $\geq 10^8 \text{ cm}^{-3}$, a total H_2 column of 10^{22} cm^{-2} , and a flow velocity of $\sim 25 \text{ km s}^{-1}$. IRS 46 does not show strong accretion signatures, and so a higher flow rate seems unlikely. Quantitative predictions in terms of velocities, column densities, densities, and temperatures of the molecular gas are needed to distinguish between the above models.

Regardless of the precise origin in the disk or disk wind, the high inferred excitation temperatures of 400–900 K and high abundances of HCN and C_2H_2 of 10^{-6} to 10^{-5} are characteristic of high-temperature chemistry. Hot chemistry in general is dominated by evaporation of the molecules from the grains with subsequent gas-phase processing. At high temperatures, the hydrocarbon and nitrogen chemistries are enhanced as most of the oxygen is converted into water by neutral-neutral reactions. The abundances of molecules such as C_2H_2 , CH_4 , and HCN can be increased by orders of magnitude (e.g., Doty et al., 2002; Rodgers & Charnley, 2003), while at the same time the formation of CO_2 is reduced since its primary formation route through OH is blocked. Interestingly, CO_2 has a lower excitation temperature in our observations. The most recent models of inner disk chemistry predict enhanced abundances of HCN and C_2H_2 . In particular, Markwick et al. (2002) give HCN, C_2H_2 , and CO_2 abundances of 10^{-6} to 10^{-5} in the inner 1 AU of a protoplanetary disk, in good agreement with the abundances found in this work.

In summary, we present the first detection of gaseous molecular absorption bands with *Spitzer* toward a solar-mass YSO, and these bands offer direct, unique probes of hot organic chemistry in its immediate environment. In addition, they provide independent constraints on the gas temperatures and velocity patterns. The most plausible scenario is that the absorption originates from the inner few AU of the circumstellar disk, perhaps at the footpoint of a disk wind. Further work, both observationally and theoretically, is required to prove this, including a determination of the velocity of IRS 46 itself and monitoring of the infrared lines at high spectral resolution to check for time variability of the radial velocity and/or absorbing column along the line of sight. This detection offers prospects for future high spectral and spatial resolution mid-infrared and submillimeter searches for these and other organic molecules in emission in more face-on disks.

Acknowledgements

We are grateful to J. Carr and J. Najita for useful discussions and to R. Tilanus for carrying out the JCMT observations. Astrochemistry in Leiden is supported by a Spinoza grant from NWO. Support for this work, part of the *Spitzer* Legacy Science Program, was provided by NASA through contracts 1224608, 1230779, and 1256316 issued by the Jet Propulsion Laboratory, California Institute of Technology, under NASA contract 1407.

Chapter 8

Infrared Molecular Starburst Fingerprints in Deeply Obscured (Ultra)Luminous Infrared Galaxy Nuclei

Abstract

High-resolution spectra of the *Spitzer* Space Telescope show vibration-rotation absorption bands of gaseous C₂H₂, HCN, and CO₂ molecules toward a sample of deeply obscured (U)LIRG nuclei. The observed bands reveal the presence of dense ($n \gtrsim 10^7 \text{ cm}^{-3}$), warm ($T_{\text{ex}} = 200 - 700 \text{ K}$) molecular gas with high column densities of these molecules ranging from a few 10^{15} to 10^{17} cm^{-2} . Abundances relative to H₂, inferred from the silicate optical depth, range from $\sim 10^{-7}$ to 10^{-6} and show no correlation with temperature. Theoretical studies show that the high abundances of both C₂H₂ and HCN exclude an X-ray dominated region (XDR) associated with the toroid surrounding an AGN as the origin of this dense warm molecular gas. Galactic massive protostars in the so-called hot-core phase have similar physical characteristics with comparable high abundances of C₂H₂, HCN, and CO₂ in the hot phase. However, the abundances of C₂H₂ and HCN and the C₂H₂/CO₂ and HCN/CO₂ ratios are much higher toward the (U)LIRGs in the cooler ($T_{\text{ex}} \lesssim 400 \text{ K}$) phase. We suggest that the warm dense molecular gas revealed by the mid-IR absorption lines is associated with a phase of deeply embedded star formation, where the extreme pressures and densities of the nuclear starburst environment have inhibited the expansion of H II regions and the global disruption of the star-forming molecular cloud cores, and have 'trapped' the star formation process in an 'extended' hot-core phase.

Lahuis, F., Spoon, H. W. W., Tielens, A. G. G. M., Doty, S. D., Armus, L., Charmandaris, V., Houck, J. R., Stauber, P., & van Dishoeck, E. F. 2007, ApJ, 659, 296

8.1 Introduction

One of the holy grails in the study of luminous and ultraluminous infrared galaxies (LIRGs and ULIRGs) is to elucidate the true nature of the central energy source. (U)LIRGs emit nearly all their energy in the mid- and far-infrared part of the spectrum. LIRGs have a luminosity $L_{8-1000\mu\text{m}} > 10^{10}L_{\odot}$ and ULIRGs $L_{8-1000\mu\text{m}} > 10^{12}L_{\odot}$, equal to the power output of quasars. (U)LIRGs are generally found in interacting and merging systems (e.g. Armus et al., 1987; Sanders et al., 1988b; Murphy et al., 1996). During the merger large amounts of gas and dust are concentrated toward the nucleus (e.g., Mihos & Hernquist, 1996), fueling a massive starburst and possibly a massive black hole (an AGN). (U)LIRGs are without doubt the most spectacular sites of star formation in the Universe, and if a substantial part of their energy originates from AGN activity, it would show the AGN in its very earliest deeply enshrouded phase.

The sensitive Infrared Spectrograph (IRS, Houck et al., 2004) on board the *Spitzer* Space Telescope (Werner et al., 2004) has revealed the richness, complexity, and diversity of the mid-infrared spectra toward a sample of deeply obscured (U)LIRGs (Armus et al., 2004, 2006, 2007; Spoon et al., 2005, 2006); see Genzel & Cesarsky (2000) for a review of results from the Infrared Space Observatory (ISO). The general characteristic of these spectra is the presence of deep, broad absorption of amorphous silicates, centered at 10 and 18 μm . In addition, the spectra show a large variety in absorption features of crystalline silicates, aliphatic hydrocarbons, water ice, and gas phase bands of hot CO (Spoon et al., 2004, 2007). Polycyclic aromatic hydrocarbons (PAH) emission bands are generally weak and in some cases absent. Absorption bands of more volatile ices (e.g. CO or CO₂), commonly detected in Galactic dense molecular clouds, are generally absent or very weak.

The very compact nuclei of deeply obscured (U)LIRGs are packed with gas. Molecular gas has been observed at millimeter wavelengths, through its low-lying pure rotational transitions, in (U)LIRG nuclei (e.g., Solomon et al., 1997; Downes & Solomon, 1998), see Aalto (2005) for a recent overview. In recent years millimeter emission lines of HCN and HCO⁺ have been observed revealing the presence of relatively dense ($n_{\text{H}} \sim 10^5 \text{ cm}^{-3}$) molecular gas (Imanishi et al., 2006; Kohno, 2005). However, the analysis of the millimeter emission lines is complicated as a result of beam dilution, which strongly depends on the molecules and transitions observed.

The IRS Short-High spectrometer (IRS-SH) on board the *Spitzer* Space Telescope allows, for the first time, the direct study of the very dense and warm molecular gas in the central regions of deeply obscured luminous and ultraluminous infrared galaxies through IR pencil-beam line-of-sight absorption spectroscopy against the continuum of individual nuclei or unresolved¹ double nuclei. In particular, the mid-infrared vibration-rotation bands of C₂H₂ and HCN uniquely trace warm ($100 < T < 1000 \text{ K}$) and dense ($n_{\text{H}} > 10^7 \text{ cm}^{-3}$) molecular gas. These bands have previously been detected primarily toward Galactic massive protostars (Lacy et al., 1989; Evans et al., 1991; Lahuis & van Dishoeck, 2000). They may prove to be a new strong tool to probe the heating sources of deeply obscured (U)LIRG nuclei (starburst or AGN activity).

¹The IRS SH slit width is 4.7'', equal to the size of the point-spread function at 19.5 μm .

Table 8.1. Observation details and basic source properties

Target	AOR key	Pipeline	Observed	Int. time ^a (sec)	z	$\log L_{\text{IR}}$ (L_{\odot})	$\tau_{9.7}$	Opt./NIR ^b Class	D_L^c (Mpc)
IRAS 17208-0014	4986624	S12.0.2	2004 Mar 27	$31 \times 6 \times 2$	0.0430	12.46	1.9	H II	188
Arp 220	4983808	S12.0.2	2004 Feb 29	$31 \times 6 \times 2$	0.0181	12.17	3.3	LINER ¹	78
IC 860	6652416	S13.2.0	2005 Feb 10	$121 \times 2 \times 2$	0.0112	10.96	2.1		48
IRAS 22491-1808	4990976	S13.2.0	2004 Jun 24	$121 \times 2 \times 2$	0.0773	12.19	1.1	Starburst ^{2,3}	346
NGC 4418	4935168	S13.2.0	2005 Jul 8	$31 \times 6 \times 2$	0.0073	11.03	4.4		31
IRAS 13218+0552	4979200	S13.2.0	2004 Jul 17	$121 \times 3 \times 2$	0.2051	12.71	0.8	QSO/Sey-1 ^{4,5}	998
IRAS 15250+3609	4983040	S12.0.2	2004 Mar 4	$31 \times 6 \times 2$	0.0554	12.05	3.8		244
IRAS 05189-2524	4969216	S13.2.0	2004 Mar 22	$31 \times 6 \times 2$	0.0426	12.19	0.4	Seyfert-2/ ¹⁶	186
Mrk 231	4978688	S13.2.0	2004 Apr 14	$31 \times 6 \times 2$	0.0422	12.52	0.8	Seyfert-1 ²	184
Mrk 273	4980224	S12.0.2	2004 Apr 14	$31 \times 6 \times 2$	0.0378	12.15	1.9	Seyfert-2	164
IRAS 00397-1312	4963584	S12.0.2	2004 Jan 4	$121 \times 3 \times 2$	0.2617	12.90	3.3		1317
IRAS 20100-4156	4989696	S13.2.0	2004 Apr 13	$121 \times 2 \times 2$	0.1296	12.65	3.3		601
UGC 5101	4973056	S13.2.0	2004 Mar 23	$31 \times 6 \times 2$	0.0400	12.00	1.7	LINER ³	164
IRAS 01003-2238	4972032	S12.0.2	2004 Jan 4	$121 \times 2 \times 2$	0.1177	12.29	0.7		542
IRAS 08572+3915	4972032	S13.2.0	2004 Apr 15	$31 \times 6 \times 2$	0.0584	12.10	4.2	LINER ¹	258
IRAS 02530+0211	6652160	S13.2.0	2005 Feb 10	$31 \times 3 \times 2$	0.0276	11.04	3.7		119
IRAS 12112+0305	4977664	S13.2.0	2004 Jan 4	$121 \times 2 \times 2$	0.0727	12.33	1.3	LINER ¹	324
IRAS 14348-1447	4981248	S13.2.0	2004 Feb 7	$121 \times 2 \times 2$	0.0827	12.35	2.1	LINER ²	372
NGC 6240	4985600	S13.2.0	2004 Mar 4	$31 \times 6 \times 2$	0.0245	11.84	1.2	LINER	119

^aRamp integration time \times number of cycles \times number of slit positions

^bOptical/near-IR spectral classifications taken from: (1) (Armus et al., 1989), (2) (Sanders et al., 1988a), (3) (Veilleux et al., 1995), (4) (Low et al., 1988), (5) (Darling & Giovanelli, 2002), (6) (Veilleux et al., 1997)

^c Assuming $H_0 = 71 \text{ km s}^{-1} \text{ Mpc}^{-1}$, $\Omega_M = 0.27$, $\Omega_\Lambda = 0.73$, and $\Omega_K = 0$

8.2 Observations

The observations presented in this paper are part of the *Spitzer* IRS observing programs (PID) 105 (IRS GTO ULIRG program, PI: J.R. Houck), 96 (IRS GTO program on nearby AGN, PI: J.R. Houck) and 1096 (Director's Discretionary Time [DDT] proposal, PI: H.W.W. Spoon). The IRS GTO ULIRG sample comprises ~ 100 ULIRGs in the redshift range $0.02 < z < 0.93$, selected primarily from the IRAS 2 Jy sample (Strauss et al., 1992), IRAS 1 Jy sample (Kim & Sanders, 1998), and the Faint Images of the Radio Sky at Twenty cm (FIRST)/IRAS radio-far-IR sample (Stanford et al., 2000). The samples of PIDs 96 and 1096 contain three additional ULIRGs (IRAS 04384–4848, IRAS 03000–2719, and IRAS 02113–2937) and three additional LIRGs (IRAS 02530+0211, IC 860, and NGC 4418). For all sources in this combined sample, low-resolution spectra ($R = \lambda/\Delta\lambda \sim 100$) have been obtained, while high-resolution spectra ($R = 600$) have been taken only for the brighter half of the sample.

All high-resolution spectra in this sample have been investigated for the presence of vibration-rotation absorption bands of C_2H_2 ($13.7 \mu\text{m}$), HCN ($14.02 \mu\text{m}$) and CO_2 ($15.0 \mu\text{m}$) against the nuclear continuum. Fifteen of the sources listed in Table 8.1 show absorption due to (some of) these species. Because of the low signal-to-noise ratio of the spectra and/or the low H column densities (as derived from the $9.7 \mu\text{m}$ silicate optical depth; see §8.3.3), the derived upper limits on the molecular column densities for all other sources do not place very stringent constraints on the C_2H_2 and HCN abundances. To illustrate this, four sources without positive detections with both a moderate-to-large hydrogen column density and good signal to noise spectra, are included in Tables 8.1 and 8.2. The upper limits on the C_2H_2 and HCN abundances fall within the range of derived abundances toward the fifteen sources.

Data reduction started from crosstalk corrected echelle images using S12 and S13 *Spitzer* archive data. Processing was done using the Cores to Disks (c2d) analysis pipeline (Kessler-Silacci et al., 2006; Lahuis et al., 2006a, , and Chapter 3). It includes echelle

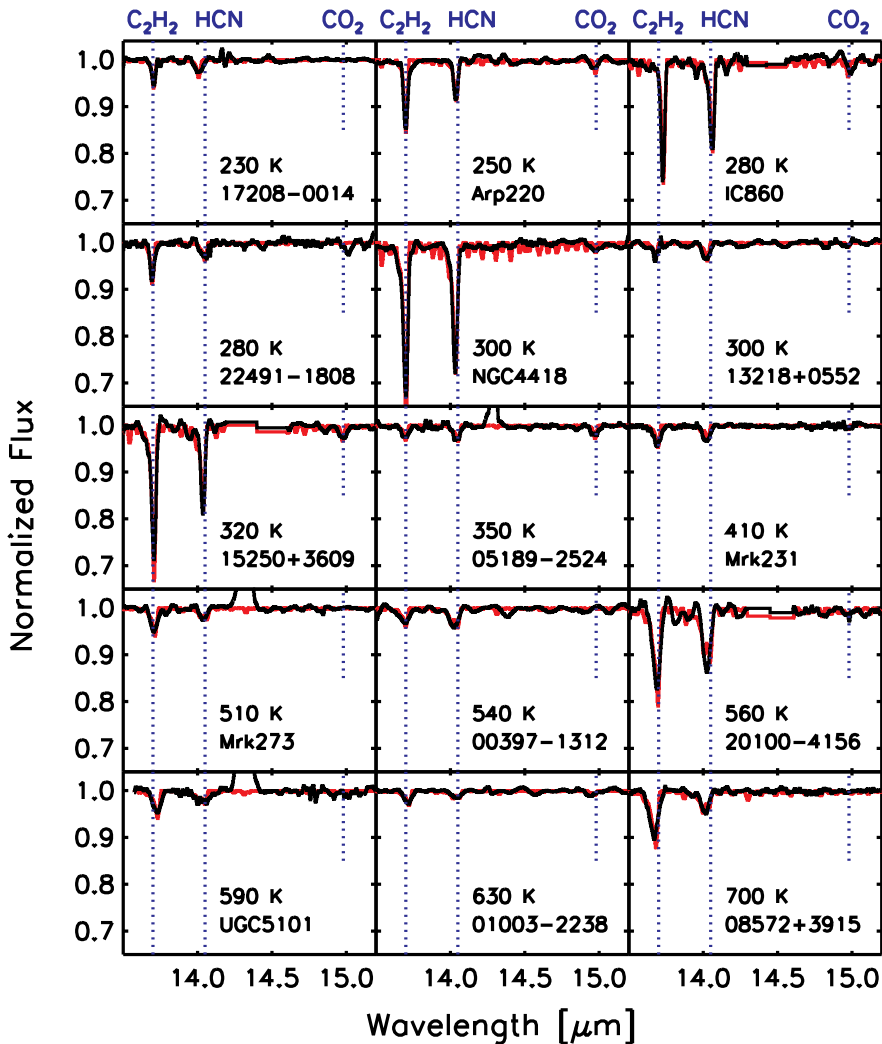


Figure 8.1 Continuum-divided *Spitzer* IRS spectra of a sample of (U)LIRGs showing the absorption bands of C_2H_2 and HCN and some of CO_2 . In the ApJ paper and the online thesis the best-fit synthetic spectra, assuming a single excitation temperature for all three molecules, are plotted in red. All spectra have been shifted to the rest wavelengths.

image analysis (among others bad pixel detection, image arithmetic, and optimal spectral extraction), defringing of the extracted spectra (Lahuis & Boogert, 2003), and spectral analysis (see §8.3.1). The optimal spectral extraction uses an analytical source profile defined and calibrated using a suite of calibrator stars. Calibration is done using MARCS stellar models provided by the *Spitzer* Science Center (Decin et al., 2004). The optimal spectral extraction employs a combined source and local sky fit. This provides wavelength-dependent sky estimates and allows discrimination between resolved and unresolved spectral features.

Figure 8.1 shows the continuum-divided, sky, and redshift-corrected spectra from 13.5 to 15.5 μm , covering the absorption bands of C_2H_2 , HCN, and CO_2 . Plotted in red are the best-fit single temperature synthetic spectra (see §8.3). Indicated with the dotted verticals are the positions of the ground-state Q -branch transitions of the three molecules. For IRAS 15250+3609, IRAS 20100–4156, and IC 860, a small section of the spectrum in between HCN and CO_2 is affected by artifacts in inter-order sections of the spectrum, and these sections have been clipped from the presented spectra.

8.3 Analysis

8.3.1 Molecular analysis

The *Spitzer* spectra unambiguously reveal the presence of the Q -branch transitions of C_2H_2 $\nu_5 = 1 - 0$, HCN $\nu_2 = 1 - 0$, and CO_2 $\nu_2 = 1 - 0$, each of which blends into a “broad” absorption feature. The corresponding P - and R -branch transitions of these species are difficult to observe with the *Spitzer* IRS due to spectral dilution at the IRS resolving power and the presence of instrumental fringe residuals with frequencies and amplitudes close to those of the P - and R -branch lines. The Q -branch transitions are analyzed using a pure absorption model assuming local thermodynamic equilibrium (LTE) excitation of the levels at a single temperature. The adopted method is described in detail in Lahuis & van Dishoeck (2000) and Boonman et al. (2003), which includes references to the molecular parameters and data used in the model. The main fit parameters are the excitation temperature and column density along the line of sight for a given intrinsic line width, defined by the Doppler b -value. It is assumed that the absorbing molecules have a covering factor of unity of the continuum, i.e. the mid-IR continuum is composed solely by the regions toward which the molecular absorption features arise. A covering factor less than unity, i.e. larger continuum emitting regions, increases the true optical depth of the absorption features, resulting in higher column densities and possibly lower temperatures (when lowest excitation lines saturate at large column densities).

The derived excitation parameters do not strongly depend on the exact value of b . Only for low values of b ($\lesssim 5 \text{ km s}^{-1}$) will saturation result in an underestimate of the column density for the sources with the largest column densities. Such low b -values are expected for quiescent gas, where thermal broadening dominates. However, non thermal broadening will likely dominate in the dense energetic interstellar medium (ISM) of the galactic nuclei and larger b -values are expected.

A direct estimate of b is obtained from spectrally resolved $\text{CO } \nu = 1 - 0$ absorption lines toward the north-west nucleus of IRAS 08572+3915 (Geballe et al., 2006), which shows a complex velocity structure. A low column density, cold CO component absorbs near the systemic velocity. The CO absorption is, however, dominated by a broad (FWHM $\sim 200 \text{ km s}^{-1}$) blueshifted warm ($\gtrsim 200 \text{ K}$) gas component. This is most likely the conglomerate of a velocity distribution over multiple lines of sight within the beam. The continuum confusion then requires a higher column density than that of $2 \times 10^{18} \text{ cm}^{-2}$ estimated from the observed optical depth by Geballe et al. (2006). We have fitted synthetic LTE absorption spectra to the higher excitation CO lines using the spectrum of Geballe et al. (2006), but with the spectral resolution reduced to match the observed profile width ($R \sim 1500$). This allows us to estimate a velocity averaged column density for a given b -value. Values $< 10 \text{ km s}^{-1}$ result in progressively poorer fits. Good fits

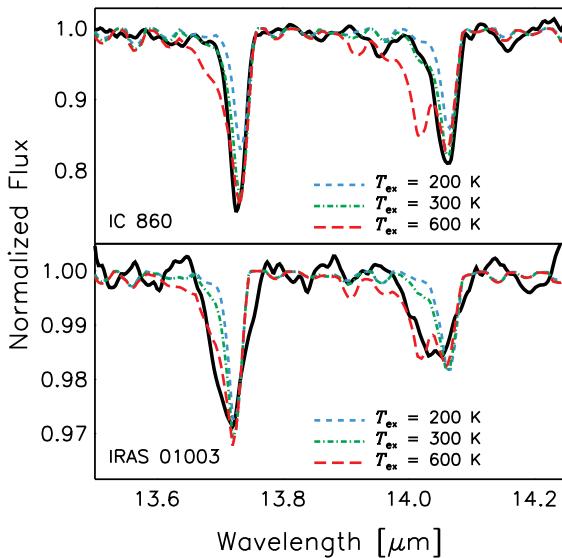


Figure 8.2 Illustration of the temperature sensitivity of the C_2H_2 and HCN Q -branch profiles in direct comparison to the observed spectra of IC 860 (best fit $T_{ex} = 280$ K) and IRAS 01003-2238 (best fit $T_{ex} = 630$ K). The shape of the Q -branch profile determines the derived excitation temperatures with an uncertainty of $\sim 30\%$. A better constrained error estimate is difficult to determine at the IRS resolution.

are made for b -values of $10 - 25 \text{ km s}^{-1}$ requiring column densities of $\sim 2 \times 10^{19}$ down to $\sim 5 \times 10^{18} \text{ cm}^{-2}$. The Doppler b -value has therefore been fixed to 20 km s^{-1} for all sources.

Recent observations using TEXES (Lacy et al., 2002), a visitor instrument on Gemini-North, have revealed spectrally resolved (FWHM $\sim 80 \text{ km s}^{-1}$) blueshifted absorption in the $C_2H_2 \nu_5 = 1 - 0 R(13)$ ro-vibrational line toward one of our sources, NGC 4418 (C. Knez 2006, private communication). The current data do not allow us to put more stringent constraints on the Doppler b -value. However, the spectrally resolved C_2H_2 absorption could be an indication that multiple (spatial and velocity) components of the warm and dense gas are common in (U)LIRG nuclei.

8.3.2 Fit results

Table 8.2 lists the derived excitation temperatures and column densities from best fit synthetic spectra to the continuum divided (U)LIRG spectra. Excitation temperatures ranging from 200 to 700 K and column densities of a few 10^{15} to 10^{17} cm^{-2} are observed. These results are derived from a simultaneous fit to the three absorption bands, in which the excitation temperature, set to be the same for all three molecules, is constrained by the Q -branch profiles of C_2H_2 and HCN. Since the analysis is restricted to analysis of the resolved Q -branches (see §8.3.1), the derived excitation temperatures are not well constrained ($\sim 30\%$). However, it does clearly allow us to discriminate between molecular gas with warm ($\sim 200 - 300$ K) and hot ($\sim 500 - 700$ K) excitation temperatures. This is illustrated in Figure 8.2 by fits to the observed absorption profiles of IC 860 and IRAS 01003-2238, for which we derive excitation temperatures of 280 and 630 K, respectively.

The Q -branch profiles of C_2H_2 and HCN reveal significant contributions to the absorption from relatively high rotational levels. Hence, given the high critical density of these levels, the absorbing gas is likely very dense ($n \gtrsim 10^7 \text{ cm}^{-3}$). Observations of

Table 8.2. LTE excitation parameters and spectral characteristics

Target	T_{ex}^{a} (K)	$N_{\text{C}_2\text{H}_2}^{\text{a}}$ 10^{16} (cm^{-2})	$N_{\text{HCN}}^{\text{a}}$ 10^{16} (cm^{-2})	$N_{\text{CO}_2}^{\text{a}}$ 10^{16} (cm^{-2})	N_{H_2} 10^{22} (cm^{-2})	$x_{\text{C}_2\text{H}_2}^{\text{b}}$ 10^{-8}	$x_{\text{HCN}}^{\text{b}}$ 10^{-8}	$x_{\text{CO}_2}^{\text{b}}$ 10^{-8}	cont. ^c (Jy)	S/N ^d
17208-0014	230	0.6	1.2	< 0.2	3.3	18	36	< 6	0.20	200
Arp 220	250	1.7	2.9	0.7	5.8	29	50	12	0.93	150
IC 860	280	3.1	7.2	0.9	3.7	84	195	24	0.09	150
22491-1808	280	1.0	1.4	< 0.3	1.9	53	74	< 16	0.07	130
NGC 4418	300	5.3	12.	< 0.4	7.7	69	156	< 5	2.34	150
13218+0552	300	0.4	1.5	< 0.5	1.4	28	107	< 36	0.26	180
15250+3609	320	4.7	7.0	0.7	6.7	70	105	10	0.27	90
05189-2524	350	0.4	1.5	0.8	0.7	57	214	114	1.05	200
Mrk 231	410	0.6	1.4	< 0.4	1.4	43	100	< 29	2.83	200
Mrk 273	510	0.9	1.7	< 0.4	3.3	27	52	< 12	0.37	200
00397-1312	540	0.6	3.0	< 0.4	5.8	10	52	< 7	0.12	150
20100-4156	560	3.8	8.9	< 0.9	5.8	66	153	< 15	0.11	70
UGC 5101	590	1.0	2.2	< 0.5	3.0	33	73	< 17	0.24	130
01003-2238	630	0.5	1.3	< 0.8	1.2	42	108	< 67	0.27	200
08572+3915	700	2.4	3.7	< 0.5	7.4	32	50	< 7	0.74	150
02530+0211	300 ^e	< 0.5	< 3	< 0.3	6.5	< 8	< 46	< 5	0.25	100
12112+0305	300 ^e	< 0.8	< 2.3	< 0.6	3.0	< 27	< 77	< 20	0.07	150
14348-1447	300 ^e	< 0.5	< 1	< 0.2	3.7	< 14	< 27	< 5	0.07	80
NGC 6240	300 ^e	< 0.2	< 0.7	< 0.6	2.1	< 10	< 33	< 29	0.68	100

^aThe excitation temperature is poorly constrained and can be uncertain up to 30%. See §8.3.2 and Figure 8.2 for details.

^bAbundances with respect to H_2 assuming $N_{\text{H}} = \tau_{9.7}(3.5 \times 10^{22}) \text{ cm}^{-2}$ and $N_{\text{H}} = 2 \times N_{\text{H}_2}$ (see §8.3.3).

^cContinuum at 14 μm in the rest wavelength frame.

^dSignal-to-noise ratio (S/N) estimated from the residuals after subtraction of the synthetic spectrum. It varies over the covered wavelength range.

^eTemperature fixed to 300 K for derivation of column density upper limit estimates.

the ro-vibrational transitions of CO in IRAS 08572+3915 and IRAS 00183-7111 indeed imply densities in excess of $3 \times 10^6 \text{ cm}^{-3}$ (Geballe et al., 2006; Spoon et al., 2004).

8.3.3 Abundances

The derived column densities are translated into abundances by using a total hydrogen column density obtained from the apparent optical depth of the 9.7 μm silicate absorption band listed in Table 8.1. The optical depth is converted assuming

$$N_{\text{H}} = \tau_{9.7}(3.5 \times 10^{22}) \text{ cm}^{-2}$$

appropriate for the dust in the solar neighbourhood (Roche & Aitken, 1984, 1985).

This relation is most appropriate for embedded (extinction dominated) sources when probing the absorption along the pencil beam line of sight toward the warm central continuum emitting region. To illustrate, for the sample of Galactic massive protostars (see §8.4.3), the hydrogen column density derived using the silicate optical depth estimated from the ISO-SWS archive spectra agrees within a factor of two with the hydrogen column density derived from CO $\nu = 1 - 0$ measurements (Mitchell et al., 1990; Lahuis & van Dishoeck, 2000).

Another estimate of the applicability of this method is provided through the analysis of the 4.6 μm CO $\nu = 1 - 0$ absorption spectrum toward the source IRAS 08572+3915 NW, which gives CO column densities of $\sim 5 \times 10^{18}$ up to $\sim 2 \times 10^{19} \text{ cm}^{-2}$, depending on the assumed value of b (see §8.3.1). Adopting $N_{\text{CO}}/N_{\text{H}} = 10^{-4}$ (all gas-phase carbon in CO), this results in $N_{\text{H}} = 5 \times 10^{22}$ to $2 \times 10^{23} \text{ cm}^{-2}$. This is in reasonable agreement with the hydrogen column density derived from the silicate optical depth ($N_{\text{H}} \sim 1.5 \times 10^{23} \text{ cm}^{-2}$). If anything, the IRAS 08572+3915 NW data suggest the hydrogen column density might be slightly overestimated (e.g. as a result of foreground

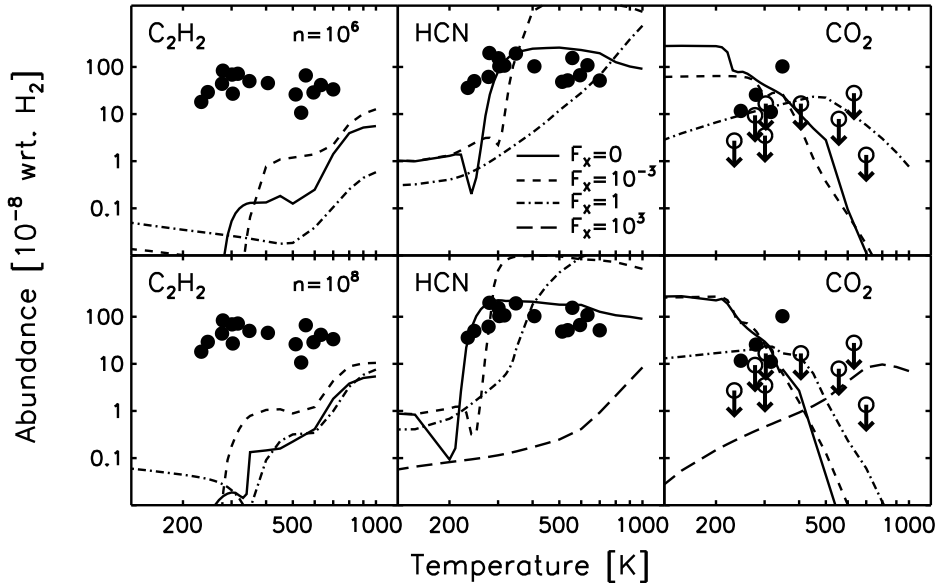


Figure 8.3 Results of equilibrium X-ray-enhanced chemical models for the three observed molecules. The calculated abundances are shown for moderate (10^6 cm $^{-3}$) and high density (10^8 cm $^{-3}$) and for four X-ray flux levels ($F_x = 0, 10^{-3}, 1$ and 10^3 erg cm $^{-2}$ s $^{-1}$ plotted with solid, dashed, dot-dashed, and long-dashed lines, respectively). Note that except for HCN and CO₂ at high density, the abundances for the highest X-ray flux are below the plotted range. Overplotted are the observed abundances. Details of the model can be found in Stäuber et al. (2005); Stäuber et al. (2006).

extinction) resulting in underestimating the derived molecular abundances. We assume a similar uncertainty for the other sources.

The derived abundances and H₂ column densities (assuming $N_{\text{H}_2} = N_{\text{H}}/2$) are listed in Table 8.2. The HCN abundance is up to three orders of magnitude higher than in cold molecular clouds (Bergin & Langer, 1997). High abundances of HCN, C₂H₂, and CO₂ have also been measured for Galactic massive protostars (see §8.4.3). Figures 8.3 and 8.4 compare the abundances to chemical models and results from studies of Galactic massive young stellar objects (§8.4).

8.3.4 Gas temperature

The derived excitation temperatures range from 200 to 700 K. While statistics are small, of the seven sources with the highest gas excitation temperatures ($T_{\text{ex}} = 400 - 700$ K), five sources show the highest $5.5 - 28 \mu\text{m}$ continuum flux ratio. These galaxies also show a rising near-IR continuum typical for hot dust while the other galaxies show a decreasing near-IR continuum characteristic for emission dominated by stellar photospheres. It seems thus that there is a connection between the observed dust and molecular excitation temperatures.

The presence of absorption (rather than emission) lines implies a strong gradient in the temperature and an underlying hot-dust continuum against which the absorption

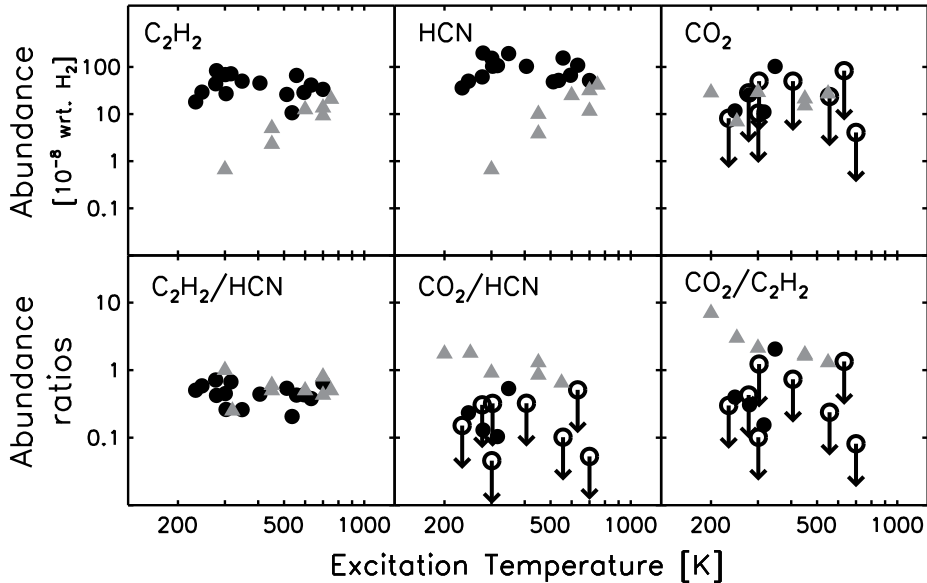


Figure 8.4 *Top*: Observed C₂H₂, HCN, and CO₂ abundances using a total H₂ column obtained from the 9.8 μm silicate absorption band. *Bottom*: Abundance ratios of C₂H₂, HCN and CO₂. Both the absolute abundances and the abundance ratios are indicated with circles and are presented as functions of excitation temperature. Included are the observed values toward a sample of Galactic massive YSOs (Boonman et al., 2003; Lahuis & van Dishoeck, 2000) plotted with grey triangles. The derived absolute abundances toward the (U)LIRGs show significant enhancements in the abundances of C₂H₂ and HCN for sources with excitation temperatures below 500 K. The C₂H₂/HCN abundance ratios are quite similar however, the CO₂/C₂H₂ and CO₂/HCN ratios toward the (U)LIRGs are systematically lower than toward the Galactic massive YSOs, suggesting that a different chemistry may apply.

lines are formed. However, the derived excitation temperatures of the molecular gas for the warmest sources ($T_{ex} = 400 - 700$ K) are higher by a factor of 2–3 than the mid-IR color temperature derived from the 5.5 – 28.0 μm flux ratio. While the discrepancy between the excitation temperatures and the mid-IR color temperature may (in part) reflect the uncertainties in the analysis, the observed colder dust continuum may point towards the importance of continuum extinction by (a shell of) colder foreground dust exterior to the C₂H₂ and HCN absorbing layer, or the predominance of emission of cold nuclear dust within the IRS aperture (i.e. a small beam filling factor for the warm dust and gas). Both may result in an added uncertainty in the derived abundances resulting from overestimating the hydrogen column density or from a covering factor of the molecule rich warm gas less than unity (see §8.3.1).

8.4 Discussion

8.4.1 Warm molecular gas in (U)LIRGs

The *Spitzer* IRS spectra reported here reveal surprisingly strong mid-IR absorption bands of C_2H_2 , HCN, and CO_2 toward a sample of (U)LIRG nuclei. These absorptions reveal the presence of copious amounts of warm molecular material and are in line with earlier detections of warm CO gas (Spoon et al., 2004, 2006; Geballe et al., 2006). This molecular gas is very dense ($n \gtrsim 3 \times 10^6 \text{ cm}^{-3}$) and warm ($T \sim 200 - 700 \text{ K}$). Given the column density and estimated density, this gas occupies only a small fraction of the nuclear region ($\sim 0.01 \text{ pc}$) and, given its high temperature, is likely located near the intrinsic mid-infrared source of luminosity of these regions.

At present there are still substantial uncertainties in accurately inferring the nature of the power source dominating the bolometric luminosity in infrared luminous galaxies. As discussed in Armus et al. (2007), it appears that there are disagreements among various diagnostic diagrams based on line ratios, continuum colors or PAH equivalent width. Perusal of the $2 - 40 \mu\text{m}$ spectra reveal that the sources with molecular gas absorptions appear to be a “mixed bag.” While most sources show a deep silicate feature, some (e.g., Mrk 231, IRAS 01003-2238, IRAS 05189-2524, and IRAS 13218+0552) do not. Indeed, the $2 - 40 \mu\text{m}$ continuum spectra of these sources show strong similarities with the spectra of bona fide AGN-dominated spectra with shallow silicate features. In contrast, sources like IRAS 17208-0014 and IRAS 22491-1808 look quite starburst-like. Finally, sources such as IRAS 08572+3915 show neither signs of starburst activity (e.g., PAH features) nor signs of AGN activity (e.g., high ionization lines or a broad $H\alpha$ line). While the presence of hot dust, as visible in the near-IR, may be taken as evidence for the presence of an embedded AGN in this source, any deeply obscured source, including deeply embedded protostars, will produce hot dust. Indeed, the overall mid-IR spectrum of IRAS 08572+3915 resembles that of many galactic massive protostars, such as AFGL 2591, with a preponderance of dust absorption features.

The C_2H_2 , HCN, and CO_2 molecular lines may provide a new probe of the conditions in the inner deeply obscured nuclei and hence shed light on the ultimate power source of (U)LIRGs; e.g., starburst phenomena versus AGN activity. In particular, the presence of copious amounts of warm molecular gas enriched in C_2H_2 , HCN, and CO_2 is common in regions of massive star formation (Boonman et al., 2003; Lahuis & van Dishoeck, 2000; Lacy et al., 1989; Evans et al., 1991), while, on the other hand, X-rays associated with a central black hole can influence molecular chemistry and abundances far beyond the mean free path length of stellar (E)UV photons. The molecular observations are discussed in the light of these scenarios in §§8.4.2, 8.4.4, and 8.4.3. While the possible errors associated with the derived abundances are recognized, the discussion will center on Figures 8.3 and 8.4.

8.4.2 AGN activity and X-ray-driven chemistry

Submillimeter studies have revealed high HCN/CO (and HCN/ HCO^+) abundance ratios in Seyfert type I nuclei, and this has been taken as an indication of the importance of X-ray illumination for the composition of the molecular gas in these nuclei (Imanishi et al., 2006; Kohno, 2005). Some of the sources in our sample are known to harbor an AGN. In particular, Mrk 231 and IRAS 13218+0552 are QSOs; IRAS 08572+3915 and

UGC 5101 are LINERs; and IRAS 01003-2238, IRAS 05189-2524, and Mrk 273 have optical LINER/Seyfert 2 spectra (see Table 8.1). Hence, the observed high abundance of HCN, and by inference of C_2H_2 (which has no pure rotational transitions), may indicate the presence of a buried AGN in all of our sources. The complex geometry and inhomogeneous dust distribution associated with the central toroid may then preclude our detection of the putative X-rays photons from the central engine driving the chemistry of the molecular gas. The mid-IR observations presented in this paper add to the submillimeter results the predominance of *warm* molecular gas. Within the AGN heating scenario, it seems obvious to attribute the high temperature of the molecular gas to the importance of X-ray heating in a so-called X-ray dominated region (XDR, Maloney et al., 1996; Meijerink & Spaans, 2005). Alternatively, Gao & Solomon (2004) argue that most (U)LIRGs are dominated by starburst power rather than AGN power, based on the HCN $J = 1 - 0$ luminosity and CO $J = 1 - 0$ luminosity relation. In a starburst scenario, the HCN/CO ratio traces the amount of dense molecular gas in the galactic ISM. Our observations may present an additional test for these two scenarios.

X-rays are not only an efficient heating agent of the gas, but also have a major influence on the chemical composition. This has been explored in the context of AGNs by Maloney et al. (1996); Meijerink & Spaans (2005), and for regions around protostars by Stäuber et al. (2005); Stauber et al. (2006). At the high densities relevant for these regions, the gas temperature is set by a balance between X-ray heating and gas-dust collisional cooling. As an example, a gas temperature of 200 K at a density of $\sim 3 \times 10^6 \text{ cm}^{-3}$ requires a X-ray flux of $\sim 30 \text{ erg cm}^{-2} \text{ s}^{-1}$, which for a typical Seyfert galaxy with an X-ray luminosity of $10^{44} \text{ erg s}^{-1}$ corresponds to a distance of 50 pc for an unobscured view of the central engine. For the molecular features to be seen in absorption, the mid-IR continuum has to arise from an inner, warmer zone (e.g., exposed to a higher X-ray flux). Since most of these (U)LIRGs show no evidence for strong X-ray emission while the column density associated with the molecular gas ($10^{22} - 10^{23} \text{ cm}^{-2}$) is small compared to X-ray attenuation lengths, in this AGN scenario, the direct view of the nucleus would have to be blocked by a high column density, edge-on toroid, while the warm molecular gas is offset to the polar regions and has a little-obstructed view of the nucleus.

An AGN origin for the high abundance of warm HCN, C_2H_2 , and CO_2 in these (U)LIRGs, however, faces severe theoretical difficulties. Specifically, the high X-ray flux required to explain the observed temperatures readily dissociates the molecules and drives the gas atomic (Maloney et al., 1996; Meijerink & Spaans, 2005). Indeed, calculated HCN abundances are typically less than 10^{-8} with respect to H in X-ray illuminated gas, while C_2H_2 is virtually destroyed for X-ray fluxes in excess of $1 \text{ erg cm}^{-2} \text{ s}^{-1}$. This is illustrated in Figure 8.3, which presents the static steady state chemical composition after equilibrium is reached ($\sim 10^5 \text{ yr}$) for clouds illuminated by X-rays. Here, “static” means that the chemistry has been evolved in time while the X-ray flux, temperature, and density are fixed until steady state is achieved in the chemical abundances (see also Stäuber et al., 2005; Stauber et al., 2006). The X-ray spectrum is assumed to be thermal in nature, with $T_X = 3 \times 10^7 \text{ K}$. The chemistry is relatively insensitive to the assumed shape of the spectrum (e.g., Maloney et al., 1996). As these models demonstrate, strong X-ray irradiation leads to decreased abundances of molecular species such as HCN and C_2H_2 . These results are consistent with earlier studies (e.g., Lepp & Dalgarno, 1996), which show an initial increase in the HCN abundance

with increasing ionization rate (ξ/n_{H} up to $10^{-18} \text{ cm}^{-3} \text{ s}^{-1}$) but then an effectively complete destruction of HCN for $\xi/n_{\text{H}} \gtrsim 10^{-17} \text{ cm}^{-3} \text{ s}^{-1}$. For comparison, the X-ray flux implied by a gas temperature of 200 K ($\simeq 30 \text{ erg cm}^{-2} \text{ s}^{-1}$) corresponds to an ionization rate of $5 \times 10^{-17} \text{ cm}^{-3} \text{ s}^{-1}$ at a density of 10^6 cm^{-3} . Clearly, the warm molecular gas revealed by these observations is inconsistent with strong X-ray illumination.

8.4.3 Static hot-core chemistry

At first sight our mid-infrared results resemble those toward a sample of massive Galactic young stellar objects (YSOs). For these, the molecular absorption features originate in the warm, dense gas near the newly formed star during the so-called hot core phase (Boonman et al., 2003; Lahuis & van Dishoeck, 2000; Lacy et al., 1989; Evans et al., 1991). This is generally thought to represent a very early phase ($\Delta t \leq 10^5 \text{ yr}$) in the formation of massive stars, during the transition from the deeply embedded stage to the phase where ionizing photons can escape the protostellar accretion envelope and create first a hyper- and later an ultra-compact HII region (see review by Cesaroni, 2005a). The molecular composition of the hot core is very different from that of cold molecular clouds. This is thought to reflect the evaporation of ices, resulting from accretion and surface chemistry during the cold preceding dark cloud phase, when the envelope is heated by the newly formed star (Walmsley & Schilke, 1993). Subsequent high temperature gas-phase chemistry significantly enhances the abundance of e.g. CH_4 , C_2H_2 , and HCN up to three orders of magnitude, compared to cold dense molecular cloud abundances, for the most evolved sources (Viti & Williams, 1999; Doty et al., 2002; Rodgers & Charnley, 2003).

In Figure 8.4 the observed abundances and abundance ratios toward the (U)LIRGs are compared to those of a sample of Galactic massive YSOs. Both the YSO and the (U)LIRG sample show comparable, large variations in gas temperature and abundances. However, the HCN and C_2H_2 abundances show a positive correlation with the gas temperature for the YSO sample but not for the (U)LIRG sample. Indeed, at low temperatures ($< 400 \text{ K}$), the (U)LIRG abundances are some two orders of magnitude larger than those in YSO spectra.

For the Galactic YSOs, the observed correlation between the excitation temperature and the observed abundances (Fig. 8.4) are in fair agreement with chemical models for such regions (Stäuber et al., 2005). The absence of a similar temperature correlation for (U)LIRGs may reflect a systematic (and large) error in the abundance determination (§8.3.3) or it may reflect a true difference between the chemical or physical evolution of the warm gas of the YSOs and (U)LIRGs. In this respect, we note that the $\text{C}_2\text{H}_2/\text{HCN}$ ratios for both samples are very similar; however, the CO_2/HCN and $\text{CO}_2/\text{C}_2\text{H}_2$ ratios are reduced for the (U)LIRG sample up to an order of magnitude. If static steady state hot-core chemistry were to apply to the (U)LIRGs as it does to the YSOs, CO_2 would have been detected toward most of the sources in our sample. The fact that it has not suggests that a different chemistry may apply to the warm molecular gas in these (U)LIRGs.

8.4.4 Pressure confined starburst chemistry

Static steady state hot-core and X-ray chemical models have difficulties consistently reproducing the observed high abundances of warm C_2H_2 and HCN gas and low abun-

dance of CO₂ gas for most of our (U)LIRG sample. Essentially, static chemistry has a hard time producing high abundance of HCN and C₂H₂ in the warm (100 – 400 K) gas characteristic for most of our (U)LIRG sample, while at the same time reducing the CO₂ abundance. One possible solution to this conundrum is to produce high C₂H₂ and HCN, and low CO₂ abundances in hot gas (\gtrsim 800 K), and then transport it outward to the cooler gas on a dynamical timescale that is rapid compared to the chemical timescale. At high temperatures, the hydrocarbon and nitrogen chemistries are enhanced, as most of the oxygen is converted into water by neutral-neutral reactions. The abundances of molecules such as C₂H₂, CH₄, and HCN can be increased by orders of magnitude (e.g., Doty et al., 2002; Rodgers & Charnley, 2003) while at the same time the formation of CO₂ is reduced as its primary formation route through OH is blocked. For cold Galactic molecular clouds, the chemical timescale is set by the cosmic ray ionization rate and is about 3×10^5 yr, independent of density (Glassgold & Langer, 1973). In a (U)LIRG (or AGN) environment, the cosmic ray flux may be increased considerably, shortening this timescale. Likewise, neutral-neutral reaction channels may open up in warm gas, further reducing the chemical timescale. In any case, these timescales are much shorter than the evolutionary timescale of massive stars or of the starburst. With the typical sizescale of the warm molecular zone ($\sim 3 \times 10^{16}$ cm), a timescale of 3×10^5 yr translates into a ‘diffusion’ velocity of only 0.03 km s⁻¹. Even a 100 times faster chemical timescale only requires a ‘diffusion’ velocity of a few km s⁻¹. Since the chemical models are well capable of explaining high abundances for both C₂H₂ and HCN and a low abundance for CO₂ at high temperatures and densities, and in light of the discussion above, this “mixing” is attributed to the global activity created by pressure-confined massive starburst activity. The strong gravitational potential in the nuclei of these galaxies inhibits the disruption of the surrounding warm molecular envelopes by H II regions and supernovae, while producing sufficient turbulent (or wind) motion to distribute warm C₂H₂- and HCN-rich and CO₂-poor gas in the colder outer envelope regions.

8.5 Summary

We have observed the absorption lines due to the *Q*-branch transitions of C₂H₂, HCN, and CO₂ in the mid-IR spectra of a large number of (U)LIRGs. These observations reveal for the first time the presence of copious amounts of warm (200-700 K), dense ($n > 10^7$ cm⁻³) molecular gas in these nuclei. The origin of this warm molecular gas is unclear. Theoretical models show that the X-ray fluxes implied by the elevated gas temperatures rapidly destroy these molecules, and hence it is unlikely that this warm molecular gas is associated with a dense toroid surrounding an active central engine. Warm, dense gas rich in C₂H₂, HCN, and CO₂ is commonly observed towards galactic massive protostars and is associated with a short-lived phase, the hot-core phase, before advancing ionization fronts disrupt the core. The high molecular abundances in galactic hot-cores are well understood chemically. However, the derived abundances of C₂H₂ and HCN for the cooler (U)LIRGs ($T_{\text{ex}} \simeq 200 - 400$ K) in our sample as well as the C₂H₂/CO₂ and HCN/CO₂ ratios are very different from those in galactic protostars. We suggest that this warm molecular gas is associated with a phase of deeply embedded star formation in (U)LIRGs, where the high pressures and densities have inhibited the disruption of the star forming, molecular cores by prohibiting the expansion of H II regions, trapping the star formation process in an extended hot-core phase. The

chemical differences between these (U)LIRGs and galactic hot-cores may then reflect enhanced mixing between warm and cold phases due to the high degree of turbulence or wind motion associated with extreme starburst environments. Pressure-confined massive starburst activity may thus be the driving energy source behind the observed C₂H₂ and HCN rich warm molecular gas and be responsible for most of the near-IR characteristics of the deeply obscured (U)LIRGs.

The current analysis is predominately based on the observed abundances derived from moderate resolution, mid-IR vibration-rotation absorption bands of C₂H₂ and HCN. This analysis can be extended using high-resolution, velocity resolved, ground-based studies of the *P*- and *R*-branches of these molecules, as well as from the $\nu = 1 - 0$ rotation-vibration band of CO. In addition, observations of more molecular rotation-vibration bands and high-excitation submillimeter lines of a large sample of molecules may be instrumental for progress in this field. Specifically, velocity and spatially resolved infrared and millimeter data can constrain the source morphology. In combination with optimized physico-chemical models for individual sources, it may become possible to draw firm conclusions about the physical characteristics of the warm molecular gas and the true nature of the power sources in the (U)LIRG nuclei.

Acknowledgements

The authors would like to thank Tom Geballe for sharing early results and the CO data of IRAS 08572+3915 NW; John Lacy and Claudia Knez for sharing the TEXES data; and Bernhard Brandl, Kees Dullemond, Masa Imanishi, David Rupke, and Marco Spaans for many useful discussions. Astrochemistry in Leiden is supported by a Spinoza grant from NWO.

Bibliography

- Aalto, S. 2005, in IAU Symposium, ed. D. C. Lis, G. A. Blake, & E. Herbst, 270
- Alexander, R. D., Clarke, C. J., & Pringle, J. E. 2005, Constraints on the ionizing flux emitted by T Tauri stars, *MNRAS*, 358, 283
- . 2006, Photoevaporation of protoplanetary discs - I. Hydrodynamic models, *MNRAS*, 369, 216
- Allamandola, L. J., Sandford, S. A., Tielens, A. G. G. M., & Herbst, T. M. 1992, Infrared spectroscopy of dense clouds in the C-H stretch region - Methanol and 'diamonds', *ApJ*, 399, 134
- André, P. & Montmerle, T. 1994, From T Tauri stars to protostars: Circumstellar material and young stellar objects in the rho Ophiuchi cloud, *ApJ*, 420, 837
- Armus, L. et al. 2006, Detection of the Buried Active Galactic Nucleus in NGC 6240 with the Infrared Spectrograph on the Spitzer Space Telescope, *ApJ*, 640, 204
- . 2007, Observations of Ultraluminous Infrared Galaxies with the Infrared Spectrograph on the Spitzer Space Telescope. II. The IRAS Bright Galaxy Sample, *ApJ*, 656, 148
- . 2004, Observations of Ultraluminous Infrared Galaxies with the Infrared Spectrograph (IRS) on the Spitzer Space Telescope: Early Results on Markarian 1014, Markarian 463, and UGC 5101, *ApJS*, 154, 178
- Armus, L., Heckman, T. M., & Miley, G. K. 1987, Multicolor optical imaging of powerful far-infrared galaxies - More evidence for a link between galaxy mergers and far-infrared emission, *AJ*, 94, 831
- . 1989, Long-slit optical spectroscopy of powerful far-infrared galaxies - The nature of the nuclear energy source, *ApJ*, 347, 727
- Azcarate, I. N., Cersosimo, J. C., & Colomb, F. R. 1986, Low density ionized gas associated with M 17, G 333.3-0.4 and RCW 74., *Revista Mexicana de Astronomia y Astrofisica*, 13, 15
- Banhidi, Z. & et al. 2007, H₂ Spectral Mapping in Serpens, , in prep
- Baraffe, I. & Chabrier, G. 1996, in ASP Conf. Ser. 98: From Stars to Galaxies: the Impact of Stellar Physics on Galaxy Evolution, ed. C. Leitherer, U. Fritze-von-Alvensleben, & J. Huchra, 209
- Bary, J. S., Weintraub, D. A., & Kastner, J. H. 2003, Detections of Rovibrational H₂ Emission from the Disks of T Tauri Stars, *ApJ*, 586, 1136
- Beltrán, M. T., Cesaroni, R., Neri, R., Codella, C., Furuya, R. S., Testi, L., & Olmi, L. 2005, A detailed study of the rotating toroids in G31.41+0.31 and G24.78+0.08, *A&A*, 435, 901
- Bergin, E. A. & Langer, W. D. 1997, Chemical Evolution in Preprotostellar and Protostellar Cores, *ApJ*, 486, 316
- Bernstein, M. P., Sandford, S. A., Allamandola, L. J., Chang, S., & Scharberg, M. A. 1995, Organic Compounds Produced by Photolysis of Realistic Interstellar and Cometary Ice Analogs Containing Methanol, *ApJ*, 454, 327
- Blake, G. A. & Boogert, A. C. A. 2004, High-Resolution 4.7 Micron Keck/NIRSPEC Spectroscopy of the CO Emission from the Disks Surrounding Herbig Ae Stars, *ApJ*, 606, L73
- Bockelée-Morvan, D. et al. 2000, New molecules found in comet C/1995 O1 (Hale-Bopp). Investigating the link between cometary and interstellar material, *A&A*, 353, 1101
- Bontemps, S. et al. 2001, ISOCAM observations of the rho Ophiuchi cloud: Luminosity and mass functions of the pre-main sequence embedded cluster, *A&A*, 372, 173
- Boogert, A. C. A. et al. 2000, ISO-SWS observations of interstellar solid ¹³CO₂: heated ice and the Galactic ¹²C/¹³C abundance ratio, *A&A*, 353, 349
- Boogert, A. C. A., Helmich, F. P., van Dishoeck, E. F., Schutte, W. A., Tielens, A. G. G. M., & Whittet, D. C. B. 1998, The gas/solid methane abundance ratio toward deeply embedded protostars, *A&A*, 336, 352
- Boonman, A. M. S., van Dishoeck, E. F., Lahuis, F., & Doty, S. D. 2003, Gas-phase CO₂ toward massive protostars, *A&A*, 399, 1063
- Boonman, A. M. S., Wright, C. M., & van Dishoeck, E. F. 1999, in The Physics and Chemistry of the Interstellar Medium, Proceedings of the 3rd Cologne-Zermatt Symposium, held in Zermatt, September 22-25, 1998, Eds.: V. Ossenkopf, J. Stutzki, and G. Winnewisser, GCA-Verlag Herdecke, ISBN 3-928973-95-9, ed. V. Ossenkopf, J. Stutzki, & G. Winnewisser, 275

- Boudin, N., Schutte, W. A., & Greenberg, J. M. 1998, Constraints on the abundances of various molecules in interstellar ice: laboratory studies and astrophysical implications, *A&A*, 331, 749
- Bouwman, J., de Koter, A., Dominik, C., & Waters, L. B. F. M. 2003, The origin of crystalline silicates in the Herbig Be star HD 100546 and in comet Hale-Bopp, *A&A*, 401, 577
- Brittain, S. D., Rettig, T. W., Simon, T., Kulesa, C., DiSanti, M. A., & Dello Russo, N. 2003, CO Emission from Disks around AB Aurigae and HD 141569: Implications for Disk Structure and Planet Formation Timescales, *ApJ*, 588, 535
- Brooke, T. Y. et al. 2007, The Spitzer c2d Survey of Nearby Dense Cores. IV. Revealing the Embedded Cluster in B59, *ApJ*, 655, 364
- Brooke, T. Y., Tokunaga, A. T., Weaver, H. A., Crovisier, J., Bockelee-Morvan, D., & Crisp, D. 1996, Detection of acetylene in the infrared spectrum of Comet Hyakutake, *Nature*, 383, 606
- Brown, J. M. & et al. 2007, Cold Disks: Spitzer Spectroscopy of Disks around Young Stars with Large Gaps, *ApJ*, in prep
- Bushouse, H. A. et al. 2002, Ultraluminous Infrared Galaxies: Atlas of Near-Infrared Images, *ApJS*, 138, 1
- Calvet, N., D'Alessio, P., Hartmann, L., Wilner, D., Walsh, A., & Sitko, M. 2002, Evidence for a Developing Gap in a 10 Myr Old Protoplanetary Disk, *ApJ*, 568, 1008
- Carr, J. S., Evans, II, N. J., Lacy, J. H., & Zhou, S. 1995, Observation of Infrared and Radio Lines of Molecules toward GL 2591 and Comparison to Physical and Chemical Models, *ApJ*, 450, 667
- Carr, J. S., Tokunaga, A. T., & Najita, J. 2004, Hot H₂O Emission and Evidence for Turbulence in the Disk of a Young Star, *ApJ*, 603, 213
- Cesaroni, R. 2005a, in IAU Symposium, ed. R. Cesaroni, M. Felli, E. Churchwell, & M. Walmsley, 59
- Cesaroni, R. 2005b, Outflow, Infall, and Rotation in High-Mass Star Forming Regions, *Ap&SS*, 295, 5
- Cesaroni, R., Neri, R., Olmi, L., Testi, L., Walmsley, C. M., & Hofner, P. 2005, A study of the Keplerian accretion disk and precessing outflow in the massive protostar IRAS 20126+4104, *A&A*, 434, 1039
- Charnley, S. B. 1997, Sulfuretted Molecules in Hot Cores, *ApJ*, 481, 396
- Charnley, S. B., Tielens, A. G. G. M., & Millar, T. J. 1992, On the molecular complexity of the hot cores in Orion A - Grain surface chemistry as 'The last refuge of the scoundrel', *ApJ*, 399, L71
- Choe, J. I., Kwak, D. K., & Kukolich, S. G. 1987, Fourier Transform Spectra of the 2100 cm⁻¹ Bands of HCN, *Journal of Molecular Spectroscopy*, 121, 75
- Choe, J. I., Tipton, T., & Kukolich, S. G. 1986, Fourier Transform Spectra of the 3300 per Centimeter Bands of HCN, *Journal of Molecular Spectroscopy*, 117, 292
- Cieza, L. A. & et al. 2007, The *Spitzer* c2d Survey of Weak-line T Tauri Stars II: New Constraints on the Timescale for Planet Building, *ApJ*, in prep
- Clarke, C. 2006, The formation of high mass stars, *Journal of Physics Conference Series*, 54, 190
- Clarke, C. J., Gendrin, A., & Sotomayor, M. 2001, The dispersal of circumstellar discs: the role of the ultraviolet switch, *MNRAS*, 328, 485
- Cunha, K., Hubeny, I., & Lanz, T. 2006, Neon Abundances in B Stars of the Orion Association: Solving the Solar Model Problem?, *ApJ*, 647, L143
- D'Alessio, P., Calvet, N., Hartmann, L., Franco-Hernández, R., & Servín, H. 2006, Effects of Dust Growth and Settling in T Tauri Disks, *ApJ*, 638, 314
- D'Alessio, P., Calvet, N., Hartmann, L., Lizano, S., & Cantó, J. 1999, Accretion Disks around Young Objects. II. Tests of Well-mixed Models with ISM Dust, *ApJ*, 527, 893
- Darling, J. & Giovanelli, R. 2002, A Search for OH Megamasers at $z > 0.1$. III. The Complete Survey, *AJ*, 124, 100
- Dartois, E., D'Hendecourt, L., Boulanger, F., Jourdain de Muizon, M., Breitfellner, M., Puget, J.-L., & Habing, H. J. 1998, Molecular gas phase counterparts to solid state grain mantles features: implication for gas/grain chemistry, *A&A*, 331, 651
- Dartois, E., Dutrey, A., & Guilloteau, S. 2003, Structure of the DM Tau Outer Disk: Probing the vertical kinetic temperature gradient, *A&A*, 399, 773
- de Geus, E. J., de Zeeuw, P. T., & Lub, J. 1989, Physical parameters of stars in the Scorpio-Centaurus OB association, *A&A*, 216, 44
- de Graauw, T. et al. 1996, Observing with the ISO Short-Wavelength Spectrometer., *A&A*, 315, L49
- de Zeeuw, P. T., Hoogerwerf, R., de Bruijne, J. H. J., Brown, A. G. A., & Blaauw, A. 1999, A HIPPARCOS Census of the Nearby OB Associations, *AJ*, 117, 354
- Decin, L., Morris, P. W., Appleton, P. N., Charmandaris, V., Armus, L., & Houck, J. R. 2004, MARCS: Model Stellar Atmospheres and Their Application to the Photometric Calibration of the Spitzer Space Telescope Infrared Spectrograph (IRS), *ApJS*, 154, 408
- Dent, W. R. F., Greaves, J. S., & Coulson, I. M. 2005, CO emission from discs around isolated HAeBe and Vega-excess stars, *MNRAS*, 359, 663

- Doppmann, G. W., Greene, T. P., Covey, K. R., & Lada, C. J. 2005, The Physical Natures of Class I and Flat-Spectrum Protostellar Photospheres: A Near-Infrared Spectroscopic Study, *AJ*, 130, 1145
- Doty, S. D., van Dishoeck, E. F., van der Tak, F. F. S., & Boonman, A. M. S. 2002, Chemistry as a probe of the structures and evolution of massive star-forming regions, *A&A*, 389, 446
- Downes, D. & Solomon, P. M. 1998, Rotating Nuclear Rings and Extreme Starbursts in Ultraluminous Galaxies, *ApJ*, 507, 615
- Draine, B. T. 2003, Interstellar Dust Grains, *ARA&A*, 41, 241
- Drake, J. J., Testa, P., & Hartmann, L. 2005, X-Ray Diagnostics of Grain Depletion in Matter Accreting onto T Tauri Stars, *ApJ*, 627, L149
- Dullemond, C. P. & Dominik, C. 2004, Flaring vs. self-shadowed disks: The SEDs of Herbig Ae/Be stars, *A&A*, 417, 159
- Dullemond, C. P., Hollenbach, D., Kamp, I., & D'Alessio, P. 2007, in *Protostars and Planets V*, ed. B. Reipurth, D. Jewitt, & K. Keil, 555
- Dutrey, A., Guilloteau, S., & Guelin, M. 1997, Chemistry of protosolar-like nebulae: The molecular content of the DM Tau and GG Tau disks., *A&A*, 317, L55
- Dutrey, A., Guilloteau, S., & Simon, M. 2003, The BP Tau disk: A missing link between Class II and III objects?, *A&A*, 402, 1003
- Duvert, G., Guilloteau, S., Ménard, F., Simon, M., & Dutrey, A. 2000, A search for extended disks around weak-lined T Tauri stars, *A&A*, 355, 165
- Duxbury, G. & Gang, Y. 1989, Fourier transform spectroscopy of HCN in the 14 μ m region, *Journal of Molecular Spectroscopy*, 138, 541
- Ehrenfreund, P., Boogert, A. C. A., Gerakines, P. A., Tielens, A. G. G. M., & van Dishoeck, E. F. 1997, Infrared spectroscopy of interstellar apolar ice analogs, *A&A*, 328, 649
- Ehrenfreund, P. & Charnley, S. B. 2000, Organic Molecules in the Interstellar Medium, Comets, and Meteorites: A Voyage from Dark Clouds to the Early Earth, *ARA&A*, 38, 427
- Eisloffel, J., Mundt, R., Ray, T. P., & Rodriguez, L. F. 2000, in *Protostars and Planets IV*, ed. V. Mannings, A. P. Boss, & S. S. Russell, 815
- Enoch, M. L. et al. 2006, Bolocam Survey for 1.1 mm Dust Continuum Emission in the c2d Legacy Clouds. I. Perseus, *ApJ*, 638, 293
- Evans, II, N. J. et al. 2003, From Molecular Cores to Planet-forming Disks: An SIRTIF Legacy Program, *PASP*, 115, 965
- Evans, II, N. J., Lacy, J. H., & Carr, J. S. 1991, Infrared molecular spectroscopy toward the Orion IRC2 and IRC7 sources - A new probe of physical conditions and abundances in molecular clouds, *ApJ*, 383, 674
- Feigelson, E. D. & Lawson, W. A. 2004, An X-Ray Census of Young Stars in the Chamaeleon I North Cloud, *ApJ*, 614, 267
- Feuchtgruber, H. et al. 2003, in *ESA SP-481: The Calibration Legacy of the ISO Mission*, ed. L. Metcalfe, A. Salama, S. B. Peschke, & M. F. Kessler, 67
- Forrest, W. J. et al. 2004, Mid-infrared Spectroscopy of Disks around Classical T Tauri Stars, *ApJS*, 154, 443
- Gail, H.-P. 2002, Radial mixing in protoplanetary accretion disks. III. Carbon dust oxidation and abundance of hydrocarbons in comets, *A&A*, 390, 253
- Gao, Y. & Solomon, P. M. 2004, The Star Formation Rate and Dense Molecular Gas in Galaxies, *ApJ*, 606, 271
- Geballe, T. R., Goto, M., Usuda, T., Oka, T., & McCall, B. J. 2006, The Interstellar Medium of IRAS 08572+3915 NW: H₃⁺ and Warm High-Velocity CO, *ApJ*, 644, 907
- Geers, V. C. et al. 2006, C2D Spitzer-IRS spectra of disks around T Tauri stars. II. PAH emission features, *A&A*, 459, 545
- Genzel, R. & Cesarsky, C. J. 2000, Extragalactic Results from the Infrared Space Observatory, *ARA&A*, 38, 761
- Genzel, R. et al. 1998, What Powers Ultraluminous IRAS Galaxies?, *ApJ*, 498, 579
- Gerakines, P. A. et al. 1999, Observations of Solid Carbon Dioxide in Molecular Clouds with the Infrared Space Observatory, *ApJ*, 522, 357
- Gibb, E. L. et al. 2000, An Inventory of Interstellar Ices toward the Embedded Protostar W33A, *ApJ*, 536, 347
- Glassgold, A. E. & Langer, W. D. 1973, Cosmic-Ray Heating and Molecular Cooling of Dense Clouds, *ApJ*, 179, L147
- Glassgold, A. E., Najita, J., & Igea, J. 2004, Heating Protoplanetary Disk Atmospheres, *ApJ*, 615, 972
- Glassgold, A. E., Najita, J. R., & Igea, J. 2007, Neon Fine-Structure Line Emission by X-Ray Irradiated Protoplanetary Disks, *ApJ*, 656, 515
- Gorti, U. & Hollenbach, D. 2004, Models of Chemistry, Thermal Balance, and Infrared Spectra from Intermediate-Aged Disks around G and K Stars, *ApJ*, 613, 424
- Gray, R. O. & Corbally, C. J. 1994, The calibration of MK spectral classes using spectral synthesis. 1: The

- effective temperature calibration of dwarf stars, *AJ*, 107, 742
- Greaves, J. S. 2005, Disks Around Stars and the Growth of Planetary Systems, *Science*, 307, 68
- Habart, E., Natta, A., Testi, L., & Carillet, M. 2006, Spatially resolved PAH emission in the inner disks of Herbig Ae/Be stars, *A&A*, 449, 1067
- Haisch, Jr., K. E., Lada, E. A., & Lada, C. J. 2001, Disk Frequencies and Lifetimes in Young Clusters, *ApJ*, 553, L153
- Hartmann, L., Megeath, S. T., Allen, L., Luhman, K., Calvet, N., D'Alessio, P., Franco-Hernandez, R., & Fazio, G. 2005, IRAC Observations of Taurus Pre-Main-Sequence Stars, *ApJ*, 629, 881
- Hartmann, L. & Raymond, J. C. 1989, Wind-disk shocks around T Tauri stars, *ApJ*, 337, 903
- Harvey, P. M. et al. 2006, The Spitzer c2d Survey of Large, Nearby, Interstellar Clouds. II. Serpens Observed with IRAC, *ApJ*, 644, 307
- Helmich, F. P. 1996, PhD thesis, Leiden University
- Helmich, F. P. & van Dishoeck, E. F. 1997, Physical and chemical variations within the W3 star-forming region. II. The 345 GHz spectral line survey, *A&AS*, 124, 205
- Henning, T., Pfau, W., & Altenhoff, W. J. 1990, Infrared and radio emission from very young and massive stellar objects, *A&A*, 227, 542
- Herbst, E. 1995, Chemistry in the Interstellar Medium, *Annu. Rev. Phys. Chem.*, 46, 27
- Higdon, S. J. U. et al. 2004, The SMART Data Analysis Package for the Infrared Spectrograph on the Spitzer Space Telescope, *PASP*, 116, 975
- Hollenbach, D. 1997, in *IAU Symp. 182: Herbig-Haro Flows and the Birth of Stars*, ed. B. Reipurth & C. Bertout, 181
- Hollenbach, D. et al. 2005, Formation and Evolution of Planetary Systems: Upper Limits to the Gas Mass in HD 105, *ApJ*, 631, 1180
- Hollenbach, D. & McKee, C. F. 1989, Molecule formation and infrared emission in fast interstellar shocks. III - Results for J shocks in molecular clouds, *ApJ*, 342, 306
- Hollenbach, D. J., Takahashi, T., & Tielens, A. G. G. M. 1991, Low-density photodissociation regions, *ApJ*, 377, 192
- Hollenbach, D. J. & Tielens, A. G. G. M. 1999, Photodissociation regions in the interstellar medium of galaxies, *Reviews of Modern Physics*, 71, 173
- Hollenbach, D. J., Yorke, H. W., & Johnstone, D. 2000, in *Protostars and Planets IV*, 401
- Houck, J. R. et al. 2004, The Infrared Spectrograph (IRS) on the Spitzer Space Telescope, *ApJS*, 154, 18
- Ilgner, M., Henning, T., Markwick, A. J., & Millar, T. J. 2004, Transport processes and chemical evolution in steady accretion disk flows, *A&A*, 415, 643
- Imanishi, K., Koyama, K., & Tsuboi, Y. 2001, Chandra Observation of the ρ Ophiuchi Cloud, *ApJ*, 557, 747
- Imanishi, M., Nakanishi, K., & Kohno, K. 2006, Millimeter Interferometric Investigations of the Energy Sources of Three Ultraluminous Infrared Galaxies, UGC 5101, Markarian 273, and IRAS 17208-0014, Based on HCN-to-HCO⁺ Ratios, *AJ*, 131, 2888
- Irvine, W. M. & Bergin, E. A. 2000, in *Astrochemistry: From Molecular Clouds to Planetary*, ed. Y. C. Minh & E. F. van Dishoeck, 447
- Jonkheid, B., Dullemond, C. P., Hogerheijde, M. R., & van Dishoeck, E. F. 2007, Chemistry and line emission from evolving Herbig Ae disks, *A&A*, 463, 203
- Jonkheid, B., Faas, F. G. A., van Zadelhoff, G.-J., & van Dishoeck, E. F. 2004, The gas temperature in flaring disks around pre-main sequence stars, *A&A*, 428, 511
- Jonkheid, B., Kamp, I., Augereau, J.-C., & van Dishoeck, E. F. 2006, Modeling the gas-phase chemistry of the transitional disk around HD 141569A, *A&A*, 453, 163
- Jørgensen, J. K. et al. 2006, The Spitzer c2d Survey of Large, Nearby, Interstellar Clouds. III. Perseus Observed with IRAC, *ApJ*, 645, 1246
- Jørgensen, J. K., Schöier, F. L., & van Dishoeck, E. F. 2002, Physical structure and CO abundance of low-mass protostellar envelopes, *A&A*, 389, 908
- Kamp, I. & Dullemond, C. P. 2004, The Gas Temperature in the Surface Layers of Protoplanetary Disks, *ApJ*, 615, 991
- Kastner, J. H., Zuckerman, B., Weintraub, D. A., & Forveille, T. 1997, X-ray and molecular emission from the nearest region of recent star formation., *Science*, 277, 67
- Kaufman, M. J. 1995, PhD thesis, The Johns Hopkins University
- Kaufman, M. J., Wolfire, M. G., & Hollenbach, D. J. 2006, [Si II], [Fe II], [C II], and H₂ Emission from Massive Star-forming Regions, *ApJ*, 644, 283
- Kaufman, M. J., Wolfire, M. G., Hollenbach, D. J., & Luhman, M. L. 1999, Far-Infrared and Submillimeter Emission from Galactic and Extragalactic Photodissociation Regions, *ApJ*, 527, 795
- Kenyon, S. J., Dobrzycka, D., & Hartmann, L. 1994, A new optical extinction law and distance estimate for

- the Taurus-Auriga molecular cloud, *AJ*, 108, 1872
- Kenyon, S. J. & Hartmann, L. 1995, Pre-Main-Sequence Evolution in the Taurus-Auriga Molecular Cloud, *ApJS*, 101, 117
- Kessler-Silacci, J. et al. 2006, c2d Spitzer IRS Spectra of Disks around T Tauri Stars. I. Silicate Emission and Grain Growth, *ApJ*, 639, 275
- Kester, D. J. M. 2003, in *ESA SP-481: The Calibration Legacy of the ISO Mission*, ed. L. Metcalfe, A. Salama, S. B. Peschke, & M. F. Kessler, 243
- Kim, D.-C. & Sanders, D. B. 1998, The IRAS 1 Jy Survey of Ultraluminous Infrared Galaxies. I. The Sample and Luminosity Function, *ApJS*, 119, 41
- Koerner, D. W. & Sargent, A. I. 1995, Imaging the Small-Scale Circumstellar Gas Around T Tauri Stars, *AJ*, 109, 2138
- Kohno, K. 2005, in *AIP Conf. Proc. 783: The Evolution of Starbursts*, ed. S. Hüttmeister, E. Manthey, D. Bomans, & K. Weis, 203
- Kratter, K. M. & Matzner, C. D. 2006, Fragmentation of massive protostellar discs, *MNRAS*, 373, 1563
- Lacy, J. H., Carr, J. S., Evans, II, N. J., Baas, F., Achtermann, J. M., & Arens, J. F. 1991, Discovery of interstellar methane - Observations of gaseous and solid CH₄ absorption toward young stars in molecular clouds, *ApJ*, 376, 556
- Lacy, J. H., Evans, II, N. J., Achtermann, J. M., Bruce, D. E., Arens, J. F., & Carr, J. S. 1989, Discovery of interstellar acetylene, *ApJ*, 342, L43
- Lacy, J. H., Richter, M. J., Greathouse, T. K., Jaffe, D. T., & Zhu, Q. 2002, TEXES: A Sensitive High-Resolution Grating Spectrograph for the Mid-Infrared, *PASP*, 114, 153
- Lada, C. J. 1987, in *IAU Symp. 115: Star Forming Regions*, ed. M. Peimbert & J. Jugaku, 1
- Lahuis, F. & Boogert, A. 2003, in *SFChem 2002: Chemistry as a Diagnostic of Star Formation*, proceedings of a conference held August 21-23, 2002 at University of Waterloo, Waterloo, Ontario, Canada N2L 3G1. Edited by Charles L. Curry and Michel Fich. NRC Press, Ottawa, Canada, 2003, p. 335., ed. C. L. Curry & M. Fich, 335
- Lahuis, F. et al. 2006a, c2d Spectroscopy Explanatory Supplement, Tech. rep., Cores to Disks, *Spitzer* legacy team, Pasadena: *Spitzer* Science Center
- Lahuis, F. & van Dishoeck, E. F. 1997, in *ESA SP-419: The first ISO workshop on Analytical Spectroscopy*, ed. A. M. Heras, K. Leech, N. R. Trams, & M. Perry, 275
- Lahuis, F. & van Dishoeck, E. F. 2000, ISO-SWS spectroscopy of gas-phase C₂H₂ and HCN toward massive young stellar objects, *A&A*, 355, 699
- Lahuis, F., van Dishoeck, E. F., Blake, G. A., II, E. N. J., Kessler-Silacci, J. E., & Pontoppidan, K. M. 2007, c2d *Spitzer* IRS Spectra of Disks around T Tauri Stars. III. [Ne II] and H₂ gas-phase lines, *ApJ*, submitted
- Lahuis, F. et al. 2006b, Hot Organic Molecules toward a Young Low-Mass Star: A Look at Inner Disk Chemistry, *ApJ*, 636, L145
- Lahuis, F. et al. 1998, in *ASP Conf. Ser. 145: Astronomical Data Analysis Software and Systems VII*, ed. R. Albrecht, R. N. Hook, & H. A. Bushouse, 224
- Langer, W. D., van Dishoeck, E. F., Bergin, E. A., Blake, G. A., Tielens, A. G. G. M., Velusamy, T., & Whittet, D. C. B. 2000, in *Protostars and Planets IV*, ed. V. Mannings, A. P. Boss, & S. S. Russell, 29
- Lee, H.-H., Bettens, R. P. A., & Herbst, E. 1996, Fractional abundances of molecules in dense interstellar clouds: A compendium of recent model results., *A&AS*, 119, 111
- Lepp, S. & Dalgarno, A. 1996, X-ray-induced chemistry of interstellar clouds., *A&A*, 306, L21
- Li, W., Evans, II, N. J., Jaffe, D. T., van Dishoeck, E. F., & Thi, W.-F. 2002, Photon-dominated Regions in Low-Ultraviolet Fields: A Study of the Peripheral Region of L1204/S140, *ApJ*, 568, 242
- Lorente, R. 1998, Spectral Resolution of SWS AOT 1, Tech. rep., Vilspa: ISO Data Centre
- Low, F. J., Cutri, R. M., Huchra, J. P., & Kleinmann, S. G. 1988, Infrared color-selected quasars and Seyfert 1 galaxies, *ApJ*, 327, L41
- Lutz, D., Veilleux, S., & Genzel, R. 1999, Mid-Infrared and Optical Spectroscopy of Ultraluminous Infrared Galaxies: A Comparison, *ApJ*, 517, L13
- Maloney, P. R., Hollenbach, D. J., & Tielens, A. G. G. M. 1996, X-Ray-irradiated Molecular Gas. I. Physical Processes and General Results, *ApJ*, 466, 561
- Markwick, A. J. & Charnley, S. B. 2004, Chemistry of Protoplanetary Disks (*ASSL Vol. 305: Astrobiology: Future Perspectives*), 33
- Markwick, A. J., Ilgner, M., Millar, T. J., & Henning, T. 2002, Molecular distributions in the inner regions of protostellar disks, *A&A*, 385, 632
- Meijerink, R. & Spaans, M. 2005, Diagnostics of irradiated gas in galaxy nuclei. I. A far-ultraviolet and X-ray dominated region code, *A&A*, 436, 397
- Meyer, M. R. et al. 2002, in *The Origin of Stars and Planets: The VLT View*, ed. J. F. Alves & M. J. McCaugh-

- rean, 463
- Mihos, J. C. & Hernquist, L. 1996, Gasdynamics and Starbursts in Major Mergers, *ApJ*, 464, 641
- Millar, T. J., Bennett, A., Rawlings, J. M. C., Brown, P. D., & Charnley, S. B. 1991, Gas phase reactions and rate coefficients for use in astrochemistry - The UMIST ratefile, *A&AS*, 87, 585
- Millar, T. J., Farquhar, P. R. A., & Willacy, K. 1997, The UMIST Database for Astrochemistry 1995, *A&AS*, 121, 139
- Mitchell, G. F., Maillard, J.-P., Allen, M., Beer, R., & Belcourt, K. 1990, Hot and cold gas toward young stellar objects, *ApJ*, 363, 554
- Murphy, Jr., T. W., Armus, L., Matthews, K., Soifer, B. T., Mazzarella, J. M., Shupe, D. L., Strauss, M. A., & Neugebauer, G. 1996, Visual and Near-Infrared Imaging of Ultraluminous Infrared Galaxies: The IRAS 2 Jy Sample, *AJ*, 111, 1025
- Najita, J., Carr, J. S., & Mathieu, R. D. 2003, Gas in the Terrestrial Planet Region of Disks: CO Fundamental Emission from T Tauri Stars, *ApJ*, 589, 931
- Neufeld, D. A. & Kaufman, M. J. 1993, Radiative Cooling of Warm Molecular Gas, *ApJ*, 418, 263
- Nomura, H., Aikawa, Y., Tsujimoto, M., Nakagawa, Y., & Millar, T. J. 2007, Molecular Hydrogen Emission from Protoplanetary Disks II. Effects of X-ray Irradiation and Dust Evolution, *ArXiv Astrophysics e-prints*
- Nomura, H. & Millar, T. J. 2005, Molecular hydrogen emission from protoplanetary disks, *A&A*, 438, 923
- Parenago, P. P. 1954, Catalogue of stars in the area of the Orion Nebula., *Trudy Gosudarstvennogo Astronomicheskogo Instituta*, 25, 1
- Pascucci, I. et al. 2006, Formation and Evolution of Planetary Systems: Upper Limits to the Gas Mass in Disks around Sun-like Stars, *ApJ*, 651, 1177
- Persi, P., Ferrari-Toniolo, M., & Spinoglio, L. 1987, in *IAU Symp. 122: Circumstellar Matter*, ed. I. Appenzeller & C. Jordan, 93
- Piétu, V., Dutrey, A., & Guilloteau, S. 2007, Probing the structure of protoplanetary disks: a comparative study of DM Tau, LkCa 15 and MWC 480, *ArXiv Astrophysics e-prints*
- Pontoppidan, K. M. & Dullemond, C. P. 2005, Projection of circumstellar disks on their environments, *A&A*, 435, 595
- Pontoppidan, K. M., Dullemond, C. P., van Dishoeck, E. F., Blake, G. A., Boogert, A. C. A., Evans, II, N. J., Kessler-Silacci, J. E., & Lahuis, F. 2005, Ices in the Edge-on Disk CRBR 2422.8-3423: Spitzer Spectroscopy and Monte Carlo Radiative Transfer Modeling, *ApJ*, 622, 463
- Pontoppidan, K. M. et al. 2003, A 3-5 μ m VLT spectroscopic survey of embedded young low mass stars I. Structure of the CO ice, *A&A*, 408, 981
- Pontoppidan, K. M., Stapelfeldt, K. R., Blake, G. A., van Dishoeck, E. F., & Dullemond, C. P. 2007, Deep Spitzer spectroscopy of the 'Flying Saucer' edge-on disk: Large grains beyond 50 AU, *ArXiv Astrophysics e-prints*
- Porras, A. et al. 2007, The Spitzer c2d Survey of Large, Nearby, Interstellar Clouds. V. Chamaeleon II Observed with IRAC, *ApJ*, 656, 493
- Preibisch, T. et al. 2005, The Origin of T Tauri X-Ray Emission: New Insights from the Chandra Orion Ultra-deep Project, *ApJS*, 160, 401
- Prinn, R. G. 1993, in *Protostars and Planets III*, ed. E. H. Levy & J. I. Lunine, 1005
- Qi, C., Kessler, J. E., Koerner, D. W., Sargent, A. I., & Blake, G. A. 2003, Continuum and CO/HCO⁺ Emission from the Disk Around the T Tauri Star LkCa 15, *ApJ*, 597, 986
- Qi, C., Wilner, D. J., Calvet, N., Bourke, T. L., Blake, G. A., Hogerheijde, M. R., Ho, P. T. P., & Bergin, E. 2006, CO J = 6-5 Observations of TW Hydrae with the Submillimeter Array, *ApJ*, 636, L157
- Rebull, L. M. et al. 2007, The Spitzer c2d Survey of Large, Nearby, Interstellar Clouds: VI. Perseus Observed with MIPS, *ArXiv Astrophysics e-prints*
- Richter, M. J., Jaffe, D. T., Blake, G. A., & Lacy, J. H. 2002, Looking for Pure Rotational H₂ Emission from Protoplanetary Disks, *ApJ*, 572, L161
- Ridge, N. A. et al. 2006, The COMPLETE Survey of Star-Forming Regions: Phase I Data, *AJ*, 131, 2921
- Roche, P. F. & Aitken, D. K. 1984, An investigation of the interstellar extinction. I - Towards dusty WC Wolf-Rayet stars, *MNRAS*, 208, 481
- . 1985, An investigation of the interstellar extinction. II - Towards the mid-infrared sources in the Galactic centre, *MNRAS*, 215, 425
- Rodgers, S. D. & Charnley, S. B. 2003, Chemical Evolution in Protostellar Envelopes: Cocoon Chemistry, *ApJ*, 585, 355
- Roelfsema, P. R., Kester, D. J. M., Wesselius, P. R., Sym, N., Leech, K., & Wieprecht, E. 1993, in *ASP Conf. Ser. 52: Astronomical Data Analysis Software and Systems II*, ed. R. J. Hanisch, R. J. V. Brissenden, & J. Barnes, 254
- Roelfsema, P. R. et al. 2003, in *ESA SP-481: The Calibration Legacy of the ISO Mission*, ed. L. Metcalfe,

- A. Salama, S. B. Peschke, & M. F. Kessler, 31
- Roellig, M. et al. 2007, A PDR-Code Comparison Study, ArXiv Astrophysics e-prints
- Rothman, L. S. et al. 1992, The HITRAN molecular data base - Editions of 1991 and 1992, *Journal of Quantitative Spectroscopy and Radiative Transfer*, 48, 469
- Sako, S., Yamashita, T., Kataza, H., Miyata, T., Okamoto, Y. K., Honda, M., Fujiyoshi, T., & Onaka, T. 2005, Search for 17 μm H₂ Pure Rotational Emission from Circumstellar Disks, *ApJ*, 620, 347
- Sanders, D. B., Soifer, B. T., Elias, J. H., Madore, B. F., Matthews, K., Neugebauer, G., & Scoville, N. Z. 1988a, Ultraluminous infrared galaxies and the origin of quasars, *ApJ*, 325, 74
- Sanders, D. B., Soifer, B. T., Elias, J. H., Neugebauer, G., & Matthews, K. 1988b, Warm ultraluminous galaxies in the IRAS survey - The transition from galaxy to quasar?, *ApJ*, 328, L35
- Schutte, W. A. et al. 1999, Weak ice absorption features at 7.24 and 7.41 μm in the spectrum of the obscured young stellar object W 33A, *A&A*, 343, 966
- Sheret, I., Ramsay Howat, S. K., & Dent, W. R. F. 2003, A search for H₂ around pre-main-sequence stars, *MNRAS*, 343, L65
- Shipman, R. F. et al. 2003, in *ESA SP-481: The Calibration Legacy of the ISO Mission*, ed. L. Metcalfe, A. Salama, S. B. Peschke, & M. F. Kessler, 107
- Shu, F. H., Adams, F. C., & Lizano, S. 1987, Star formation in molecular clouds - Observation and theory, *ARA&A*, 25, 23
- Solomon, P. M., Downes, D., Radford, S. J. E., & Barrett, J. W. 1997, The Molecular Interstellar Medium in Ultraluminous Infrared Galaxies, *ApJ*, 478, 144
- Spoon, H. W. W. et al. 2004, Fire and Ice: Spitzer Infrared Spectrograph (IRS) Mid-Infrared Spectroscopy of IRAS F00183-7111, *ApJS*, 154, 184
- Spoon, H. W. W., Keane, J. V., Cami, J., Lahuis, F., Tielens, A. G. G. M., Armus, L., & Charmandaris, V. 2005, in *IAU Symposium*, ed. D. C. Lis, G. A. Blake, & E. Herbst, 281
- Spoon, H. W. W., Marshall, J. A., Houck, J. R., Elitzur, M., Hao, L., Armus, L., Brandl, B. R., & Charmandaris, V. 2007, Mid-Infrared Galaxy Classification Based on Silicate Obscuration and PAH Equivalent Width, *ApJ*, 654, L49
- Spoon, H. W. W. et al. 2006, The Detection of Crystalline Silicates in Ultraluminous Infrared Galaxies, *ApJ*, 638, 759
- Stanford, S. A., Stern, D., van Breugel, W., & De Breuck, C. 2000, The FIRST Sample of Ultraluminous Infrared Galaxies at High Redshift. I. Sample and Near-Infrared Morphologies, *ApJS*, 131, 185
- Stäuber, P., Benz, A. O., Jorgensen, J. K., van Dishoeck, E. F., Doty, S. D., & van der Tak, F. F. S. 2006, Tracing high energy radiation with molecular lines near deeply embedded protostars, ArXiv Astrophysics e-prints
- Stäuber, P., Doty, S. D., van Dishoeck, E. F., & Benz, A. O. 2005, X-ray chemistry in the envelopes around young stellar objects, *A&A*, 440, 949
- Sternberg, A. & Neufeld, D. A. 1999, The Ratio of Ortho- to Para-H₂ in Photodissociation Regions, *ApJ*, 516, 371
- Straizys, V., Cernis, K., & Bartasiute, S. 1996, Interstellar extinction in the area of the Serpens cauda molecular cloud., *Baltic Astronomy*, 5, 125
- Strauss, M. A., Huchra, J. P., Davis, M., Yahil, A., Fisher, K. B., & Tonry, J. 1992, A redshift survey of IRAS galaxies. VII - The infrared and redshift data for the 1.936 Jansky sample, *ApJS*, 83, 29
- Takeuchi, T., Clarke, C. J., & Lin, D. N. C. 2005, The Differential Lifetimes of Protostellar Gas and Dust Disks, *ApJ*, 627, 286
- Telleschi, A., Guedel, M., Briggs, K. R., Audard, M., & Palla, F. 2006, X-ray Emission from T Tauri Stars and the Role of Accretion: Inferences from the XMM-Newton Extended Survey of the Taurus Molecular Cloud, ArXiv Astrophysics e-prints
- Thi, W. F. et al. 2001, H₂ and CO Emission from Disks around T Tauri and Herbig Ae Pre-Main-Sequence Stars and from Debris Disks around Young Stars: Warm and Cold Circumstellar Gas, *ApJ*, 561, 1074
- Thi, W.-F., van Zadelhoff, G.-J., & van Dishoeck, E. F. 2004, Organic molecules in protoplanetary disks around T Tauri and Herbig Ae stars, *A&A*, 425, 955
- van Boekel, R., Min, M., Waters, L. B. F. M., de Koter, A., Dominik, C., van den Ancker, M. E., & Bouwman, J. 2005, A 10 μm spectroscopic survey of Herbig Ae star disks: Grain growth and crystallization, *A&A*, 437, 189
- van Boekel, R., Waters, L. B. F. M., Dominik, C., Bouwman, J., de Koter, A., Dullemond, C. P., & Paresce, F. 2003, Grain growth in the inner regions of Herbig Ae/Be star disks, *A&A*, 400, L21
- van den Ancker, M. 1999, PhD thesis, University of Amsterdam
- van den Ancker, M. E., de Winter, D., & Tjin A Djie, H. R. E. 1998, HIPPARCOS photometry of Herbig Ae/Be stars, *A&A*, 330, 145
- van der Tak, F. F. S., van Dishoeck, E. F., Evans, II, N. J., Bakker, E. J., & Blake, G. A. 1999, The Impact of the

- Massive Young Star GL 2591 on Its Circumstellar Material: Temperature, Density, and Velocity Structure, *ApJ*, 522, 991
- van der Tak, F. F. S., van Dishoeck, E. F., Evans, II, N. J., & Blake, G. A. 2000, Structure and Evolution of the Envelopes of Deeply Embedded Massive Young Stars, *ApJ*, 537, 283
- van Dishoeck, E. F. 1998, in Chemistry and Physics of Molecules and Grains in Space. Faraday Discussions No. 109, 31
- van Dishoeck, E. F. & Blake, G. A. 1998, Chemical Evolution of Star-Forming Regions, *ARA&A*, 36, 317
- van Dishoeck, E. F. & Helmich, F. P. 1996, Infrared absorption of H₂O toward massive young stars., *A&A*, 315, L177
- van Dishoeck, E. F. et al. 1996, A search for interstellar gas-phase CO₂. Gas: solid state abundance ratios., *A&A*, 315, L349
- van Dishoeck, E. F. & Hogerheijde, M. R. 1999, in NATO ASIC Proc. 540: The Origin of Stars and Planetary Systems, ed. C. J. Lada & N. D. Kylafis, 97
- van Dishoeck, E. F. & Tielens, A. G. G. M. 2001, Space-borne observations of the lifecycle of interstellar gas and dust (Dordrecht: Kluwer: The Century of Space Science), 607
- van Zadelhoff, G.-J., van Dishoeck, E. F., Thi, W.-F., & Blake, G. A. 2001, Submillimeter lines from circumstellar disks around pre-main sequence stars, *A&A*, 377, 566
- Vandenbussche, B. et al. 2003, in ESA SP-481: The Calibration Legacy of the ISO Mission, ed. L. Metcalfe, A. Salama, S. B. Peschke, & M. F. Kessler, 455
- Veilleux, S., Goodrich, R. W., & Hill, G. J. 1997, Infrared Spectroscopy of Seyfert 2 Galaxies: A Look through the Obscuring Torus? II., *ApJ*, 477, 631
- Veilleux, S., Kim, D.-C., Sanders, D. B., Mazzarella, J. M., & Soifer, B. T. 1995, Optical Spectroscopy of Luminous Infrared Galaxies. II. Analysis of the Nuclear and Long-Slit Data, *ApJS*, 98, 171
- Viti, S. & Williams, D. A. 1999, Time-dependent evaporation of icy mantles in hot cores, *MNRAS*, 305, 755
- Walmsley, C. M. & Schilke, P. 1993, Observations of Hot Molecular Cores (Dust and Chemistry in Astronomy), 37
- Walmsley, M., Des Forêts, G. P., & Flower, D. 2005, in IAU Symposium, ed. D. C. Lis, G. A. Blake, & E. Herbst, 135
- Werner, M. W. et al. 2004, The Spitzer Space Telescope Mission, *ApJS*, 154, 1
- Whittet, D. C. B., Prusti, T., Franco, G. A. P., Gerakines, P. A., Kilkenny, D., Larson, K. A., & Wesselius, P. R. 1997, On the distance to the Chamaeleon I and II associations, *A&A*, 327, 1194
- Whittet, D. C. B. et al. 1996, An ISO SWS view of interstellar ices: first results., *A&A*, 315, L357
- Wieprecht, E. et al. 1998, in ASP Conf. Ser. 145: Astronomical Data Analysis Software and Systems VII, ed. R. Albrecht, R. N. Hook, & H. A. Bushouse, 279
- Wieprecht, E. et al. 2003, in ESA SP-481: The Calibration Legacy of the ISO Mission, ed. L. Metcalfe, A. Salama, S. B. Peschke, & M. F. Kessler, 285
- Wieprecht, E., Wiezorrek, E., & Haser, L. 2000, SWS-Detector Glitch Effect Correction, *Experimental Astronomy*, 10, 199
- Willner, S. P. et al. 1982, Infrared spectra of protostars - Composition of the dust shells, *ApJ*, 253, 174
- Wolk, S. J., Harnden, Jr., F. R., Flaccomio, E., Micela, G., Favata, F., Shang, H., & Feigelson, E. D. 2005, Stellar Activity on the Young Suns of Orion: COUP Observations of K5-7 Pre-Main-Sequence Stars, *ApJS*, 160, 423
- Young, C. H. et al. 2004, A "Starless" Core that Isn't: Detection of a Source in the L1014 Dense Core with the Spitzer Space Telescope, *ApJS*, 154, 396

Nederlandse Samenvatting

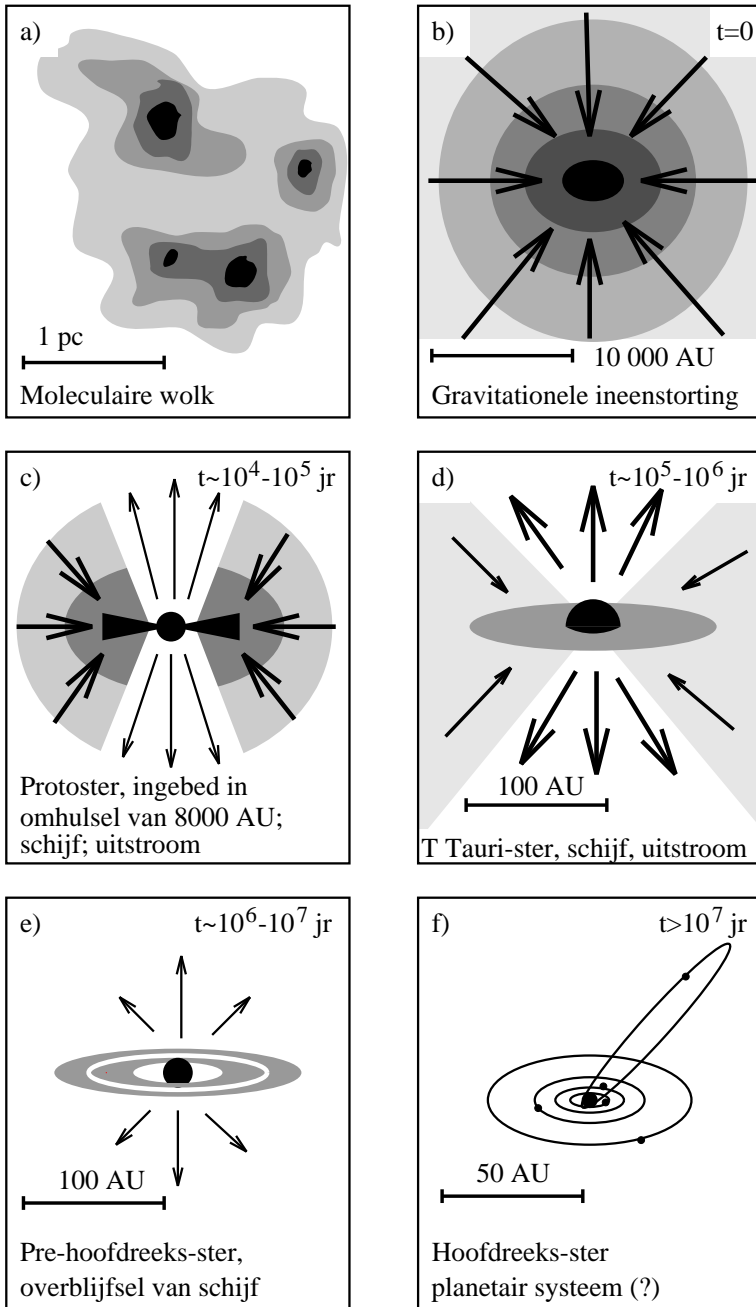
Het onderzoek in dit proefschrift concentreert zich op het warme gas dichtbij jonge pas gevormde sterren. De bestudeerde gebieden bevinden zich zowel in ons Melkwegstelsel als ook in ver verwijderde sterrenstelsels. Om dit gas waar te nemen is gebruik gemaakt van instrumenten aan boord van satellieten buiten de dampkring van onze aarde. Of zoals in de titel van mijn proefschrift is verwoord:

*Moleculaire vingerafdrukken van stervorming door het heelal
– een infrarood studie vanuit de ruimte –*

Een belangrijk deel van de sterrenjeugd vindt plaats in gebieden waar met het blote oog niets te zien is. Sterren worden geboren in dichte wolken van koud stof en gas die vrijwel geen zichtbaar licht doorlaten. De stofdeeltjes zijn kleine silicaat deeltjes zoals het zand aan het Noordzeestrand, maar dan veel kleiner. Het gas bestaat voornamelijk uit waterstof, de brandstof van sterren. Het stof neemt de energie van het zichtbare licht van de jonge sterren op, wordt warmer en straalt warmtestraling (infrarood licht) uit.

Het zichtbare licht dat wij mensen kunnen zien is maar een klein deel van het spectrum waaruit licht bestaat. Naast de zichtbare kleuren die we zien in een regenboog, bevinden zich röntgen (X-ray), ultraviolet (UV), en het voornoemde infrarood licht. Sommige dieren hebben ogen die gevoelig zijn voor UV of infrarood licht. De ogen van valken zijn bijvoorbeeld gevoelig voor ultraviolet licht om de urine-sporen van muizen te zien die sterk oplichten in het UV. Padden, adders en veel vissen kunnen infrarood licht zien zodat zij in het donker een prooi kunnen onderscheiden als die warmer is dan de omgeving.

Als wij mensen in het donker willen zien moeten we gebruik maken van instrumenten zoals nachtkijkers. Voor de bestudering van jonge sterren diep in grote stofwolken is dat echter niet voldoende. Ook infrarood camera's op grote telescopen zijn niet toereikend. Onze dampkring bestaat voor een groot gedeelte uit stoffen zoals waterdamp en koolstofdioxide. Deze moleculen absorberen heel efficiënt infrarood licht. Het gevolg is dat er vrijwel niets van de infrarood straling uit de ruimte op de aarde terechtkomt. Om deze toch waar te kunnen nemen moeten we infrarood instrumenten in de ruimte buiten de dampkring van onze aarde plaatsen aan boord van satellieten.



Michiel Hogerheijde (1998, proefschrift), naar Shu, Adams, & Lizano (1987).

Figure 1 Een pictogram weergave van lage massa stervorming met aangegeven de typische tijdsfasen voor de verschillende stadia in de ontwikkeling van de ster en de bijbehorende afmetingen. AU staat voor astronomical unit en is gelijk aan de gemiddelde afstand van de aarde tot de zon, ongeveer 150 miljoen kilometer. Een pc (parsec) is gelijk aan ongeveer 206 duizend AU.

Kosmische kraamkamers

Sterren ontstaan in een grote variëteit van klein tot super groot en worden ruwweg ingedeeld in lage massa sterren en hoge massa sterren. Lage massa sterren hebben een massa en lichtsterkte tot een paar maal die van de zon (één zonsmassa = 2×10^{30} kg). Hoge massa sterren hebben massa's tot een aantal tientallen zonsmassa met een lichtsterkte tot wel honderd duizendmaal die van de zon.

De geboorte van een ster begint als een deel van een koude stof- en gaswolk ineens stort. Dit kan spontaan gebeuren als in een deel van de wolk een voldoende grote concentratie aan stof en gas is zodat dit deel van de wolk door zijn eigen zwaartekracht instort. Ook kunnen sterren gevormd worden als er een drukgolf door de wolk gaat die het gas en stof sterk samenperst. Zo'n drukgolf kan bijvoorbeeld afkomstig zijn van supernovae, massieve sterren die aan het eind van hun leven exploderen, dichtbij de wolk.

De meest extreme vorm van stervorming, een sterren geboortegolf, vindt plaats in de kernen van sommige sterrenstelsels. Als twee sterrenstelsels elkaar op korte afstand passeren of elkaar raken wordt het stof en gas sterk samengedrukt. Dit kan zo sterk zijn dat op vrijwel hetzelfde moment door het gehele stelsel sterren gevormd worden, dit noemen sterrenkundigen een *starburst*. Een extreme vorm van starburst activiteit vinden we in de centrale delen van ULIRGs (Ultra Luminous Infrared Galaxies, super heldere infrarode sterrenstelsels). ULIRGs komen meestal voort uit de botsing van twee sterrenstelsels waarbij vrijwel al het stof in het centrum wordt samengeperst en een extreme starburst ontstaat. ULIRGs behoren tot de meest heldere objecten in het gehele heelal, zo helder als honderden normale sterrenstelsels zoals ons Melkwegstelsel tezamen. Figuur 1.2 laat een bekende starburst, M82, zien. Deze laat een plaatje zien in voor ons zichtbaar licht (links) en een in infrarood licht (rechts). Links lijkt M82 een vrij normaal stelsel, echter het infrarood geeft een heel ander beeld. Daar zien we een enorme hoeveelheid gas dat door de starburst, veroorzaakt door de gravitationele inwerking van de grote broer M81, sterk verhit is en uit het stelsel wordt weggeblazen alsof het gehele stelsel explodeert.

Lage massa versus hoge massa jonge sterren

Het best bestudeerde scenario van stervorming is dat van lage massa sterren. Er zijn een paar eenvoudige redenen waarom dit zo is. De eerste is simpelweg dat de meeste sterren die gevormd worden een lage massa hebben. De tweede reden is dat de tijdsperiode waarover lage massa sterren gevormd worden (enkele miljoenen jaren) een factor tien langer is dan die voor hoge massa sterren. Jonge hoge massa sterren worden bovendien gedurende een relatief langere tijd omgeven door een dicht omhulsel van stof en gas. Hierdoor zijn de hoge massa jonge sterren zelf en hun directe omgeving moeilijker te bestuderen.

De groei van een lage massa ster doorloopt een viertal stadia. In het begin is de net gevormde ster geheel omgeven door een wolk van stof en gas. Doordat er altijd wel enige vorm van draaiing in de wolk aanwezig is vormt er zich een schijf van stof en gas om de ster. De nog aanwezige wolk wordt door sterwinden langzaam aan weggeblazen en de ster met schijf blijft over. In deze schijf kunnen zich later planeten vormen. Het overgebleven gas wordt als de ster bijna volwassen is als het ware uit de

schijf verdampt en een ster met mogelijk een planetenstelsel blijft over. Figuur 1 geeft een pictogram weergave van de verschillende ontwikkelingsstadia van een lage massa ster.

Een actuele vraag is of hoge massa sterren een vergelijkbare ontwikkeling doormaken. De laatste paar jaar zijn er aanwijzingen dat dit inderdaad het geval kan zijn. Een hoge massa ster heeft echter een veel sterker stralingsveld die inwerkt op zijn omgeving. Het kan dus zijn dat bij veel hoge massa sterren zich wel een schijf vormt, maar dat deze schijf ook snel weer vernietigd wordt.

Een belangrijk verschijnsel in de ontwikkeling van hoge massa sterren is de *hot-core* fase. De hot-core ontstaat door de inwerking van het sterke stralingsveld van de jonge massieve ster op de wolk om de ster. Hierdoor wordt het binnenste deel hiervan zeer heet, tot wel meer dan 1000 °C, en neemt de druk sterk toe. Deze combinatie van een hoge druk en een hoge temperatuur zorgt voor een bijzondere chemie waarbij de aanmaak van bepaalde moleculen zoals aceyleen en blauwzuur zeer groot is.

Chemische laboratoria

Stervormingsgebieden zijn als het ware super chemische fabrieken. De processen die zich afspelen in deze gebieden zijn zeer gevarieerd. Voordat sterren gevormd worden is de wolk zeer koud en bevinden veel van de moleculen, zoals water, koolstofdioxide, methaan, en koolstofmonoxide, zich in laagjes ijs op de stofdeeltjes. In deze ijslagen vinden reacties plaats tussen de moleculen en kunnen er grotere en complexere moleculen gevormd worden. Als een ster zich vormt en de wolk instort wordt deze van binnenuit door de ster opgewarmd. De ijslagen verdampen van de stofdeeltjes en de moleculen die zich in het ijs bevinden, het water, koolstofdioxide, methaan, koolstofmonoxide, en de complexere moleculen, veranderen zodoende de samenstelling van het gas. Bovendien veranderen bij het opwarmen de chemische reacties en worden er andere moleculen gemaakt dan op het koude ijsoppervlak op de stofdeeltjes.

Welke reacties overheersen hangt af van de plaats waar het ijs en gas zich bevindt. In gebieden die blootstaan aan de directe straling van de ster worden veel van de complexere moleculen weer afgebroken en vind je meer kleine moleculen en atomen, de bouwstenen waaruit moleculen zijn opgebouwd. In gebieden die afgeschermd worden maar wel voldoende verhit worden kunnen de moleculen overleven en vinden gas-fase reacties plaats die de aanwezigheid van bepaalde molecuulsoorten sterk verhogen. In gebieden die verder verwijderd of sterk afgeschermd zijn van het sterlicht wordt de temperatuur niet hoog genoeg om de ijslagen van het stof af te dampen. Ook kan gas dat bij hogere temperaturen van samenstelling veranderd is door turbulentie naar koudere gebieden getransporteerd worden waar het weer uit kan vriezen op de stofdeeltjes.

Een deel van het stof, ijs, en gas met de eenvoudige en ook complexe moleculen zal deel gaan uitmaken van planeten, hun manen, en de kometen. De samenstelling en verdere ontwikkeling van de planeten en hun manen zal dan ook sterk afhangen van waar deze gevormd worden. Zo bestaat de atmosfeer van Venus voor het grootste gedeelte uit koolstofdioxide met wolken van zwavelzuur. De atmosfeer van Titan, de grootste maan van Saturnus, bestaat voor een groot gedeelte uit stikstof en methaan, zoals de aardse oeratmosfeer er waarschijnlijk uit heeft gezien.

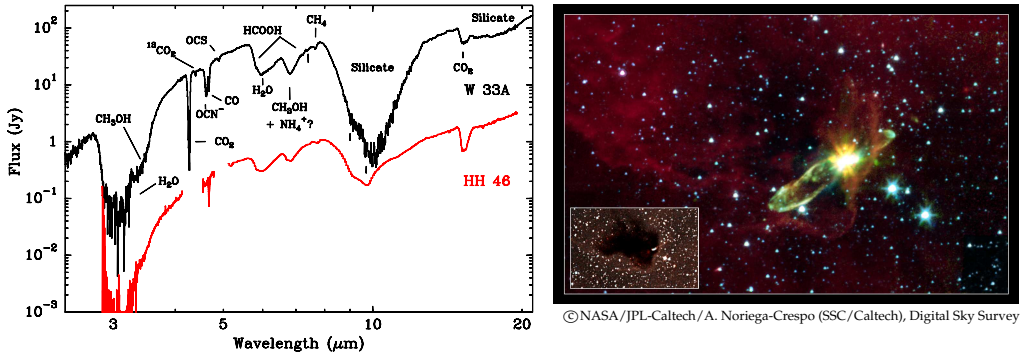


Figure 2 Links een deel van het ISO SWS spectrum van de massieve jonge ster W33A en een deel van het *Spitzer* IRS spectrum van de lage massa ster HH 46 plus spectra bij 3 en 4 μm van de grond. Met name het spectrum van W33A laat een grote verscheidenheid aan spectrale vingerafdrukken zien. Dit zijn absorptiebanden van silicaat stofdeeltjes en van moleculen in ijs, zoals water (H_2O), koolstofmonoxide (CO), koolstofdioxide (CO_2), en methaan (CH_4). Het rechter plaatje laat een *Spitzer* infrarode opname zien van HH 46 met gas weggeblazen van de jonge ster. Het kleine plaatje linksonder in beeld toont een opname in zichtbaar licht van hetzelfde gebied. Hier is alleen een donkere vlek, de wolk waarin HH 46 zich bevindt, te zien. De protooster zelf is onzichtbaar in zichtbaar licht.

Infrarood spectroscopie

Moleculen zijn opgebouwd uit atomen volgens een voor ieder molecuul unieke structuur. Deze structuur ligt vast, maar het molecuul kan wel vibreren, roteren, en uitrekken. Deze bewegingen zijn niet continue, maar vinden plaats in discrete stappen, van één toestand naar een andere. Als een molecuul in een andere toestand overgaat verandert zijn energietoestand. Deze energieverandering vindt plaats middels het uitzenden of absorberen van licht. De golflengte of kleur hiervan is direct gerelateerd aan de energieovergangen die verschillend zijn voor alle overgangen en voor verschillende moleculen.

Moleculen in gas en ijs die zich bevinden voor een sterk stralende achtergrond zien we over het algemeen in absorptie. Moleculen en atomen die zich niet voor een heldere achtergrond bevinden kunnen we, als ze genoeg verhit worden, in emissie zien doordat ze licht uitstralen. Aan de hand van de golflengte van de absorptie of emissie lijnen kunnen we bepalen welke moleculen er in het gas of het ijs aanwezig zijn. Uit de sterkte van verschillende lijnen van een molecuul of de vorm van een absorptieband (een golflengtegebied waar veel lijnen dicht bij elkaar liggen en niet afzonderlijk zijn waar te nemen) kunnen we afleiden hoeveel van die moleculen er zijn en welke temperatuur ze hebben.

Deze informatie gebruiken we vervolgens om uit te vinden wat de structuur, de dichtheid en de temperatuur, van de wolk is. De verhouding waarin de moleculen aanwezig zijn vertelt ons iets over de chemische en fysieke processen die zich afspelen in het gebied. Dit geeft ons dan weer informatie over de ontwikkelingsfase waarin het bestudeerde object zich bevindt.

Dit proefschrift

In dit proefschrift maak ik gebruik van twee infrarood instrumenten aan boord van twee verschillende satellieten. De eerste is de Short Wave Spectrometer (SWS), gebouwd in Groningen, aan boord van de Infrared Space Observatory (ISO) van de Europese ruimtevaart organisatie ESA. ISO was operationeel van eind 1995 tot midden 1998. Het tweede instrument is de Infrared Spectrograph (IRS) aan boord van de *Spitzer* ruimte telescoop. De *Spitzer* telescoop is gelanceerd op 25 Augustus 2003 en is nog steeds operationeel.

Met de SWS zijn spectra van massieve jonge sterren waargenomen die gebruikt zijn om moleculen te bestuderen die karakteristiek zijn voor de hot-cores, het hete compacte binnenste van de omhulsels om deze jonge sterren (Hoofdstuk 4). Deze zelfde moleculen zijn vervolgens bestudeerd in *Spitzer* spectra van geheel andere objecten. Als eerste was dat in het spectrum van IRS 46, een jonge lage massa ster (Hoofdstuk 7 en Figuur 1.3 in de introductie van dit proefschrift). Gebruikmakend van theoretische modellen kon worden aangetoond dat deze moleculen zich in het hete binnenste deel van de schijf om deze jonge ster bevinden, in het gebied waar zich later planeten kunnen vormen. Daarna werden dezelfde moleculen ontdekt in de spectra van kernen van super heldere sterrenstelsels (ULIRGs) op een afstand van meer dan honderd miljoen lichtjaar (één lichtjaar is 9.460.730.472.580.800 meter). In Hoofdstuk 8 worden deze spectra geanalyseerd en wordt aangetoond dat deze moleculen waarschijnlijk geassocieerd zijn met sterke stervorming, lokale starburst concentraties, verborgen in de compacte kernen van deze sterrenstelsels. In Hoofdstuk 5 en 6 worden spectrale lijnen van waterstof en atomen, waargenomen met *Spitzer* gebruikt voor het bestuderen van het gas om lage massa sterren. In Hoofdstuk 5 is dit het gas in de schijven rond deze sterren en in Hoofdstuk 6 in de omhulsels om nog jongere sterren waarbij de ster en de schijf nog niet zichtbaar zijn. De waargenomen lijnen worden gebruikt om te achterhalen welke processen een rol spelen bij het verwarmen van het gas om lage massa sterren.

De toekomst

De toekomst voor onderzoek aan stervormingsgebieden is zeer veelbelovend. Op dit moment zijn er meerdere grote projecten met infrarood en submillimeter (straling met een iets langere golflengte dan infrarood) instrumenten in ontwikkeling die in de komende tien jaar operationeel zullen zijn. Voor onderzoek in het verlengde van wat is gepresenteerd in dit proefschrift is het Mid-Infrared Instrument (MIRI) voor de James Webb ruimte telescoop van groot belang. MIRI bestrijkt ongeveer hetzelfde golflengtegebied als de *Spitzer* IRS maar heeft een nog grotere gevoeligheid, een grotere spiegel waardoor het kleinere ruimtelijke details waar kan nemen, en een grotere spectrale resolutie waardoor de spectrale lijnen en banden van de moleculen nauwkeuriger waargenomen kunnen worden. MIRI is nu in ontwikkeling en de James Webb ruimte telescoop wordt in 2013 gelanceerd.

Curriculum Vitae

Op 4 April 1965 zag ik het levenslicht in het Drentse Smilde. Aldaar heb ik tijdens mijn jeugd een goede basis gelegd voor mijn latere studie in Groningen door niet alleen examen voor Mavo en Havo te doen, maar ook nog voor het Atheneum. Na in 1985 één jaar natuurkunde te hebben gestudeerd koos ik voor de studie sterrenkunde. Tijdens de studie organiseerde ik in 1989, namens de fysisch mathematische faculteitsvereniging (FMF), een studiereis naar de Sovjet Unie met bezoeken aan Leningrad, Moskou, Novosibirsk en Kalinin, waarvan ook een reisverslag is gepubliceerd. In de twee laatste jaren van mijn studie werkte ik, als uitzendkracht, bij SRON voor software ontwikkeling en gebruikers ondersteuning voor de IRAS satelliet. Mijn afstudeerscriptie ging over "Radio continuum properties and extinction of H II regions in the spiral galaxy Messier 33."

Na mijn afstuderen ging ik als support astronoom aan de slag op het Rutherford Appleton Laboratory (RAL) dichtbij Oxford te Groot-Brittannië, dit keer voor de nieuwe satelliet ISO. Toen deze gelanceerd was, werd ik al snel betrokken bij het SWS Instrument Dedicated Team te Villafranca op de Spaanse hoogvlakte. Samen met mijn vriendin Claudia ging ik in El Escorial wonen en genoten wij van het mooie Spaanse land. Een van de vele reizen voerde mij naar Erice op Sicilie om een zomerschool te volgen alwaar ik kennis maakte met mijn latere promotor, Professor Ewine van Dishoeck. Mijn wetenschappelijke belangstelling kreeg hier een nieuwe richting door samen met haar te beginnen aan een onderzoek over de vorming van massieve sterren. In 1998 vertrokken Claudia en ik weer naar Groningen, onze dochter Rosana zat echter al in de buik van haar moeder.

Van 1998 tot 2001 was ik werkzaam bij SRON-Groningen als software engineer voor pipeline en gebruikers software van ISO-SWS. Eind 2001 werd onze tweede dochter Marike geboren. Van 2002 tot 2005 was ik in dienst van de Universiteit van Leiden voor datareductie voor het *Spitzer* legacy team "From Cores to Disks" (c2d). Daarnaast maakte ik al een begin met wat later mijn promotieonderzoek zou worden. In 2005 was ik drie en halve maand werkzaam op het Max Planck Instituut te Heidelberg binnen de "Star and Planet Formation" groep o.l.v. Professor Thomas Henning. Mijn gezin heeft een deel van de tijd ook in Duitsland gewoond.

Na dit Duitse uitstapje werkte ik van zomer 2005 tot heden aan mijn promotieonderzoek over moleculaire vingerafdrukken van stervorming in gebieden binnen ons eigen Melkwegstelsel en in de kernen van ver verwijderde sterrenstelsels. Na mijn promotie ga ik beginnen aan een nieuw avontuur met het MIRI instrument voor de James Webb ruimte telescoop.

Papers in Refereed Journals

- Lahuis, F., et al., *c2d Spitzer IRS Spectra of Disks around T Tauri Stars. III. [Ne II] and H₂ Gas-Phase Lines*, 2007, ApJ, submitted
- Merín, B., et al., *Abundant Crystalline Silicates in the Disk of a Very Low Mass Star*, 2007, ApJ, in press
- Lahuis, F., et al., *Infrared Molecular Starburst Fingerprints in Deeply Obscured (U)LIRG Nuclei*, 2007, ApJ, in press
- Quanz, S. P., Henning, Th., Bouwman, J., Linz, H., Lahuis, F., *Deeply Embedded Objects and Shocked Molecular Hydrogen: The Environment of the FU Orionis Stars RNO 1B/1C*, 2007, ApJ, in press
- Pontoppidan, K. M., et al., *Modeling Spitzer Observations of VV Ser. I. The Circumstellar Disk of a UX Orionis Star*, 2007, ApJ, 656, 980
- Geers, V. C., et al., *C2D Spitzer IRS Spectra of Disks Around T Tauri Stars. II. PAH Emission Features*, 2006, A&A, 459, 545
- Kessler-Silacci J., et al., *c2d Spitzer IRS Spectra of Disks around T Tauri Stars. I. Silicate Emission and Grain Growth*, 2006, ApJ, 639, 275
- Lahuis F., et al., *Hot Organic Molecules toward a Young Low-Mass Star: A Look at Inner Disk Chemistry*, 2006, ApJ, 636, L145
- Knez C., et al., *Spitzer Mid-Infrared Spectroscopy of Ices toward Extincted Background Stars*, 2005, ApJ, 635, L145
- Jørgensen J. K., Lahuis F., et al., *Protostellar Holes: Spitzer Space Telescope Observations of the Protostellar Binary IRAS 16293-2422*, 2005, ApJ, 631, L77
- Pontoppidan K. M., et al., *Ices in the Edge-on Disk CRBR 2422.8-3423: Spitzer Spectroscopy and Monte Carlo Radiative Transfer Modeling*, ApJ, 2005, 622, 463
- Boogert A. C. A., et al., *Spitzer Space Telescope Spectroscopy of Ices toward Low-Mass Embedded Protostars*, 2004, ApJS, 154, 359
- Boonman A. M. S., van Dishoeck E. F., Lahuis F., et al., *Gas-phase CO₂, C₂H₂, and HCN toward Orion-KL*, 2003, A&A 399, 1047
- Boonman A. M. S., van Dishoeck E. F., Lahuis F., Doty S. D., *Gas-phase CO₂ toward Massive Protostars*, 2003, A&A, 399, 1063
- Lahuis F. & van Dishoeck E. F., *ISO-SWS Spectroscopy of Gas-Phase C₂H₂ and HCN toward Massive Young Stellar Objects*, 2000, A&A 355, p. 699
- Heras A. M., et al., *The ISO-SWS Detectors: Performance Trends and Space Radiation Effects*, 2000, Experimental Astronomy, 10, 177
- Beintema D. A., van Hoof P. A. M., Lahuis F., et al., *The Central Stars of the Planetary Nebulae NGC 7027 and NGC 6543.*, 1996, A&A 315, L253
- Roelfsema P. R., de Jong T. and Lahuis F., *The Heritage of the IRAS Low Resolution Spectrograph*, 1996, Infrared Physics, 2/3, 439
- Lynch D. K., et al., *IRAS LRS Spectra of Comets Tempel 1 and Tempel 2.*, 1995, Icarus, 114, 197

Nawoord

De eigenlijke basis voor dit proefschrift is jaren geleden gelegd, op een bankje naast het kasteel van Erice tijdens een zomerschool van Mayo Greenberg. Tijdens mijn werk in Vilspa zocht ik mogelijkheden om meer te doen met de SWS data. Na een zeer nuttig gesprek met de SWS P.I. Thijs de Graauw besloot ik de stoute schoenen aan te trekken en contact op te nemen met Professor Ewine van Dishoeck. Ik was verheugd over het enthousiasme en de openheid waarmee zij mijn verzoek ontving. In Erice kwamen we snel tot het besluit om samen aan een artikel over massieve jonge sterren te werken. Deze samenwerking mondde later uit in mijn werk voor het c2d team en nu in deze promotie.

Een proefschrift geschreven na meer dan 10 jaar predoc ervaring kent natuurlijk veel inspiratiebronnen. Er zijn dan ook teveel mensen die ik zou moeten noemen en voor wie ik mijn waardering moet uitspreken. Een aantal van hen wil ik hier onder de aandacht brengen, als groep of bij naam. Het ISO support team en het ISO LWS team op Rutherford en met name mijn kamergenoten Sarah en David. Het SIDT team plus aanhang en alle andere teams in Vilspa voor een paar zeer aangename jaren in Spanje. Bart die behalve een goed collega ook een plezierig huisgenoot was in het Casita. Alle ISO promovendi en postdocs waarvan ik meerdere nog regelmatig tegenkom op conferenties en werkbezoeken. Henrik waarmee ik in 1994 al door het Spaanse land fietste. Annemieke met wie ik heel veel ISO spectra heb bekeken. Mijn DIDAC collegae voor een fijne ISO post-mission tijd. Alle collegae in Groningen en Leiden en met name de leden van de astrochemistry en ISM groepen. De laatste jaren natuurlijk de leden van het c2d IRS team. Jes en Klaus die er altijd voor in waren om met mij uit eten te gaan en na te tafelen in de Burcht. Professor Thomas Henning, dankzij wie ik een tijd in Heidelberg heb kunnen werken. Jeroen, Sascha en de andere mensen op MPIA die gezorgd hebben dat ik daar met veel plezier heb gewerkt. De geldschietters, met name het LKBF, die het mij mogelijk maakten om naar conferenties te gaan en werkbezoeken naar het buitenland te maken. SRON, die mij de laatste jaren een werkplek verschaftte en mijn laatste promotiejaar gefinancierd heeft.

Ik kan natuurlijk niet eindigen zonder mijn vriendin en onze fantastische dochters te noemen. Claudia, Rosana en Marike zijn voor mij het belangrijkste wat er is. Rosana en Marike, het was altijd erg fijn om al die leuke verhalen en tekeningen via de e-mail te krijgen als ik weer eens op reis was naar Amerika, of een ander ver oord.